Phase stability and defect structures in (Ti1-x,Alx)Ny hard coatings

Katherine Calamba

▶ **To cite this version:**

Katherine Calamba. Phase stability and defect structures in (Ti1-x,Alx)Ny hard coatings. Materials. Université de Lorraine; Université de Linköping (Suède), 2019. English. NNT : 2019LORR0322 . tel-02875071

HAL Id: tel-02875071

https://hal.univ-lorraine.fr/tel-02875071

Submitted on 19 Jun 2020

HAL is a multi-disciplinary open access archive for the deposit and dissemination of scientific research documents, whether they are published or not. The documents may come from teaching and research institutions in France or abroad, or from public or private research centers.

L'archive ouverte pluridisciplinaire **HAL**, est destinée au dépôt et à la diffusion de documents scientifiques de niveau recherche, publiés ou non, émanant des établissements d'enseignement et de recherche français ou étrangers, des laboratoires publics ou privés.

AVERTISSEMENT

Ce document est le fruit d'un long travail approuvé par le jury de soutenance et mis à disposition de l'ensemble de la communauté universitaire élargie.

Il est soumis à la propriété intellectuelle de l'auteur. Ceci implique une obligation de citation et de référencement lors de l'utilisation de ce document.

D'autre part, toute contrefaçon, plagiat, reproduction illicite encourt une poursuite pénale.

Contact : ddoc-theses-contact@univ-lorraine.fr

LIENS

Code de la Propriété Intellectuelle. articles L 122. 4
Code de la Propriété Intellectuelle. articles L 335.2- L 335.10
http://www.cfcopies.com/V2/leg/leg_droi.php
http://www.culture.gouv.fr/culture/infos-pratiques/droits/protection.htm

UNIVERSITÉ DE LORRAINE

Institut Jean Lamour

École doctorale C2MP

THÈSE

Pour l'obtention du titre de

DOCTEUR de L'UNIVERSITÉ DE LORRAINE

Science et Ingénierie des Matériaux

Présentée par:

Katherine CALAMBA

Phase stability and defect structures in $(Ti_{1-x},Al_x)N_y$ hard coatings

Thèse soutenue publiquement le 18 Juin 2019 à Linköping devant le jury composé de:

Gregory ABADIAS	Professeur, Physics Department, University of Poitiers (UP)	Rapporteur
Mats HALVARSSON	Professeur, Department of Physics, Chalmers University of Technology	Rapporteur
Ru PENG	Professeur, Department of Management and Engineering (IEI), Linköping University	Examinateur
David HORWAT	Professeur, Institut Jean Lamour, Université de Lorraine (Nancy)	Examinateur
Ching-Lien HSIAO	Associate Professor (Docent), IFM, Linköping University	Invité
Jean-François PIERSON	Professeur, Institut Jean Lamour, Université de Lorraine (Nancy)	Directeur de Thèse
Magnus Odén	Professeur, IFM, Linköping University	Co-directeur de Thèse

Institut Jean Lamour - UMR 7198 - Département CP2S - Equipe 202 POEME
2 allée André Guinier - Campus Artem - BP 50840 - 54011 NANCY Cedex
Université de Lorraine - Pôle M4 : matière, matériaux, métallurgie, mécanique

Linköping Studies in Science and Technology
Dissertation No. 1996

Phase stability and defect structures in (Ti,Al)N hard coatings

Katherine Calamba

Nanostructured Materials
Department of Physics, Chemistry, and Biology (IFM)
Linköping University, Sweden

Part of
Joint European Doctoral Program in Materials Science and Engineering (DocMASE) in collaboration of Institute Jean Lamour
University of Lorraine, France

2019

© [Katherine Calamba, 2019]

Printed in Sweden by LiU-Tryck, Linköping 2019

ISSN: 0345-7524
ISBN: 978-91-7685-041-1

Abstract

This study highlights the role of nitrogen vacancies and defect structures in engineering hard coatings with enhanced phase stability and mechanical properties for high temperature applications. Titanium aluminum nitride (Ti,Al)N based materials in the form of thin coatings has remained as an outstanding choice for protection of metal cutting tools due to its superior oxidation resistance and high-temperature wear resistance. High-temperature spinodal decomposition of metastable (Ti,Al)N into coherent c-TiN and c-AlN nm-sized domains results in high hardness at elevated temperatures. Even higher thermal input leads to transformation of c-AlN to w-AlN, which is detrimental to the mechanical properties of the coating. One mean to delay this transformation is to introduce nitrogen vacancies.

In this thesis, I show that by combining a reduction of the overall N-content of the c-(Ti,Al)N_y ($y < 1$) coating with a low substrate bias voltage during cathodic arc deposition an even more pronounced delay of the c-AlN to w-AlN phase transformation is achieved. Under such condition, age hardening is retained until 1100 ˚C, which is the highest temperature reported for (Ti,Al)N films. During cutting operations, the wear mechanism of the cathodic-arc-deposited c-($Ti_{0.52}Al_{0.48}$)N_y with N-contents of y = 0.92, 0.87, and 0.75 films are influenced by the interplay of nitrogen vacancies, microstructure, and chemical reactions with the workpiece material. The y = 0.75 coating contains the highest number of macroparticles and has an inhomogeneous microstructure after machining, which lower its flank and crater wear resistance. Age hardening of the y = 0.92 sample causes its superior flank wear resistance while the dense structure of the y = 0.87 sample prevents chemical wear that results in excellent crater wear resistance.

Heteroepitaxial c-(Ti_{1-x},Al_x)N_y (y = 0.92, 0.79, and0.67) films were grown on MgO(001) and (111) substrates using magnetron putter deposition to examine the details of their defect structures during spinodal decomposition. At 900 ˚C, the films decompose to form coherent c-AlN- and c-TiN- rich domains with elongated shape along the elastically soft <001> direction. Deformation maps show that most strains occur near the interface of the segregated domains and inside the c-TiN domains. Dislocations favorably aggregate in c-TiN rather than c-AlN because the later has stronger directionality of covalent chemical bonds. At elevated temperature, the domain size of (001) and (111)- oriented c-(Ti,Al)N_y films increases with the nitrogen content. This indicates that there is a delay in coarsening due to the presence of more N vacancies in the film.

The structural and functional properties $(Ti_{1-x},Al_x)N_y$ are also influenced by its Al content (x). TiN and $(Ti_{1-x},Al_x)N_y$ (y = 1, x = 0.63 and x = 0.77) thin films were grown on MgO(111) substrates using magnetron sputtering technique. Both TiN and $Ti_{0.27}Al_{0.63}N$ films are single crystals with cubic structure. $(Ti_{0.23},Al_{0.77})N$ film has epitaxial cubic structure only in the first few atomic layers then it transitions to an epitaxial wurtzite layer, with an orientation relationship of c-$(Ti_{0.23},Al_{0.77})$N(111)[1-10]||w-$(Ti_{0.23},Al_{0.77})$N(0001)[11-20]. The w-$(Ti_{0.23},Al_{0.77})N$ shows phase separation of coherent nm-sized domains with varying chemical composition during growth. After annealing at high temperature, the domains in w-$(Ti_{0.23},Al_{0.77})N$ have coarsened. The domains in w-$(Ti_{0.23},Al_{0.77})N$ are smaller compared to the domains in c-$(Ti_{0.27},Al_{0.63})N$ film that has undergone spinodal decomposition. The results that emerged from this thesis are of great importance in the cutting tool industry and also in the microelectronics industry, because the layers examined have properties that are well suited for diffusion barriers.

Résumé étendu

Cette étude met en évidence le rôle des lacunes d'azote et des défauts structuraux dans l'ingénierie de revêtements durs à stabilité de phase améliorée et dont les propriétés mécaniques sont compatibles avec des applications à haute température. Le nitrure de titane et d'aluminium (Ti,Al)N sous forme de revêtements est un matériau de choix pour la protection des outils de coupe pour métaux en raison de sa résistance supérieure à l'oxydation et à l'usure à haute température. La décomposition spinodale à haute température de la phase métastable cubique (Ti,Al)N en domaines cohérents de taille nanométrique de c-TiN et de c-AlN donne une dureté importante aux températures élevées. Un apport thermique encore plus élevé conduit à la transformation de c-AlN en w-AlN, ce qui nuit aux propriétés mécaniques du revêtement. Un moyen de retarder cette transformation est d'introduire des lacunes d'azote.

Dans cette thèse, je montre que la combinaison d'une réduction de la teneur globale en azote du revêtement c-(Ti,Al)N_y(y <1) avec une faible tension de polarisation du substrat lors du dépôt par arc cathodique induit un retard encore plus prononcé de la transformation de la phase c-AlN en w-AlN. Dans de telles conditions, le durcissement par vieillissement est conservé jusqu'à 1100 ° C, ce qui correspond à la température la plus élevée signalée pour les films de (Ti,Al)N. Au cours des opérations de coupe, le mécanisme d'usure des films c-($Ti_{0.52}$,$Al_{0.48}$)N_y déposés par arc cathodique avec des teneurs en N de y = 0.92, 0.87 et 0.75 est influencé par l'interaction des lacunes d'azote, de la microstructure et des réactions chimiques avec le matériau de la pièce. Le revêtement y = 0.75 contient le plus grand nombre de macroparticules et présente, après usinage, une microstructure non homogène qui en abaisse la résistance à l'usure sur les flancs et les cratères. Le durcissement par vieillissement de l'échantillon y = 0.92 entraîne une résistance supérieure à l'usure sur le flanc, tandis que la structure dense de l'échantillon y = 0.87 empêche l'usure chimique qui se traduit par une excellente résistance à l'usure sur les cratères.

Des films hétéroépitaxiés c-(Ti_{1-x},Al_x)N_y (y = 0.92, 0.79 et 0.67) ont été déposés sur des substrats de MgO(001) et (111) en utilisant une technique de pulvérisation magnétron pour examiner en détail les défauts structuraux pendant la décomposition spinodale. À 900 °C, les films se décomposent pour former des domaines cohérents riches en c-AlN et c-TiN de forme allongée le long de la direction <001>. Les cartographies de déformation montrent que la

plupart des contraintes se trouvent près de l'interface des domaines ségrégés et à l'intérieur des domaines c-TiN. Les dislocations s'agrègent favorablement dans c-TiN plutôt que dans c-AlN car ce dernier a une directionnalité plus forte des liaisons chimiques covalentes. À température élevée, la taille de domaine des films de c-(Ti,Al)N_y orientés (001) et (111) augmente avec la teneur en azote.

Les propriétés structurelles et fonctionnelles des films de (Ti_{1-x},Al_x)N_y sont également influencées par leur teneur en Al (x). Des films minces de TiN et (Ti_{1-x},Al_x)N (y = 1, x = 0.63 et x = 0.77) ont été déposés sur des substrats de MgO (111) en utilisant une technique de pulvérisation cathodique magnétron. Les films TiN et ($Ti_{0.37}$,$Al_{0.63}$)N sont des monocristaux à structure cubique. Le film ($Ti_{0.23}$,$Al_{0.77}$)N est épitaxié seulement dans les premières couches atomiques, puis il se transforme en une couche épitaxiée de wurtzite, avec une relation d'orientation de c-($Ti_{0.23}$,$Al_{0.77}$)N(111)[1-10]||w-($Ti_{0.23}$,$Al_{0.77}$)N(0001)[11-20]. Le w-($Ti_{0.23}$,$Al_{0.77}$)N montre une séparation de phases en domaines cohérents de taille nanométrique avec une composition chimique variable au cours de la croissance. Après recuit à haute température, les domaines de w-($Ti_{0.23}$,$Al_{0.77}$)N ont grossi mais restent plus petits que ceux du film c-($Ti_{0.27}$,$Al_{0.63}$)N ayant subi une décomposition spinodale. Les résultats de cette thèse revêtent une grande importance pour l'industrie des outils de coupe, ainsi que pour l'industrie de la microélectronique, car les couches ainsi développées ont des propriétés bien adaptées pour des applications en tant que barrières de diffusion.

Le but de cette étude est d'avoir une compréhension en profondeur de l'évolution de la microstructure, de la structure des défauts et des transitions de phases dans (Ti,Al)N. La première partie étudie la réponse thermique et l'évolution structurelle de films de c-(Ti,Al)N polycristallins déficitaires en azote élaborés avec différentes tensions de polarisation. Ensuite, des films de c-(Ti,Al)N ayant différentes teneurs en azote ont été soumis à un test de coupe du métal afin d'examiner leur mécanisme d'usure et leur comportement pendant l'utilisation. Cette étude vise également à déterminer l'évolution locale des contraintes et les détails de la structure des défauts lors de la décomposition spinodale en caractérisant des films monocristallins orientés (001)- et (111) orientés (N, Ti, Al) de composition chimique différente.

Cette thèse contient les articles annexés montrant des résultats complets. Le papier 1 aborde l'influence des défauts ponctuels générés lors du dépôt par arc cathodique sur la stabilité de phase et le développement microstructural de films minces de (Ti_{1-x},Al_x)N_y déficitaires en azote. L'influence de la tension de

polarisation sur la concentration de défauts ponctuels (par exemple auto-interstitiels et anti-sites) dans les alliages c-$(Ti_{0.54},Al_{0.46})N_{0.87}$ et, par conséquent, sur leurs propriétés microstructurales et mécaniques à hautes températures ont ainsi été montrées. L'amélioration de la force motrice pour la séparation de phase à une tension de polarisation élevée de -80 V a été montrée et attribuée à l'annihilation retardée des défauts ponctuels entraînant une augmentation de l'énergie interne du système. L'effet de durcissement par vieillissement des films est conservé jusqu'à 1100 °C (c'est-à-dire la température la plus élevée signalée pour les films de (Ti,Al)N en appliquant une tension de polarisation faible et en réduisant la concentration en azote du revêtement pendant le dépôt. Les résultats ouvrent des pistes de conception futures pour les revêtements de nitrure de métaux de transition et permettent de mieux comprendre l'effet des défauts ponctuels générés lors du dépôt physique en phase vapeur.

Le papier 2 présente les principaux facteurs influençant le comportement à l'usure des revêtements $(Ti_{1-x},Al_x)N_y$ déficitaires en azote lors du découpage à grande vitesse d'une pièce en acier. La condition de polarisation optimale précisée dans le document 1 a été utilisée pour la synthèse de films (Ti,Al)N avec différentes teneurs en azote. Ensuite, l'interaction des lacunes en azote, de la microstructure et de la réaction chimique des revêtements c-$(Ti_{0.52}Al_{0.48})N_y$ avec une concentration moyenne en N de y = 0.92, y = 0.87 et y = 0.75 a été étudiée. Le revêtement y = 0.75 contient le plus grand nombre de macroparticules et présente une microstructure non homogène après usinage contenant des phases c-$(Ti_{0.52}Al_{0.48})N_y$, Ti_2AlN (phase MAX) et des couches alternées de phases AlN et Fe-Ti à proximité des macroparticules. Dans ce cas, l'altération chimique au sein du revêtement et la présence de macroparticules ont contribué à sa relativement faible résistance à l'usure des flancs et des cratères. L'échantillon y = 0.92 présente une décomposition spinodale plus précoce en domaines riches en c-AlN et en c-TiN, par rapport aux autres échantillons. Cette structure décomposée présente des dislocations inadaptées (comme observé dans le document 3) qui ont provoqué la diffusion accélérée de Fe et de Co à partir de la pièce et du substrat à travers le revêtement, ce qui affaiblirait la structure du revêtement et le rendrait plus susceptible à l'usure. Il y a un retard dans la décomposition de l'échantillon y = 0.87, qui est causée par la présence de lacunes d'azote qui abaissent l'énergie libre du système. La survenue d'un durcissement lié au vieillissement dans l'échantillon y = 0.92 a entraîné une résistance supérieure à l'usure des flancs parmi les échantillons, tandis que la structure dense de l'échantillon y = 0.87 qui empêchait l'usure chimique due à la diffusion a provoqué son excellente résistance à l'usure dans les cratères. Cette étude donne un aperçu du rôle des lacunes d'azote dans la

réaction chimique et le comportement à l'usure des revêtements de nitrure de métal de transition au cours de l'usinage.

Le papier 3 s'attache à l'étude des défauts structuraux de la phase monocristalline de c-($Ti_{0.37}$,$Al_{0.63}$)N durant sa décomposition spinodale. Des couches minces hétéroépitaxiées de c-($Ti_{0.37}$,$Al_{0,63}$)N ont été déposées sur des substrats de MgO (001) et (111) par pulvérisation cathodique magnétron. Les films monocristallins avec un haut niveau de pureté permettent de déterminer les détails de leur structure de dislocation en utilisant des techniques de diffraction et d'imagerie à haute résolution. La qualité cristalline des films monocristallins (Ti,Al)N a été examinée par DRX à haute résolution, par cartographies réciproques (RSM) et par microscopie électronique à transmission par balayage en champ sombre annulaire à grand angle (HAADF-STEM). Les mesures RSM montrent que le film recuit (c'est-à-dire ayant subit une décomposition spinodale) a une corrélation latérale inférieure, une largeur à mi-hauteur plus importante et une mosaïté supérieure par rapport au film brut de dépôt. Les images HAADF-STEM montrent que les films ainsi déposés ont une composition homogène, sans signe de ségrégation élémentaire, tandis que les films recuits se décomposent pour former des domaines cohérents riches en c-AlN et c-TiN de forme allongée selon la direction <001>. Les cartographies de déformation contenant les composantes du tenseur de contraintes (par exemple ε_{xx}, ε_{yy} et ε_{xy}) de c-(Ti,Al)N ont été présentées pour la première fois dans cette étude par analyse de phase géométrique (GPA) sur des micrographies HAADF-STEM. Les résultats révèlent que les déformations se trouvent près de l'interface des domaines ségrégés et que les domaines c-TiN hébergent plus de dislocations que les domaines c-AlN. Ceci est attribué à la forte directionnalité des liaisons chimiques covalentes de c-AlN, qui permet aux dislocations de s'agréger favorablement dans c-TiN. Les résultats indiquent que l'état de la liaison chimique et les propriétés élastiques des domaines séparés affectent la structure des défauts de (Ti,Al)N pendant la décomposition spinodale.

Le papier 4 montre pour la première fois la croissance épitaxiale du film w-($Ti_{0.23}$,$Al_{0.77}$)N (0001) sur un substrat de MgO(111). Le film a été développé à 700 °C en utilisant un système de pulvérisation cathodique magnétron UHV DC. Un film monocristallin de c-($Ti_{0.23}$,$Al_{0.77}$)N est d'abord développé jusqu'à une épaisseur critique (entre 10 et 30 nm) en utilisant une couche tampon de TiN(111) déposée sur MgO(111). Au-delà de cette épaisseur, il se produit une transition de la structure cubique vers la structure wurtzite, avec une interface en zigzag entre les deux structures. L'interface présente une relation d'orientation de c-($Ti_{0.23}$,$Al_{0.77}$)N(111)[1-10]||w-($Ti_{0.23}$,$Al_{0.77}$)N(0001)[11-20]. La

poursuite des dépôts a pour conséquence une décomposition progressive de la croissance épitaxique en croissance polycristalline de colonnes de wurtzite à degré de texture élevé. Les images TEM dans le plan montrent que les grains de wurtzite grossissent à mesure que le film s'épaissit. Cette étude compare également la stabilité thermique des structures épitaxiques w-$(Ti_{0.23},Al_{0.77})N(0001)$ et c-$(Ti_{0.37},Al_{0.63})N(111)$. Le dépôt w-$(Ti_{0.23},Al_{0.77})N(0001)$ tel que déposé montre un regroupement de domaines cohérents de taille nanométrique tandis que c-$(Ti_{0.37},Al_{0.63})N(111)$ reste homogène. Après un recuit à 900 °C, le film cubique a subi une décomposition spinodale pour former des domaines allongés riches en c-AlN et c-TiN selon la direction [001] (c'est-à-dire comme indiqué dans le papier 3), tandis que le film de wurtzite présente des domaines de taille légèrement supérieure à celle du film bruet d'élaboration. La structure wurtzite présente une vitesse de grossissement plus lente comparée à celle de la forme cubique, ce qui indique une plus grande stabilité thermique.

Le papier 5 étudie la croissance et la stabilité thermique de films épitaxiés de $(Ti_{1-x},Al_x)N_y$ avec une teneur moyenne en azote de y = 0.67, 0.79 et 0.92 déposés par pulvérisation cathodique magnétron sur des substrats de MgO orientés (111) et (001) . L'épitaxie de c-$(Ti_{1-x},Al_x)N_y(111)$ sur MgO (111) est maintenue selon toute l'épaisseur du film. Les cartographies spatiales réciproques (RSM) de ces films montrent que la longueur de la corrélation latérale est supérieure et que la propagation de la mosaïcité est plus lente pour les films ayant une teneur en N plus faible. Des couches épitaxiques de c-$(Ti_{1-x},Al_x)N_y(001)$ ont été déposées sur MgO(001) pendant une certaine épaisseur (quelques nanomètres), puis une transition vers une croissance polycristalline se produit. L'épaisseur de la couche épitaxique de c-$(Ti_{1-x},Al_x)N_y(001)$ augmente à mesure que la teneur en azote diminue. La meilleure qualité cristalline des films à faible teneur en azote est attribuée à la grande mobilité de surface des cations dans des conditions déficitaires en azote. Les couches épitaxiées de c-(Ti,Al)N(111) et de c-(Ti,Al)N(001) sont homogènes à l'état déposé, puis des domaines ségrégés apparaissent après un recuit à 950 ° C. Les films c-(Ti,Al)N(111) ont des domaines plus grands que ceux de c-(Ti,Al)N(001) et la taille des domaines des films de c-(Ti,Al)N orientés (001) et (111) augmente avec la teneur en azote. Cela indique qu'il y a un retard dans le grossissement des grains en présence de lacunes d'azote. Des caractéristiques uniques sont observées dans les films de $(Ti_{1-x},Al_x)N_{0.67}$, qui contiennent la plus grande quantité de lacunes d'azote. Le film de $(Ti_{1-x},Al_x)N_{0.67}(111)$ sur MgO(111) cristallise dans une structure de type wurtzite avec une orientation cohérente avec w-$(Ti_{1-x},Al_x)N_{0.67}(0001)$ dans certaines régions situées au sommet du film. Le film de $(Ti_{1-x},Al_x)N_{0.67}(001)$ élaboré sur MgO(001) présente une

microstructure conique avec des domaines séparés déjà dès la synthèse des films et reste stable lorsqu'il est recuit à 950 °C. La taille de domaine de ce film augmente légèrement après le recuit à 1100 ºC. La vitesse de grossissement des domaines coniques est plus lente que celle des domaines de la couche épitaxiée à des températures élevées. La concentration de lacunes d'azote affecte la stabilité thermique des films minces épitaxiés $(Ti_{1-x},Al_x)N_y$.

Populärvetenskaplig Sammanfattning

Nitrider av övergångsmetaller är intressanta på grund av deras goda elektriska, termodynamiska och mekaniska egenskaper. Bland metallnitriderna uppvisar titanaluminiumnitrid (Ti,Al)N särskilt hög slitstyrka vid högtemperaturtillämpningar. Detta beror på en kombination av oxidationsbeständighet och åldringshärdning. Det senare kommer av ett spinodal sönderfall av den metastabila c-(Ti,Al)N fasen till c-TiN och c-AlN vid förhöjda temperaturer. Ytterligare temperaturökning resulterar i en transformation av c-AlN till dess mest stabila form, dvs wurtzit (w-AlN). Närvaro av wurtzit i skikten är menligt för dess mekaniska egenskaper. Fördröjning av fastransformationen av AlN är nödvändig för att förbättra den termiska stabiliteten och åstadkomma förbättringar av skiktets mekaniska egenskaper vid höga temperaturer. I denna avhandling har mikrostrukturen hos (Ti,Al)N-skikt studerats på detaljnivå, eftersom detta starkt påverkar skiktens fysikaliska egenskaper.

I den första delen av avhandlingen undersöks inverkan av substratpotentialen som används under tillväxt med katodförångning och kvävevakansinnehållet på den termiska stabiliteten hos $(Ti_{0.54},Al_{0.46})N_y$ (y <1) skikt. Katodförångning används ofta för beläggning av skikt inom skärverktygsindustrin på grund av att mycket god vidhäftning av skiktet till substratet erhålls och dess höga deponeringshastighet. $(Ti_{0.54},Al_{0.46})N_{0.87}$-skikt med lågt kväveinnehåll växtes med olika substratpotential, vilket medförde signifikanta förändringar av deras mikrostruktur. En fördröjning i fastransformationen av c-AlN till w-AlN uppnåddes genom att använda låg substratpotential under beläggningen och låg N-halt i skikten. Åldringshärdningsen behålls till 1100 ° C, dvs den högsta temperatur rapporterad för (Ti,Al)N. Vid svarvning påverkas också nötningsmekanismerna hos $(Ti_{0.52},Al_{0.48})N_y$-skikt på grund av samspelet mellan kvävevakanser, mikrostruktur och kemiska reaktioner med arbetsstycket .

Det finns många studier av effekten av deponeringsparametrar på egenskapen hos (Ti,Al)N skikt. Emellertid är mikrostrukturen för de flesta syntetiserade filmerna inte så välordnad vilket försvårar och ofta omöjliggör studier på en tillräckligt detaljerad nivå, t.ex. gällande defektstrukturer och termodynamik såväl som motsvarande funktionella egenskaper. Den andra delen av denna avhandling undersöker dislokationstrukturen och utvecklingen av lokala töjningar i enkristallina (Ti,Al)N skikt. DC magnetronsputtring är den beläggningsteknik som använts då den möjliggör syntes av homogena

mikrostrukturer och eliminerar närvaron av makropartiklar. Heteroepitaxiella c-(Ti_{1-x},Al_x)N_y(y = 0.92, 0.79 och 0.67) skikt växtes på MgO (001) och (111) substrat genom magnetronsputtring och detaljerna av deras defektstrukturer under spinodal sönderdelning undersöktes. Vid 900 ˚C segregerar skikten och bildar koherenta c-AlN- och c-TiN-rika domäner med långsträckt form längs den elastiskt komplianta <001> riktningen. Deformationskartor visar att töjningen är lokaliserad nära gränsytorna för de segregerade domänerna samt inuti c-TiN-domänerna. Domänstorleken för c-(Ti,Al)N_y-skikt med tillväxtriktning (001) och (111) ökar med kvävehalten, d.v.s. förgrovningen fördröjs i närvaron av N-vakanser i skiktet.

(Ti_{1-x},Al_x)N_y skikts strukturella och funktionella egenskaperna påverkas också av dess Al-innehåll (x). TiN och (Ti_{1-x},Al_x)N (x = 0.63 och x = 0.77) skikt växtes på MgO (111) substrat med magnetronsputtering. Både TiN och ($Ti_{0.27}$,$Al_{0.63}$)N-skikten är enkristaller med kubisk struktur medan ($Ti_{0.23}$,$Al_{0.77}$)N-skiktet har en epitaxiell kubisk struktur endast i de första atomlagren och sedan övergår till en eptitaxiell wurtzit struktur. w-($Ti_{0.23}$,$Al_{0.77}$)N visar klustring av koherenta Al- och Ti-rika nm-stora domäner medan c-($Ti_{0.27}$,$Al_{0.63}$)N är kemiskt homogen efter beläggningen. Efter värmebehandling vid hög temperatur sker kemisk segregation i den kubiska filmen och långsträckta c-AlN- och c-TiN-rika domäner har bildats via spinodal sönderfall medan wurtzitfilmen har en liknande mikrostruktur som innan värmebehandlingen.

Resultaten som framkommit i denna avhandling är av stor betydelse inom skärverktygsindustrin men också mikroelektronikindustrin, eftersom de undersökta skikten har egenskaper som är väl lämpade som diffusionsbarriärer.

Preface

This thesis is the summary of my doctoral studies conducted within the framework of the *Erasmus Mundus* Joint Doctoral Program in Material Science and Engineering (DocMASE) between October 2014 and June 2019. I worked in the research groups of Nanostructured Materials Division at the Department of Physics, Chemistry, and Biology (IFM) at Linköping University (Linköping, Sweden) and at the Elaboration et Fontionnalités de Couches Minces at the Intitut Jean Lamour (IJL) at Université de Lorraine (Nancy, France). The cathodic arc depositions were done in Seco Tools AB (Fagersta, Sweden). This work is financially supported by EU (DocMASE), the Swedish Research Council, and Vinnova (FunMat-II).

Katherine M. Calamba

Linköping, May 2019

Included papers and author's contribution

Paper 1

Enhanced thermal stability and mechanical properties of nitrogen deficient titanium aluminum nitride ($Ti_{0.54}Al_{0.46}N_y$) thin films by tuning the applied negative bias voltage

K. Calamba, I. Schramm, M. Johansson Jõesaar, J. Ghanbaja, J. Pierson, F. Mücklich, and M. Odén

Journal of Applied Physics 122, 065301 (2017)

Paper 2

The effect of nitrogen vacancies on initial wear in arc deposited ($Ti_{0.52}$,$Al_{0.48}$)N_y, ($y < 1$) coatings during machining

K. Calamba, M. Johansson Jõesaar, S. Bruyère, J. Pierson, R. Boyd, J. Andersson, M. Odén

Surface & Coatings Technology 358, 452–460 (2019)

Paper 3

Dislocation structure and microstrain evolution during spinodal decomposition of reactive magnetron sputtered heteroepixatial c-($Ti_{0.37}$,$Al_{0.63}$)N/c-TiN films grown on MgO(001) and (111) substrates

K. Calamba, J. Pierson, Bruyère, A. Febvrier, P. Eklund, J. Barrirero, F. Mücklich, R. Boyd, M.P. Johansson Jõesaar, and M. Odén

Journal of Applied Physics 125, 105301 (2019)

Paper 4

Growth and high temperature decomposition of epitaxial metastable wurtzite (Ti_{1-x},Al_x)N(0001) thin films

K. Calamba, J. Barrirero, M. Johansson Jõesaar, S. Bruyère, J. Pierson, A. Febvrier, Mücklich, R. Boyd, and M. Odén

Submitted for publication

Paper 5

Effect of vacancies on the dislocation structure and and phase stability of nitrogen deficient single crystal (Ti_{1-x},Al_x)N_y thin films

K. Calamba, J. Salamania, M. Johansson Jõesaar, R. Boyd, S. Bruyère, J. Pierson, M. Sortica, D. Primetzhofer, and M. Odén

In manuscript

Related but not included paper

Adhesive-deformation relationships and mechanical properties of nc-AlCrN/a-SiN_x hard coatings deposited at different bias voltages
M. Haršáni, N. Ghafoor, K. Calamba, P. Zacková, M. Sahul, T. Vopát, L. Satrapinskyy, M. Čaplovičová and Ľ. Čaplovič
Thin Solid Films 650, 11-19 (2018)

My contribution to the included papers

I was involved in the planning and design of the experiments. I took part in the cathodic arc depositions and did all the sputter depositions. I did the majority of the sample preparations and characterizations including differential scanning calorimetry, x-ray diffractometry (theta-2theta, phi scan, gracing incidence, residual stress measurements, pole figures, and reciprocal space maps), nanoindentation, 4-point probe, crater and flank wear measurements, scanning electron microscopy, ion milling, transmission electron microscopy and geometric phase analysis. I wrote the first draft of the papers.

Acknowledgements

I am very grateful for the valuable help and support of the following:

Magnus Odén, my supervisor in LiU.

Jean Pierson, my supervisor in UoL.

Mats Johansson Jöesaar, my supervisor in Seco Tools AB.

Collaborators. Isabella Schramm, Jeni Barrirero, Stéphanie Bruyere, Janella Salamania, Robert Boyd, Marian Haršáni, Per Eklund, Arnaud le Febvrier, Jaafar Ghanbaja, Mauricio Sortica, Daniel Primetzhofer, Franck Mücklich, and Jon Andersson.

Wei Wan, Sylvie Migot, Michelle Villamayor, Magnus Garbrecht, Fredrik Erickson, Alexandra Serban, and Davide Sangiovanni for their technical help and scientific input.

Research groups. Nanostructured Materials and Elaboration et Fontionnalités de Couches Minces.

Funding institutions. EU (DocMASE), the Swedish Research Council, and Vinnova (FunMat-II).

Friends in Linkoping University, University of Lorraine, University of the Philippines, TCSHS, Östergötland, and Värmland, especially Michelle, Martin, Sebastian, Jay-el, Klein, Janella, Rommel, Carl, Rafael, Tyna, Natalia, Yan, Hongling, Lianlian, Larry, Divina, Joyme, Vanessa, Karen, and Marjory.

Brethren in Lakas Angkan Inc. and Koinonia International, especially my bible study network, cell group (Desiree, Hajdi, Linda, Jovita, Dolores, and Sarah), Eliza, Esther ladies, Ate Ellen, Kuya Elson, Del Rosario family, and Rubio family.

Mark, Ate Luz, and my family (Lovenessa, Aristotle, Antonina, and Ernesto).

All glory to him who alone is God, our Savior through Jesus Christ our Lord. All glory, majesty, power, and authority are his before all time, and in the present, and beyond all time - *Jude 1:25.*

Contents

Acronyms and symbols

1D	one-dimensional
3D	three-dimensional
APT	atom probe tomography
c-	cubic crystal structure
DC	direct current
DSC	differential scanning calorimetry
E	internal energy
EDX	energy dispersive x-ray spectroscopy
EFTEM	energy filtered transmission electron microscopy
ERDA	elastic recoil detection
FFT	Fast Fourier transform
FIB	Focused ion beam
G	Gibb's free energy
GPA	geometric phase analysis
H	enthalpy
HAADF	high-angle annular dark field
HR	high resolution
P	pressure
PVD	physical vapor deposition
RBS	Rutherford backscattering spectrometry
RSM	reciprocal space maps
S	entropy
SAED	selected area electron diffraction
STEM	scanning transmission electron micrography
TEM	transmission electron microscopy
T	temperature
TOF	Time-of-flight
TMN	transition metal nitride
w-	wurtzite crystal structure
V	volume
XRD	X-ray diffractometry

1. Introduction

A majority of mechanical parts used in industries such as aerospace and power generation are used under severe working conditions. Steel and titanium or their alloys are the commonly utilized materials for such application because of their properties that are suitable for such conditions (e.g. high specific strength at high temperature, resistance to corrosion, and chemical inertness) [1, 2]. One of the outstanding challenges is to machine these materials into a specific geometry. Thus, it is necessary to have cutting tool materials that have high mechanical strength and have high resistance to the heat generated during the machining process. Coating deposition on carbide inserts has been developed for cutting applications because it results in higher wear and heat resistance than uncoated inserts and it improves the machining accuracy and lifetime of the mechanical parts [3-5].

Among the coating materials, titanium aluminum nitride (Ti,Al)N is a widely utilized material system because of its superior oxidation resistance and ability to age hardening [6, 7]. The latter attribute is due to the spinodal decomposition of metastable (Ti,Al)N into iso-structurally coherent c-TiN and c-AlN domains at elevated temperatures [8, 9]. Further annealing results in the transformation of c-AlN to its most stable form w-AlN, which is detrimental to the high temperature hardness of the coating [8]. Delaying the phase transformation of AlN is therefore necessary to enhance the thermal stability and mechanical properties of (Ti,Al)N.

The thermodynamics of a ternary alloy is mainly influenced by its chemical composition and point defect concentrations [10-12], besides external factors such as temperature and pressure. Investigating the materials related factors could lead to the determination of the optimum conditions for synthesizing hard coatings. *Ab initio* calculations recently showed that nitrogen vacancies have significant effect on the thermal stability of *c*-(Ti,Al)N [13]. Following reports have confirmed through experiments that N vacancies suppress the driving force for phase transformation and causes shifts of the c-AlN to w-AlN transformation to higher temperatures [14, 15].

In this study, the aim was to have an in-depth understanding of the microstructural evolution, defect structure and phase transitions in (Ti,Al)N. The first part investigates the thermal response and structural evolution of nitrogen deficient poly-crystalline *c*-(Ti,Al)N films with different applied negative bias voltage. Then, *c*-(Ti,Al)N films with different N contents were

subjected to metal cutting test to examine their wear mechanism and behavior during service. This study also aims to determine the local strain evolution and the details of the defect structure during spinodal decomposition by characterizing (001)- and (111)- oriented mono-crystalline (Ti,Al)N films with different chemical composition.

In chapter 2, the thermodynamics and kinetics of the phase transformation of (Ti,Al)N material system are presented. The role of point and line defects on the phase stability of (Ti,Al)N is elaborated in Chapter 3. Chapter 4 describes the physical vapor deposition techniques used to fabricate poly- and mono-crystalline films with different stoichiometry. The effect of the microstructural and chemical changes of the coatings after subjecting to metal cutting on the wear behavior are shown in Chapter 5. Chapter 6 describes the characterization techniques used in this thesis. A summary of the appended papers and the future work are presented in Chapter 7 and Chapter 8, respectively. The last part of the thesis contains the appended papers showing comprehensive results.

2. (Ti,Al)N hard coating

Thin ceramic coatings are used in cutting industries because they significantly improves the lifetime of cutting tools. Titanium nitride (TiN) is one of the first hard coatings utilized due to its high hardness, corrosion resistance, and aesthetic appearance (i.e. golden color). When Ti atoms in the metal sublattice of TiN are randomly replaced with Al, the $(Ti_{1-x},Al_x)N$ material system is formed. In cutting tool operations, this material offers numerous advantages as compared to TiN in terms of oxidation resistance and high temperature hardness [6, 16].

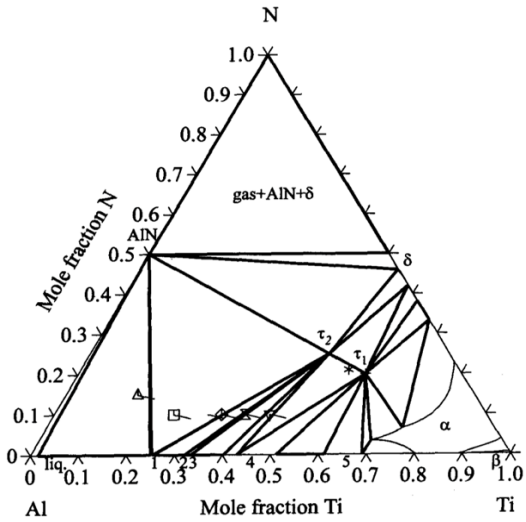

Fig 2.1. Phase diagram of Ti-Al-N system at 1000 °C. (τ_1:Ti_3AlN, τ_2:Ti_2AlN, δ: TiN, 1:$TiAl_3$, 2: Ti_5Al_{11}, 3:$TiAl_2$, 4: γTiAl, 5:αTi_3Al), reprinted with permission [17].

2.1 Phase Stability

The ternary phase diagram at 1000 °C of Ti-Al-N system is shown in Figure 2.1. In this material system, the Ti_3AlN and Ti_2AlN phases are the only stable ternary compounds. The widely utilized $(Ti_{1-x},Al_x)N_y$ is a metastable solid solution, which can be synthesized using thin film deposition techniques. Plasma based physical vapor deposition techniques (e.g. cathodic arc deposition and magnetron sputtering) enables the growth of metastable and non-equilibrium phases because of its low substrate temperature, which

quench a homogeneous solution into the miscibility gap [7, 18]. The coating deposition of $(Ti_{1-x},Al_x)N$ is further discussed in Chapter 4.

The thermodynamic stability of $(Ti_{1-x},Al_x)N$ solid solution can be described by its Gibb's free energy (G), which is a function of composition and temperature. The free energy of every system is given by:

$$G = E + PV - TS = H - TS \tag{2.1}$$

where E is the internal energy, H is the enthalpy, and S is the entropy of the system. The thermodynamic variables, P, V, and T are the pressure, volume, and temperature, respectively. From the Gibb's free energy vs. composition diagram at constant P and T, the region where the alloy is stable can be determined by constructing a common tangent of the free energy curve of each phase.

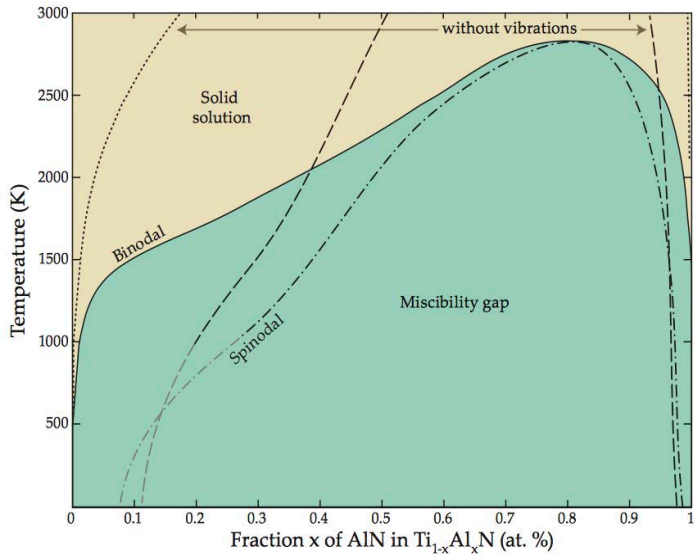

Figure 2.2. The calculated phase diagram of $(Ti_{1-x},Al_x)N$, reprinted with permission [19].

The calculated quasi-binary TiN-AlN phase diagram for $(Ti_{1-x},Al_x)N$ (Figure 2.2) shows a miscibility gap for wide range of x composition, which contains two distinct regions (i.e. spinodal and binodal). Inside the miscibility gap, it is favorable for phase separation to occur. In the spinodal region, the metastable c-$(Ti_{1-x},Al_x)N$ decompose spontaneously into isostructural and coherent c-TiN- and c-AlN- rich domains, while in the binodal region, the domains are formed through nucleation and growth. The alloy is within the spinodal region if the

second concentration derivative of the Gibb's free energy is negative, while it is in the binodal region if the second derivative is positive. The phase diagram also shows that when configurational and vibrational entropy are included, the maximum of the miscibility gap is lowered to 2860 K and the solubility of AlN in TiN is increased. Outside the miscibility gap, the solid solution of c-($Ti_{1-x}Al_x$)N system remains homogeneous at equilibrium. The asymmetric shape of the miscibility gap is due to the electronic structure mismatch between TiN and AlN [20]. The miscibility gap is skewed right, indicating that the there is a higher driving force for segregation of (Ti_{1-x},Al_x)N with a high Al content [19]. In addition, the phase stability of (Ti_{1-x},Al_x)N is also influenced by pressure [21-23]. These studies have shown that hydrostatic compression increases the tendency for spinodal decomposition and suppresses the formation of w-AlN phase.

2.2 Diffusional Transformations

The minimization of overall Gibb's free energy is the driving force for phase transformations [24]. Typical mechanisms for the transformation of (Ti_{1-x},Al_x)N alloys are spinodal decomposition and nucleation and growth [8, 10]. Up-hill diffusion occurs during spinodal decomposition while down-hill diffusion occurs during nucleation and growth [24]. Phase transformation occurs in (Ti_{1-x},Al_x)N alloys when subjected to high temperature because it enables diffusional processes to occur. The diffusion of atoms is the most fundamental process that occurs during such transformation because it results to a decrease in free energy of the system [25].

2.2.1 Spinodal decomposition

Spinodal decomposition is a process in which an alloy decomposes into two phases without a nucleation barrier [26]. The phase transformation is determined solely by diffusion since there is no thermodynamic barrier to the reaction. In a spinodal region, the alloy is unstable with respect to small compositional fluctuations [27]. The concentration gradient causes up-hill diffusion, in which atoms move towards regions already enriched of that atom [28].

At high temperature conditions, the c-(Ti_{1-x},Al_x)N system undergoes spinodal decomposition until a metastable state is reached, wherein nanometer-sized domains are formed [29]. This process has been experimentally verified by *in-*

situ high temperature synchrotron X-ray diffraction studies as a function of time and temperature, shown in Figure 2.3 [30]. As the temperature is increased, broadening of the c-$(Ti_{1-x},Al_x)N$ peaks occur (marked) indicating a gradual segregation of c-$(Ti_{1-x},Al_x)N$ into coherent c-TiN and c-AlN- rich domains. At a certain temperature, distinct diffraction peaks of metastable c-AlN and c-TiN are observed. The separation of these domains occurs during decomposition because such process leads to a decrease in free energy. Due to different lattice constant, the formation of coherent c-TiN and c-AlN domains in a spinodally-decomposed state causes the well-known age hardening of c-$(Ti_{1-x},Al_x)N$ [8, 31, 32]. The coherency strains and the elastic stiffness differences of the domains obstruct dislocation motion thus the hardness of this alloy increases [33-35].

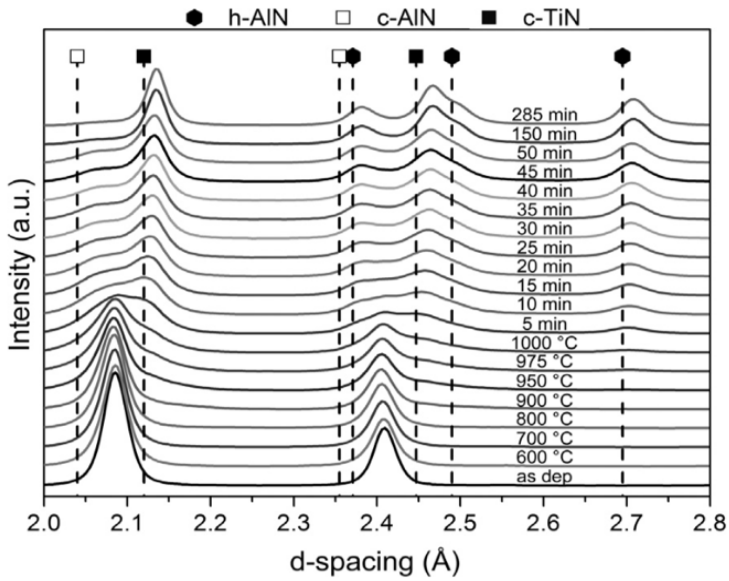

Figure 2.3. *In-situ* XRD of $(Ti_{0.36},Al_{0.64})N$ at different temperature and different isothermal annealing time held at 1000 °C, reprinted with permission [30].

2.2.2 Coarsening

The decomposition pathway of c-$(Ti_{1-x},Al_x)N$ is given by the following [36]:

$$\text{c-(Ti,Al)N} \rightarrow \text{c-TiN} + \text{c-AlN} \rightarrow \text{c-TiN} + \text{w-AlN}$$

The first stage is governed by spinodal decomposition as discussed in the previous section. If the thermal energy is further increased (i.e. enough to overcome the free energy barrier), the metastable c-AlN transforms to its equilibrium phase w-AlN [30]. It is energetically favorable for domains to coarsen because such process minimizes the free energy of the system. As the precipitates continue to grow, the coherency between the domains is lost [8]. In addition, accompanying the onset of w-AlN, the hardness significantly drops because of the large volume mismatch of the domains that enhance the tendency of dislocation movements [10].

2.3 Crystal Structure

The crystal structure of transition metal nitrides (TMN) is primarily determined by the number of sp valence electrons per atom (e/a) in the system [7, 8] The most common crystal structures of TMN are cubic B1, hexagonal B_k, and wurtzite B4 structures [11]. For most TMN, a change from cubic B1 to wurtzite B4 is observed as the e/a ratio decreases [11, 37]. The crystal structure can also be stabilized to a different phase (such as from cubic B1 to wurtzite B4) under high pressure [38, 39] or by using a substrate with a similar lattice parameter [40].

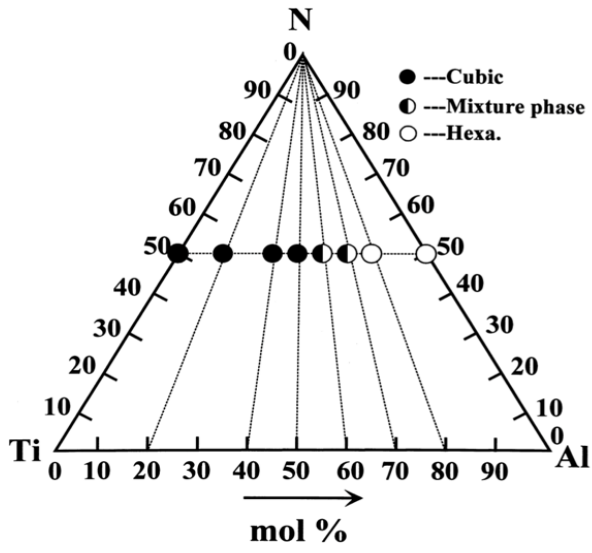

Figure 2.4. Crystal structures in the $(Ti_{1-x},Al_x)N$ material system, reprinted with permission [41].

The $(Ti_{1-x},Al_x)N$ system has two phases (cubic B1 and wurtzite B4 crystal structures), which is highly dependent on Al composition (Figure 2.4). A study has shown that film thickness also influences the crystal structure of $(Ti_{0.38},Al_{0.62})N$, wherein a transition from cubic B1 to wurtzite B4 is observed for a critical thickness of about 3µm [42]. Majority of the researches on $(Ti_{1-x},Al_x)N$ are focused on its cubic B1 structure because of the outstanding high temperature mechanical behavior. It is also important to investigate its wurtzite B4 structure because other properties such heat conductivity, electrical resistivity and optical reflectance are correlated with structural changes [43, 44].

In Paper 4, epitaxial growth of $(Ti_{1-x},Al_x)N$ films with Al content of x = 0.63 and x = 0.77 has been investigated [45]. $(Ti_{0.27},Al_{0.63})N(111)$ film has pure cubic B1 structure while $(Ti_{0.23},Al_{0.77})N$ film contains thin cubic $(Ti_{0.27},Al_{0.63})N(111)$ in the first atomic layers due to epitaxial stabilization then a transition to epitaxial $(Ti_{0.23},Al_{0.77})N(0001)$ with coherent interface occurs. The microstructure, thermal stability, and functional properties of wurtzite and cubic structures of $(Ti_{1-x},Al_x)N$ are further discussed in this paper.

3. Defects

Transition metal nitrides (TMN) are widely investigated because they have remarkable properties such as high mechanical strength, good electrical conductivity, and high melting points [11, 46]. The defect structure of TMN is also among its distinctive properties because the presence of vacancies and interstitials significantly affects its mechanical, electrical, and thermodynamic characteristics [11]. The (Ti,Al)N system is among these metal nitrides that has been utilized in wide range of applications [3, 6, 47]. However, there are only few reports that investigate on its defect structure [48, 49]. In this section, the emphasis is on the role of point and line defects in engineering (Ti,Al)N films with improved properties.

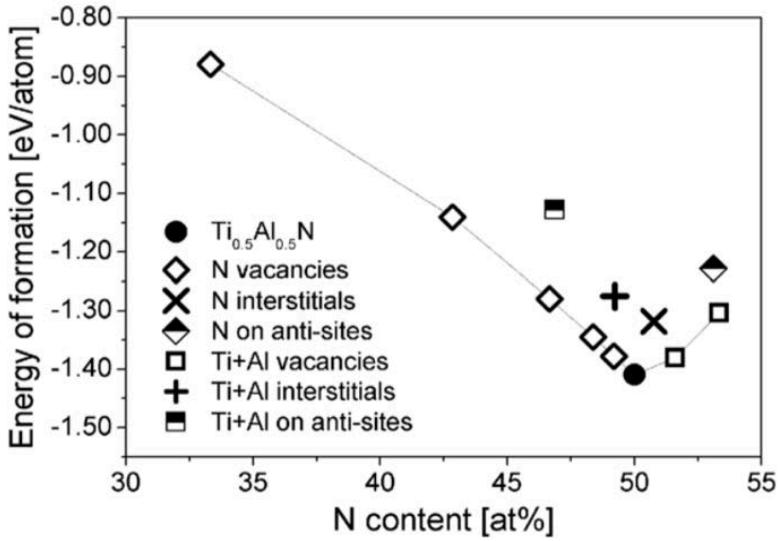

Figure 3.1 Energy of formation of $(Ti_{0.5},Al_{0.5})N_y$ for different point defects, reprinted with permission [50].

3.1 Point Defects

The first theoretical study on the effect of point defects on the phase stability of (Ti,Al)N system is done by Alling et al. [13], which showed that nitrogen vacancies in c-$(Ti_{1-x},Al_x)N_{1-y}$ ($0 \leq x, y \leq 1$) influence the energetically preferred decomposition pattern in the x-y composition space. to Baben et al. [50] further investigated the induced changes of N concentration in c-$(Ti_{0.5},Al_{0.5})N_y$

using *ab initio* calculations. Figure 3.1 shows that for y < 1, the energy of formation of N vacancies is smaller than those of Ti and Al interstitials, Ti and Al vacancies, and on anti-sites (i.e. occupation of metal ions or atoms on the lattice sites of nitrogen and nitrogen on the metal lattice sites). For y > 1, the energy of formation of Ti and Al vacancies is the smallest among the point defects. This indicates that N vacancies are stable in sub-stoichiometric $(Ti_{1-x},Al_x)N_y$ films while metal vacancies are stable in over-stoichiometric films.

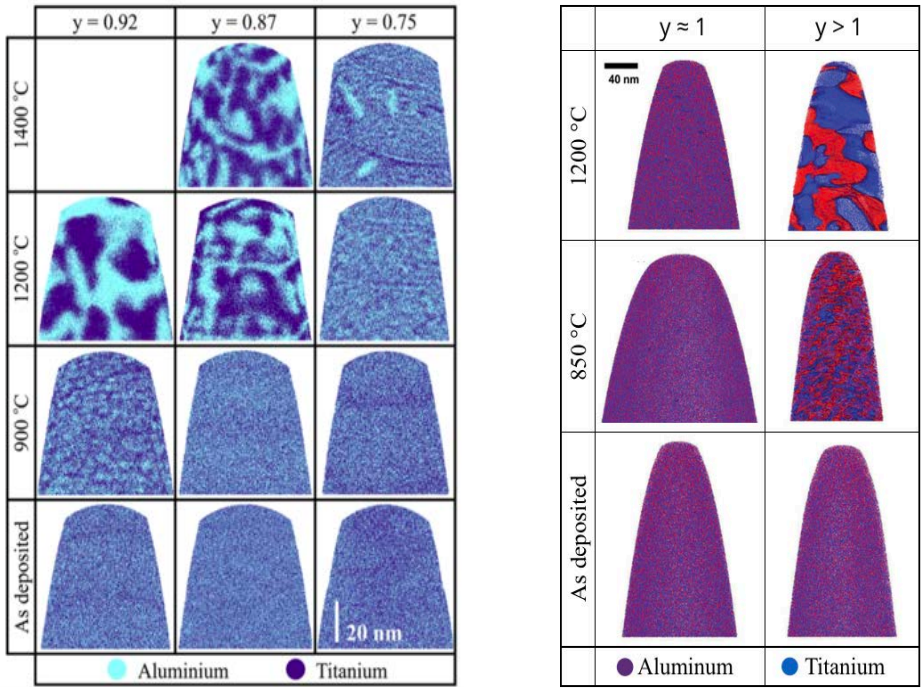

Figure 3.2. 3D atom probe tomography (APT) reconstructions of (left) $(Ti_{0.52},Al_{0.48})N$ with y < 1 [14] and (right) $(Ti_{0.5},Al_{0.5})N$ with y ≥ 1 [51] in the as-deposited state and after annealing, reprinted with permission.

The effects of N concentration on the structural evolution of $(Ti_{1-x},Al_x)N_y$ films after annealing were recently confirmed by 3D atom probe tomography (APT) [14, 51]. Schramm et al. [14] has shown that the presence of N vacancies in $(Ti_{0.52},Al_{0.48})N$ (y < 1) coatings enhance its thermal stability because the detrimental w-AlN phase evolution occurs at higher temperatures. By APT, it is clearly demonstrated that the Ti and Al domains of the close-to-stoichiometric samples have started to segregate at 900 ˚C while the segregation of the sub-stoichiometric at 1200 ˚C (Figure 3.2a). Baben et. al [51] has shown an unprecedented thermal stability of $(Ti_{0.5},Al_{0.5})N_y$ thin films by tuning the nitrogen-to-metal ratio of the film (Figure 3.2b). The metal vacancies in the

over-stoichiometric sample ($y \geq 1$) enhance decomposition since there is no energy needed for vacancy formation on the metal sub-lattice but only the activation energy for changing atomic position for the diffusion processes to occur. These studies suggest that point defect engineering as a route for synthesizing $(Ti_{1-x},Al_x)N_y$ coatings with enhanced properties.

The synthesis method used also affects the material defect structure. Oettel et al. [52] reported that physical vapor deposition techniques (e.g. cathodic arc evaporation) introduce point defects such as interstitials, vacancies, and anti-sites in (Ti,Al)N films. These defects have characteristic activation energies for diffusion and thus have different thermal stabilities [53]. One of the deposition parameters that cause the generation of such point defects is the substrate bias voltage. In Paper 1, the effect of bias voltage on the residual stress and thermal stability of nitrogen deficient $(Ti_{0.54},Al_{0.46})N_{0.87}$ films was examined [54]. The film grown with an applied bias of -80 V had the highest compressive residual stress. For (Ti,Al)N system, residual stresses are mainly caused by N interstitials and anti-sites [52].

During cathodic arc deposition, the metal ion energy of, e.g., Ti^{2+}, Ti^{+}, Al^{+} ions can be more than hundred electron volts, depending on the applied substrate bias [52]. These metal ions have sufficient energies to cause defects on the growing film, e.g. by knocking-off nitrogen atoms near the surface into irregular lattice sites (i.e. interstitial and metal lattice sites) and then by replacing these nitrogen sites. The incorporation of the metal ions into the nitrogen sites and the presence of the nitrogen interstitials within the crystal cause compressive stress in the film. Applying high bias voltage increases the strain energy stored in the system and results to lattice strain formation in the crystallites and at the interfaces [55]. These factors contribute to an increase in internal energy of the system and consequently enhance the onset of decomposition for highly biased samples [54].

The enhanced phase stability in nitrogen deficient $(Ti_{0.54},Al_{0.46})N_{0.87}$ coatings, obtained by tuning the applied bias voltage results in optimal mechanical behavior. Paper 1 shows that the age hardening of low biased $(Ti_{0.54},Al_{0.46})N_{0.87}$ films is retained until 1100 °C, the highest temperature reported for $(Ti_{1-x},Al_x)N_y$ coatings. The wear behavior of these films with different applied bias voltages is shown in Chapter 6. In Paper 2, the wear mechanism of films with different nitrogen concentration and fixed bias voltage of -55 V (i.e. the optimum condition) was reported.

3.2 Dislocation structure

In addition to point defects, the presence of dislocations, interfaces and grain boundaries also affect the phase transformation of TMN thin films. This is because the diffusivity of atoms is enhanced and the equilibrium conditions of a system are influenced in the vicinity of these defects [26]. Theoretical studies used to describe the thermodynamic energies involved in phase separation of (Ti,Al)N system are based on Cahn–Hilliard equation [27], which describes a concentration dependent mobility. Results show that spinodal decomposition of c-(Ti,Al)N is affected by the anisotropic elastic properties of c-AlN and c-TiN- rich domains because they generate strain and associated strain energy [34, 35, 56]. In these studies, the strain effects generated by dislocations or other defects were ignored.

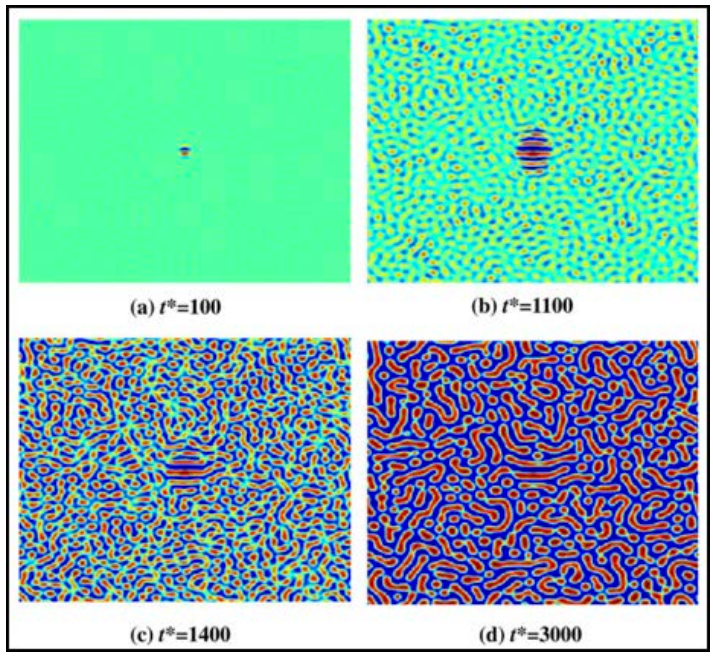

Figure 3.3. Phase separation with an edge dislocation in Fe–Cr alloy, reprinted with permission [57].

Phase-field modelling of spinodal decomposition in alloys have recently accounted the formation and dynamics of dislocation [57-59]. Figure 3.3 shows the model result of the spinodal decomposition process for an alloy with an edge dislocation. The simulations illustrate that phase separation is faster near a dislocation, enhanced by its dislocation stress field [57]. This field enables

the phase separation process even without initial compositional fluctuation [57].

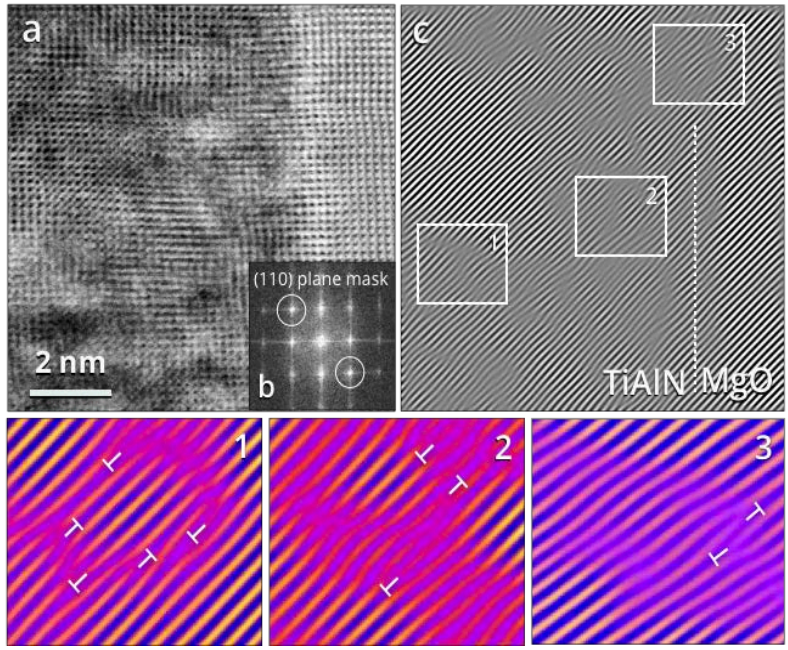

Figure 3.4. (a) High-resolution STEM cross section and (b) FFT of ($Ti_{0.6}$,$Al_{0.4}$)N on MgO(100). (c) A reconstructed image of the masked FFT image (marked in (b)) through inverse FFT algorithm keeping only the contribution of (110) and (1-10) planes. The insets 1, 2, and 3 are zoom on crystal defects.

In $Ti_{1-x}Al_xN_y$ thin films, it is likely that dislocations are generated during the deposition process that could influence the spinodal decomposition at elevated temperatures [49]. Figure 3.4a shows a scanning transmission electron micrograph (STEM) of single crystalline c-($Ti_{0.6}$,$Al_{0.4}$)N films on MgO (100) substrate. Starting from the STEM image, an FFT algorithm has been used to process the real-space image. Figure 3.4b shows the FFT with well-defined spots, which corresponds to the contribution of different crystallographic planes. A mask is applied on specific 110 spots in the FFT image then inverse FFT algorithm is performed to reconstruct a high-resolution real space image (Figure 3.4c). The insets 1, 2 and 3 are three different regions showing the presence of defects such as lattice distortions and edge dislocations in the (110) planes. From this technique, the presence of mismatch-related defects as well as dislocations from Ti-rich or Al-rich regions could be observed. The small differences in the lattice parameters (a_0) and coefficient of thermal expansions (α) of (Ti,Al)N film and MgO substrate would result to a generation of strain in the epitaxially grown films. This is because the lattice mismatch values

between the film and the substrate results in misfit dislocations and the difference in α results in biaxial residual stress [60, 61].

The dislocation structure and microstrain evolution during spinodal decomposition of epitaxially grown c-$(Ti_{1-x},Al_x)N$ are presented in Paper 3 [62] and Paper 5 [71]. It is essential to fabricate single crystal $(Ti_{1-x},Al_x)N_y$ films with low level of impurities in order to observe the details of their defect structure. In the paper, geometric phase analysis (GPA) on high-resolution STEM images was employed for the atomic resolution strain analysis. The study shows that the chemical bonding state and elastic properties of the TiN- and AlN- rich domains have influenced the defect structure and strain generation during decomposition.

4. Coating Deposition

The $(Ti_{1-x},Al_x)N_y$ thin films used in this study are fabricated using cathodic arc deposition and DC magnetron sputtering, which are both plasma based physical vapor deposition (PVD) techniques. Cathodic arc deposition was used to deposit poly-crystalline wear resistive coatings on WC-Co substrates for metal cutting applications while the magnetron sputtering was used to deposit single-crystalline model system thin film materials on MgO substrates. The fundamental principle and mechanism of these two deposition techniques are described in this chapter.

4.1 Cathodic arc evaporation

Cathodic arc deposition is a technique widely used in coating industries because it has significantly higher deposition rate as compared to other PVD methods such as magnetron sputtering [63]. The deposition process starts by igniting an arc, which is typically done by a rapid contact of a mechanical trigger wire with the cathode [64]. This generates a cathode spot, which is a small highly energetic emitting area with high-localized temperature (5000 to 10000 ˚C) [65]. The solid material in the cathode spot transforms to a high-power density cathodic arc, which comprises of multiple charged metal ions, neutral particles, clusters, and macroparticles. A cathodic arc is a high current, low voltage discharge that is usually operated in the continuous direct current (DC) mode with an arc current between 50 to 150 A [63]. In a reactive arc deposition, a reactive gas such as N_2 is introduced in the chamber during the evaporation process. Dissociation, ionization and excitation occur in the interaction between the reactive gas and the ion flux [66]. These plasma particles condense on the substrate to form the compound film.

The investigated $(Ti_{1-x}Al_x)N_y$ films in Paper 1 and Paper 2 are grown using an industrial scale arc-evaporation deposition system [54, 67], which is schematically illustrated in Figure 4.1a. Three cathodes with different composition are placed in a vertical row (positions A-C) while substrates are placed at different heights (positions 1-5) opposite to the cathodes on a rotating cylinder. Through plasma mixing, thin films with different compositions were synthesized in one batch of deposition (Figure 4.1b). The nitrogen content of the $(Ti_{1-x},Al_x)N_y$ films were controlled by varying the ratio

of the gas flow ratio of the $N_2/(Ar+N_2)$ gas mixture. The gases were introduced through pipes positioned vertically in the chamber.

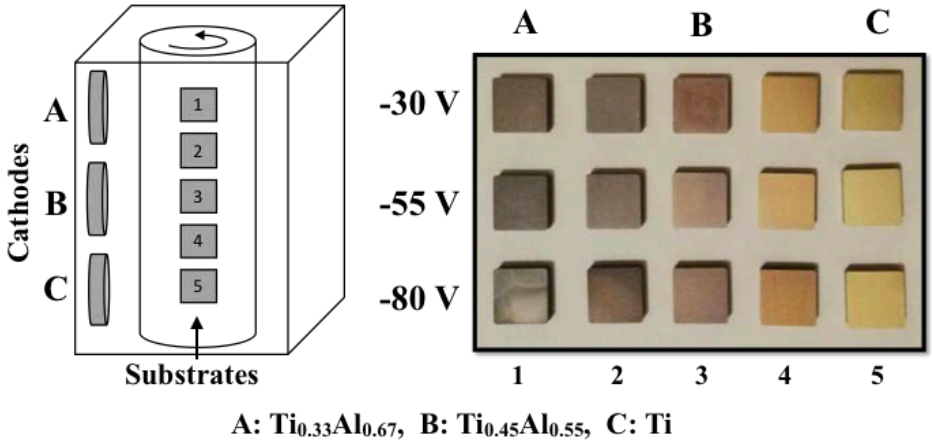

Figure 4.1. (left) Schematic diagram of the cathodic arc deposition set-up and (right) the films with varying nitrogen flow rate and applied bias voltage that were produced in this set-up.

The microstructure and phase evolution of $(Ti_{1-x}Al_x)N_y$ films are influenced by the nitrogen vacancies and the applied bias voltage on the substrates. Schramm et al. [14, 68] have pioneered the experimental investigation of the effect of nitrogen vacancies on polycrystalline cathodic arc films. In Paper 1, the effects of the applied bias voltage on the microstructural evolution and phase transition of nitrogen deficient films are investigated [54]. Bias voltage is a critical factor in this study because it affects the ion energy impinging on surface and influence the nucleation and growth kinetics during the film growth.

One drawback of the cathodic arc deposition technique is the presence of macroparticles. Our study shows that both the amount and size of macroparticles are dependent on the applied negative substrate bias voltage on the substrate (Paper 1) and the N content in the films (Paper 2). The amount of macroparticles increases as the applied substrate bias and the film N content decrease. Figure 4.2 shows the high-angle annular dark field (HAADF) STEM micrograph and STEM-EDX (energy dispersive x-ray spectroscopy) of $(Ti_{0.52},Al_{0.48})N_{0.75}$ (i.e. coating with the lowest nitrogen content among the studied samples), which reveals an inhomogeneous concentration of elements inside the macroparticle. A relatively high concentration of Ti elements is observed in the bottom region of the macroparticle, which are excess neutral atoms commonly observed in (Ti,Al)N films deposited using cathodic arc

technique [6, 69, 70]. The detrimental effect of macroparticles on the wear behavior of $(Ti_{1-x},Al_x)N_y$ films is discussed in Chapter 6.

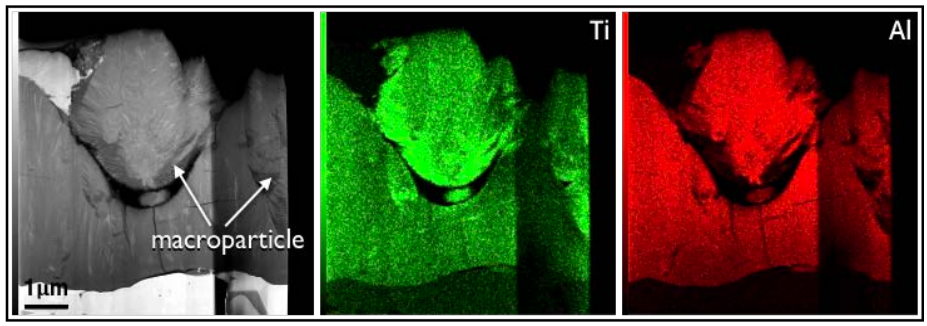

Figure 4.2. HAADF-STEM and STEM-EDX of $(Ti_{0.52}Al_{0.48})N_{0.75}$ coatings.

4.2 DC magnetron sputtering

DC magnetron sputtering is a deposition technique utilized in this thesis for growth of single crystalline $(Ti_{1-x},Al_x)N_y$ films (examined in Papers 3 to 5) [45, 67, 71]. These films exhibit homogeneous microstructures free of macroparticles. In sputtering process, the surface or near-surface atoms of cathode (target) are ejected by the bombardment of incident particles with sufficient energy to break bonds and dislodge atoms [72]. In contrast to cathodic arc, sputter deposition is a high-voltage, low current discharge process. Figure 4.3 shows the schematic diagram of a typical sputtering set-up. The process starts by applying voltage across electrodes to generate an electric field that accelerates free electrons towards the anode. These electrons gain energy and collide with the chemically inert sputtering gas such as Ar, causing the gas to breakdown into a plasma discharge. The ions are accelerated to the negatively biased cathode and cause collision cascade and sputtering of the target surface atoms. This ion bombardment also causes the ejection of secondary electrons from the target, which results to further ionization of gas atoms that can sustain the discharge.

In magnetron sputtering, a magnetic field is placed parallel to the target surface to confine the secondary electrons close to the target surface. The magnetic field captures and prolongs the electron spiral motion along the field lines. This technique increases the sputtering rate because highly concentrated electron gas will have more collisions, resulting to an increase in ion bombardment of the target surface. Consequently, the deposition rate of the magnetron sputtering is enhanced. In this thesis, a reactive nitrogen gas (N_2) is

also introduced in the chamber. The sputtered particles undergo a chemical reaction with the reactive gas on the film surface to form the compound. The nitrogen content of the $(Ti_{1-x},Al_x)N_y$ films is controlled by varying the N_2 to Ar flow ratio.

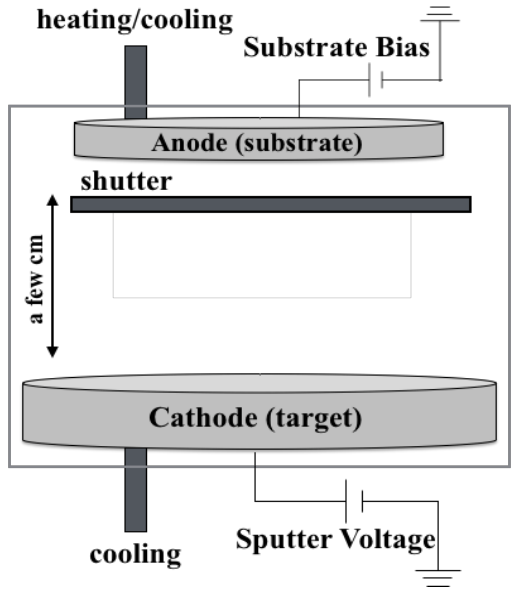

Figure 4.3. Schematic diagram of a sputtering set-up.

4.2.1 Growth Conditions

During sputtering deposition, the energetic particles (adatoms, ions, etc.) impinging on the growth surface, their energy distributions and their effect on film formation (nucleation and growth mechanism) are mainly controlled by: sputter voltage, gas flow rate and pressure, substrate bias voltage, and substrate temperature [6, 72, 73].

In the present study, the discharge current (i.e. directly proportional to the sputter yield) was held constant and no substrate bias was applied. Further, the substrate temperature, gas pressure, and gas flow rate were optimized to yield single crystalline (Ti,Al)N films [11, 12, 49]. The substrate temperature of the films must be high enough to provide sufficient adatom mobilities promoting epitaxial growth [13]. In a previous study on epitaxial TiN growth, it was reported that a minimum substrate temperature of 200 °C was required to attain epitaxial growth on MgO substrate [74]. To obtain TiN films with a crystal coherence length comparable to the film thickness required a growth

temperature of at least to 600 °C [74]. The fabricated single crystalline (Ti,Al)N films in this study are deposited at a substrate temperature of 700 °C [45, 62, 71].

The preferred orientation of the deposited (Ti,Al)N on this study is controlled by the balance between surface energy and strain energy, which are influenced by working pressure and nitrogen gas flow rate [11, 12]. At a high N_2 flow, the surface mobility of the adatoms decreases and thus favors the growth of (200) lattice crystal planes having a higher ledge energy and a shorter diffusion distance relative to planes with lower energy sites [14, 15]. Further increase of the N_2 is not necessary because it would reduce the deposition rate and would also lead to nitrogen-poisoned growth mode [16]. In fact, the overall pressure should not be too high, because the electrons need to gain enough energy between collisions, nor too low, since gas collisions are essential in sustaining the plasma. Growth of single crystalline (Ti,Al)N films on MgO substrates as a function of N-content are studied in Paper 5 [71].

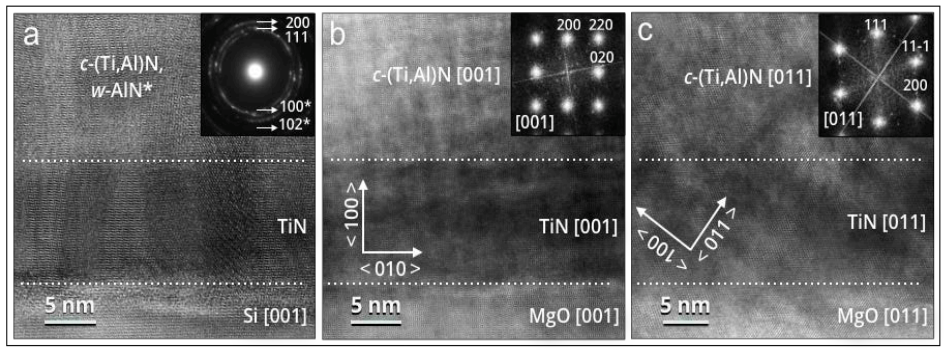

Figure 4.4. (a) HRTEM with SAED inset of (Ti,Al)N on Si, (b) HRTEM with FFT inset of (Ti,Al)N on MgO(001), and (c) HRTEM with FFT inset of (Ti,Al)N on MgO(111). The diameter of the sample area used for SAED is 100nm.

4.2.2 Effect of Substrate

It is necessary that the lattice parameters of the substrate and the film have a good match to achieve heteroepitaxial growth. The theory of Frank and van der Merwe predicts that a lattice parameter mismatch of less than 9 % is required to obtain an epitaxial layer [22]. A too large lattice mismatch would result in the growth of polycrystalline film due to the existence of a high dislocation density at the substrate-film interface [23].

Another important aspect for the conditions of epitaxial growth is the effect of thermal strain, which may exceed the lattice mismatch strain for a given film/substrate system. A large difference in the thermal expansion coefficients between the film and the substrate in combination with a high growth temperature can cause a large thermal strain when cooling down to room temperature [24]. Thus, it is also necessary that the thermal coefficients of both film and substrate to be in the same order of magnitude to grow high quality epitaxial films. Figure 4.4 shows high resolution transmission electron microscopy (HRTEM) images of (Ti,Al)N films deposited on Si, MgO (001) and MgO (111) substrates. Epitaxial films are only achieved on MgO substrates. This demonstrate that MgO is a good choice of substrate because the lattice mismatch between the nitride films is less than 9% and their thermal coefficients are of the same order. The lattice mismatch of MgO and c-TiN buffer layer with respect to the film is 1.43% and 2.12%, respectively (details of the computation are shown in the manuscript). The thermal coefficients of MgO, TiN, and (Ti,Al)N are $\alpha_{MgO} \approx 4.0 \times 10^{-6}/°C$, $\alpha_{TiN} \approx 10.3 \times 10^{-6}/°C$, and $\alpha_{MgO} \approx 7.5 \times 10^{-6}/°C$, respectively [25, 26].

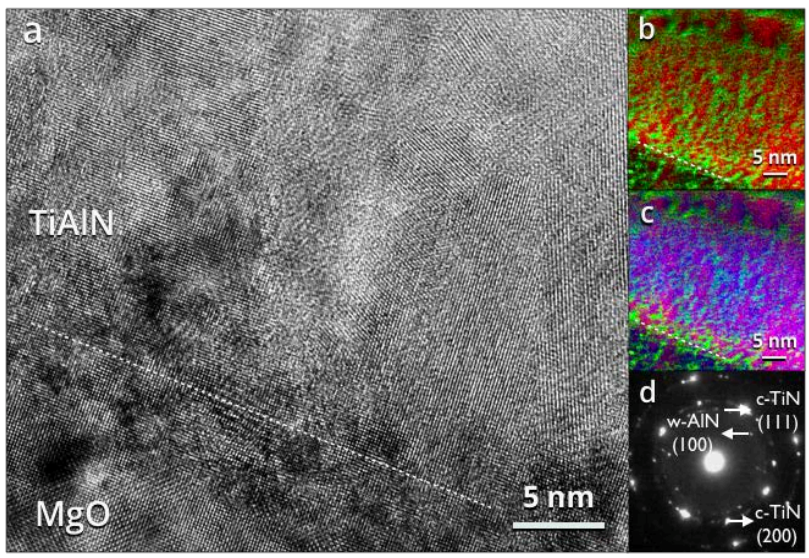

Figure 4.5. (a) HR-TEM, (b) EFTEM: Ti (red), Al (green), (c) EFTEM: Ti (red), Al (green), N(blue), and d) SAED of (Ti,Al)N/MgO annealed at 900 ºC.

Figure 4.5a shows the HRTEM micrographs of (Ti,Al)N film grown directly on MgO and was subsequently annealed at 900 ºC. Different orientations of domains and grain boundaries are observed in the annealed sample. Figures 4.5b and 4.5c show energy filtered TEM (EFTEM) images of the film revealing

the clear segregation on the metal sublattice while N-sublattice segregation cannot be detected. Al has diffused on to the MgO substrate because Al and Mg chemically reacts to form spinel [75]. At this temperature, (Ti,Al)N has already decomposed and an early sign of w-AlN transformation can be seen, as confirmed from the selected area electron diffraction (SAED) pattern (Figure 4.5d). The studied (Ti,Al)N films in Papers 3, 4, and 5 were all grown with TiN buffer layers [45, 62, 71]. The thin TiN buffer layer prevents high temperatures chemical reaction between Al and Mg.

5. Metal Cutting

By tuning the nitrogen content and point defect concentration in c-(Ti,Al)N films, we have demonstrated a significant enhancement of its thermal stability, i.e. which results in a delayed onset of the detrimental w-AlN phase to 1100 °C (Paper 1) [54]. The improved thermal stability in nitrogen deficient $(Ti_{1-x}Al_x)N_y$ ($y < 1$) coatings has been explained by the presence of N vacancies and a reduced driving force for decomposition [13]. The thermal stability and mechanical properties of these coatings were determined by examining their microstructure and hardness after annealing in a vacuum furnace to high temperatures where decomposition has already taken place. During machining, the coatings are subjected to harsh conditions such as high temperature, pressure and corrosive chemistry, which for example results in high stress levels and chemical interactions with the workpiece material, which lead to wear and plastic deformation [76-78]. In this chapter, the microstructure and chemical reaction of nitrogen deficient coatings that are exposed to a cutting process is discussed to gain insight on the wear mechanism of cutting tools.

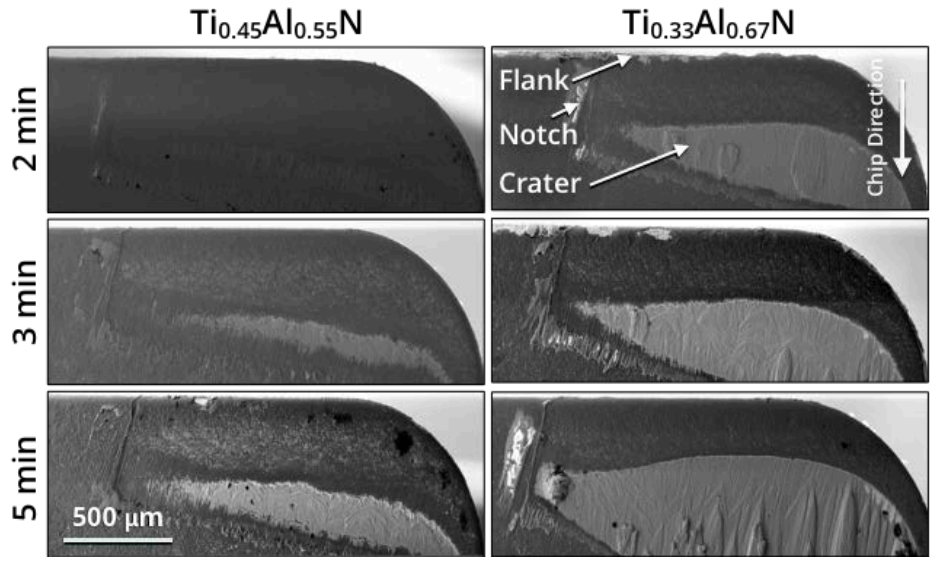

Figure 5.1 SEM micrographs of $(Ti_{1-x},Al_x)N_y$ ($y \approx 1$) films with different Al content after 2min, 3min, and 5min exposure to metal cutting.

5.1 Wear Mechanism

The wear mechanism of a cutting tool during machining depends on the workpiece material, properties of the cutting tool, cutting conditions, and cooling or lubrication system [79]. The most common types of tool wear are crater wear, flank wear, and notch wear (depth-of-cut) (Figure 5.1). During cutting, the sliding of the chip that has been removed from the workpiece material generates high temperatures and shear stresses in the contact area of the rake face [80]. This leads to the generation of crater wear, which is a major cause of accelerated tool failure during the machining of metal alloy components. Flank wear occurs on the relief face and it is mainly due to the abrasion of the cutting edge. A notch wear occurs at the point of contact between the tool and the free edge of the chip and it is mainly due to abrasion and oxidation if a coolant is used.

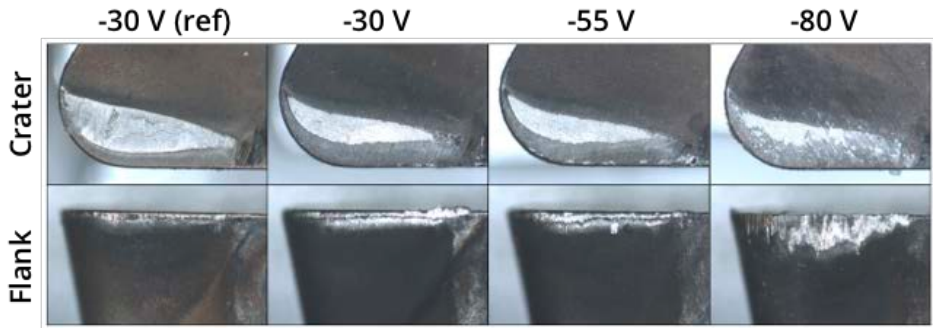

Figure 5.2 Crater and flank wear of a stoichiometric $(Ti_{0.54},Al_{0.46})N$ film biased at -30 V and nitrogen deficient $(Ti_{0.54}Al_{0.46})N_{0.87}$ films biased at -30 V, -55 V, and -80 V.

The progression of wear on stoichiometric $(Ti_{1-x},Al_x)N$ coatings with Al content of x = 0.54 and x = 0.67 is shown in Figure 5.1. The $(Ti_{0.46},Al_{0.54})N$ coating has higher wear resistance than $(Ti_{0.33},Al_{0.67})N$ because less w-AlN is formed [30]. In paper 1, the effect of bias voltage on the ex-situ high temperature hardness of nitrogen deficient $(Ti_{0.46},Al_{0.54})N_{0.87}$ was investigated [54]. The cutting performance of these films was tested in steel and the results are shown in Figure 5.2. The low biased nitrogen deficient films (-30 V and -55 V) have better crater and flank wear resistance as compared to the high biased sample (-80 V) and the stoichiometric film biased at -30 V. The film biased at -80 V has the least wear resistance among the samples. The $(Ti_{0.46},Al_{0.54})N_{0.87}$ film, grown with a biased of -55V exhibits a higher hardness and a lower amount of macroparticles as compared to the film biased at -30 V (shown in Paper 1). Figure 5.3 shows that after a prolonged exposure of the c-$(Ti_{0.48},Al_{0.52})N_{0.87}$ coating to metal cutting, crack has propagated from the macroparticles. One of

the major causes of failure during wear cycling is the presence of these local macroscopic droplets [6]. In paper 2, the applied negative bias voltage was held constant at -55 V and the effect of nitrogen content on the wear behavior of the c-($Ti_{0.46}$,$Al_{0.54}$)N_y (y = 0.92, y = 0.87, y = 0.75) coatings are investigated [67].

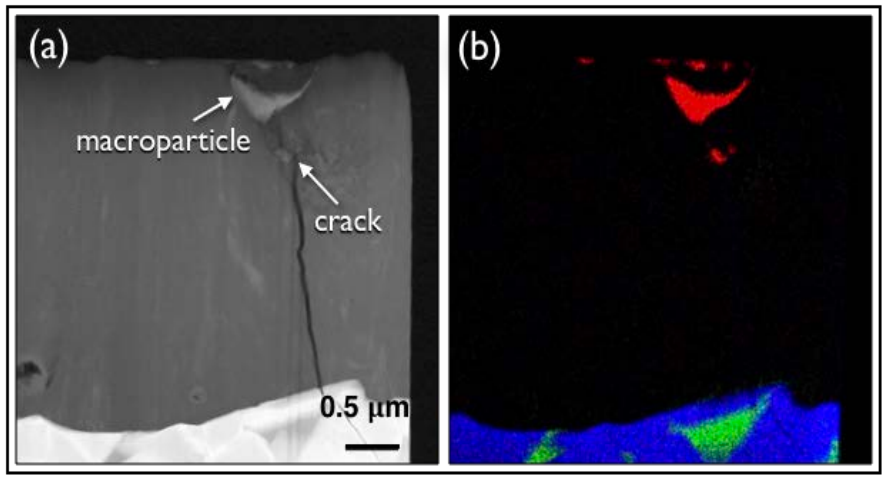

Figure 5.3. HAADF-STEM and STEM-EDX of c-($Ti_{0.52}$,$Al_{0.48}$)N_y coatings with y = 0.92 after metal cutting. The colored areas are Fe (red) from the chip and Co (green) and W (blue) in the substrate.

5.2 Effect of microstructure and chemical interaction

It has been shown that c-(Ti,Al)N coatings are in a coarsened and decomposed state after 10 min of continuous turning of a carbon steel [81]. However, the initial state of their microstructure during turning is still unknown. Knowing such information is essential in determining the mechanism driving the wear behavior of such coatings. Figure 5.4 shows the crater wear of c-(Ti_{1-x},Al_x)N_y (y = 0.92, y = 0.87, and y = 0.75) coatings after 1 min of cutting. In this initial stage of cutting, the crater wear of samples with different x and y compositions are similar. However, the microstructure and chemical interactions between these samples are different. FIB samples were taken along the chip direction near crater wear at around half of the cutting length at the chip-rake interface, where maximum temperature and maximum shear stress are expected.

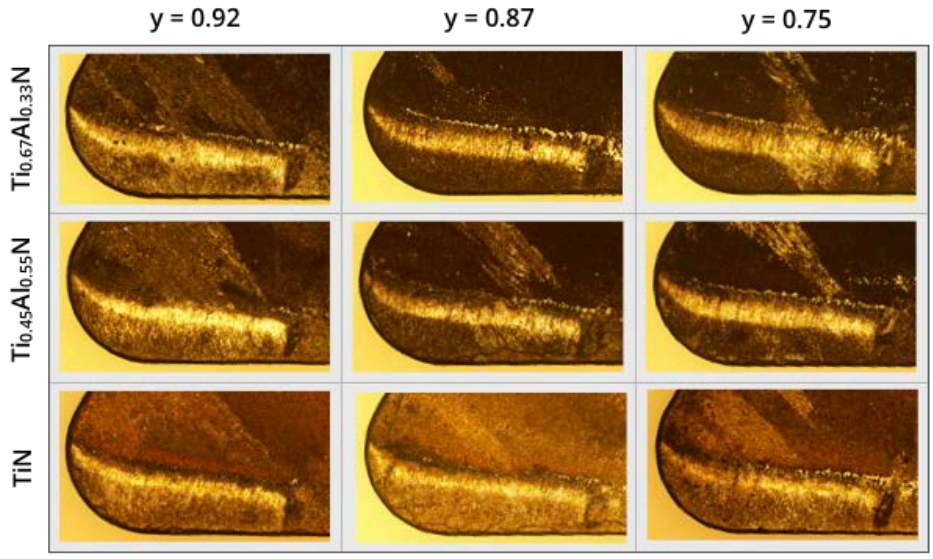

Figure 5.4 Optical micrographs of nitrogen deficient c-$(Ti_{1-x},Al_x)N_y$ film after 1 min of metal cutting.

High resolution cross-sectional dark field STEM images and the corresponding EDX maps of c-$(Ti_{0.52},Al_{0.48})N_y$ (y = 0.92, y = 0.87, and y = 0.75) coatings with different N stoichiometry after they are exposed to 1 min of metal cutting are shown in Figure 5.5. The y = 0.92 sample has a phase segregation of coherent c-TiN rich and c-AlN rich domains due to spinodal decomposition while the y = 0.87 sample has retained its as-deposited c-(Ti,Al)N structure. The microstructure is less dense in a decomposed state, thus it is more favorable for Fe from the workpiece to diffuse through the coating. The c-$(Ti_{0.52},Al_{0.48})N_y$ (y = 0.75) contains Ti_2AlN MAX phase in some parts of the coating because high amount of nitrogen vacancies has as a driving force for the stabilization of hexagonal MAX phases [13]. Flank wear is mainly affected by the hardness of the coatings [82, 83]. The c-$(Ti_{0.52}Al_{0.48})N_{0.92}$ coating has the best flank wear resistance it exhibits an age hardening effect due to spinodal decomposition. The c-$(Ti_{0.52},Al_{0.48})N_{0.75}$ coating has the least flank wear resistance due the occurrence of Ti_2AlN MAX phase within the coating, which has lower hardness than c-(Ti,Al)N [84].

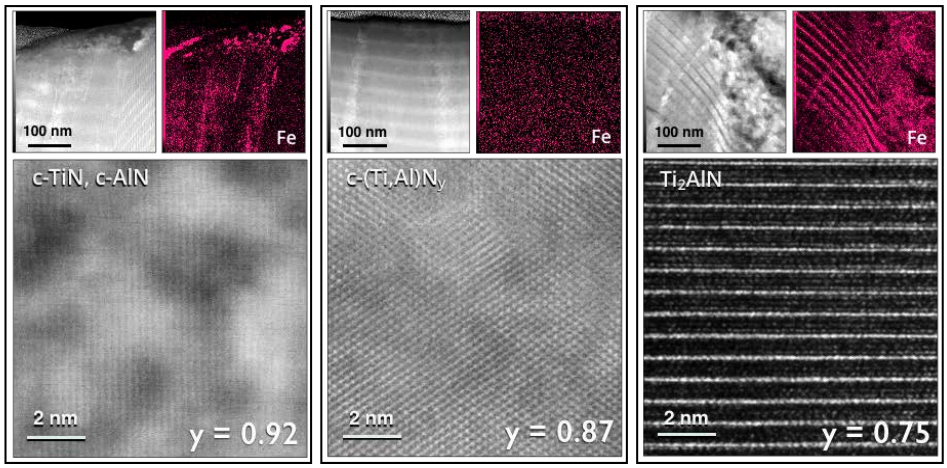

Figure 5.5 HAADF-STEM images and STEM-EDX of c-$(Ti_{0.52},Al_{0.48})N_y$ coatings with y = 0.92, y = 0.87, and y = 0.75 after 1 min of metal cutting.

The high-speed cutting of the steel workpiece has facilitated the abrasive wear, chemical interaction with the chip, and plastic deformation of the c-$(Ti_{1-x}Al_x)N_y$ (y = 0.92, y = 0.87, and y = 0.75) coatings of the tool inserts. The overview of the cross sectional STEM images and the corresponding EDX maps of c-$(Ti_{0.52},Al_{0.48})N_y$ coatings with different N content after exposure to 1 min of metal cutting are shown in Figure 5.6. Large macroparticles are observed in the y = 0.75 sample. Chemical maps of the cross sections show that the elements from the workpiece material, for example Fe and Cr, are mostly concentrated to the top surface and at macroparticle boundaries. There is no cobalt found in the y = 0.92 and y = 0.87 samples while cobalt has diffused from the WC-Co substrate to the large macroparticle in the y = 0.75 sample. In paper 2, the compositional homogeneity and the chemical reaction between elements from the workpiece and the coatings are further discussed. Crater wear is mainly caused by chemical wear due to diffusion [76]. The c-$(Ti_{0.52},Al_{0.48})N_{0.87}$ coating has better crater wear resistance than c-$(Ti_{0.52},Al_{0.48})N_{0.92}$ because there it contains lesser chip elements that diffused through the coating. The c-$(Ti_{0.52},Al_{0.48})N_{0.75}$ coating has the least crater wear resistance among the samples due to its high amount of macroparticles, which facilitate the diffusion of chip elements (e.g. Fe and Co) and can weaken its structure through recrystallization [85].

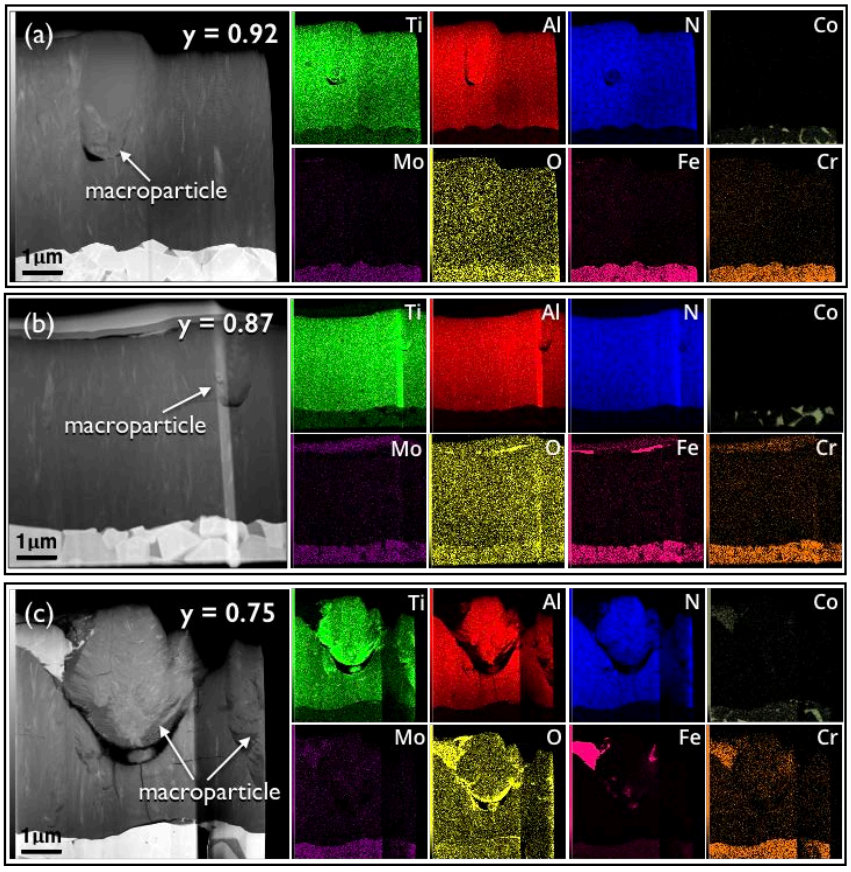

Figure 5.6. HAADF-STEM and STEM-EDX of $(Ti_{0.52},Al_{0.48})N_y$ coatings with (a) y = 0.92, (b) y = 0.87, and (c) y = 0.75 after 1 min of metal cutting. The regions in the right side of the FIB samples are thinner in comparison to the other side. The transition in thickness is indicated by the sharp brightness difference in the STEM and STEM-EDX images.

6. Characterization techniques

6.1 XRD

X-ray diffraction (XRD) techniques are used to obtain crystallographic information and phase structure of the poly- and single- crystalline (Ti,Al)N films. This technique is based on Bragg's law, given by:

$$2dsin\,\theta = n\lambda \quad [5.1]$$

where *d* is the interplanar distance, θ is the scattering angle of the incident or diffracted ray, *n* is an integer, and λ is the wavelength of the of the incident ray. In this technique, incident x-rays are first directed towards the crystalline sample. Diffraction is produced at certain angles (Bragg's angle) where x-rays are coherently scattered. The X-ray diffraction θ-2θ scans, azimuthal scans, rocking curves, residual stress, and reciprocal space maps of the films were acquired using PANalytical Empyrean and PANalytical X'Pert PRO MRD diffractometers with Cu K_α radiation.

6.1.1 Residual stress

The strain measurements of the nitrogen deficient c-$(Ti_{0.54},Al_{0.46})N_y$ films deposited using cathodic arc technique were obtained using the $\sin^2(\psi)$ method [86] on the 422 diffraction line. In this technique, the (hkl) plane spacings are measured by using θ-2θ scans in directions inclined by the angle ψ. Then, the lattice spacing (ϵ_ψ) vs. $\sin^2\psi$ are plotted to get the slope of the curve. The in-plane stress ($\sigma_{||}$) can be obtained because it is related to the measured slope, elastic modulus (*E*), and Poisson ratio (ν) of the material. The fundamental equation used in the XRD residual stress analysis is shown in Eq. (1).

$$\epsilon_\psi = \frac{d_\psi - d_0}{d_0} = \frac{1+\nu}{E}\sigma_{||}sin^2\psi - \frac{2\nu}{E}\sigma_{||} \quad [5.2]$$

where *E* and ν of the films are taken from *ab initio* calculations [34].

6.1.2 Reciprocal space maps

Symmetric and asymmetric x-ray diffraction reciprocal space maps (RSM) of epitaxial $(Ti_{1-x},Al_x)N_y$ films were acquired using a PANalytical Empyrean diffractometer with Cu K_α radiation. In this technique, the reciprocal lattice vectors Q_c and Q_a are obtained using Eqs. (2) and (3), which are related to the out-of-plane (d_c) and in-plane (d_a) lattice parameters of the films, respectively.

$$\boldsymbol{Q}_{\mathrm{c}} = \frac{4\pi}{\lambda} sin\theta cos(\theta - \omega) = \frac{2\pi}{d_{\mathrm{c}}} \quad [5.3]$$

$$\boldsymbol{Q}_{\mathrm{a}} = \frac{4\pi}{\lambda} sin\theta sin(\theta - \omega) = \frac{2\pi}{d_{\mathrm{a}}} \quad [5.4]$$

where ω and θ are the instrumental coordinates and λ is the x-ray wavelength.

6.1.2 Pole Figures

A pole figure shows a 2D stereographic projection of the orientation for a selected set of crystal plane. The XRD pole figures of the $(Ti_{0.23},Al_{0.77})N$ films grown on MgO(111) substrates were obtained using a PANalytical Empyrean diffractometer with a 4-axis goniometer, a channel-cut 2-bounce Ge(220) monochromator (primary optics), and a parallel plate collimator (secondary optics).

6.2 SEM

The surface morphologies of the $(Ti_{1-x},Al_x)N_y$ coatings were obtained using FEI Helios nanolab 600 and Leo 1550 Gemini scanning electron microscopes (SEM). The wear behavior of the $(Ti_{0.48},Al_{0.52})N_y$ coatings was determined by measuring the area of the exposed substrate (crater wear) and the average flank wear land width from the SEM images. The Leo 1550 Gemini SEM equipped with energy dispersive X-ray spectroscopy (EDS) (Oxford X-Max) was used to determine the atomic composition of the targets and to obtain the elemental maps of the $(Ti_{1-x},Al_x)N_y$ inserts after metal cutting.

6.3 FIB

Focused ion beam (FIB) - SEM dual beam systems (Helios Nanolab 600i and Zeis Neon 40) were used to obtain cross-sectional transmission electron microscope (TEM) lamella. An *in situ* lift-out technique [87] was used to obtain samples with approximately 50 nm uniform thickness. Figure 6.1 shows the FIB images of the nitrogen deficient $(Ti_{0.48},Al_{0.52})N_y$ (y = 0.92, 0.87, and 0.75) coatings which are taken from the center of the crater area of the insert after metal cutting. Plan-view TEM samples of $(Ti_{0.23},Al_{0.77})N$ were prepared by FIB-SEM dual beam system (Zeis Neon 40).

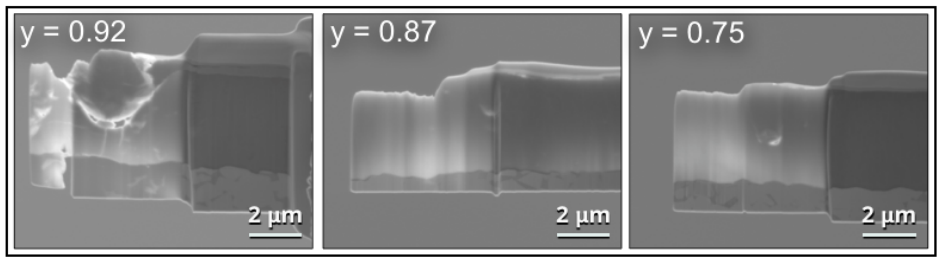

Figure 6.1 FIB images of the c-$(Ti_{0.52},Al_{0.48})N_y$ coatings after 1 min of metal cutting.

6.4 TEM

Microstructural characterizations from TEM, energy-filtered TEM (EFTEM), dark field TEM, scanning TEM (STEM), and selected area electron diffraction (SAED) images of the c-$(Ti_{1-x},Al_x)N_y$ films were obtained using JEOL ARM 200 Cold FEG and Fei Tecnai G^2 TF 20 UT analytical TEM equipment. The TEMs are equipped with EDS for the chemical analyses of the samples. They were operated at an acceleration voltage of 200 kV. The samples were prepared using either FIB or the conventional technique (i.e. mechanical grinding and polishing, followed by sputter etching until the sample has <100 nm thickness). The TEM samples used for the geometric phase analysis (GPA) analysis were prepared by FIB to ensure a uniform thickness.

6.5. GPA Analysis

The strain maps of the single crystalline c-(Ti,Al)N/c-(TiN) films on MgO substrates were obtained using a geometric phase analysis (GPA) script [88] added in the Gatan's Digital Micrograph. GPA is an image analysis method,

which calculates the strain tensors of a high-resolution transmission electron microscope (TEM) image by measuring the positions of atomic columns relative to a reference region [89]. Figure 6.2 shows an example of a strain map from an HRTEM image.

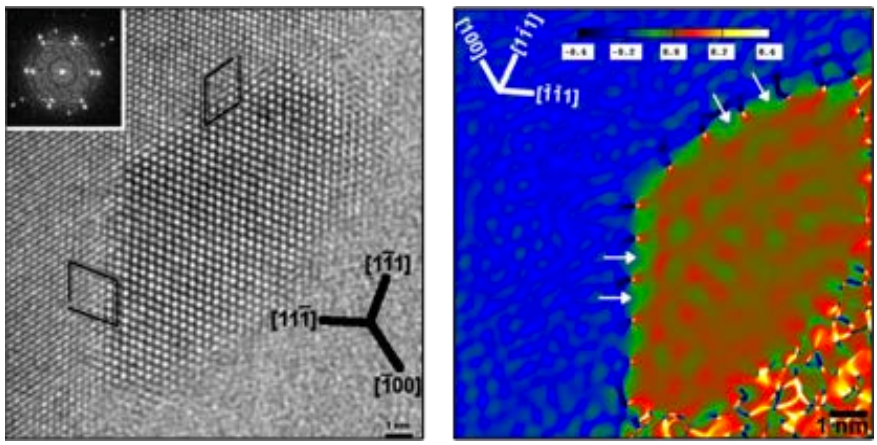

Figure 6.2. Strain mapping along Al-Pb interfaces.

The equations below show the important phase relations involved in GPA. The intensity of a particular set of fringes in a high resolution TEM image, which is selected by applying a filter on Fourier component **g** is represented as:

$$\boldsymbol{I_g(r)} = A_g(\boldsymbol{r})\exp\left[i\boldsymbol{P_g(r)}\right] \quad [5.5]$$

where $A_g(\boldsymbol{r})$ is the contrast level while $\boldsymbol{P_g(r)}$ is the relative phase shift induced by a small displacement of the fringes $\boldsymbol{u(r)}$ with respect to a reference lattice, described as:

$$\boldsymbol{P_g(r)} = -2\pi \boldsymbol{g}\cdot\boldsymbol{u(r)} \quad [5.6]$$

The 2D displacement field is obtained by two non-collinear $\boldsymbol{g}$:

$$\boldsymbol{u(r)} = -\frac{1}{2\pi}\left[\boldsymbol{P_{g1}(r)a_1} + \boldsymbol{P_{g2}(r)a_2}\right] \quad [5.7]$$

where $\boldsymbol{a_1}$ and $\boldsymbol{a_2}$ are the real space lattice vector of $\boldsymbol{g_1}$ and $\boldsymbol{g_1}$, respectively. The derivatives of $\boldsymbol{u(r)}$ are the strain tensor and rotation for a small deformation:

$$\boldsymbol{\varepsilon_{ij}} = \frac{1}{2}\left(\frac{\partial u_i}{\partial x_j} + \frac{\partial u_j}{\partial u x_i}\right) \quad [5.8]$$

$$\omega_{xy} = \frac{1}{2}\left(\frac{\partial u_y}{\partial x} - \frac{\partial u_x}{\partial y}\right) \quad [5.9]$$

The strain tensor components shown in the GPA maps were obtained from HAADF-STEM images to obtain atomic resolution strain analysis. The c-TiN buffer layer was used as a reference because it has the minimum strain (i.e. the closest to the MgO substrates). Figure 6.3 below shows an example that both TiN and MgO have the minimum strain thus they can be used as reference for the GPA analysis. The amount of strain in the TiN buffer layer is almost like that of the MgO, wherein no significant contrast variation is observed. When the MgO substrate is used as the reference instead of TiN, it has a very similar result. In Paper 3, the TiN buffer layer has been consistently used as the reference because it is closest to the film thus difference in foil thickness is more unlikely. The distinct spots in the FFTs of the high-resolution STEM images confirm that both buffer layer and film are in the same zone axis.

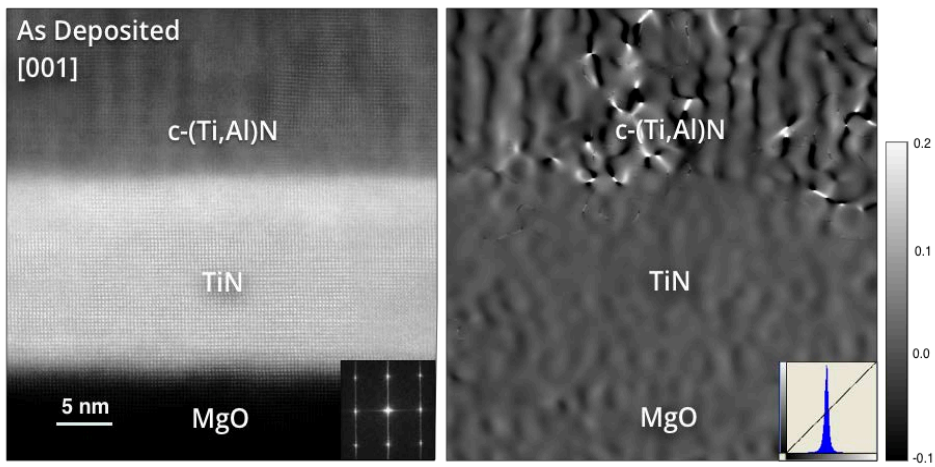

Figure 6.3. (a) HAADF-STEM with FFT inset and the corresponding deformation maps for (b) ε_{xx} strain tensor of as-deposited c-$(Ti_{0.38},Al_{0.62})N$/c-TiN(001).

6.6 APT

The chemical compositions of c-$(Ti_{1-x}Al_x)N_y$ films were obtained from a local electrode atom probe (Cameca LEAP 3000 X HR). The standard lift out technique [90] using FIB was used to produce the atom probe tomography (APT) tips. The tips were extracted at different positions along the thin film thickness. The tip shape was optimized to reduce the thermal tails and obtain high quality mass-to-charge spectra in APT. The composition analysis of the

APT technique the sample is based on at least 10 million ions per tip and 5 to 10 tips were used for each composition determination. This resulted in differences between spectra of less than 1 at. % of the elemental composition (Al, Ti, N). The nitrogen per metal fraction and the Al metal fraction were calculated by using the atomic percentages of the three main elements (Al, Ti and N). The errors reported have two contributions: the statistical error obtained from the reconstruction program (IVAS) and the composition average obtained from measuring several tips at different positions along the thin film thickness (propagation of errors is included). The main contribution to the error is due to intrinsic fluctuation in the as deposited state as describe by frequency distribution analysis and Pearson coefficient in previous work [14, 91].

A proximity histogram (proxigram) was used to obtain the composition profiles across the interfaces of the decomposed Al- and Ti-rich domains. It is a data compilation technique that generates a composition profile in 3D relative and in the vicinity to a reference surface [92]. Based from Gault et. al [93], the general steps for generating a proxigrams in the reconstruction program (IVAS) are the following: first, the creation of an isosurface which highlights the microstructure feature to be analyzed. Then, the composition is examined normal to the isosurface in layers (shells) at increasing or decreasing distances, therefore no restriction in the surface geometry is imposed. Then, from each shell a concentration distribution profile (histogram) of each element present is generated. Finally, the data extracted from the histograms (average composition) is plotted as a proxigram composition profile.

6.7 Nanoindentation

The hardness values of the coatings were measured using UMIS nanoindenter and Hysitron Triboindenter TI-950 that are equipped with a Berkovich diamond tip. Polished tapered cross-sections of the coatings deposited using cathodic arc technique were used for the depth-sensing indentation while polished top surfaces were used for the coatings deposited using sputtering technique. At least 25 indents were performed for each sample. The Oliver and Pharr method [94] was used to determine the average hardness values that were extracted from the load-displacement curves. The contact area of the tip versus penetration depth was measured by using a fused silica as reference.

6.8 Thermal Analysis

The differential scanning calorimetry (DSC) method is used to measure the enthalpy changes when heating a material. This is done by measuring the difference in energy input into a substance and a reference material as a function of temperature. The DSC curve was used to calculate enthalpies of transitions by integrating the peak corresponding to a given transition. In this study, the thermal response of the (Ti,Al)N powders (i.e extracted from the coatings deposited on the Fe foils [22]) was examined using Netsch STA 449C DSC. Two heating cycles were performed, in which the second cycle was used as the baseline correction.

6.9 Ion beam analysis

The atomic compositions of single crystalline (Ti,Al)N coatings that were synthesized using different N flow rate were measured using ion-beam based material analysis. A 5 MV 15SDH-2 tandem accelerator at the Tandem Laboratory in Uppsala University was used for generation of ion beams. Time-of-flight elastic recoil detection analysis (TOF-ERDA) technique was used to determine the elemental distributions of the coatings. This is performed with a 36 MeV $^{127}I^{8+}$ beam with a recoil angle of 45° and incident angle of 67.5° with the surface normal. The Rutherford backscattering spectrometry (RBS) was used to determine the stoichiometry. This is performed with a 2 MeV $^{4}He^{+}$ beam with scattering angle of 170°, an incidence angle of 5° with respect to the surface normal, and a wiggling algorithm during acquisition to minimize channeling effects on the crystalline substrate.

7. Summary of papers and contribution to the field

7.1 Paper 1

This study tackles the influence of point defects generated during cathodic arc deposition on the phase stability and microstructural evolution of nitrogen deficient $(Ti_{1-x},Al_x)N_y$ thin films. The influence of applied negative bias voltage on the point defect concentration (e.g. self-interstitials and anti-sites) in *c*-$(Ti_{0.54},Al_{0.46})N_{0.87}$ alloys and consequently the microstructural and mechanical properties at high temperatures were shown. The enhancement of the driving force for phase separation at high bias voltage of -80 V was shown and attributed to the delayed annihilation of point defects resulting to an increase in internal energy of the system. The age hardening effect of the films is retained until 1100 ˚C (i.e. highest temperature reported for (Ti,Al)N films) by applying low bias voltage and reducing the overall N content of the coating during deposition. The results open up possible future design routes for transition metal nitride coatings and allow a better understanding on the effect of point defects that are generated in physical vapor deposition.

7.2 Paper 2

The main factors influencing the wear behavior of nitrogen deficient $(Ti_{1-x},Al_x)N_y$ coatings during high-speed cutting of a steel workpiece are shown in this study. The optimum bias condition that was reported in Paper 1 was employed in synthesizing (Ti,Al)N films with different N contents. Then, the interplay of nitrogen vacancies, microstructure, and chemical reaction of c-$(Ti_{0.52},Al_{0.48})N_y$ coatings with average N concentration of y = 0.92, y = 0.87, and y = 0.75 during cutting tests was investigated. The y = 0.75 coating contains the highest number of macroparticles and has an inhomogeneous microstructure after machining, containing c-$(Ti_{0.52},Al_{0.48})N_y$, Ti_2AlN MAX phases, and alternating layers of AlN and Fe-Ti phases near the macroparticles. In this case, both the chemical alteration within the coating and the presence of macroparticles has contributed to its relatively low flank and crater wear resistance. The y = 0.92 sample has an earlier onset of spinodal decomposition to c-AlN and c-TiN- rich domains as compared to the other samples. This decomposed structure has misfit dislocations (as observed in Paper 3) that caused the accelerated diffusion of Fe and Co from the

workpiece and the substrate though the coating, which would weaken the structure of the coating and make it more susceptible to wear. There is a delay in decomposition of the y = 0.87 sample, which is caused by the presence of nitrogen vacancies that lowers the free energy of the system. The occurrence of age hardening in y = 0.92 sample has caused its superior flank wear resistance among the samples while the dense structure of y = 0.87 sample that prevented chemical wear due to diffusion has caused its excellent crater wear resistance. This study gives insight on the role of nitrogen vacancies on the chemical reaction and wear behavior of transition metal nitride coatings during cutting service.

7.3 Paper 3

The defect structure of single crystal c-($Ti_{0.37}$,$Al_{0.63}$)N during spinodal decomposition is discussed in this study. Heteroepitaxial c-($Ti_{0.37}$,$Al_{0.63}$)N thin films were grown on MgO(001) and (111) substrates by magnetron sputtering. Single crystalline films with high level of purity allow the determination of the details of their dislocation structure using high-resolution diffraction and imaging techniques. The crystal quality of the single crystalline (Ti,Al)N films were examined by high-resolution XRD, reciprocal space maps (RSM), and high-angle annular dark-field imaging scanning transmission electron micrographs (HAADF-STEM). RSM measurements show that the annealed film (i.e. undergoes spinodal decomposition) has lower lateral correlation, broader FWHM and higher mosaicity as compared to the as-deposited film. HAADF-STEM images show that as-deposited films have homogeneous composition with no indication of elemental segregation while annealed films decompose to form coherent c-AlN- and c-TiN- rich domains with elongated shape along the elastically soft <001> direction. The deformation maps containing the strain tensor components (e.g. ε_{xx}, ε_{yy}, and ε_{xy}) of *c*-(Ti,Al)N were shown for the first time in this study through geometric phase analysis (GPA) on HAADF-STEM micrographs. Results reveal that strains occur near the interface of the segregated domains and the c-TiN domains accommodate more dislocations than the c-AlN domains. This is attributed to the strong directionality of the covalent chemical bonds of c-AlN, making the dislocations favorably aggregate in c-TiN. The findings point out that the chemical bonding state and elastic properties of the segregated domains affects the defect structure of (Ti,Al)N during spinodal decomposition.

7.4 Paper 4

Epitaxial growth of wurtzite w-($Ti_{0.23}$,$Al_{0.77}$)N(0001) film on MgO(111) substrate has been shown for the first time in this study. The film was grown at 700 °C using a UHV DC magnetron sputtering system. A single crystal cubic c-($Ti_{0.23}$,$Al_{0.77}$)N film is first grown to a critical thickness (between 10 and 30 nm) using a TiN(111) buffer layer deposited on MgO(111). Above this thickness, a transition from cubic to wurtzite film occurs, with a zigzag interface between the two structures. The interface has orientation relationship of c-($Ti_{0.23}$,$Al_{0.77}$)N$(111)[1\bar{1}0]$||w-($Ti_{0.23}$,$Al_{0.77}$)N$(0001)[11\bar{2}0]$. Continued deposition results to a gradual break-down of the epitaxial growth towards polycrystalline growth of wurtzite columns with a high degree of 0001 texture. Plan-view TEM images show that the wurtzite grains grow larger as the film thickens.

This study also compares the thermal stability of epitaxial w-($Ti_{0.23}$,$Al_{0.77}$)N(0001) and epitaxial c-($Ti_{0.37}$,$Al_{0.63}$)N(111). The as-deposited w-($Ti_{0.23}$,$Al_{0.77}$)N(0001) shows a clustering of coherent nm-sized domains while c-($Ti_{0.37}$,$Al_{0.63}$)N(111) remains homogeneous. After annealing at 900 °C, the cubic film has segregated to form elongated c-AlN and c-TiN- rich domains along [001] direction via spinodal decomposition (i.e as reported in Paper 3) while the wurtzite film has domains with slightly larger sizes than that of the as-deposited. The wurtzite structure has a slower coarsening rate of the compared to cubic, which is indicative of a higher thermal stability.

7.5 Paper 5

Epitaxial (Ti_{1-x},Al_x)N_y with average N concentration of y = 0.67, 0.79, and 0.92 are deposited on (111)- and (001)- oriented MgO substrates by DC magnetron sputtering technique. Epitaxial c-(Ti_{1-x},Al_x)N_y(111) on MgO(111) is sustained all through the film thickness. Epitaxial c-(Ti_{1-x},Al_x)N_y(001) layers are grown on MgO(001) for a certain thickness (few nanometers) then a transition to polycrystalline growth occurs. The thickness of epitaxial c-(Ti_{1-x},Al_x)N_y(001) layer increases as the N content decreases. The better crystalline quality of films with low N contents is attributed to the high adatom surface mobility in N deficient conditions. The epitaxial c-(Ti,Al)N(111) and c-(Ti,Al)N(001) layers are homogeneous in the as-deposited state. The strain maps of the HAADF-STEM images of epitaxial c-($Ti_{1-x}Al_x$)N_y(111) films show that films with higher N vacancies have more strain fluctuation. After annealing at 950 °C, the c-(Ti,Al)N(111) films have undergone spinodal decomposition. The domain size

of (001) and (111)- oriented epitaxial c-(Ti,Al)N films increases with the nitrogen content. Strain maps show that decomposition increase the strain fluctuation of the system. The coherency strain and dislocations generated during decomposition resulted to an increase in hardness of the films. Annealing the films at 1100 ºC have caused the domain sizes of the films to further increase and the strain concentration to decrease. At this temperature, the hardness of the y = 0.79, and 0.92 films have decreased because the coherency has decreased when the domains have coarsen. Whilst, the hardness of the y = 0.67 film still increase because there is a delay in coarsening with high N vacancies.

Unique features are observed in $(Ti_{1-x},Al_x)N_{0.67}$ films, which has the highest N vacancies. The $(Ti_{1-x},Al_x)N_{0.67}$(111) film on MgO(111) contains some coherently oriented wurtzite w-$(Ti_{1-x},Al_x)N_{0.67}$(0001) structure in some regions at the top of the film. The $(Ti_{1-x},Al_x)N_{0.67}$(001) film on MgO(001) contains conical features with segregated domains already in the as-deposited state and remains stable when annealed at 950 °C. The domain size of this film has slightly increased after annealing at 1100 ºC. The coarsening rate of the domains inside the conical feature is slower than that of the domains in the epitaxial layer at high temperatures. N vacancy concentration affects the defect structures and thermal stability of $(Ti_{1-x},Al_x)N_y$ thin films.

8. Future work

The potential research works based on the results obtained in this thesis are the following:

- Cathodic arc deposited films. A delay in decomposition is observed as N content of $(Ti_{0.5},Al_{0.5})N_y$ ($y < 1$) films decreases. This results to a higher thermal stability (Paper 1) and crater wear resistance (Paper 2) of nitrogen deficient films. However, low N content of films also results to an increase in the number of macroparticles, which is detrimental to the mechanical properties of the coatings. The presence of macroparticles also facilitates diffusion of chip elements into the coatings during machining and causes chemical wear. Filtered cathodic arc system is recommended to minimize macroparticles of $(Ti_{0.5},Al_{0.5})N_y$ ($y < 1$) films and further improve their functional properties.

- Elastic Properties. In Paper 1 and Paper 3, *ab initio* cubic elastic constants are used for the strain measurements. It is recommended to use experimental techniques to measure elastic constants of the single crystal c-$(Ti_{1-x},Al_x)N_y$ films such as by TEM and optical characterizations. Elastic constants of wurtzite $(Ti_{1-x},Al_x)N_y$ are missing in the literature. These are needed to obtain more information on the elastic properties of this structure.

- Wurtzite (Ti,Al)N
    - In Paper 4, the growth and microstructural features at high temperature of epitaxial w-$(Ti_{1-x},Al_x)N_y$(111) film have been shown. Theoretical studies on the microstructural and strain evolution of single crystal w-(Ti,Al)N should be investigated. Besides hardness, functional properties of this structure such as thermal and electrical conductivities are of interest.

    - In Paper 5, experimental studies show the formation of wurtzite structures in $(Ti_{1-x},Al_x)N_y$ film with high N vacancies on MgO(111) substrate. Theoretical calculations on the effect of N vacancies and other defects (e.g. interstitials, anti-sites, and line defects) on the thermodynamics and kinetics of w-(Ti,Al)N should be investigated.

- In-situ decomposition studies. In Paper 5, N vacancies concentration has effect on the coarsening rate of the Ti- and Al- rich domains in $(Ti_{1-x},Al_x)N_y$ single crystal films.
    - It is recommended to do STEM imaging and chemical analysis during annealing of single crystal films with different N contents in order to obtain more details on the microstructural evolution and chemical composition of domains during decomposition. Visualization on how N vacancies affect decomposition kinetics is important.

    - It is of interest to investigate the dislocation structure and strain evolution of single crystal films during annealing. These would provide us more insight on how dislocations can affect the kinetics and thermodynamics of c-$(Ti_{1-x},Al_x)N_y$ at elevated temperatures.

- Deformation Mechanism
    - Detailed studies of the plastic zone in single crystal c-$(Ti_{1-x},Al_x)N_y$ films induced by nanoindentation is recommended. Characterizations can be done by TEM.

    - It is recommended to synthesize w-$(Ti_{1-x},Al_x)N_y$ single crystal films with different growth orientations and evaluate its deformation mechanism.

- Material Systems. It is recommended to investigate in detail the dislocation structure, effect of point defects, and strain evolution of other transition metal nitrides (e.g. Zr, Ta, and Hf nitrides), high entropy alloys, and multilayers. This can be done by utilizing the state-of-the-art techniques used in this study such as high resolution XRD, TEM, and GPA analysis.

- Applications. The performance of the synthesized polycrystalline (Ti,Al)N coatings during cutting tests has been investigated in this study. The synthesized single crystalline cubic and wurtzite (Ti,Al)N films have potential applications in electronics and semiconductor industries.

References

[1] G. Welsch, R. Boyer, E. Collings, Materials properties handbook: titanium alloys, ASM international 1993.

[2] P.D. Harvey, Engineering properties of steel, American Society for Metals Metals Park, OH 1982.

[3] P. Jindal, A. Santhanam, U. Schleinkofer, A. Shuster, Performance of PVD TiN, TiCN, and TiAlN coated cemented carbide tools in turning, Int. J. Refract. Met. Hard Mater., 17 (1999) 163-170.

[4] H. Holleck, Material selection for hard coatings, J. Vac. Sci. Technol., A 4(1986) 2661-2669.

[5] J. Musil, Hard and superhard nanocomposite coatings, Surf. Coat. Technol., 125 (2000) 322-330.

[6] S. PalDey, S. Deevi, Single layer and multilayer wear resistant coatings of (Ti, Al) N: a review, Mater. Sci. Eng., A 342 (2003) 58-79.

[7] H. Holleck, H. Schulz, Advanced layer material constitution, Thin Solid Films, 153 (1987) 11-17.

[8] P.H. Mayrhofer, A. Hörling, L. Karlsson, J. Sjölén, T. Larsson, C. Mitterer, L. Hultman, Self-organized nanostructures in the Ti–Al–N system, Appl. Phys. Lett., 83 (2003) 2049-2051.

[9] M. Oden, L. Rogström, A. Knutsson, M. Terner, P. Hedström, J. Almer, J. Ilavsky, In situ small-angle x-ray scattering study of nanostructure evolution during decomposition of arc evaporated TiAlN coatings, Appl. Phys. Lett., 94 (2009) 053114.

[10] I.A. Abrikosov, A. Knutsson, B. Alling, F. Tasnádi, H. Lind, L. Hultman, M. Odén, Phase stability and elasticity of TiAlN, Materials, 4 (2011) 1599-1618.

[11] S.T. Oyama, Introduction to the chemistry of transition metal carbides and nitrides, The chemistry of transition metal carbides and nitrides, Springer 1996, pp. 1-27.

[12] J. Margrave, L. Toth, Transition metal carbides and Nitrides, Academic Press, New York, 1971.

[13] B. Alling, A. Karimi, L. Hultman, I.A. Abrikosov, First-principles study of the effect of nitrogen vacancies on the decomposition pattern in cubic Ti1–xAlxN1–y, Appl. Phys. Lett., 92 (2008) 071903.

[14] I.C. Schramm, M.P. Johansson Jõesaar, J. Jensen, F. Mücklich, M. Odén, Impact of nitrogen vacancies on the high temperature behavior of (Ti1–xAlx)Ny alloys, Acta Mater., 119 (2016) 218-228.

[15] I.C. Schramm, C. Pauly, M.P. Johansson Jõesaar, S. Slawik, S. Suarez, F. Mücklich, M. Odén, Effects of nitrogen vacancies on phase stability and mechanical properties of arc deposited (Ti0.52Al0.48)Ny (y<1) coatings, Surf. Coat. Technol., 330 (2017) 77-86.

[16] W.D. Münz, Titanium aluminum nitride films: A new alternative to TiN coatings, J. Vac. Sci. Technol., A 4 (1986) 2717-2725.

[17] Q. Chen, B. Sundman, Thermodynamic assessment of the Ti-Al-N system, Journal of Phase Equilibria, 19 (1998) 146.

[18] M. Ohring, Materials science of thin films, Elsevier 2001.

[19] N. Shulumba, O. Hellman, Z. Raza, B. Alling, J. Barrirero, F. Mücklich, I.A. Abrikosov, M. Odén, Lattice Vibrations Change the Solid Solubility of an Alloy at High Temperatures, Phys. Rev. Lett., 117 (2016) 205502.

[20] B. Alling, A.V. Ruban, A. Karimi, O.E. Peil, S. Simak, L. Hultman, I. Abrikosov, Mixing and decomposition thermodynamics of c– Ti 1– x Al x N from first-principles calculations, Phys. Rev. B, 75 (2007) 045123.

[21] B. Alling, M. Odén, L. Hultman, I. Abrikosov, Pressure enhancement of the isostructural cubic decomposition in Ti1–xAlxN, Appl. Phys. Lett., 95 (2009) 181906.

[22] N. Norrby, H. Lind, G. Parakhonskiy, M.P. Johansson, F. Tasnádi, L.S. Dubrovinsky, N. Dubrovinskaia, I.A. Abrikosov, M. Odén, High pressure and high temperature stabilization of cubic AlN in Ti0.60Al0.40N, J. Appl. Phys., 113 (2013) 053515.

[23] D. Holec, F. Rovere, P.H. Mayrhofer, P.B. Barna, Pressure-dependent stability of cubic and wurtzite phases within the TiN–AlN and CrN–AlN systems, Scripta Mater., 62 (2010) 349-352.

[24] F.C. Campbell, Elements of metallurgy and engineering alloys, ASM International 2008.

[25] G.N. Haidemenopoulos, Physical Metallurgy: Principles and Design, CRC Press 2018.

[26] D. Porter, K. Esterling, Phase transformations, Metals and Alloys, second ed., Chapman & Hall, London 1992.

[27] J.W. Cahn, J.E. Hilliard, Free energy of a nonuniform system. I. Interfacial free energy, The Journal of chemical physics, 28 (1958) 258-267.

[28] R. Haskell, Introduction to the thermodynamics of spinodal decomposition, Journal of the American Ceramic Society, 56 (1973) 355-360.

[29] A. Knutsson, M. Johansson, P.Å. Persson, L. Hultman, M. Odén, Thermal decomposition products in arc evaporated TiAlN/TiN multilayers, Appl. Phys. Lett., 93 (2008) 143110.

[30] N. Norrby, L. Rogström, M.P. Johansson-Jõesaar, N. Schell, M. Odén, In situ X-ray scattering study of the cubic to hexagonal transformation of AlN in Ti1−xAlxN, Acta Mater., 73 (2014) 205-214.

[31] A. Knutsson, M. Johansson, L. Karlsson, M. Odén, Thermally enhanced mechanical properties of arc evaporated Ti0.34Al0.66N/TiN multilayer coatings, J. Appl. Phys., 108 (2010) 044312.

[32] R. Rachbauer, S. Massl, E. Stergar, D. Holec, D. Kiener, J. Keckes, J. Patscheider, M. Stiefel, H. Leitner, P. Mayrhofer, Decomposition pathways in age hardening of Ti-Al-N films, J. Appl. Phys., 110 (2011) 023515.

[33] F. Wang, I.A. Abrikosov, S.I. Simak, M. Odén, F. Mücklich, F. Tasnádi, Coherency effects on the mixing thermodynamics of cubic Ti 1− x Al x N/TiN (001) multilayers, Phys. Rev. B, 93 (2016) 174201.

[34] F. Tasnádi, I.A. Abrikosov, L. Rogström, J. Almer, M.P. Johansson, M. Odén, Significant elastic anisotropy in Ti1−xAlxN alloys, Appl. Phys. Lett., 97 (2010) 231902.

[35] N. Shulumba, O. Hellman, L. Rogström, Z. Raza, F. Tasnádi, I.A. Abrikosov, M. Odén, Temperature-dependent elastic properties of Ti1−xAlxN alloys, Appl. Phys. Lett., 107 (2015) 231901.

[36] A. Hörling, L. Hultman, M. Odén, J. Sjölén, L. Karlsson, Thermal stability of arc evaporated high aluminum-content Ti1−xAlxN thin films, J. Vac. Sci. Technol., A 20 (2002) 1815-1823.

[37] N. Engel, Copper, copper alloys and the electron concentration concept, Acta Metallurgica, 15 (1967) 557-563.

[38] S. Uehara, T. Masamoto, A. Onodera, M. Ueno, O. Shimomura, K. Takemura, Equation of state of the rocksalt phase of III–V nitrides to 72 GPa or higher, Journal of Physics and Chemistry of Solids, 58 (1997) 2093-2099.

[39] T. Sasaki, M. Akaishi, S. Yamaoka, Y. Fujiki, T. Oikawa, Simultaneous crystallization of diamond and cubic boron nitride from the graphite relative boron carbide nitride (BC2N) under high pressure/high temperature conditions, Chemistry of Materials, 5 (1993) 695-699.

[40] M. Garbrecht, L. Hultman, M. Fawey, T. Sands, B. Saha, Void-mediated coherency-strain relaxation and impediment of cubic-to-hexagonal transformation in epitaxial metastable metal/semiconductor TiN/Al0.72Sc0.28N multilayers, Physical Review Materials, 1 (2017) 033402.

[41] M. Zhou, Y. Makino, M. Nose, K. Nogi, Phase transition and properties of Ti–Al–N thin films prepared by r.f.-plasma assisted magnetron sputtering, Thin Solid Films, 339 (1999) 203-208.

[42] Y. Pinot, M.H. Tuilier, M.J. Pac, C. Rousselot, D. Thiaudière, C. Ulhaq-Bouillet, Influence of film thickness on the structural transition cubic/hexagonal within Ti0.38Al0.62N films, Thin Solid Films, 649 (2018) 160-166.

[43] U. Wahlström, L. Hultman, J.E. Sundgren, F. Adibi, I. Petrov, J.E. Greene, Crystal growth and microstructure of polycrystalline Ti1−xAlxN alloy films deposited by ultra-high-vacuum dual-target magnetron sputtering, Thin Solid Films, 235 (1993) 62-70.

[44] R. Rachbauer, J.J. Gengler, A.A. Voevodin, K. Resch, P.H. Mayrhofer, Temperature driven evolution of thermal, electrical, and optical properties of Ti–Al–N coatings, Acta Mater., 60 (2012) 2091-2096.

[45] K. Calamba, J. Barrirero, M.P. Johansson Jõesaar, S. Bruyère, J. Pierson, A.l. Febvrier, P. Eklund, F. Mücklich, R. Boyd, M. Odén, Growth and high temperature decomposition of epitaxial metastable wurtzite (Ti1-x,Alx)N(0001) thin films, (Unpublished results).

[46] L. Toth, Transition metal carbides and nitrides, Elsevier 2014.

[47] F. Burmeister, C. Kohn, R. Kuebler, G. Kleer, B. Bläsi, A. Gombert, Applications for TiAlN- and TiO2-coatings with nanoscale surface topographies, Surf. Coat. Technol., 200 (2005) 1555-1559.

[48] H. Ljungcrantz, M. Odén, L. Hultman, J. Greene, J.E. Sundgren, Nanoindentation studies of single-crystal (001)-,(011)-, and (111)-oriented TiN layers on MgO, J. Appl. Phys., 80 (1996) 6725-6733.

[49] F. Adibi, I. Petrov, L. Hultman, U. Wahlström, T. Shimizu, D. McIntyre, J. Greene, J.E. Sundgren, Defect structure and phase transitions in epitaxial metastable cubic Ti0. 5Al0. 5N alloys grown on MgO (001) by ultra-high-vacuum magnetron sputter deposition, J. Appl. Phys., 69 (1991) 6437-6450.

[50] M. to Baben, L. Raumann, D. Music, J.M. Schneider, Origin of the nitrogen over- and understoichiometry in Ti0.5Al0.5N thin films, J Phys-Condens Mat, 24 (2012) 155401.

[51] M. to Baben, M. Hans, D. Primetzhofer, S. Evertz, H. Ruess, J.M. Schneider, Unprecedented thermal stability of inherently metastable titanium aluminum nitride by point defect engineering, Mater. Res. Lett., 5:3 (2016) 158-169.

[52] H. Oettel, R. Wiedemann, S. Preißler, Residual stresses in nitride hard coatings prepared by magnetron sputtering and arc evaporation, Surf. Coat. Technol., 74 (1995) 273-278.

[53] L. Tsetseris, N. Kalfagiannis, S. Logothetidis, S.T. Pantelides, Role of N Defects on Thermally Induced Atomic-Scale Structural Changes in Transition-Metal Nitrides, Phys. Rev. Lett. , 99 (2007) 125503.

[54] K. Calamba, I. Schramm, M. Johansson Jõesaar, J. Ghanbaja, J. Pierson, F. Mücklich, M. Odén, Enhanced thermal stability and mechanical properties of nitrogen deficient titanium aluminum nitride (Ti0.54Al0.46Ny) thin films by tuning the applied negative bias voltage, J. Appl. Phys., 122 (2017) 065301.

[55] D. Rafaja, C. Wüstefeld, C. Baehtz, V. Klemm, M. Dopita, M. Motylenko, C. Michotte, M. Kathrein, Effect of Internal Interfaces on Hardness and Thermal Stability of Nanocrystalline Ti0.5Al0.5N Coatings, Metall. Mater. Trans. A, 42 (2011) 559-569.

[56] L. Rogström, J. Ullbrand, J. Almer, L. Hultman, B. Jansson, M. Odén, Strain evolution during spinodal decomposition of TiAlN thin films, Thin Solid Films, 520 (2012) 5542-5549.

[57] Y.-S. Li, S.-X. Li, T.-Y. Zhang, Effect of dislocations on spinodal decomposition in Fe–Cr alloys, Journal of Nuclear Materials, 395 (2009) 120-130.

[58] A. Minami, A. Onuki, Dislocation formation in two-phase alloys, Phys. Rev. B, 70 (2004) 184114.

[59] C. Shen, N. Zhou, Y. Wang, Phase Field Modeling of Microstructural Evolution in Solids: Effect of Coupling among Different Extended Defects, Metall. Mater. Trans. A, 39 (2008) 1630-1637.

[60] B. Muhammad, and R. Rahmatalla, Growth and Characterization of Metastable Wide and-gap AllnN Epilayers, Dissertation No. 1027, Linkoping University Press 2008.

[61] H. Larsson, Growth of Thick GaN Layers on Sapphire by Hydride Vapour Phase Epitaxy, Dissertation No. 958, Linkoping University Press 2005.

[62] K. Calamba, J. Pierson, S. Bruyère, A.l. Febvrier, P. Eklund, J. Barrirero, F. Mücklich, R. Boyd, M.P. Johansson Jõesaar, M. Odén, Dislocation structure and microstrain evolution during spinodal decomposition of reactive magnetron sputtered heteroepixatial c-(Ti0.36,Al0.64)N/c-TiN films grown on MgO(001) and (111) substrates, J. Appl. Phys., 125 (2019) 105301.

[63] A. Anders, Cathodic arcs: from fractal spots to energetic condensation. Springer Science & Business Media, 50 (2009).

[64] A.A. Snaper, Arc deposition process and apparatus, U.S. Patent 3,625,848 (1971).

[65] T. Utsumi, Measurements of cathode spot temperature in vacuum arcs, Appl. Phys. Lett., 18 (1971) 218-220.

[66] A. Anders, B. Yotsombat, R. Binder, Correlation between cathode properties, burning voltage, and plasma parameters of vacuum arcs, J. Appl. Phys., 89 (2001) 7764-7771.

[67] K.M. Calamba, M.P. Johansson Jõesaar, S. Bruyère, J.F. Pierson, R. Boyd, J.M. Andersson, M. Odén, The effect of nitrogen vacancies on initial wear in arc deposited (Ti0.52,Al0.48)Ny, ($y < 1$) coatings during machining, Surf. Coat. Technol., 358 (2019) 452-460.

[68] I.C. Schramm, C. Pauly, M.P. Johansson Jõesaar, S. Slawik, S. Suarez, F. Mücklich, M. Odén, Effects of nitrogen vacancies on phase stability and mechanical properties of arc deposited (Ti0.52Al0.48)Ny (y<1) coatings, Surf. Coat. Technol., 330 (2017) 77-86.

[69] W. Münz, D. Lewis, S. Creasey, T. Hurkmans, T. Trinh, W. Ijzendorn, Defects in TiN and TiAlN coatings grown by combined cathodic arc/unbalanced magnetron technology, Vacuum, 46 (1995) 323-330.

[70] R.L. Boxman, S. Goldsmith, Macroparticle contamination in cathodic arc coatings: generation, transport and control, Surf. Coat. Technol., 52 (1992) 39-50.

[71] K. Calamba, J. Salamania, M.P. Johansson Jõesaar, R. Boyd, S. Bruyère, J. Pierson, M.A. Sortica, D. Primetzhofer, M. Odén, Effect of vacancies on the dislocation structure and thermal stability of nitrogen deficient single crystal (Ti1-x,Alx)Ny thin films, (Unpublished results).

[72] K.K. Schuegraf, Handbook of thin-film deposition processes and techniques: principles, methods, equipment, and applications, Noyes Data Corporation/Noyes Publications1988.

[73] R.V. Stuart, Vacuum technology, thin films, and sputtering: an introduction, Academic Press 2012.

[74] A. Ingason, F. Magnus, S. Olafsson, J. Gudmundsson, Morphology of TiN thin films grown on MgO (001) by reactive dc magnetron sputtering, J. Vac. Sci. Technol., A 28 (2010) 912-915.

[75] A. McLeod, C. Gabryel, Kinetics of the growth of spinel, MgAl2O4, on alumina particulate in aluminum alloys containing magnesium, Metall. Trans. A 23 (1992) 1279-1283.

[76] B. Kramer, N. Suh, Tool wear by solution: a quantitative understanding, Journal of Engineering for Industry, 102 (1980) 303-309.

[77] B.V. Manoj Kumar, J.R. Kumar, B. Basu, Crater wear mechanisms of TiCN–Ni–WC cermets during dry machining, Int. J. Refract. Met. Hard Mater. , 25 (2007) 392-399.

[78] S. Ruppi, M. Halvarsson, TEM investigation of wear mechanisms during metal machining, Thin Solid Films, 353 (1999) 182-188.

[79] D.A. Stephenson, J.S. Agapiou, Metal cutting theory and practice, CRC press 2016.

[80] R. M'Saoubi, S. Ruppi, Wear and thermal behaviour of CVD α-Al2O3 and MTCVD Ti(C,N) coatings during machining, CIRP Annals, 58 (2009) 57-60.

[81] N. Norrby, M.P. Johansson, R. M'Saoubi, M. Odén, Pressure and temperature effects on the decomposition of arc evaporated Ti0.6Al0.4N coatings in continuous turning, Surf. Coat. Technol. , 209 (2012) 203-207.

[82] S. Ruppi, B. Ho¨grelius, M. Huhtiranta, Wear characteristics of TiC, Ti(C,N), TiN and Al2O3 coatings in the turning of conventional and Ca-treated steels, Int. J. Refract. Met. Hard Mater., 16 (1998) 353-368.

[83] N. Norrby, M.P. Johansson-Jõesaar, M. Odén, Improved metal cutting performance with bias-modulated textured Ti0.50Al0.50N multilayers, Surf. Coat. Technol., 257 (2014) 102-107.

[84] M.W. Barsoum, T. El-Raghy, M. Ali, Processing and characterization of Ti2AlC, Ti2AlN, and Ti2AlC0.5N0.5, Metall. Mater. Trans. A, 31 (2000) 1857-1865.

[85] S. Veprek, M.G.J. Veprek-Heijman, P. Karvankova, J. Prochazka, Different approaches to superhard coatings and nanocomposites, Thin Solid Films, 476 (2005) 1-29.

[86] M. Birkholz, Thin film analysis by X-ray scattering, John Wiley & Sons2006.

[87] R. Langford, A.J.J.o.V.S. Petford-Long, S. Technology A: Vacuum, Films, Preparation of transmission electron microscopy cross-section specimens using focused ion beam milling, 19 (2001) 2186-2193.

[88] H. Rösner, C.T. Koch, G. Wilde, Strain mapping along Al–Pb interfaces, Acta Mater., 58 (2010) 162-172.

[89] M.J. Hÿtch, E. Snoeck, R. Kilaas, Quantitative measurement of displacement and strain fields from HREM micrographs, Ultramicroscopy, 74 (1998) 131-146.

[90] K. Thompson, D. Lawrence, D.J. Larson, J.D. Olson, T.F. Kelly, B. Gorman, In situ site-specific specimen preparation for atom probe tomography, Ultramicroscopy, 107 (2007) 131-139.

[91] L.J.S. Johnson, M. Thuvander, K. Stiller, M. Odén, L. Hultman, Spinodal decomposition of Ti0.33Al0.67N thin films studied by atom probe tomography, Thin Solid Films, 520 (2012) 4362-4368.

[92] O.C. Hellman, J.A. Vandenbroucke, J. Rüsing, D. Isheim, D.N. Seidman, Analysis of Three-dimensional Atom-probe Data by the Proximity Histogram, Microsc. Microanal., 6 (2002) 437-444.

[93] B. Gault, M.P. Moody, J.M. Cairney, S.P. Ringer, Atom probe microscopy, Springer Science & Business Media 2012.

[94] W.C. Oliver, G.M. Pharr, An improved technique for determining hardness and elastic modulus using load and displacement sensing indentation experiments, Journal of Materials Research, 7 (2011) 1564-1583.

Paper 1

Enhanced thermal stability and mechanical properties of nitrogen deficient titanium aluminum nitride ($Ti_{0.54}Al_{0.46}N_y$) thin films by tuning the applied negative bias voltage

K. Calamba, I. Schramm, M. Johansson Jõesaar, J. Ghanbaja, J. Pierson, F. Mücklich, and M. Odén

Journal of Applied Physics 122, 065301 (2017)

Reprinted with permission
© 2017, AIP Publishing

Enhanced thermal stability and mechanical properties of nitrogen deficient titanium aluminum nitride ($Ti_{0.54}Al_{0.46}N_Y$) thin films by tuning the applied negative bias voltage

K. M. Calamba, I. C. Schramm, M. P. Johansson Jõesaar, J. Ghanbaja, J. F. Pierson, F. Mücklich, and M. Odén

Citation: Journal of Applied Physics **122**, 065301 (2017);
View online: https://doi.org/10.1063/1.4986350
View Table of Contents: http://aip.scitation.org/toc/jap/122/6
Published by the American Institute of Physics

Articles you may be interested in

Study of atmospheric pressure plasma jet parameters generated by DC voltage driven cold plasma source
Journal of Applied Physics **122**, 063301 (2017); 10.1063/1.4986636

External electric field effects on Schottky barrier at $Gd_3N@C_{80}$/Au interface
Journal of Applied Physics **122**, 065102 (2017); 10.1063/1.4986878

High field electron transport in indium gallium nitride and indium aluminium nitride
Journal of Applied Physics **122**, 065701 (2017); 10.1063/1.4986576

Current from a nano-gap hyperbolic diode using shape-factors: Theory
Journal of Applied Physics **122**, 064501 (2017); 10.1063/1.4997457

Tutorial: Reactive high power impulse magnetron sputtering (R-HiPIMS)
Journal of Applied Physics **121**, 171101 (2017); 10.1063/1.4978350

Unprecedented Al supersaturation in single-phase rock salt structure VAlN films by Al^+ subplantation
Journal of Applied Physics **121**, 171907 (2017); 10.1063/1.4977813

Enhanced thermal stability and mechanical properties of nitrogen deficient titanium aluminum nitride ($Ti_{0.54}Al_{0.46}N_y$) thin films by tuning the applied negative bias voltage

K. M. Calamba,[1,2,a)] I. C. Schramm,[1,3] M. P. Johansson Jõesaar,[1,4] J. Ghanbaja,[2] J. F. Pierson,[2] F. Mücklich,[3] and M. Odén[1]

[1]*Nanostructured Materials, Department of Physics, Chemistry and Biology (IFM), Linköping University, Linköping SE 58183, Sweden*

[2]*Institut Jean Lamour (UMR CNRS 7198), Université de Lorraine, Nancy 54011, France*

[3]*Functional Materials, Department Materials Science, Saarland University, Saarbrucken 66041, Germany*

[4]*SECO Tools AB, Fagersta SE-73782, Sweden*

(Received 4 June 2017; accepted 23 July 2017; published online 8 August 2017)

Aspects on the phase stability and mechanical properties of nitrogen deficient $(Ti_{0.54}Al_{0.46})N_y$ alloys were investigated. Solid solution alloys of (Ti,Al)N were grown by cathodic arc deposition. The kinetic energy of the impinging ions was altered by varying the substrate bias voltage from −30 V to −80 V. Films deposited with a high bias value of −80 V showed larger lattice parameter, finer columnar structure, and higher compressive residual stress resulting in higher hardness than films biased at −30 V when comparing their as-deposited states. At elevated temperatures, the presence of nitrogen vacancies and point defects (anti-sites and self-interstitials generated by the ion-bombardment during coating deposition) in $(Ti_{0.54}Al_{0.46})N_{0.87}$ influence the driving force for phase separation. Highly biased nitrogen deficient films have point defects with higher stability during annealing, which cause a delay of the release of the stored lattice strain energy and then accelerates the decomposition tendencies to thermodynamically stable *c*-TiN and *w*-AlN. Low biased nitrogen deficient films have retarded phase transformation to *w*-AlN, which results in the prolongment of age hardening effect up to 1100 °C, i.e., the highest reported temperature for Ti-Al-N material system. Our study points out the role of vacancies and point defects in engineering thin films with enhanced thermal stability and mechanical properties for high temperature hard coating applications. *Published by AIP Publishing.* [http://dx.doi.org/10.1063/1.4986350]

I. INTRODUCTION

Investigation on the thermal stability of transition metal nitride thin films is of importance because it is a key factor in determining their distinctive physical properties, e.g., hardness, wear resistance, and electrical properties.[1–3] Among the metal nitrides, titanium aluminum nitride (Ti,Al)N based coating has remained as an outstanding material system partly due to its excellent high temperature resistance combined with an age hardening behavior resulting in good wear resistance.[2,4] The latter is based on a spinodal decomposition of the metastable cubic (*c*) solid solution *c*-(Ti,Al)N[5] into isostructurally coherent *c*-TiN and *c*-AlN rich domains at elevated temperatures.[6,7] The latter generates a hardness enhancement and hence improved mechanical properties of the *c*-(Ti,Al)N due to fluctuating strain fields[8] caused by coherency strains[9] and elastic stiffness differences[10,11] that obstruct dislocation motion. At even higher thermal loads, however, the *c*-AlN transform into its most stable phase, i.e., wurtzite *w*-AlN,[12] which is detrimental for the mechanical properties of the coating.[13] Suppressing or delaying the *w*-AlN formation is therefore expected to enhance the thermal stability and the mechanical properties of (Ti,Al)N thin film and extend its operational envelope to higher temperatures.

Ab initio calculations on *c*-$Ti_{1-x}Al_xN_{1-y}$ ($0 \le x,\ y \le 1$) have shown that nitrogen vacancies (V_N) has significant effect on the driving force for decomposition and the preferred decomposition direction.[14] This was experimentally confirmed by Schramm *et al.*,[15] where the presence of V_N enhanced the phase stability, i.e., delaying the onset of decomposition of cathodic arc evaporated $(Ti,Al)N_y$ ($y < 1$). It was shown that the onset of *w*-AlN phase transformation in $(Ti_{0.52}Al_{0.48})N_{0.87}$ occurred at about 1200 °C,[15] which is about 300 °C higher than what typically is reported for stoichiometric $(Ti_{0.5}Al_{0.5})N$ thin films.[16,17] Primary decomposition occurs on the metal sublattice, and Baben *et al.*[18] also reports an improved thermal stability of close to stoichiometric $(Ti,Al)N_y$ ($y \approx 1$) as compared to over-stoichiometric $(Ti,Al)N_y$ ($y > 1$). The faster decomposition in over-stoichiometric ($y > 1$) films is attributed to an enhanced diffusivity in the presence of metal vacancies. It has to be noted that in addition to vacancies, structural modifications in the film such as lattice strain also play a decisive role in determining its thermal stability since it is correlated to the energetic balance during the decomposition process of cubic ternary transition metal nitride.[19,20] Another approach to control the structure and properties of coatings is through the substrate bias condition.[21–23] It is well known that the bias determines the kinetic energy of the ions bombarding the growing film. In this context, cathodic arc deposition is

a)Electronic mail: katherine.calamba@liu.se.

advantageous since its plasma typically comprises a high degree of ionized metal vapor, and therefore, tuning the negative bias is an effective means to change the arrival energy of the condensing species[24] and hence also the microstructure and its point defect density (interstitials and anti-sites).[25]

In this study, the influence of such point defects in combination with nitrogen vacancies on the thermal stability of cathodic arc deposited $Ti_{0.54}Al_{0.46}N_{0.87}$ thin films were investigated. The Ti/Al ratio and amount of nitrogen vacancies was fixed at a level found by Schramm *et al.*[15] to yield substantially improved phase stability. The substrate bias voltage was varied from −30 V to −80 V in reference to the anode potential. At elevated temperatures, high biased films presented an enhanced phase separation while low biased films showed the highest phase stability. It is noteworthy that the age hardening effect of these coatings is retained to a temperature higher than ever before reported for Ti-Al-N materials. This paper also highlights the interplay between nitrogen vacancies and microstructure on transformation kinetics, which is of relevance for the understanding of metastable transition metal nitrides' thermal stability and mechanical properties.

II. MATERIAL AND METHODS

$(Ti_{1-x}Al_x)N_y$ films were deposited using an industrial scale (Metaplas MZR-323) reactive cathodic arc deposition system. A powder metallurgical manufactured $Ti_{0.45}Al_{0.55}$ cathode with a diameter of 100 mm was used as a target. Fe foils (Goodfellow Cambridge, Ltd., FE000400) and polished cemented carbide (WC-Co) inserts (12 wt. % Co, ISO SNUN120408) were used as substrates. The substrates were cleaned in an alkaline solution prior to inserting the substrates in the deposition chamber. In the chamber, they were mounted on a rotating cylinder fixture (3 rpm) facing the cathode. Pure N_2 was used to obtain $(Ti_{1-x}Al_x)N$ reference samples with compositions close to stoichiometric value[15] while an atmosphere mixture of 40% $N_2/(Ar + N_2)$ was used to synthesize the nitrogen deficient coatings. During deposition, a total gas pressure of 2 Pa was used for both conditions. The flow rates of N_2 and Ar were set to 120 sccm and 180 sccm, respectively, to obtain the 40% $N_2/(Ar + N_2)$ mixture, and the gasses were introduced through pipes positioned vertically in the chamber. An arc current of 13.7 A was required to achieve stable deposition conditions, which resulted in plasma heating of the substrates. To improve coating adhesion, additional heating was supplied by a heater positioned on the chamber wall. Collectively this resulted in a deposition temperature of 550 °C. Thin films were grown to a thickness of about 3 μm with a deposition rate of 250 nm/min. All deposition conditions were kept constant between depositions for each deposition atmosphere, except for the substrate bias voltage that was set to −30 V, −43 V, −55 V, −68 V, or −80 V for the different coatings.

A differential scanning calorimeter (DSC, Netsch STA 449C) was used to examine the thermal response of the as-deposited films. Powder samples were used in the analysis and extracted from the coatings deposited on the Fe foils. Powder samples were obtained by first thinning of the Fe foil by mechanical grinding its backside and then dissolving it in concentrated (37%) HCl.[26] DSC measurements were performed with two heating cycles, in which the second cycle was used as baseline correction. The sample mass used per run was 30 mg. The powder samples were initially outgassed for 1 h at 250 °C after which the measurement started by heating up the sample to 1400 °C in 50 sccm flow of Ar. The heating and cooling rates were kept constant at 20 °C/min.

X-ray diffractograms of the powdered samples and coatings on substrates recorded with a PANalytical X'Pert PRO MRD diffractometer and were used for phase analysis. Residual stress measurements of the coatings on substrates were obtained using a PANalytical Empyrean diffractometer. The $\sin^2\psi$ method was used to determine the strain state in the coating using the 422 diffraction line. The elastic constants used to convert the strain measurements to stress are $E = 460$ GPa and $\nu = 0.20$, obtained from *ab initio* calculations.[10] All x-ray diffractometry measurements were performed using Cu K_α radiation.

Isothermal annealing of the thin films deposited on the WC-Co substrates was performed in a tube furnace under vacuum with a base pressure of 7×10^{-4} Pa. The samples were held for 15 min at the maximum temperature of either 800 °C, 900 °C, 1000 °C, 1100 °C, or 1200 °C. The heating and cooling rates were set to 20 °C/min.

Morphological and microstructural characterizations of the thin films were performed using a scanning electron microscope (SEM) (FEI Helios nanolab 600), scanning transmission electron microscope (STEM), energy-filtered analytical transmission electron microscopes (EFTEM) (JEOL ARM 200 Cold FEG), and analytical transmission electron microscope (TEM) (Fei Tecnai G^2 TF 20 UT). The analytical TEM was used to obtain the selected area electron diffraction (SAED) images. A focus ion beam (FIB) integrated in the SEM was used for producing cross section cuts. Both TEMs were operated at an acceleration voltage of 200 kV. Cross sectional TEM samples were prepared through mechanical grinding and polishing, followed by sputter etching (Gatan 691 precision ion polishing system) until the sample was electron transparent (<100 nm).

The 3D chemical composition was obtained from a local electrode atom probe (Cameca LEAP 3000 X HR) operated in the laser mode with a wavelength of 532 nm, a pulse frequency of 200 kHz, and a pulse energy of 0.5 nJ. The evaporation rate was set to 5 atoms per 1000 laser pulses, and the sample was set to a ground temperature of 60 K. Data reconstruction was performed in the IVAS package (version 3.6.8, Cameca) using the voltage mode. The reconstruction parameters were obtained using Kingham curves[27] and SEM images of the tip before and after run, where an evaporation field of 40 V per nm and a field factor between 3.5 and 3.8 were obtained. Atom probe tomography (APT) tips were produced using the FIB equipment via the standard lift out technique.[28]

The hardness values of the coatings were measured using UMIS nanoindenter equipped with a Berkovich diamond tip. Depth-sensing indentation was performed on polished tapered cross-sections of the coatings using a maximum load of 50 mN. The indentation depths for this amount of load were around 250 nm, which is less than 10% of the film's thickness.

TABLE I. Composition of $(Ti_{1-x}Al_x)N_y$ films in an atmosphere mixture of 40% $N_2/(Ar+N_2)$ at different negative bias voltages.

Bias voltage (V)	x = Al/(Al + Ti)	y = N/(Al + Ti)
−30	0.46 ± 0.01	0.87 ± 0.02
−43	0.46 ± 0.01	0.87 ± 0.01
−55	0.46 ± 0.02	0.87 ± 0.03
−68	0.46 ± 0.01	0.86 ± 0.01
−80	0.46 ± 0.01	0.87 ± 0.02

The average hardness values were extracted from the load-displacement curves using the Oliver and Pharr method.[29] At least 30 indents for were used for each samples, and fused silica was used as reference to compute the contact area of the tip versus penetration depth.

III. RESULTS

The chemical composition of as-deposited $(Ti_{1-x}Al_x)N_y$ films deposited in an atmosphere mixture of 40% $N_2/(Ar+N_2)$ at different negative bias voltages is shown in Table I. The composition values were obtained via APT, and only the main elements (Al, Ti, and N) were used for the values of x = Al/(Al + Ti) and y = N/(Al + Ti). These films are referred as the nitrogen deficient samples. The total content of impurity elements such as O, C, and Ar is less than 0.5 at. %. Results show that the chemical composition of the thin films is not altered with the variation of the bias voltage.

The X-ray diffraction patterns of the nitrogen deficient $(Ti_{0.54}Al_{0.46})N_{0.87}$ films at different bias voltage are shown in Fig. 1(a). The XRD peaks at 37.16°, 43.15°, and 62.66° correspond to the *c*-(Ti,Al)N 111, 200, and 220 diffraction peaks, respectively. The other peaks originate from the WC-Co substrate. XRD reveals that the bias voltage does not alter the phase composition and all as-deposited $(Ti_{0.54}Al_{0.46})N_{0.87}$ thin films have of a single phase with cubic NaCl-structure. Diffractograms show that an increase in the bias voltage leads to a small shift to lower 2θ values. Peak shifts are mainly caused by strain or by compositional changes.[30] APT measurements show that the elemental compositions of the films are not altered by bias voltage; thus, the observed shifts are attributed to changes in compressive stress. The measured compressive residual stresses of the films biased at −30 V, −55 V, and −80 V are −2.8 ± 0.4 GPa, −2.9 ± 0.8 GPa, and −5.6 ± 1 GPa, respectively. The increase in compressive stress is accompanied with line broadening, which indicates increasing microstrains. The high compressive residual stress in the as-deposited films with increased negative bias voltage has been observed for several materials synthesized by cathodic arc deposition.[21,23,31] In addition, a clear decrease in the 200 peak intensity and a change of preferred orientation to (111) and (220) are observed as a consequence of increasing the negative substrate bias voltage. The X-ray diffractograms of the $(Ti_{0.54}Al_{0.46})N$ reference samples [Fig. 1(b)] also show that they also crystallize in the cubic structure in the as-deposited state [Fig. 1(b)]. These films also exhibit peak shifts and line broadening when the applied bias voltage is increased, similar with the nitrogen deficient samples. The relative intensity of the 220 peak is more pronounced under high biasing conditions. The peak intensity ratio I^{111}/I^{200} of the nitrogen deficient coatings is higher as compared to the reference samples.

The surface morphologies of the as-deposited $(Ti_{0.54}Al_{0.46})N_{0.87}$ films with two different bias voltages (−30 V and −80 V) are presented in Figs. 2(a) and 2(b). SEM micrographs reveal that macroparticle density and diameter decrease with increasing biased voltage resulting in smoother surfaces. The corresponding microstructures of the films biased at −30 V and −80 V are shown in Figs. 2(c) and 2(d), respectively. Cross sectional TEM micrographs show that highly biased films have finer columnar structure. The sample biased at −80 V has a column width of 0.21 ± 0.04 μm while that biased at −30 V has a width of 0.57 ± 0.12 μm. The measured column widths are typical for (Ti,Al)N films deposited via arc technique and their decrease with increasing bias has been also observed in previously.[32,33] The SAED patterns of the coatings biased at −30 V and −80 V confirm that the films all have cubic structure in the as deposited state, in agreement with the XRD results.

The heat flow responses of $(Ti_{0.54}Al_{0.46})N_y$ samples synthesized at different bias voltages were evaluated by DSC as shown in Fig. 3. The $(Ti_{0.54}Al_{0.46})N_{0.87}$ coating biased at −30 V has a broad peak (T_1) at 900 °C (in 600 °C to 1100 °C range) while the sample biased at −80 V has peak at 800 °C (in 500 °C to 1000 °C range). These peaks correspond to several exothermic reactions, including recovery processes of lattice point defect complexes at different activation energies and phase separation via spinodal decomposition of

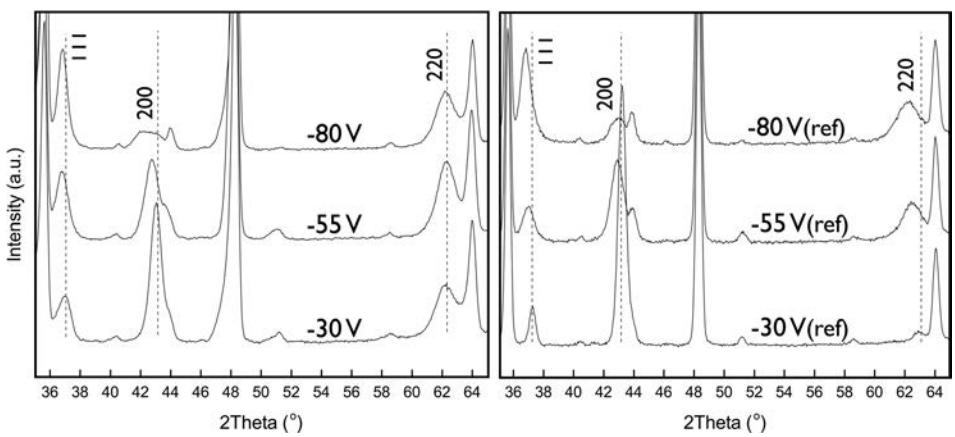

FIG. 1. X-ray diffractograms of as-deposited $(Ti_{0.54}Al_{0.46})N_y$ (a) nitrogen deficient and (b) reference coatings at different negative bias voltages. The unmarked peaks originate from the WC-Co substrate.

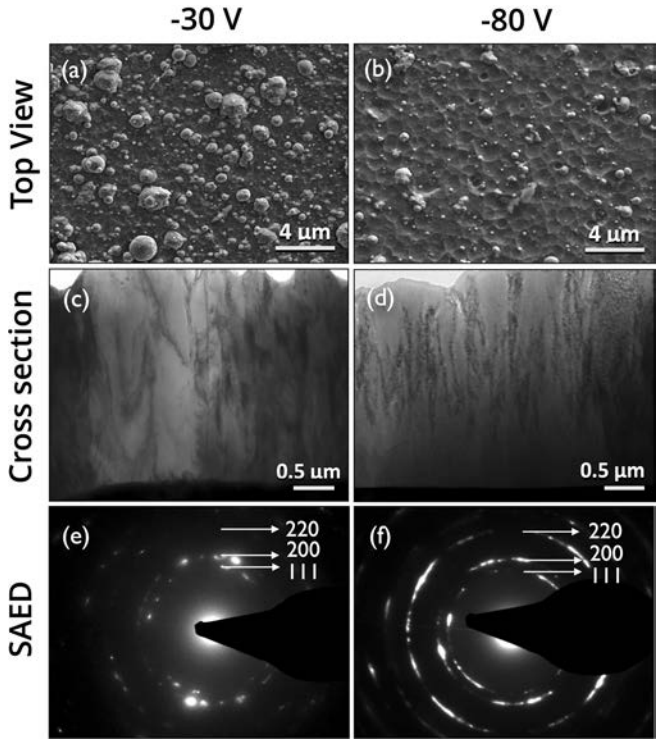

FIG. 2. Top-view SEM micrographs of as-deposited $(Ti_{0.54}Al_{0.46})N_{0.87}$ films with negative bias voltages of (a) −30 V and (b) −80 V, the cross-sectional TEM images of (c) −30 V and (d) −80 V, and SAED of (e) −30 V and (f) −80 V.

c-(Ti,Al)N.[34,35] The $(Ti_{0.54}Al_{0.46})N$ reference samples have resolved the T_2 peak corresponding to spinodal decomposition.[35,36] The $(Ti_{0.54}Al_{0.46})N$ reference samples biased at −30 V and −80 V and the nitrogen deficient samples biased at −80 V show another peak (T_3) at around 1200 °C corresponding to the transformation of the *c*-AlN into *w*-AlN. This peak is not clearly observed in the nitrogen deficient sample biased at −30 V and is expected to occur at higher temperature starting from 1200 °C, where a weak peak is observed. The T_1 to T_3 peaks are labeled in reference to the XRD result shown in Fig. 4. The peak at 1100 °C is an instrumental artifact caused by a phase transition in the furnace. The thermal response of the coatings reveals that highly biased nitrogen deficient samples have transformed to *w*-AlN

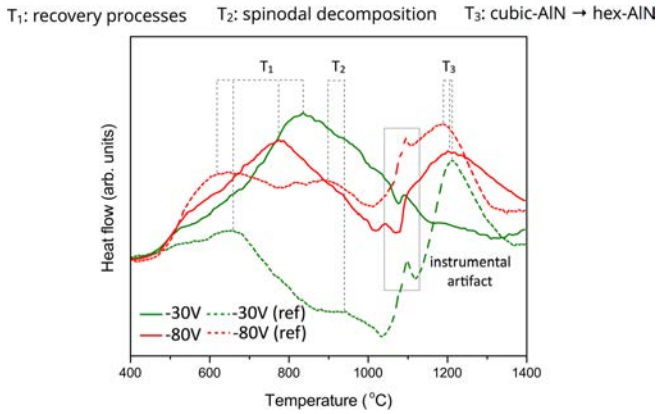

FIG. 3. Exothermal response of $(Ti_{0.54}Al_{0.46})N_{0.87}$ (solid line) and reference coatings (dashed line) at applied bias voltages of −30 V (green) and −80 V (red).

at earlier temperature in comparison to samples grown at lower bias voltage. There is no significant difference on the critical temperatures (T_1 to T_3) for phase transformation between the reference samples with different applied negative biases, similar to what was previously reported.[8]

The as-deposited $(Ti_{0.54}Al_{0.46})N_{0.87}$ films were annealed at different temperatures to examine their phase transformation at elevated temperatures. Figure 4 shows their x-ray diffractograms measured at room temperature after annealing. The sample biased at −30 V presents similar diffractograms in its as-deposited state and after annealing at 1000 °C. This indicates that the material still consists primarily of a solid solution of *c*-(Ti,Al)N, and only a slight shift to higher angles takes place between 700 and 1000 °C due to crystal recovery processes that cause stress relaxation.[13] The recovery is due to the rearrangement of defects and not due to recrystallization[25] since there has been no change in texture even at elevated temperatures. The *c*-(Ti,Al)N peaks broaden above 1000 °C, indicating the formation of *c*-AlN domains and Ti-enriched *c*-(Ti,Al)N domains via spinodal decomposition.[7] Well resolved diffraction peaks from both phases are observed at 1200 °C. Further annealing causes the *c*-AlN peaks to vanish while the *w*-AlN peaks increase in the intensity since metastable *c*-AlN transforms to its most stable form at high thermal loadings.[12] The sample biased at −80 V exhibits

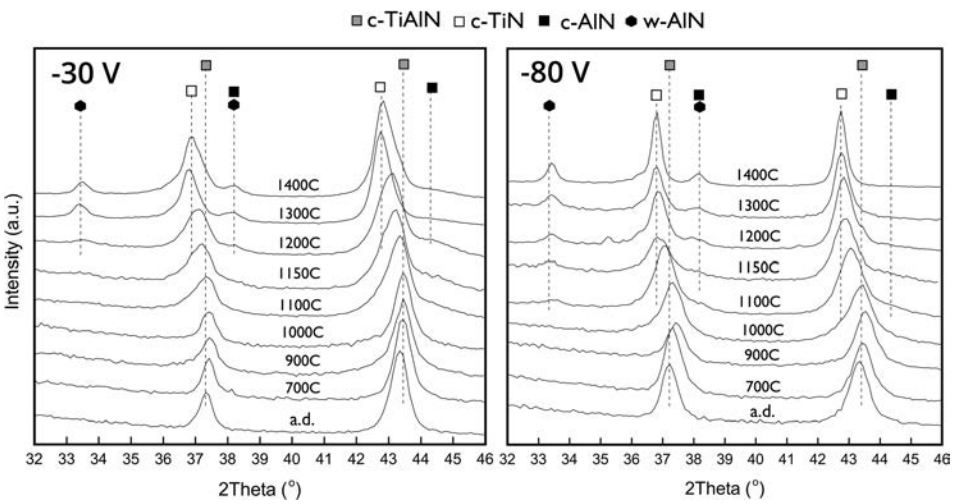

FIG. 4. X-ray diffractograms of $(Ti_{0.54}Al_{0.46})N_{0.87}$ biased at −30 V and −80 V after different annealing temperatures.

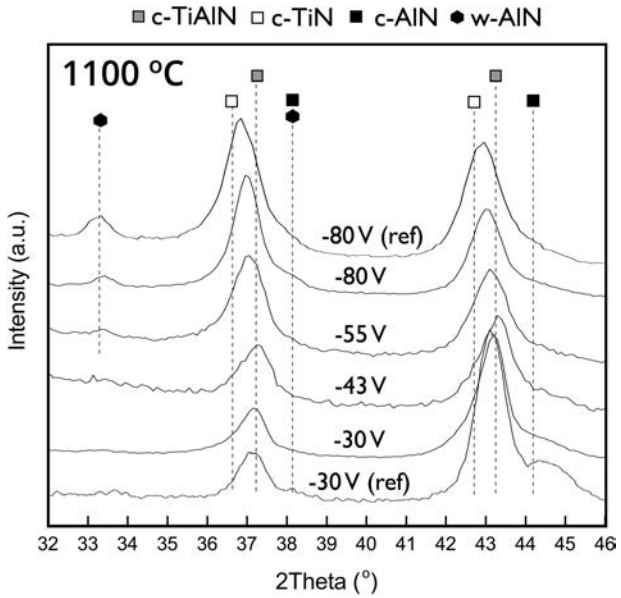

FIG. 5. X-ray diffractograms of $(Ti_{0.54}Al_{0.46})N_{0.87}$ with bias voltages of −30 V, −43 V, −55 V, and −80 V and reference coatings with bias voltages of −30 V (Ref. 15) and −80 V annealed at 1100 °C.

peak shifting to higher angles between 700 and 900 °C (due to crystal recovery processes) and peak broadening at 1000 °C (due to spinodal decomposition). The peak corresponding to *w*-AlN starts to appear at 1100 °C and becomes more distinct at higher temperatures. A similar trend is observed between samples biased at −30 V and −80 V, but the latter exhibits phase transformation at earlier temperatures.

A more detailed view of the bias voltage effect on the phase transformations of *c*-$(Ti_{0.54}Al_{0.46})N_{0.87}$ is shown in Fig. 5 at two temperatures, 1100 °C and 1200 °C. At 1100 °C, broadening of *c*-(Ti,Al)N peaks starts to occur for sample –30 V, wherein the peaks shift to left and small bump occurs to the right. The reference coating biased at −30 V heated at this temperature has a higher *c*-AlN peak intensity as compared to nitrogen deficient coatings. The *w*-AlN peaks are only resolved for samples with bias voltage −55 V and above, and the peaks become more pronounced by increasing the bias. The increase in *w*-AlN peak intensity with bias voltage is observed in both nitrogen deficient and reference coatings. However, the reference coating has higher *w*-AlN peak intensity as compared to the nitrogen deficient coating signifying that it is in a more advanced decomposed state.

The microstructure of $(Ti_{0.54}Al_{0.46})N_{0.87}$ coating grown with a bias of −55 V and heat-treated at 900 °C is shown in Fig. 6(a). The STEM micrograph in Fig. 6(b) shows bright and dark contrast, which arises from compositional segregation. The EFTEM images in Figs. 6(c) and 6(d) confirm segregation on the metal sublattice resulting from the chemical fluctuation during the deposition[37] while segregation on the N-sublattice cannot be detected. The artificial layers caused by rotating the samples during deposition can also be seen. They arise due to preferential resputtering of the lighter elements.[38,39] The observed segregation at 900 °C is less pronounced compared to coatings with stoichiometric N-content,[39] which indicates a higher phase stability.

Figure 7 shows the cross sectional SEM micrographs of the samples biased at −30 V, −55 V, and −80 V then

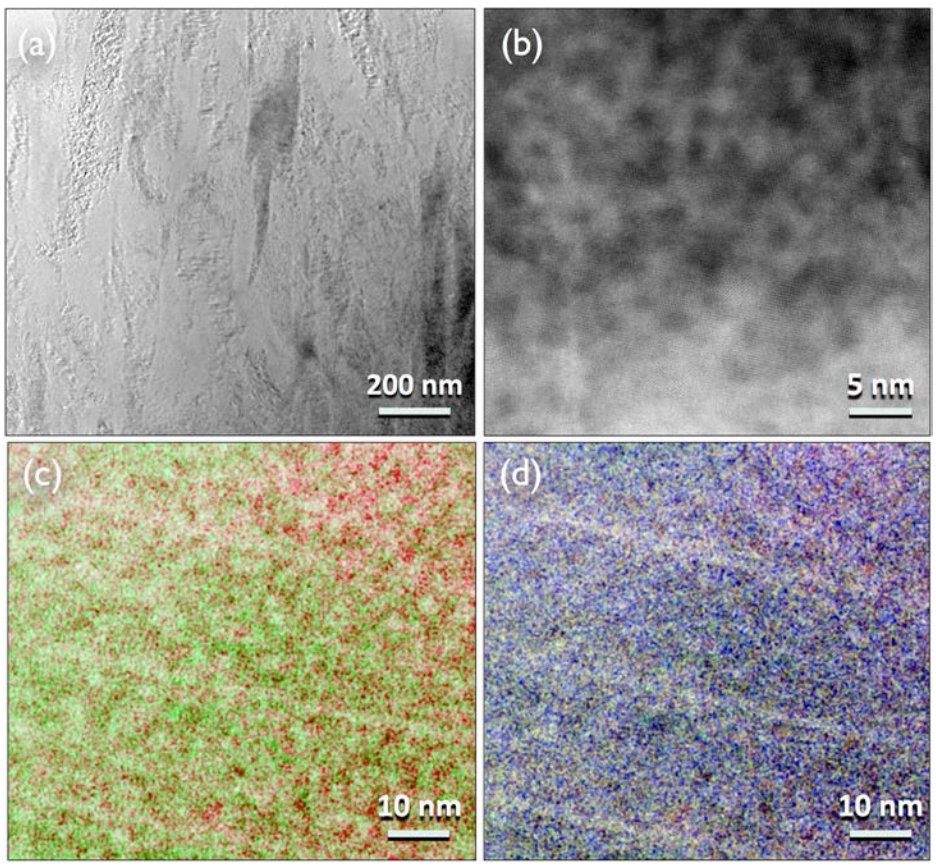

FIG. 6. (a) TEM (b) STEM, (c) EFTEM [Ti(red), Al(green)], and (d) EFTEM [Ti(red), Al(green), N(blue)] micrographs of $(Ti_{0.54}Al_{0.46})N_{0.87}$ grown with a bias voltage of −55 V and heated at 900 °C.

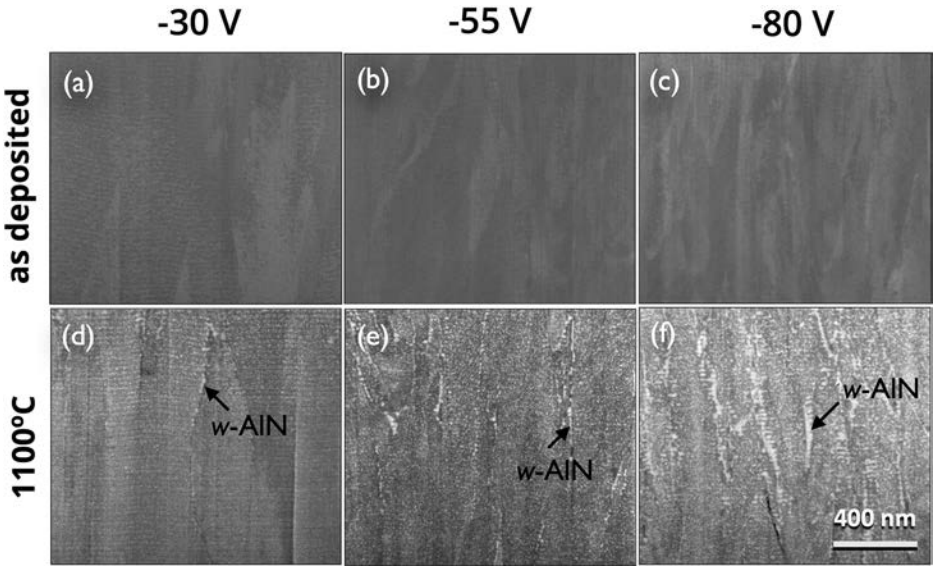

FIG. 7. Cross-sectional HRSEM micrographs of $(Ti_{0.54}Al_{0.46})N_{0.87}$ in as-deposited state with negative bias voltages of (a) −30 V, (b) −55 V, and (c) −80 V and heated at 1100 °C with negative bias voltages of (d) −30 V, (e) −55 V, and (f) −80 V.

post-annealed at 1100 °C, i.e., the critical temperature where *w*-AlN were observed in some samples from the XRD result. It can be observed that large *w*-AlN domains are growing mainly at grain boundaries. Sample biased at −80 V presents a higher amount of grain boundaries in comparison to the lower biased samples. Therefore, it is expected that highly biased samples have a larger volume fraction of *w*-AlN, as also observed from the XRD result. The high-resolution TEM images of samples biased at −30 V and −80 V and their corresponding SAED patterns are shown in Fig. 8. When the coatings are heated at 1100 °C, the sample biased at −30 V retains its *c*-(Ti,Al)N structure while the −80 V sample has segregated to *c*-TiN and *w*-AlN.

3D-APT data from $(Ti_{0.54}Al_{0.46})N_{0.87}$ coatings biased at −30 V and −80 V and annealed at 1100 °C are presented in Fig. 9. Figures 9(a) and 9(b) show elemental contrast overviews of the reconstructed tips. For clarity, only Al and Ti elements are shown. The morphology of the segregated aluminum- and titanium-rich domains is displayed in Figs. 9(c) and 9(d), where aluminum iso-concentration surfaces were drawn for the same reconstructed tips at an Al value of 26 at. %. Both biased samples presented a 3D interconnected segregation network. For the sample biased at −30 V, the domains are rounded while at −80 V the domains are slightly elongated. The segregated domains of the reference coatings have similar morphology as the nitrogen deficient coatings (figure not shown). There is no significant difference of the size of the domains between coatings with different N-stoichiometry and applied negative bias. The composition profiles across the interfaces of the decomposed Al- and Ti-rich domains were obtained by using proximity concentration histogram perpendicular to the surface as described by Gault *et al.*[40] Elemental composition of the samples annealed at 1100 °C is obtained from the concentration profiles across the Al-rich and Ti-rich clusters. Table II shows that the composition of the domains for the two samples. The composition of the domains is similar in the two samples.

The hardness evolution of the biased $(Ti_{0.54}Al_{0.46})N_{0.87}$ films as a function of annealing temperature is shown in Fig. 10. For the as-deposited state, the hardness increases with applied negative bias voltage. The hardness values of the films are retained until 800 °C. Age hardening is observed for all samples when annealed above this temperature. The occurrence of hardness enhancement has been prolonged when the coatings have lesser bias. A significant drop in hardness is observed when the samples are further annealed

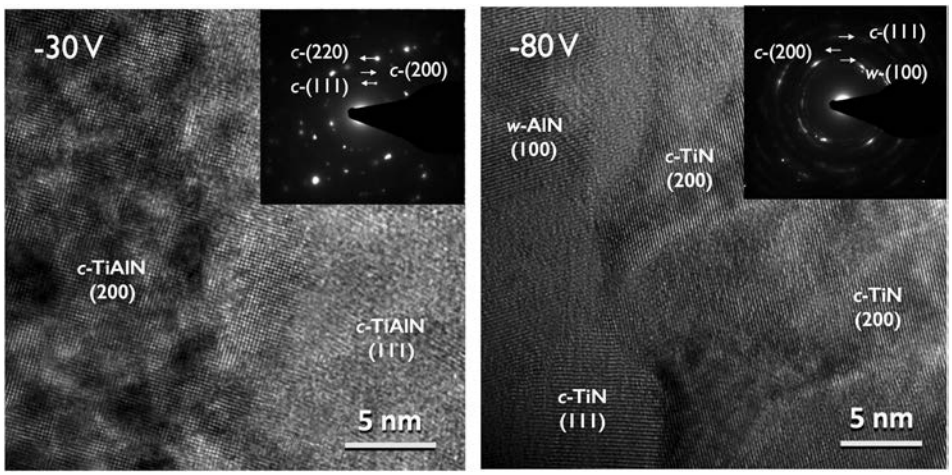

FIG. 8. HR-TEM of $(Ti_{0.54}Al_{0.46})N_{0.87}$ heated at 1100 °C and biased at (a) −30 V and (b) −80 V and SAED of (c) −30 V and (d) −80 V.

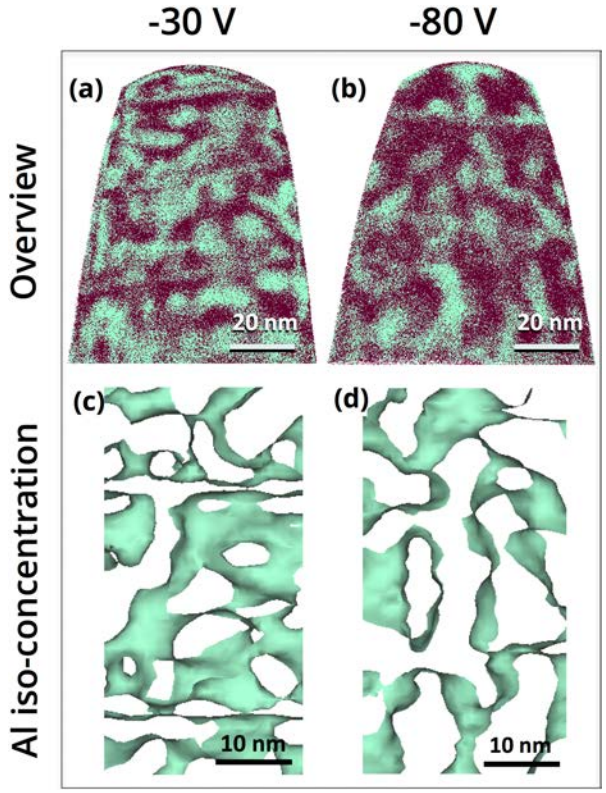

FIG. 9. An overview of the 3D reconstructed tip [Ti(red), Al(green)] of $(Ti_{0.54}Al_{0.46})N_{0.87}$ films annealed at 1100 °C with bias voltage of (a) −30 V and (b) −80 V and the Al iso-concentration surfaces for (c) −30 V and (d) −80 V.

to higher temperatures. The hardness drops at 1200 °C for the low biased samples (−30 V and −55 V) while the more highly biased sample (−80 V) decreases at 1000 °C. The indentation results show that the sample with the lowest bias had the most prolonged age hardening. The reference coating biased at −30 V has hardness value comparable to the nitrogen deficient $(Ti_{0.54}Al_{0.46})N_{0.87}$ in the as-deposited state; however, the former exhibits age hardening at lower temperature of around 800 °C and its hardness started to drop at 900 °C. The $(Ti_{0.54}Al_{0.46})N_{0.87}$ coating biased at −55 V showed the optimal mechanical behavior since the hardness values are relatively high and age hardening occurred at higher temperature and retained for a longer temperature range.

IV. DISCUSSION

Previous studies have shown that the presence of nitrogen vacancies significantly improves the phase stability of (Ti,Al)N-alloys, in which spinodal decomposition is retarded

TABLE II. Elemental composition inside Ti- and Al-rich domains of $(Ti_{0.54}Al_{0.46})N_{0.87}$ films biased at −30 V and −80 V annealed at 1100 °C.

Bias voltage (V)	Al (at. %)	Ti (at. %)	N (at. %)
−30 (Al-rich)	50.9 ± 0.4	2.2 ± 0.1	46.7 ± 0.4
−80 (Al-rich)	48.3 ± 0.4	4.4 ± 0.2	46.8 ± 0.4
−30 (Ti-rich)	3.3 ± 0.1	48.2 ± 0.3	48.2 ± 0.3
−80 (Ti-rich)	4.5 ± 0.1	46.2 ± 0.3	48.9 ± 0.3

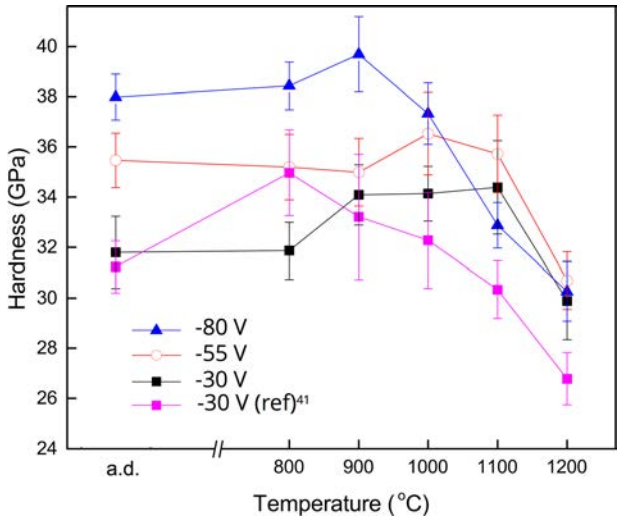

FIG. 10. Hardness at different temperatures of $(Ti_{0.54}Al_{0.46})N_{0.87}$ films biased at −30 V, −55 V, and −80 V and the reference sample.[41]

and *w*-AlN formation is shifted to higher temperatures.[14,15] These results suggest defect engineering as a route for new and improved materials. However, the synthesis method used may affect the defect structure. It has been reported that cathodic arc deposition introduces self-interstitials and antisites in the film[25] and one key deposition parameter affecting such point defect generation is the substrate bias voltage.[23,25] In this study, we build on the concept of vacancy improved thermal stability and include the effect of point defects generated during growth. We kept other parameters constant to isolate the effect of bias voltage, which included a constant coating composition. We will divide the discussion of our findings in three parts: address the effect of bias voltage on the growth of nitrogen deficient (Ti,Al)N, discuss how it affects the coatings' thermal stability, and describe the effect of microstructural evolution on their mechanical properties.

A. Microstructure of as-deposited films

The microstructure of nitrogen deficient (Ti,Al)N coatings is significantly affected when the growth-conditions are altered by changing the bias voltage. When applying a negative bias voltage to the substrate during arc deposition, positively charged metal ions are attracted towards the growing film surface, wherein additional kinetic energy and momentum transfer change the film forming conditions. This alters the morphology and grain size of the films because energetic ions directly associated with high bias voltage enhance surface diffusion, recrystallization, and resputtering.[42,43] The $(Ti_{0.54}Al_{0.46})N_{0.87}$ coatings grown with higher bias voltage results in finer columnar structure since enhanced energy of incoming ions generates more point defects, which increases the nucleation rates and defect density of the coatings during growth.[44] When the defect density is high, the local epitaxial growth of individual columns is interrupted by the occurrence of repeated nucleation.[45,46]

As-deposited $(Ti_{0.54}Al_{0.46})N_y$ coatings grown at different bias voltages all show single-phase solid solution NaCl-structure. The correlation of the peak intensity ratio and

applied negative bias voltage from the XRD results is due to a change in crystallographic texture and not an alteration of the films' stoichiometry. The change in preferred orientation from (001) to (111) and (110) by increasing the bias is a consequence of increasing ion bombardment. In general, the lowest overall energy condition resulting from the competition of surface energy, strain energy, and stopping energy of different lattice planes determines the preferred orientation of a multi-component fcc crystal with NaCl-type structure.[47,48] High bombardment energy of incoming and adsorbed spices would favor (111) and (110) growth, which have the lowest strain energy and lowest stopping energy, respectively. The preference of (110) is also attributed to an ion channeling effect,[49] in which the planes with lower resputtering rate becomes dominant since they survive the high ion bombardment best.

The cathodic arc deposition technique involves bombardment of high energetic ions during the film growth and thus the intrinsic stress of the coatings can be very high. Compressive residual stresses are generated when the number of atoms per unit volume of the film increases through implantation of incoming ions without any atomic rearrangement.[50] For (Ti,Al)N, residual stresses are mainly caused by interstitials and anti-sites (occupation of metal ions or atoms on the lattice sites of nitrogen and nitrogen on the metal lattice sites), which increase the compressive strain fields of the surrounding lattice.[25] The anti-site and interstitial defect concentrations increase with bias voltage or the energy of the incoming ions because it enhances the collision cascade. Consequently, applying a high bias voltage increases the strain energy stored in the system[51] and may affect the diffusion kinetics and evolution of the microstructure when exposed to high temperature. The films deposited with a high applied bias of −80 V have the highest compressive residual stress, which causes the interplanar distances parallel and perpendicular to the growth direction to differ.[42] Dispersion of the lattice parameter can result in considerable changes in the activation of processes such as vacancy and interstitial migration when the coatings are subjected to different temperatures. In Sec. IV B, the role of point defects on the observed changes during annealing will be discussed with respect to the thermal stability of nitrogen deficient (Ti,Al)N.

B. Thermal stability of $Ti_{1-x}Al_xN_y$

Nitrogen deficient $(Ti_{0.54}Al_{0.46})N_{0.87}$ coatings have shown enhanced phase stability, wherein phase transformation from *c*-AlN to *w*-AlN occurs at higher temperatures as compared to the same transition in stoichiometric films.[16,17,19,52,53] For $(Ti_{0.54}Al_{0.46})N_y$ where $y < 1$, *ab initio* calculations indicate that nitrogen vacancies is the fundamental reason for the lack of nitrogen in the coatings.[54] The delayed phase transformation to *w*-AlN of these coatings is mainly attributed to the reduction of mixing enthalpy and the alteration of the phonon dispersion in the presence of nitrogen vacancies.[15] It is expected that the miscibility gap is reduced when nitrogen vacancies are present and as a consequence, the spinodal line is suppressed to lower temperatures.

Stress relaxation and phase transformation occur when the coatings are subjected to increasing temperatures as indicated by the heat flow responses of the DSC curve. A system under such condition seeks to minimize its total energy during which atoms tend to rearrange into configuration giving lower stress provided that they have sufficient time and mobility. The relaxation is attained through migration, redistribution, and annihilation of stress-generating lattice defects.[23,55] The primary defects present in (Ti,Al)N coatings annealed above their deposition temperature are the less mobile point defects, which are the metal interstitials and vacancies.[55] Nitrogen interstitials have low activation energy, and thus, they easily migrate through diffusion to nitrogen vacancies, inner boundaries, or to the surface when annealed at low temperatures (<500 °C).[56] Metal and nitrogen vacancies affect significantly the thermal stability of TiAlN, but in different ways. The low onset temperature for spinodal decomposition of overstoichiometric $(Ti,Al)N_y$ is attributed to their existing metal vacancies, which enhance diffusion on the metal sublattice.[18] Diffusion requires energy to overcome the energy barriers for vacancy formation and changing atomic positions. Decomposition is then favored in the presence of metal vacancies because only the activation energy for changing atomic positions is needed. In $(Ti_{0.54}Al_{0.46})N_{0.87}$, nitrogen vacancies are prevalent in the system rather than metal vacancies. The presence of nitrogen vacancies in the $(Ti_{0.54}Al_{0.46})N_{0.87}$ material system may also allow diffusion of substitutional metal atoms such that temporary anti-site occupation occurs. However, the formation of anti-lattice sites is associated with high-energy barriers and actually less likely to occur. Nitrogen vacancies also have high activation energy for migration and exhibits slight repulsion, which delays decomposition.[15,56] Thus, nitrogen vacancy concentration in $(Ti_{0.54}Al_{0.46})N_{0.87}$ would contribute to the thermal stability enhancement of in contrast to metal vacancies.

In-situ XRD diffraction study on $Ti_{0.5}Al_{0.5}N$ coatings has shown that increasing the negative bias voltage delays the lattice strain reduction resulting in an accelerated phase decomposition of the material, i.e., *w*-AlN formation already occurs at 850 °C.[16] Strain reduction happens when the inherent structural defects undergo thermally activated rearrangement and then annihilated or migrate to lower energy sites. The larger size of T_1 peak from the DSC curve of the $(Ti_{0.54}Al_{0.46})N_{0.87}$ coatings biased at −30 V as compared to the coatings biased at −80 V indicates that many point defects were already annihilated at lower temperatures at lower biasing condition. This signifies that the defects caused by high ion energy bombardment in the presence of N vacancies are more stable than that by low ion energy bombardment,[57,58] contrary to the stoichiometric case $(Ti_{0.35}Al_{0.65})N$ observed by Rogström *et al.*,[8] perhaps by forming more complex defect structures that are more stable. The film biased at −80 V has delayed the lattice strain reduction to higher temperature; thus, there are considerable amount of defects that cause the internal energy of the system to increase and consequently accelerate the decomposition tendencies of *c*-(Ti,Al)N to its most stable form, i.e., *c*-TiN and *w*-AlN.

Koller *et al.*[59] have presented the idea that microstructure affects the phase separation of the thin film coatings. It was suggested that under-dense column boundaries caused by lowly biased coatings accelerates decomposition because they provide higher diffusion and reduce retarding forces against volume changes. In this study, the applied negative bias voltage was increased to obtain more dense films. However, the high biased coatings have shown to exhibit decomposition at earlier temperature. *In-situ* x-ray scattering studies have indicated that the size of the Al-rich domains also affects the transformation rate of *c*-AlN to *w*-AlN in $Ti_{1-x}Al_xN$.[8,12] In the case of $(Ti_{0.54}Al_{0.46})N_{0.87}$, the size of the Al-rich domains of both low and high biased films is similar, but later has shown earlier transformation of *c*-AlN to *w*-AlN. Thus, the accelerated decomposition of the highly biased nitrogen deficient (Ti,Al)N is not attributed to the grain density nor domain size changes.

C. Mechanical properties

In this study, defects and residual stresses have been shown to be beneficial to the film's physical properties (e.g., high hardness) in the as-deposited state. The high grain boundary density, high residual stress, and reduction of crystallite size of the $(Ti_{0.54}Al_{0.46})N_{0.87}$ film biased at −80 V contribute to its higher as-deposited hardness value as compared to film biased at −30 V. A significant increase in hardness is observed when the coatings are subjected to high temperatures. The age hardening observed for the coatings are due to the changes in the microstructure caused by spinodal deposition of *c*-(Ti,Al)N into coherent *c*-TiN and *c*-AlN domains. This mechanism creates composition fluctuation and differences in elastic properties, which prevents dislocations to propagate and thus resists plastic deformation,[7,36,53] known as coherency and Kohler hardening.[10,60]

Further annealing to higher temperatures causes the transformation of *c*-AlN to *w*-AlN. This transformation is detrimental to the film's mechanical properties as it causes the hardness values to significantly drop. The high rate of phase transformation of the coatings biased at −80 V is attributed to their high density of grain and column boundaries, which serve as high diffusion paths.[17] The grain size modification of the thin films induced by biasing may play lesser role on their spinodal decomposition; however, it has a considerable effect on other phenomena, such as nucleation. The formation of *w*-AlN at grain boundaries is enhanced when the decomposition is suppressed inside the grains.[15,61] The phase transformation would cause an increase in unit cell volume up to around 20%, which obliterates the coherency and increase the likelihood of dislocation movements.[36] It is essential to observe that the critical temperatures for the hardness drop vary with bias voltage. The low biased samples had hardness drop at higher temperatures, which signifies higher phase stability since they have prolonged age hardening effect of the (Ti,Al)N system.

V. CONCLUSIONS

The microstructure and thermal stability of nitrogen deficient $(Ti_{0.54}Al_{0.46})N_{0.87}$ films with different applied bias voltage were investigated. In the as-deposited state, the highly biased film showed improvements in hardness, morphology, and microstructure because of the enhanced ion bombardment that caused high compressive stresses and densification. At elevated temperature, this ternary material with nitrogen vacancies has shown high thermal stability, in which the phase transformation of c-AlN to w-AlN is suspended to higher temperatures compared to reference samples with compositions close to stoichiometric value. Adding the factor of bias voltage to the nitrogen deficient film has influenced the thermal stability of the material in addition to nitrogen vacancies. The highly biased films have enhanced the driving force for phase separation because of the delayed annihilation of point defects at high temperature, resulting in an increase in internal energy of the system. The low biased film has delayed phase transformation to *w*-AlN, thus improving the mechanical properties of the coatings, i.e., age hardening effect has been prolonged to the highest reported temperature. Point defect concentration generated during deposition plays a critical role in designing (Ti,Al)N films with desired thermal stability and mechanical properties suitable for hard coating applications.

ACKNOWLEDGMENTS

The work was supported by the European Union's Erasmus Mundus doctoral program in Materials Science and Engineering (DocMASE), the Swedish Research Council (Grant No. 621-2012-4401), the Swedish government strategic research area grant AFM – SFO MatLiU (2009-00971) and VINNOVA (M – Era.net project MC2 Grant No. 2013-02355). The atom probe was financed by the DFG and the federal state government of Saarland (INST 256/298-1 FUGG). Funding for FIB/SEM instrument was granted by the European Regional Development Fund (Project No. AME-Lab C/4-EFRE-13/2009/Br).

[1]J. E. Sundgren and H. Hentzell, J. Vac. Sci. Technol., A **4**, 2259 (1986).
[2]P. Jindal, A. Santhanam, U. Schleinkofer, and A. Shuster, Int. J. Refract. Met. Hard Mater. **17**, 163 (1999).
[3]J. Musil, Surf. Coat. Technol. **125**, 322 (2000).
[4]S. PalDey and S. Deevi, Mater. Sci. Eng., A **342**, 58 (2003).
[5]N. Shulumba, O. Hellman, Z. Raza, B. Alling, J. Barrirero, F. Mücklich, I. A. Abrikosov, and M. Odén, Phys. Rev. Lett. **117**, 205502 (2016).
[6]M. Oden, L. Rogström, A. Knutsson, M. Terner, P. Hedström, J. Almer, and J. Ilavsky, Appl. Phys. Lett. **94**, 053114 (2009).
[7]A. Hörling, L. Hultman, M. Odén, J. Sjölén, and L. Karlsson, Surf. Coat. Technol. **191**, 384 (2005).
[8]L. Rogström, J. Ullbrand, J. Almer, L. Hultman, B. Jansson, and M. Odén, Thin Solid Films **520**, 5542 (2012).
[9]F. Wang, I. A. Abrikosov, S. I. Simak, M. Odén, F. Mücklich, and F. Tasnádi, Phys. Rev. B **93**, 174201 (2016).
[10]F. Tasnádi, I. A. Abrikosov, L. Rogström, J. Almer, M. P. Johansson, and M. Odén, Appl. Phys. Lett. **97**, 231902 (2010).
[11]N. Shulumba, O. Hellman, L. Rogström, Z. Raza, F. Tasnádi, I. A. Abrikosov, and M. Odén, Appl. Phys. Lett. **107**, 231901 (2015).
[12]N. Norrby, L. Rogström, M. P. Johansson-Jõesaar, N. Schell, and M. Odén, Acta Mater. **73**, 205 (2014).
[13]P. H. Mayrhofer, A. Hörling, L. Karlsson, J. Sjölén, T. Larsson, C. Mitterer, and L. Hultman, Appl. Phys. Lett. **83**, 2049 (2003).
[14]B. Alling, A. Karimi, L. Hultman, and I. A. Abrikosov, Appl. Phys. Lett. **92**, 071903 (2008).
[15]I. C. Schramm, M. P. Johansson Jõesaar, J. Jensen, F. Mücklich, and M. Odén, Acta Mater. **119**, 218 (2016).
[16]C. Wüstefeld, D. Rafaja, M. Dopita, M. Motylenko, C. Baehtz, C. Michotte, and M. Kathrein, Surf. Coat. Technol. **206**, 1727 (2011).

[17]R. Rachbauer, S. Massl, E. Stergar, D. Holec, D. Kiener, J. Keckes, J. Patscheider, M. Stiefel, H. Leitner, and P. Mayrhofer, J. Appl. Phys. **110**, 023515 (2011).
[18]M. to Baben, M. Hans, D. Primetzhofer, S. Evertz, H. Ruess, and J. M. Schneider, Mater. Res. Lett. **5**, 158 (2017).
[19]F. Rovere, D. Music, S. Ershov, H.-G. Fuss, P. H. Mayrhofer, and J. M. Schneider, J. Phys. D: Appl. Phys. **43**, 035302 (2010).
[20]P. H. Mayrhofer, F. D. Fischer, H. J. Böhm, C. Mitterer, and J. M. Schneider, Acta Mater. **55**, 1441 (2007).
[21]M. Pfeiler, K. Kutschej, M. Penoy, C. Michotte, C. Mitterer, and M. Kathrein, Surf. Coat. Technol. **202**, 1050 (2007).
[22]H. Ljungcrantz, L. Hultman, J. E. Sundgren, and L. Karlsson, J. Appl. Phys. **78**, 832 (1995).
[23]M. Ahlgren and H. Blomqvist, Surf. Coat. Technol. **200**, 157 (2005).
[24]A. Anders, Appl. Phys. Lett. **80**, 1100 (2002).
[25]H. Oettel, R. Wiedemann, and S. Preißler, Surf. Coat. Technol. **74**, 273 (1995).
[26]N. Norrby, H. Lind, G. Parakhonskiy, M. P. Johansson, F. Tasnádi, L. S. Dubrovinsky, N. Dubrovinskaia, I. A. Abrikosov, and M. Odén, J. Appl. Phys. **113**, 053515 (2013).
[27]D. R. Kingham, Surf. Sci. **116**, 273 (1982).
[28]K. Thompson, D. Lawrence, D. J. Larson, J. D. Olson, T. F. Kelly, and B. Gorman, Ultramicroscopy **107**, 131 (2007).
[29]W. C. Oliver and G. M. Pharr, J. Mater. Res. **7**, 1564 (1992).
[30]B. D. Cullity, S. R. Cullity, and S. Stock, *Elements of X-Ray Diffraction* (Prentice Hall, New Jersey, 2001).
[31]C. Wüstefeld, D. Rafaja, V. Klemm, C. Michotte, and M. Kathrein, Surf. Coat. Technol. **205**, 1345 (2010).
[32]N. Norrby, M. P. Johansson-Jõesaar, and M. Odén, Surf. Coat. Technol. **257**, 102 (2014).
[33]O. Piot, C. Gautier, and J. Machet, Surf. Coat. Technol. **94**, 409 (1997).
[34]A. Knutsson, M. Johansson, L. Karlsson, and M. Odén, J. Appl. Phys. **108**, 044312 (2010).
[35]P. H. Mayrhofer, C. Mitterer, L. Hultman, and H. Clemens, Prog. Mater. Sci. **51**, 1032 (2006).
[36]I. A. Abrikosov, A. Knutsson, B. Alling, F. Tasnádi, H. Lind, L. Hultman, and M. Odén, Materials **4**, 1599 (2011).
[37]L. J. S. Johnson, M. Thuvander, K. Stiller, M. Odén, and L. Hultman, Thin Solid Films **520**, 4362 (2012).
[38]A. O. Eriksson, J. Q. Zhu, N. Ghafoor, M. P. Johansson, J. Sjölen, J. Jensen, M. Odén, L. Hultman, and J. Rosén, Surf. Coat. Technol. **205**, 3923 (2011).
[39]A. Knutsson, J. Ullbrand, L. Rogström, N. Norrby, L. Johnson, L. Hultman, J. Almer, M. J. Jöesaar, B. Jansson, and M. Odén, J. Appl. Phys. **113**, 213518 (2013).
[40]B. Gault, M. P. Moody, J. M. Cairney, and S. P. Ringer, *Atom Probe Microscopy* (Springer Science & Business Media, 2012), Vol. 160.
[41]I. C. Schramm, C. Pauly, M. P. Johansson Jõesaar, S. Suarez, F. Mücklich, and M. Odén, "Effects of N vacancies on phase stability and mechanical properties of arc deposited $(Ti_{0.52}Al_{0.48})N_y$" (unpublished).
[42]S. M. Rossnagel and J. J. Cuomo, Vacuum **38**, 73 (1988).
[43]A. Raveh, I. Zukerman, R. Shneck, R. Avni, and I. Fried, Surf. Coat. Technol. **201**, 6136 (2007).
[44]J. Almer, M. Odén, L. Hultman, and G. Håkansson, J. Vac. Sci. Technol., A **18**, 121 (2000).
[45]I. Petrov, P. Barna, L. Hultman, and J. Greene, J. Vac. Sci. Technol., A **21**, S117 (2003).
[46]I. Petrov, L. Hultman, J. E. Sundgren, and J. Greene, J. Vac. Sci. Technol., A **10**, 265 (1992).
[47]J. Zhao, X. Wang, Z. Chen, S. Yang, T. Shi, and X. Liu, J. Phys. D: Appl. Phys. **30**, 5 (1997).
[48]J. Pelleg, L. Z. Zevin, S. Lungo, and N. Croitoru, Thin Solid Films **197**, 117 (1991).
[49]L. S. Yu, J. M. Harper, J. J. Cuomo, and D. A. Smith, J. Vac. Sci. Technol., A **4**, 443 (1986).
[50]M. M. M. Bilek, D. R. McKenzie, and W. Moeller, Surf. Coat. Technol. **186**, 21 (2004).
[51]D. Rafaja, C. Wüstefeld, C. Baehtz, V. Klemm, M. Dopita, M. Motylenko, C. Michotte, and M. Kathrein, Metall. Mater. Trans. A **42**, 559 (2011).
[52]P. H. Mayrhofer, C. Mitterer, and H. Clemens, Adv. Eng. Mater. **7**, 1071 (2005).
[53]A. Hörling, L. Hultman, M. Odén, J. Sjölén, and L. Karlsson, J. Vac. Sci. Technol., A **20**, 1815 (2002).
[54]M. T. Baben, L. Raumann, D. Music, and J. M. Schneider, J. Phys.: Condens. Matter **24**, 155401 (2012).
[55]L. Hultman, Vacuum **57**, 1 (2000).
[56]L. Tsetseris, N. Kalfagiannis, S. Logothetidis, and S. T. Pantelides, Phys. Rev. Lett. **99**, 125503 (2007).
[57]L. Karlsson, A. Hörling, M. P. Johansson, L. Hultman, and G. Ramanath, Acta Mater. **50**, 5103 (2002).
[58]P. H. Mayrhofer and C. Mitterer, Surf. Coat. Technol. **133–134**, 131 (2000).
[59]C. M. Koller, R. Hollerweger, C. Sabitzer, R. Rachbauer, S. Kolozsvari, J. Paulitsch, and P. H. Mayrhofer, Surf. Coat. Technol. **259**, 599 (2014).
[60]J. S. Koehler, Phys. Rev. B **2**, 547 (1970).
[61]R. Forsén, M. P. Johansson, M. Odén, and N. Ghafoor, Thin Solid Films **534**, 394 (2013).

Paper 2

The effect of nitrogen vacancies on initial wear in arc deposited $(Ti_{0.52},Al_{0.48})N_y$, $(y < 1)$ coatings during machining

K. Calamba, M. Johansson Jõesaar, S. Bruyère, J. Pierson, R. Boyd, J. Andersson, M. Odén

Surface & Coatings Technology 358, 452–460 (2019)

Reprinted with permission
© 2018, Elsevier B.V.

Surface & Coatings Technology 358 (2019) 452–460

Contents lists available at ScienceDirect

Surface & Coatings Technology

journal homepage: www.elsevier.com/locate/surfcoat

The effect of nitrogen vacancies on initial wear in arc deposited ($Ti_{0.52}$, $Al_{0.48}$)N_y, ($y < 1$) coatings during machining

K.M. Calamba[a,b,*], M.P. Johansson Jõesaar[a,c], S. Bruyère[b], J.F. Pierson[b], R. Boyd[a], J.M. Andersson[c], M. Odén[a]

[a] Nanostructured Materials, Department of Physics, Chemistry and Biology (IFM), Linköping University, Linköping SE 58183, Sweden
[b] Université de Lorraine, CNRS, IJL, F-54000 Nancy, France
[c] SECO Tools AB, Fagersta SE-73782, Sweden

ARTICLE INFO

Keywords:
Wear mechanism
Nitrogen vacancies
(Ti,Al)N
Spinodal decomposition
MAX-phase
Cathodic arc

ABSTRACT

Nitrogen deficient c-($Ti_{0.52}Al_{0.48}$)N_y, y = 0.92, y = 0.87, and y = 0.75 coatings were prepared in different N_2/Ar discharges on WC-Co inserts by reactive cathodic arc deposition. The microstructure of the y = 0.92 coating show that spinodal decomposition has occurred resulting in the formation of coherent c-TiN- and c-AlN rich domains during cutting. The y = 0.87 and y = 0.75 coatings have exhibited a delay in decomposition due to the presence of nitrogen vacancies that lowers the free energy of the system. In the decomposed structure, grain boundaries and misfit dislocations enhance the diffusion of elements from the workpiece and the substrate (e.g. Fe, Cr, and Co) into the coatings and it becomes more susceptible to crater wear. The y = 0.87 sample displays the highest crater wear resistance because of its dense grain boundaries that prevent chemical wear. The y = 0.92 sample has the best flank wear resistance because the decomposition results in age hardening. The y = 0.75 sample contains the MAX-phase Ti_2AlN after cutting. The chemical alteration within the y = 0.75 sample and its high amount of macroparticles cause its low wear resistance. The different microstructure evolution caused by different amount of N-vacancies result in distinctive interactions between chip and coating, which also causes difference in the initial wear mechanism of the (Ti,Al)N_y coatings.

1. Introduction

Titanium aluminum nitride (Ti,Al)N based materials are widely used as a protective tool coating against thermal and mechanical loads in a wide range of applications [1,2]. In particular, due to its excellent wear, temperature, and oxidation resistance properties, metastable cubic B1 structured c-(Ti,Al)N coatings are well suited in metal machining [3,4]. In part, these properties have been attributed to age hardening of c-(Ti,Al)N as a result of a spinodal decomposition into isostructural coherent cubic c-TiN and c-AlN rich domains at elevated temperature [5–7]. At even higher thermal loads, c-AlN transform into wurtzite B4 w-AlN structure [8,9], also correlated to an impairment of the (Ti,Al)N coating mechanical properties [10]. In addition to the heat generated during service, the metal cutting process is also associated with high pressure conditions at the tool-chip contact area, wear zone [9,11], which may affect the spinodal decomposition of c-(Ti,Al)N [12].

Studies of the thermal stability and mechanical properties when tuning the nitrogen stoichiometry and point defect concentrations in c-(Ti,Al)N films have shown promises of improved coating properties [13–15]. Among others, a significant enhancement of the thermal stability with a delayed onset of the film hardness degrading w-AlN phase to about 1100 °C is demonstrated. Alling et al. predicted improved thermal stability in nitrogen deficient ($Ti_{1-x}Al_x$)N_y, $y < 1$ coatings due to the presence of N vacancies and a reduced driving force for spinodal decomposition [16].

During metal cutting operations, the highest temperature and shear stress occur on the rake face of the tool at about half of the contact length of the tool-chip interface [17,18], referred to as the crater wear zone. The wear mechanisms in this zone commonly combine abrasive- and chemical wear due to diffusion of elements from the work piece chip [19,20]. Mühlbacher et al. showed in a theoretical study that atomic diffusion is the prevalent mechanism controlling stoichiometry in transition metal nitride systems [21]. In nitrogen deficient (Ti,Al)N_y ($y < 1$), however, the interplay between the presence of N vacancies and the diffusion of atomic species from the chip during machining remains unexplored. The N vacancies, which have a low defect formation energy [21] could influence the metal diffusion process in (Ti,Al)N_y coatings.

* Corresponding author at: Nanostructured Materials, Department of Physics, Chemistry and Biology (IFM), Linköping University, Linköping SE 58183, Sweden.
E-mail address: katherine.calamba@liu.se (K.M. Calamba).

https://doi.org/10.1016/j.surfcoat.2018.11.062
Received 29 September 2018; Received in revised form 19 November 2018; Accepted 20 November 2018
Available online 22 November 2018
0257-8972/ © 2018 Published by Elsevier B.V.

In this study, the microstructural evolution and chemical interactions of nitrogen deficient $(Ti_{0.52}Al_{0.48})N_y$ (y = 0.92, 0.87, and 0.75) coatings, exposed to different cutting times were investigated. The coatings were fabricated using cathodic arc deposition with a substrate bias of −55 V and otherwise deposition conditions that results in an optimized high-temperature hardness [14]. Focused ion beam (FIB) samples were taken near the formed crater along the chip direction and subsequently characterized using high resolution techniques such as aberration-corrected transmission electron microscopy (TEM), scanning TEM (STEM), and spectroscopic mapping by STEM-EDS. The results are discussed with respect to the role of nitrogen vacancies on the wear behavior during metal cutting in two different steels.

2. Material and methods

$(Ti_{0.52}Al_{0.48})N_y$ (y < 1) coatings were deposited on cemented carbide (WC-Co, 12 wt% Co) triangular inserts (ISO TPUN160308) for metal cutting tests and square inserts (ISO SNUN120408) for coating characterization using an industrial scale reactive cathodic arc deposition system (Metaplas MZR-323). Prior to deposition, the substrates were cleaned in ultrasonic baths of an alkali solution and alcohol. The substrates were mounted on a one-axis rotational drum fixture. Three circular (100 mm in diameter) arc sources, fitted with $Ti_{0.45}Al_{0.55}$ cathodes, were mounted in a straight line from bottom to top on the chamber wall, facing the fixture. A cathode current of 150 A was applied resulting in a burning voltage of about 21 V in a 2 Pa (N_2 + Ar) gas mixture with a N_2-content $[N_2]/([Ar] + [N_2])$ of 100%, 40%, and 36%. For more details, see refs. [13, 22]. With this setup, coatings were grown with a fixture rotation of 3 rpm, a substrate bias voltage of −55 V and a deposition temperature of about 550 °C resulting in a deposition rate of about 0.25 μm/min. The different N_2-contents in the gas mixture resulted in different nitrogen content of the $(Ti_{0.52}Al_{0.48})N_y$ coatings with y = 0.92, y = 0.87, and y = 0.75, respectively. The chemical compositions of the as-deposited coatings were determined by atom probe tomography and reported for coatings grown in the same batch as the ones studied here [13,14]. The total coating thickness was held constant to about 3 μm for the three coatings.

X-ray diffractometry (XRD) by θ-2θ scans of the $(Ti_{0.52}Al_{0.48})N_y$ coatings were obtained with a PANalytical X'Pert PRO MRD diffractometer. The measurements were performed using Cu K_α radiation in a Bragg-Brentano configuration.

The cutting performance and initial wear of N deficient $(Ti_{0.52}Al_{0.48})N_y$ coated inserts was tested by turning in an alloy steel 42CrMoS4 (255 HB) for 1, 2, and 3 min. A new cutting edge was used for each cutting time. The turning tests were performed with a coolant consisting of a mixture of 6% Cimcool™ in water and the following cutting parameters: cutting speed v_c = 175 m/min, feed f = 0.25 mm/rev and depth-of-cut a_p = 2 mm. A second turning test was conducted in a ball bearing steel 100Cr6 (207 HB) for 1, 3, 5 and 10 min without cooling and v_c = 200 m/min, f = 0.20 mm/rev and a_p = 2 mm. The turning tests on 100Cr6 with lower hardness were performed to observe the progression of the wear in the coatings. They were conducted without coolant to ensure high enough temperature for spinodal decomposition of the (Ti,Al)N coatings [9]. Table 1 shows the chemical composition and hardness of the 42CrMoS4 and 100Cr6 work piece materials.

Cross-sectional TEM samples of the inserts after metal cutting were prepared using a FIB integrated in a scanning electron microscope (SEM) (Helios Nanolab 600i). An in-situ lift-out technique was used in the preparation [23]. FIB samples were obtained at around half of the cutting length of the chip-rake interface and parallel to the chip flow direction as illustrated in Fig. 1.

Table 1
Chemical composition (wt%) and hardness of the work piece materials with Fe as the balancing element.

Steel	C	Si	Mn	Cr	Mo	S	Hardness
42CrMoS4	0.42	0.25	0.75	1.10	0.22	0.020	255 HB
100Cr6	1.00	0.25	0.30	1.40	–	–	207 HB

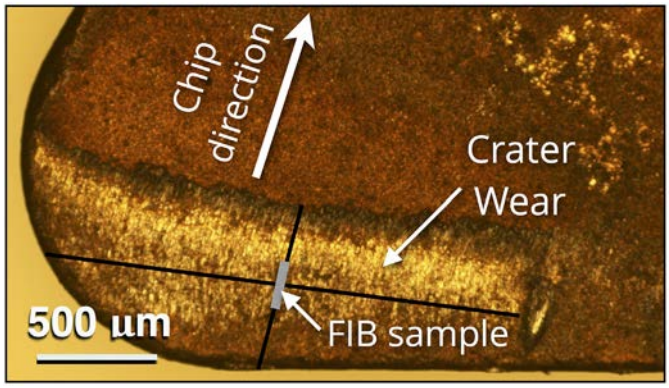

Fig. 1. Optical micrograph of $(Ti_{0.52}Al_{0.48})N_y$ coating on WC-Co insert after metal cutting that shows the position where a FIB sample is obtained.

Morphological characterizations of the coatings were performed using an optical microscope and a Leo 1550 Gemini SEM. Energy dispersive X-ray spectroscopy (EDS) (Oxford X-Max) in the SEM with an acceleration voltage of 20 kV was used to obtain elemental maps of the inserts after cutting. The wear behavior of the coatings was determined using the SEM. The area of the exposed substrate (crater wear) and the average flank wear land width were measured using the ImageJ-Fiji software.

Electron micrographs of the samples were obtained using a JEOL ACCEL ARM 200F-Cold FEG microscope operated at an acceleration voltage of 200 kV. Chemical analyses of the samples were performed using EDS (JEOL Centurio EDS 1sr).

3. Results

Fig. 2 shows X-ray diffractograms of the as-deposited $(Ti_{0.52}Al_{0.48})N_y$ coatings with average nitrogen concentration of y = 0.92, y = 0.87, and y = 0.75. The XRD peaks reveal that all coatings are solid solutions

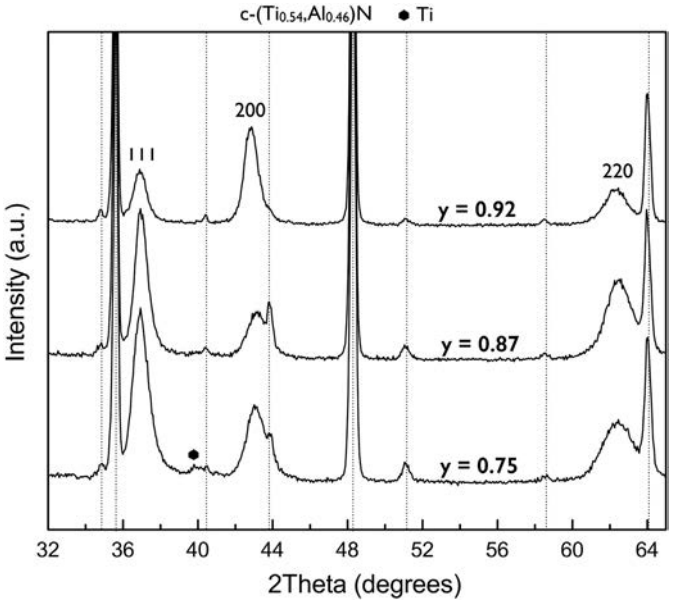

Fig. 2. X-ray diffractograms of as-deposited c-$(Ti_{0.52}Al_{0.48})N_y$ coatings with y = 0.92, 0.87, and 0.75. The peaks marked with dotted lines correspond to the WC-Co substrate.

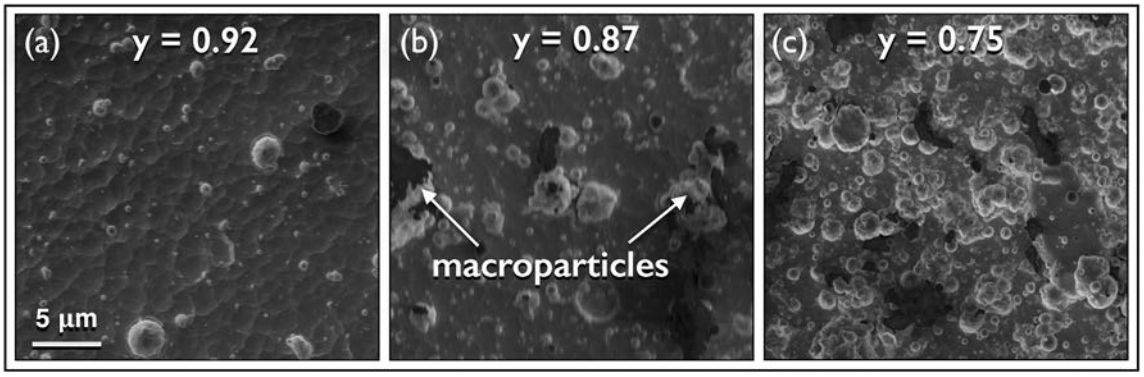

Fig. 3. Top-view SEM micrographs of as-deposited c-$(Ti_{0.52}Al_{0.48})N_y$ coatings with (a) y = 0.92, (b) y = 0.87, and (c) y = 0.75.

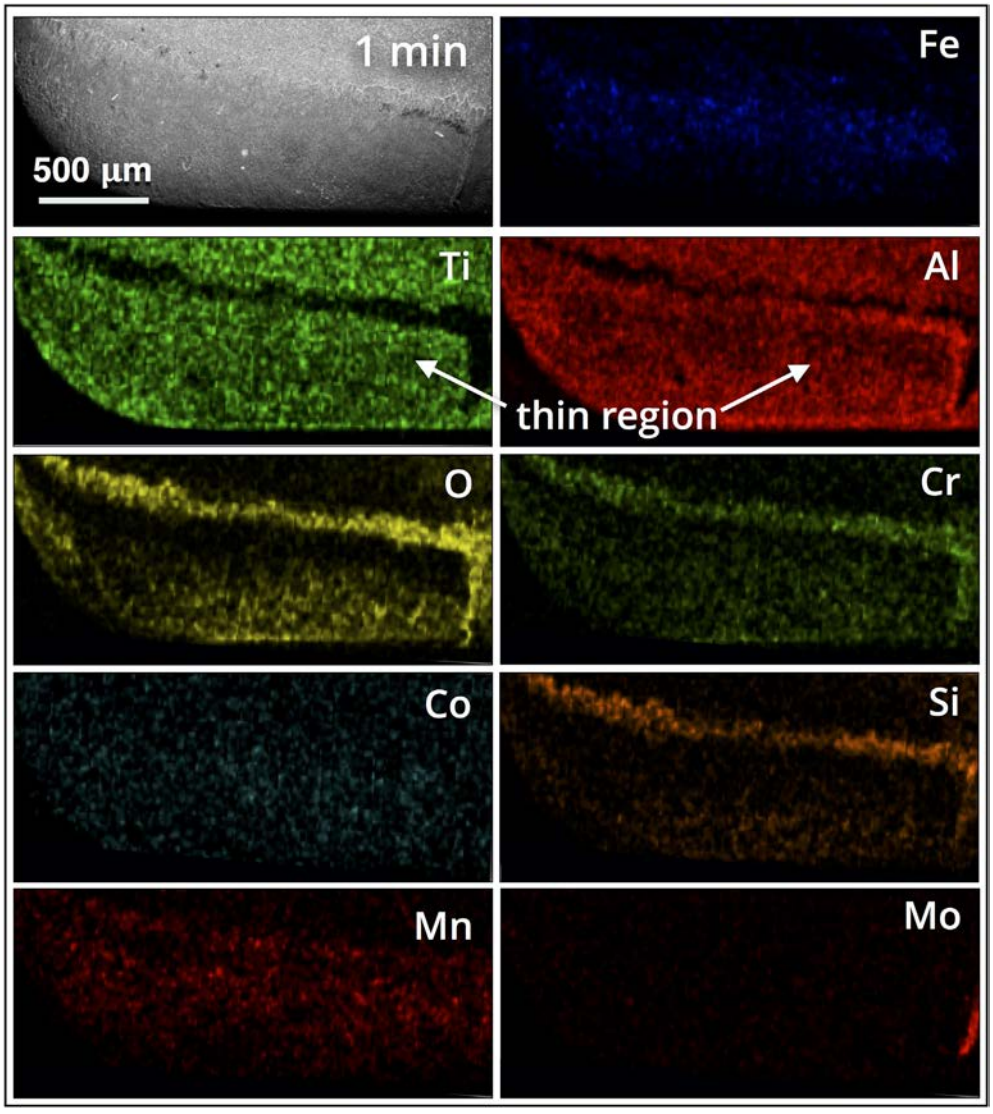

Fig. 4. SEM-EDS elemental distribution maps with enhanced contrast of selected elements at the rake face of the inserts coated with $(Ti_{0.52}Al_{0.48})N_{0.92}$ after 1 min of metal cutting on 42CrMoS4 with cooling.

with a cubic B1-structure. The y = 0.75 sample, which has the lowest N content among the studied coatings, shows an additional peak corresponding to elemental Ti [24]. As the nitrogen content decreases, the peaks become broader and the relative peak intensity evolves indicating a change in the preferred orientation of the coating. At high nitrogen content, 200 is the strongest peak while 111 is stronger at low nitrogen contents. The observed correlation between peak broadening, relative peak intensities, and nitrogen contents of $(Ti_{0.52}Al_{0.48})N_y$ films are in line with the results of Schramm et al. [24]. The broadening of peaks is attributed to the increase in chemical fluctuation of the films as the nitrogen contents decrease (i.e. chemical fluctuations were measured by APT technique in previous studies [13,22,24]). The change in

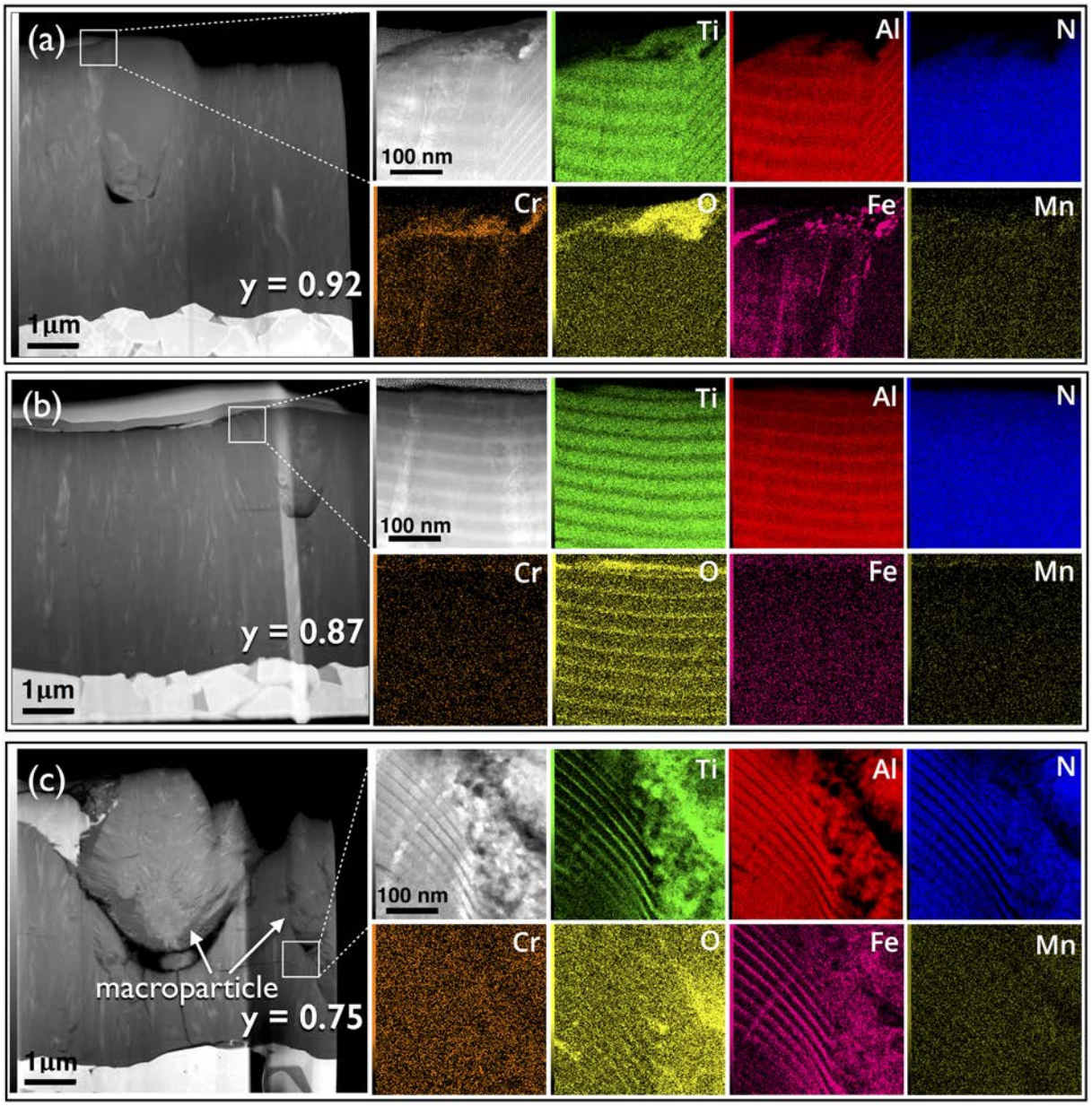

Fig. 5. HAADF-STEM and STEM-EDS of $(Ti_{0.52}Al_{0.48})N_y$ coatings with (a) y = 0.92, (b) y = 0.87, and (c) y = 0.75 after 1 min of metal cutting on 42CrMoS4 with cooling. The regions in the right side of the FIB samples are thinner in comparison to the other side. The transition in thickness is indicated by the sharp brightness difference in the STEM and STEM-EDS images.

relative peak intensity is due to a change in the structure factor with decreasing the N content [13].

The surface morphologies of the as-deposited c-$(Ti_{0.52}Al_{0.48})N_y$ coatings with different N-concentrations are shown in Fig. 3. The density and size of the macroparticles increase as the N content of the films decreases which is consistent with other results of (Ti,Al)N coatings deposited by the cathodic arc technique [13,25]. Macroparticles are known to contain a metallic core of Ti [26] and the large quantity of macroparticles seen in Fig. 3c is a reason why this sample displays additional elemental Ti peaks in XRD, e.g. as shown in Fig. 2.

Fig. 4 shows plan view SEM micrograph with corresponding elemental EDS maps of c-$(Ti_{0.52}Al_{0.48})N_y$ coatings with y = 0.92 after 1 min of metal cutting on 42CrMoS4 steel work piece. At this early stage of cutting, coating wear has commenced in a zone on the rake face and a shallow crater has formed around the center of the cutting length, indicated by the fainter color in the elemental maps of Ti and Al. Elements from the work piece material such as Fe, Cr, Si, Mo, and Mn have adhered to the surface of the coatings. The preferential placement of the adhered materials, within the contact area of the insert, depends on the type of element. Fe is mainly found at the center while Mn and Cr elements are spread over the entire contact area, whilst O, Mo, and Si are concentrated to the edges of the contact area. The presence of O suggests that oxides are formed at the edges. A similar trend is observed for the y = 0.87 and y = 0.75 samples (figures not shown).

Fig. 5 shows cross sectional view STEM micrographs of c-$(Ti_{0.52}Al_{0.48})N_y$ coatings with different N stoichiometries after exposure to 1 min of metal cutting on 42CrMoS4 with cooling. Large macroparticles are observed in the y = 0.75 sample which is in agreement with our SEM results (cf. Fig. 3). Due to the high amount of macroparticles on the y = 0.75 sample, it was not possible to prepare a thin foil lamella exempt of macroparticles. Fig. 5 also show higher magnification cross sectional view STEM micrographs with corresponding elemental EDS maps of the c-$(Ti_{0.52}Al_{0.48})N_y$ coatings. The compositional homogeneity and the chemical reaction between elements from

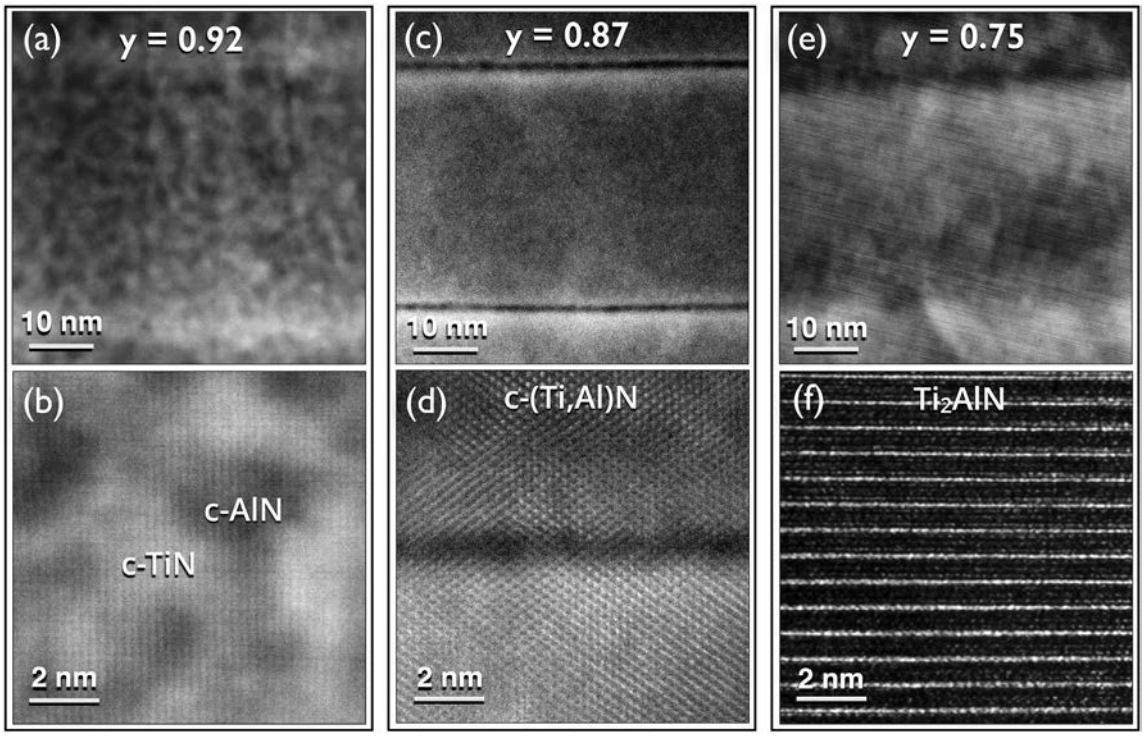

Fig. 6. (a) HAADF-STEM and (b) higher resolution HAADF-STEM of c-$(Ti_{0.52}Al_{0.48})N_y$ coating with y = 0.92, (c) HAADF-STEM and (d) higher resolution HAADF-STEM of coating with y = 0.87, and (e) HAADF-STEM and (f) HRTEM of coating with y = 0.87 after 1 min of metal cutting on 42CrMoS4 with cooling.

the workpiece and the coatings are observed. For the close-to-stoichiometric y = 0.92 sample, Fe and Cr have diffused into the coating and they are mostly present near grain boundaries as shown in Fig. 5a. This contrasts with the sample y = 0.87, which does not display high concentration of Fe and Cr in the bulk of the coating (Fig. 5b). An artificial multi-layer structure has formed throughout the film thickness with a repetition period that follows the substrate rotation during growth via similar processes as described elsewhere [27]. The thinner layers with a brighter contrast are enriched in Al and O (EDS). The presence of vacancies in this sample has facilitated the diffusion of oxygen into the coatings to form the Al oxide layers. In the y = 0.75 sample, a significant amount of Fe and Ti are identified in the thin artificial layers while the thicker layers are enriched in Al and N (Fig. 5c). Moreover, the y = 0.75 sample has diagonal layers due to macroparticle shadowing effect during growth. Co-existing signals from O and Ti are detected from the top surface of the y = 0.92 sample (Fig. 5a) and inside the macroparticles from the y = 0.75 sample (Fig. 5c).

Fig. 6 shows the microstructure of c-$(Ti_{0.52}Al_{0.48})N_y$ coatings in cross section with different N contents after 1 min of metal cutting on 42CrMoS4 with cooling. The y = 0.92 sample has decomposed into coherent c-TiN and c-AlN rich domains as indicated by the bright and dark contrast in the HAADF-STEM images (Fig. 6a and b), which is expected due to spinodal decomposition [8]. The coherence between c-TiN and c-AlN is readily observed in the higher resolution HAADF-STEM micrograph below (Fig. 6b). The y = 0.87 sample retains its c-(Ti,Al)N structure, similar to the as-deposited state. The artificial multi-layer structure contains thin Al-rich layer (dark contrast) in between Ti-rich layers (bright contrast), which are coherent (Fig. 6c and d). The y = 0.75 sample has developed a two phase structure containing c-(Ti,Al)N and the MAX phase Ti_2AlN. The HRTEM image in Fig. 6f shows the structure of the Ti_2AlN [22], located near a macroparticle.

After 3 min of service on 42CrMoS4, the coating is worn through and the WC-Co substrate is exposed at the central part of the wear zone on the rake face (center of the as-formed crater). Fig. 7 shows plan view SEM micrograph with corresponding elemental EDS maps of a c-$(Ti_{0.52}Al_{0.48})N_y$, y = 0.92 after 3 min of metal cutting. The center of the crater contains Fe, Cr, Mn, and Co elements from the work piece material and the WC-Co substrate. The edges of the wear zone contain a spread of O, Cr, and Si. The preferential placement of these elements around the contact zone of the y = 0.92 sample is similar for the y = 0.87 and y = 0.75 samples (figures not shown).

Fig. 8 shows cross sectional STEM micrographs with corresponding EDS maps of c-$(Ti_{0.52}Al_{0.48})N_y$, y = 0.92 and y = 0.87 after 3 min of metal cutting on 42CrMoS4 with cooling. Diffusion of Co from the WC-Co substrate and Fe from the workpiece material into the coating have occurred in the y = 0.92 sample (Fig. 8a). Such migration of Fe and Co is not detected for y = 0.87 sample (Fig. 8d). w-AlN has formed in the y = 0.92 sample while the y = 0.87 sample has retained its cubic structure as observed in the selected area electron diffraction (SAED) patterns (Fig. 8b and e). The y = 0.92 sample after 3 min of cutting (Fig. 8c) has larger c-AlN- and c-TiN-rich domains as compared to the sample exposed to only 1 min of cutting (cf. Fig. 6a). Slight chemical segregation and formation of domains are observed in the y = 0.87 sample after the prolonged cutting exposure (Fig. 8f).

Figs. 9 and 10 show the evolution of wear for c-$(Ti_{0.52}Al_{0.48})N_y$ coatings with the average nitrogen contents of y = 0.92, y = 0.87, and y = 0.75 as a function of cutting time in 100Cr6 and 42CrMoS4. The initial crater wear behavior (Fig. 9) shows a similar trend for both steels up to 3 min in cut. In contrast, the flank wear (Fig. 10) of the coatings is different even at this early stage of cutting. After 3 min of cutting on both steels, the y = 0.75 has the lowest flank wear resistance while the y = 0.92 and y = 0.87 samples have similar flank wear. After a prolonged cutting exposure on the 100Cr6 work piece, a clear difference in crater and flank wear behavior of the coatings is observed. The y = 0.87 sample shows the best crater wear resistance while the y = 0.92 sample has the best flank wear resistance. The y = 0.75 sample has consistently exhibited the least wear resistance among the samples.

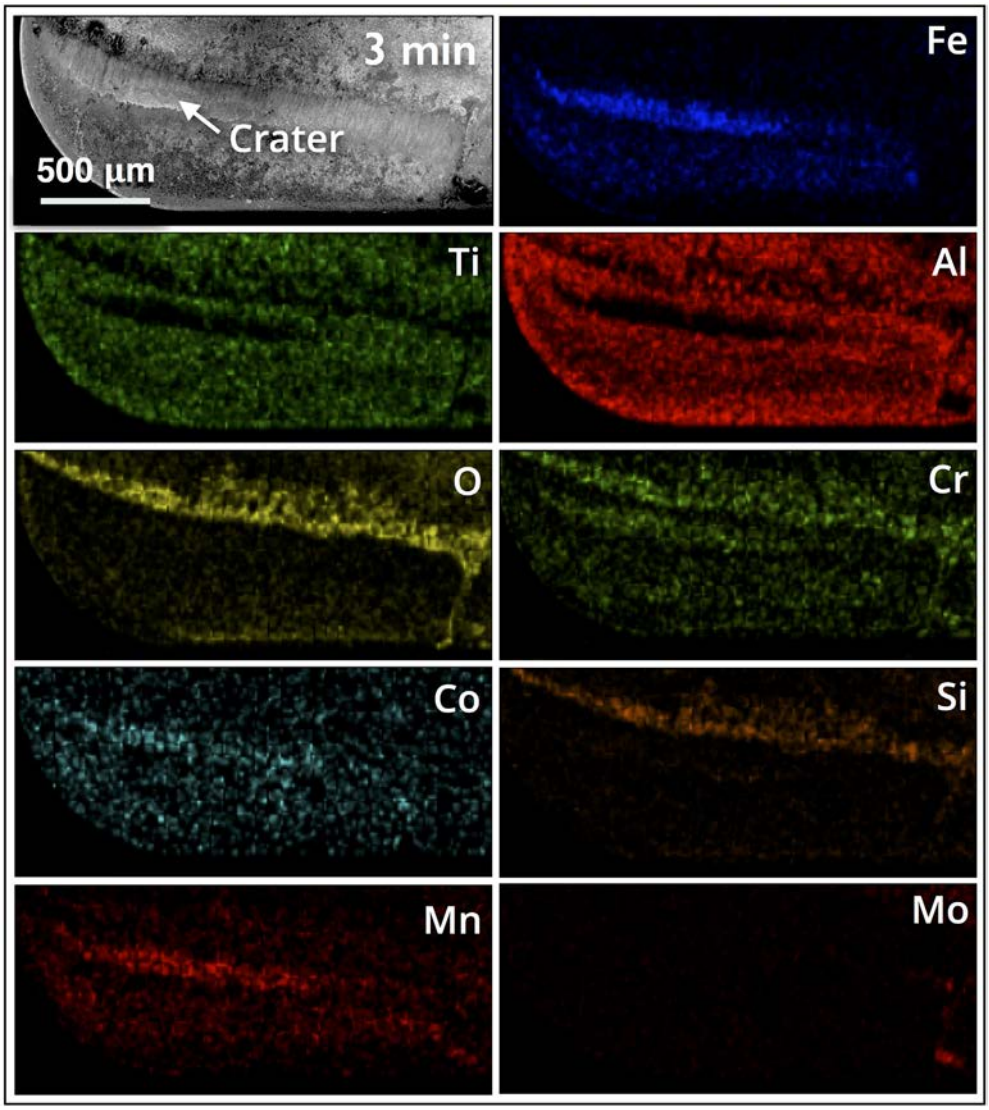

Fig. 7. SEM-EDS elemental distribution maps with enhanced contrast of selected elements at the rake face of the inserts coated with $(Ti_{0.52}Al_{0.48})N_{0.92}$ after 3 min of metal cutting on 42CrMoS4 with cooling.

4. Discussion

The wear mechanism of a cutting tool during service is, among other things, dependent on the workpiece material, properties of the tool material, cutting conditions, and the cooling or lubrication system. Overall, both abrasive- and chemical wear seems to be active in all c-$(Ti_{0.52}Al_{0.48})N_y$, y = 0.92, y = 0.87, and y = 0.75 coated inserts used during machining. During the early stages of cutting, the substrate is not exposed and the tool-chip contact (wear zone) is between the coating and the work piece material. The preferential adhesion of workpiece materials in this zone is attributed to the difference in reactivity of each element. Deposits of Fe, Cr, and Mn from the workpiece material are concentrated around the center of the contact area, where maxima in both temperature and load are expected [28]. These elements have the same energy level or electron shells, i.e. d block 3d orbital fillings, as the Ti in the coating thus chemical reaction between them is preferable. On the edge of the wear zone, Si- and Cr oxides are formed because these elements are more stable in their oxidized state. The high temperature generated by frictional heating induces the formation of metal oxides on the surface of the cutting insert. However, most of the oxide layer in the center of the crater region is continuously removed during cutting due to rubbing of the hard carbide asperities from the chip (work piece). Oxygen from the atmosphere is also more accessible in the outer parts of the contact.

The observed Al- and Ti-rich layering in the cross-sections of the c-$(Ti_{0.52}Al_{0.48})N_y$ coatings are induced by substrate rotation due to anisotropic growth conditions [27]. When the coating is heated during metal cutting, the layering is amplified due to mechanisms driving segregation. One mechanism causing such increase is surface directed spinodal decomposition, which is known to occur in TiAlN/TiN multilayers [29]. In a nitrogen deficient $(Ti,Al)N_y$, $y < 1$ system, N vacancies are the prevalent defects because they have lower formation energy in comparison to other point defects such as Ti and Al interstitials or Ti and Al anti-sites [30]. The presence of N vacancies could aid the diffusion of the elements from the chip to the coating through vacancy diffusion mechanism [31]. However, the diffusion of Fe and Cr elements from the chip to the c-$(Ti_{0.52}Al_{0.48})N_y$ coatings is more significant for the y = 0.92 sample in comparison to the y = 0.87 sample. The high migration rate of the elements through the sample with the highest N-content is attributed to its decomposed microstructure. After only 1 min exposure to metal cutting on 42CrMoS4, a phase segregation of coherent c-TiN and c-AlN rich domains has occurred in the y = 0.92 sample due to spinodal decomposition while the y = 0.87 sample has retained its as-deposited c-(Ti,Al)N structure. The c-TiN and c-AlN

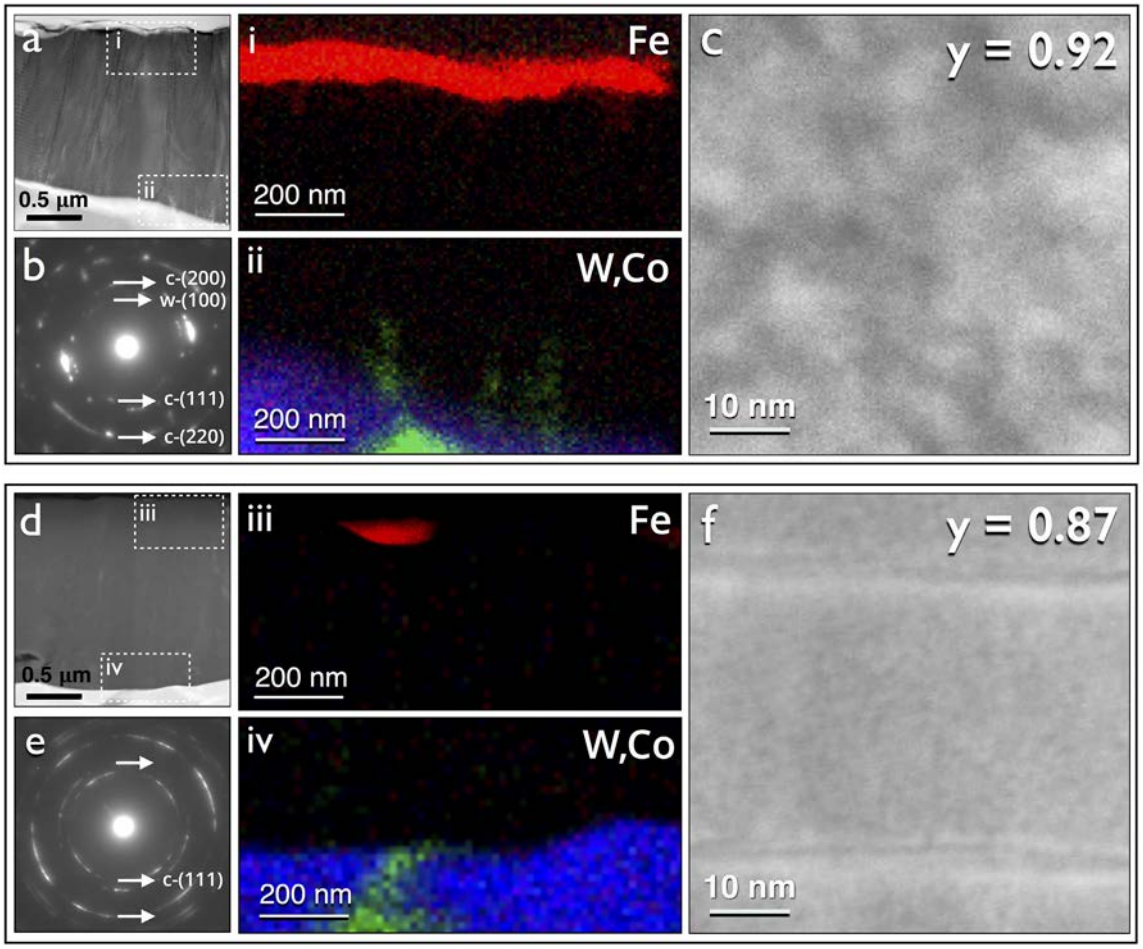

Fig. 8. (a) HAADF-STEM, (b) SAED images, and (c) higher resolution HAADF-STEM of c-$(Ti_{0.52}Al_{0.48})N_{0.92}$ coating and (d) HAADF-STEM, (e) SAED images, and (f) higher resolution HAADF-STEM of c-$(Ti_{0.52}Al_{0.48})N_{0.87}$ coating after 3 min of metal cutting on 42CrMoS4 with cooling. The colored areas in STEM-EDS images are Fe (red) from the chip and Co (green) and W (blue) in the substrate. (For interpretation of the references to color in this figure legend, the reader is referred to the web version of this article.)

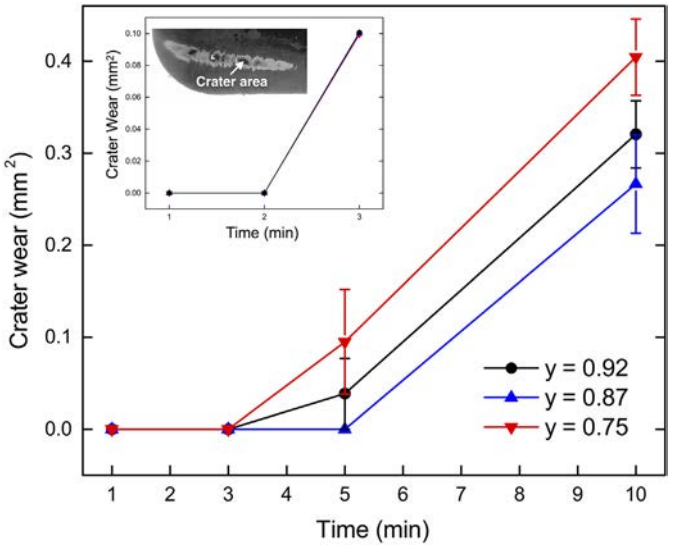

Fig. 9. Crater wear as function of time in cut of c-$(Ti_{0.52}Al_{0.48})N_y$ coatings with y = 0.92, y = 0.87, and y = 0.75 on 100Cr6 steel and 42CrMoS4 steel (inset).

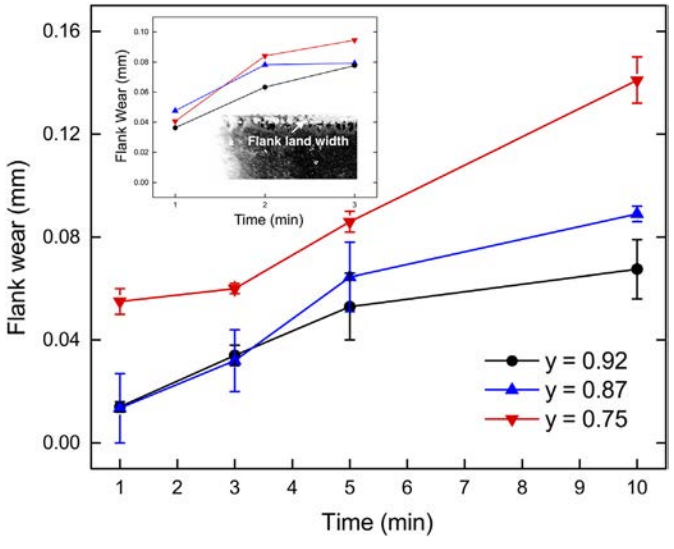

Fig. 10. Flank wear as function of time in cut of c-$(Ti_{0.52}Al_{0.48})N_y$ coatings with y = 0.92, y = 0.87, and y = 0.75 on 100Cr6 steel and 42CrMoS4 steel (inset).

domains contain misfit dislocations [32], which lowers the activation energy for atom diffusion [33]. In this case, it is suggested that the diffusion of chip elements through the coating is enhanced in the increased presence of misfit dislocation. The delayed decomposition of sub-stoichiometric y = 0.87 coating is mainly attributed to the presence of nitrogen vacancies in the system, which cause a reduction of mixing

enthalpy and alteration of phonon dispersion [13,34]. This lowers the Gibb's free energy of the y = 0.87 coating and its driving force for decomposition. Thus, it takes longer time for it to decompose than the close to stoichiometric sample.

In the c-($Ti_{0.52}Al_{0.48}$)N_y coating with y = 0.75, Fe is mostly observed near the macroparticles, which serve as pathways for diffusion and could facilitate a chemical reaction. In this sample, Al-N and Fe-Ti layers are formed in the region near the macroparticle. This is because in a nitrogen deficient (Ti,Al)N_y, y < 1 system with medium Al content, N preferably sticks to Al to form Al-N due to the semiconducting character of its covalent bonding [16]. At the high temperature generated during cutting, the solubility of Fe in the (Ti,Al)N system increases and it is likely that Fe atoms reside on the Al-site and react to form an intermetallic Fe-Ti alloy. Fe and Ti elements are transition metals with the same outer electronic configuration (d-block elements) and with almost the same size, thus it is favorable for them to form a solid solution [35]. The sample y = 0.75 has an inhomogeneous microstructure and contains the MAX phase Ti_2AlN in some parts of the coating. A c-(Ti,Al)N_y system, which contains high amount of nitrogen vacancies, has as a driving force for formation of hexagonal MAX phases [16]. Complex unit cells such as MAX phases are formed at high temperature conditions because of the enhanced mobility of species [36,37] and the local alterations in chemical concentration [38,39]. Ti_2AlN was recently observed in nitrogen deficient c-(Ti,Al)N_y coating that was deposited using cathodic arc and subsequently annealed to high temperatures [22]. During cutting, high temperature is generated in the process which prompted the chemical interaction and phase evolution of nitrogen deficient c-(Ti,Al)N_y coating to Ti_2AlN. It is expected that c-(Ti,Al)N_y serves as the precursor to Ti_2AlN transformation because the shared edges of the M_6X octahedral in MAX phases and the B1 structure of MX binaries are similar [40].

After a prolonged cutting exposure of c-($Ti_{0.52}Al_{0.48}$)N_y, the WC-Co substrate in the center of the contact area has been exposed. Fe particles are preferentially concentrated on the substrate because of their stronger affinity to the cemented carbide substrate rather than the coating [41]. It is also more likely for Fe to adhere in this region because of geometrical effects, i.e. material from the chips is accumulated in the formed crater. At the cross-section of c-($Ti_{0.52}Al_{0.48}$)N_y with y = 0.92, significant diffusion of Fe and Co into the coating is attributed to its decomposed microstructure. The decomposition of this coating has proceeded further into the domain coarsening stage as larger domains are observed. The coarsened domains contain more dislocations near the interfaces that would enhance diffusivity because such population of defects acts as diffusion paths.

The wear behavior of the c-($Ti_{0.52}Al_{0.48}$)N_y coatings are similar when subjected to machining of hard (42CrMoS4) and soft (100Cr6) steels. The progression of wear is more observable with the soft ball bearing steel work piece because of the prolonged contact time with the coated inserts. The improved crater wear resistance of c-($Ti_{0.52}Al_{0.48}$)N_y coating with y = 0.87 is attributed to its dense grain boundaries, which prevent the elements from the chip and the substrate such as Fe and Co to diffuse into the coating. This is in contrast with the y = 0.92 sample, which contains coarsened domains and w-AlN that result in a less dense microstructure. This allows the diffusion of elements from the workpiece material to the coating that would weaken its structure through recrystallization [42] and make it more susceptible to wear. This is consistent with the theoretical work of Kramer et al. [19], which predicted that crater wear is largely affected by a chemical wear due to diffusion. On the other hand, flank wear is generally attributed to the abrasion between the workpiece and the cutting tool and its progression is determined by the hardness of the coatings [43,44]. The y = 0.92 sample has undergone spinodal decomposition thus it exhibits an age hardening that results in good flank wear resistance. The flank face has a lower temperature as compared to the crater zone thus, it is expected that the detrimental w-AlN transformation has not occurred in this sample. The y = 0.75 coating contains a greater number of macroparticles than y = 0.92 and y = 0.87 thus it has the lowest wear resistance. These local macroscopic droplets are one of the major causes of failure during cyclic wear [1]. The formation of Ti_2AlN, which has a lower hardness than c-(Ti,Al)N [45] in some areas of the y = 0.75 coating also contributes to its wear behavior. The enhanced flank wear resistance of the c-($Ti_{0.52}Al_{0.48}$)$N_{0.92}$ coating during cutting is then attributed to age hardening and its more homogenous microstructure. However, the Co and Fe diffusion that is accommodated by a coarsened structure will weaken the crater wear properties.

5. Conclusions

The factors affecting the initial wear mechanism of nitrogen deficient c-($Ti_{0.52}Al_{0.48}$)N_y coatings with average N concentration of y = 0.92, y = 0.87, and y = 0.75 in metal cutting were examined. The elements from the workpiece materials such as Fe, Cr, and Mn have preferentially adhered on the center of the crater wear zone. The microstructure of c-($Ti_{0.52}Al_{0.48}$)N_y coatings show that the close to stoichiometric y = 0.92 sample has an earlier onset of spinodal decomposition to c-AlN and c-TiN-rich domains as compared to the other samples. The delay in decomposition of the samples containing less N is attributed to the presence of nitrogen vacancies, which lowers the free energy of the system. Particles of Fe and Co from the workpiece and the substrate, respectively are observed in the y = 0.92 coating with a decomposed structure because it contains misfit dislocations and grain boundaries that enhance the diffusion of these elements. The y = 0.87 sample has the best crater wear resistance because it is least affected by a chemical wear due to diffusion while the y = 0.92 coating has the best flank wear resistance because of the age hardening effect during the decomposition. The y = 0.75 coating contains the most number of macroparticles and has an inhomogeneous microstructure after machining, containing c-($Ti_{0.52}Al_{0.48}$)N_y, Ti_2AlN MAX phases, and alternating layers of AlN and Fe-Ti phases near the macroparticles. In this case, both the chemical alteration within the coating and the presence of macroparticles contribute to its lower wear resistance. The microstructure, presence of vacancies, and chemical changes during chip and coating interaction are the major factors influencing the wear behavior of nitrogen deficient (Ti,Al)N_y coatings on a cutting insert.

Acknowledgments

The work was financially supported by the European Union's Erasmus Mundus doctoral program in Materials Science and Engineering (DocMASE), the Swedish Research Council (grant nos. 2017-03813 and 2017-06701), the Swedish government strategic research area grant AFM, LiU (2009-00971) and VINNOVA (FunMat-II project grant no. 2016-05156). The authors thank Sylvie Migot for the TEM sample preparation and Jaafar Ghanbaja for the acquisition of TEM images.

References

[1] S. PalDey, S. Deevi, Single layer and multilayer wear resistant coatings of (Ti, Al) N: a review, Mater. Sci. Eng. A 342 (2003) 58–79.
[2] T. Leyendecker, O. Lemmer, S. Esser, J. Ebberink, The development of the PVD coating TiAlN as a commercial coating for cutting tools, Surf. Coat. Technol. 48 (1991) 175–178.
[3] P. Jindal, A. Santhanam, U. Schleinkofer, A. Shuster, Performance of PVD TiN, TiCN, and TiAlN coated cemented carbide tools in turning, Int. J. Refract. Met. Hard Mater. 17 (1999) 163–170.
[4] J.G. Han, J.S. Yoon, H.J. Kim, K. Song, High temperature wear resistance of (TiAl)N films synthesized by cathodic arc plasma deposition, Surf. Coat. Technol. 86-87 (1996) 82–87.
[5] M. Oden, L. Rogström, A. Knutsson, M. Terner, P. Hedström, J. Almer, J. Ilavsky, In situ small-angle X-ray scattering study of nanostructure evolution during decomposition of arc evaporated TiAlN coatings, Appl. Phys. Lett. 94 (2009) 053114.
[6] A. Hörling, L. Hultman, M. Odén, J. Sjölén, L. Karlsson, Mechanical properties and machining performance of Ti1 − xAlxN-coated cutting tools, Surf. Coat. Technol. 191 (2005) 384–392.
[7] N. Shulumba, O. Hellman, L. Rogström, Z. Raza, F. Tasnádi, I.A. Abrikosov,

M. Odén, Temperature-dependent elastic properties of Ti1 − xAlxN alloys, Appl. Phys. Lett. 107 (2015) 231901.
[8] A. Hörling, L. Hultman, M. Odén, J. Sjölén, L. Karlsson, Thermal stability of arc evaporated high aluminum-content Ti1 − xAlxN thin films, J. Vac. Sci. Technol. A 20 (2002) 1815–1823.
[9] N. Norrby, L. Rogström, M.P. Johansson-Jõesaar, N. Schell, M. Odén, In situ X-ray scattering study of the cubic to hexagonal transformation of AlN in Ti1 − xAlxN, Acta Mater. 73 (2014) 205–214.
[10] P.H. Mayrhofer, A. Hörling, L. Karlsson, J. Sjölén, T. Larsson, C. Mitterer, L. Hultman, Self-organized nanostructures in the Ti–Al–N system, Appl. Phys. Lett. 83 (2003) 2049–2051.
[11] M.P. Johansson Jõesaar, N. Norrby, J. Ullbrand, R. M'Saoubi, M. Odén, Anisotropy effects on microstructure and properties in decomposed arc evaporated Ti1-xAlxN coatings during metal cutting, Surf. Coat. Technol. 235 (2013) 181–185.
[12] B. Alling, M. Odén, L. Hultman, I. Abrikosov, Pressure enhancement of the isostructural cubic decomposition in Ti1 − xAlxN, Appl. Phys. Lett. 95 (2009) 181906.
[13] I.C. Schramm, M.P. Johansson Jõesaar, J. Jensen, F. Mücklich, M. Odén, Impact of nitrogen vacancies on the high temperature behavior of (Ti1 − xAlx)Ny alloys, Acta Mater. 119 (2016) 218–228.
[14] K. Calamba, I. Schramm, M. Johansson Jõesaar, J. Ghanbaja, J. Pierson, F. Mücklich, M. Odén, Enhanced thermal stability and mechanical properties of nitrogen deficient titanium aluminum nitride (Ti0. 54Al0. 46Ny) thin films by tuning the applied negative bias voltage, J. Appl. Phys. 122 (2017) 065301.
[15] M. to Baben, M. Hans, D. Primetzhofer, S. Evertz, H. Ruess, J.M. Schneider, Unprecedented thermal stability of inherently metastable titanium aluminum nitride by point defect engineering, Mater. Res. Lett. 5 (2017) 158–169.
[16] B. Alling, A. Karimi, L. Hultman, I.A. Abrikosov, First-principles study of the effect of nitrogen vacancies on the decomposition pattern in cubic Ti1 − xAlxN1 − y, Appl. Phys. Lett. 92 (2008) 071903.
[17] R. M'Saoubi, S. Ruppi, Wear and thermal behaviour of CVD α-Al2O3 and MTCVD Ti (C,N) coatings during machining, CIRP Ann. 58 (2009) 57–60.
[18] K.D. Bouzakis, G. Skordaris, S. Gerardis, G. Katirtzoglou, S. Makrimallakis, M. Pappa, E. Lill, R. M'Saoubi, Ambient and elevated temperature properties of TiN, TiAlN and TiSiN PVD films and their impact on the cutting performance of coated carbide tools, Surf. Coat. Technol. 204 (2009) 1061–1065.
[19] B. Kramer, N. Suh, Tool wear by solution: a quantitative understanding, J. Eng. Ind. Trans. ASME 102 (1980) 303–309.
[20] A. Senthil Kumar, A. Raja Durai, T. Sornakumar, Machinability of hardened steel using alumina based ceramic cutting tools, Int. J. Refract. Met. Hard Mater. 21 (2003) 109–117.
[21] M. Mühlbacher, A.S. Bochkarev, F. Mendez-Martin, B. Sartory, L. Chitu, M.N. Popov, P. Puschnig, J. Spitaler, H. Ding, N. Schalk, Cu diffusion in single-crystal and polycrystalline TiN barrier layers: a high-resolution experimental study supported by first-principles calculations, J. Appl. Phys. 118 (2015) 085307.
[22] I.C. Schramm, C. Pauly, M.P. Johansson Jõesaar, P. Eklund, J. Schmauch, F. Mücklich, M. Odén, Solid state formation of Ti4AlN3 in cathodic arc deposited (Ti1 − xAlx)Ny alloys, Acta Mater. 129 (2017) 268–277.
[23] R. Langford, A. Petford-Long, Preparation of transmission electron microscopy cross-section specimens using focused ion beam milling, J. Vac. Sci. Technol. A 19 (2001) 2186–2193.
[24] I.C. Schramm, C. Pauly, M.P. Johansson Jõesaar, S. Slawik, S. Suarez, F. Mücklich, M. Odén, Effects of nitrogen vacancies on phase stability and mechanical properties of arc deposited (Ti0.52Al0.48)Ny (y < 1) coatings, Surf. Coat. Technol. 330 (2017) 77–86.
[25] J. Bujak, J. Walkowicz, J. Kusiński, Influence of the nitrogen pressure on the structure and properties of (Ti,Al)N coatings deposited by cathodic vacuum arc PVD process, Surf. Coat. Technol. 180-181 (2004) 150–157.
[26] W.D. Münz, D.B. Lewis, S. Creasey, T. Hurkmans, T. Trinh, W. Ijzendorn, Defects in TiN and TiAlN coatings grown by combined cathodic arc/unbalanced magnetron technology, Vacuum 46 (1995) 323–330.
[27] J. Sjölén, L. Karlsson, S. Braun, R. Murdey, A. Hörling, L. Hultman, Structure and mechanical properties of arc evaporated Ti–Al–O–N thin films, Surf. Coat. Technol. 201 (2007) 6392–6403.
[28] N. Norrby, M.P. Johansson, R. M'Saoubi, M. Odén, Pressure and temperature effects on the decomposition of arc evaporated Ti0.6Al0.4N coatings in continuous turning, Surf. Coat. Technol. 209 (2012) 203–207.
[29] A. Knutsson, I. Schramm, K. Asp Grönhagen, F. Mücklich, M. Odén, Surface directed spinodal decomposition at TiAlN/TiN interfaces, J. Appl. Phys. 113 (2013) 114305.
[30] M. to Baben, L. Raumann, D. Music, J.M. Schneider, Origin of the nitrogen over- and understoichiometry in Ti0.5Al0.5N thin films, J. Phys. Condens. Matter 24 (2012) 155401.
[31] M. Ohring, Materials Sciencee of Thin Films, Elsevier, 2001.
[32] K. Calamba, J. Pierson, S. Bruyère, A.I. Febvrier, P. Eklund, J. Barrirero, F. Mücklich, R. Boyd, M.P. Johansson Jõesaar, M. Odén, Dislocation structure and microstrain evolution during spinodal decomposition of reactive magnetron sputtered heteroepixatial c-(Ti0.36,Al0.64)N/c-TiN films grown on MgO(001) and (111) substrates, (Unpublished results).
[33] M. Aminpour, O. Trushin, T.S. Rahman, Effect of misfit dislocation on surface diffusion, Phys. Rev. B 84 (2011) 035455.
[34] N. Shulumba, O. Hellman, Z. Raza, B. Alling, J. Barrirero, F. Mücklich, I.A. Abrikosov, M. Odén, Lattice vibrations change the solid solubility of an alloy at high temperatures, Phys. Rev. Lett. 117 (2016) 205502.
[35] H. Bo, J. Wang, L. Duarte, C. Leinenbach, L.-b. Liu, H.-s. Liu, Z.-p. Jin, Thermodynamic re-assessment of Fe–Ti binary system, Trans. Nonferrous Metals Soc. China 22 (2012) 2204–2211.
[36] P. Eklund, M. Beckers, U. Jansson, H. Högberg, L. Hultman, The Mn + 1AXn phases: materials science and thin-film processing, Thin Solid Films 518 (2010) 1851–1878.
[37] O. Wilhelmsson, J.P. Palmquist, E. Lewin, J. Emmerlich, P. Eklund, P.O.Å. Persson, H. Högberg, S. Li, R. Ahuja, O. Eriksson, L. Hultman, U. Jansson, Deposition and characterization of ternary thin films within the Ti–Al–C system by DC magnetron sputtering, J. Cryst. Growth 291 (2006) 290–300.
[38] C. Höglund, M. Beckers, N. Schell, J.V. Borany, J. Birch, L. Hultman, Topotaxial growth of Ti 2 Al N by solid state reaction in Al N/Ti (0001) multilayer thin films, Appl. Phys. Lett. 90 (2007) 174106.
[39] V. Dolique, M. Jaouen, T. Cabioc'h, F. Pailloux, P. Guérin, V. Pélosin, Formation of (Ti, Al) N/Ti 2 Al N multilayers after annealing of Ti N/Ti Al (N) multilayers deposited by ion beam sputtering, J. Appl. Phys. 103 (2008) 083527.
[40] M.W. Barsoum, The MN + 1AXN phases: a new class of solids: thermodynamically stable nanolaminates, Prog. Solid State Chem. 28 (2000) 201–281.
[41] L. Rogström, M.P. Johansson-Jõesaar, L. Landälv, M. Ahlgren, M. Odén, Wear behavior of ZrAlN coated cutting tools during turning, Surf. Coat. Technol. 282 (2015) 180–187.
[42] S. Veprek, M.G.J. Veprek-Heijman, P. Karvankova, J. Prochazka, Different approaches to superhard coatings and nanocomposites, Thin Solid Films 476 (2005) 1–29.
[43] N. Norrby, M.P. Johansson-Jõesaar, M. Odén, Improved metal cutting performance with bias-modulated textured Ti0.50Al0.50N multilayers, Surf. Coat. Technol. 257 (2014) 102–107.
[44] S. Ruppi, B. Högrelius, M. Huhtiranta, Wear characteristics of TiC, Ti(C,N), TiN and Al2O3 coatings in the turning of conventional and Ca-treated steels, Int. J. Refract. Met. Hard Mater. 16 (1998) 353–368.
[45] M.W. Barsoum, T. El-Raghy, M. Ali, Processing and characterization of Ti2AlC, Ti2AlN, and Ti2AlC0.5N0.5, Metall. Mater. Trans. A 31 (2000) 1857–1865.

Paper 3

Dislocation structure and microstrain evolution during spinodal decomposition of reactive magnetron sputtered heteroepixatial c-$(Ti_{0.37},Al_{0.63})N$/c-TiN films grown on MgO(001) and (111) substrates

K. Calamba, J. Pierson, Bruyère, A. Febvrier, P. Eklund, J. Barrirero, F. Mücklich, R. Boyd, M.P. Johansson Jõesaar, and M. Odén

Journal of Applied Physics 125, 105301 (2019)

Reprinted with permission
© 2019, AIP Publishing

Journal of Applied Physics

Dislocation structure and microstrain evolution during spinodal decomposition of reactive magnetron sputtered heteroepixatial c-($Ti_{0.37}$,$Al_{0.63}$)N/c-TiN films grown on MgO(001) and (111) substrates

Cite as: J. Appl. Phys. **125**, 105301 (2019); https://doi.org/10.1063/1.5051609
Submitted: 10 August 2018 . Accepted: 24 February 2019 . Published Online: 08 March 2019

K. M. Calamba, J. F. Pierson, S. Bruyère, A. L. Febvrier, P. Eklund, J. Barrirero, F. Mücklich, R. Boyd, M. P. Johansson Jõesaar, and M. Odén

View Online Export Citation CrossMark

ARTICLES YOU MAY BE INTERESTED IN

Growth and characterization of β-Ga_2O_3 thin films on different substrates
Journal of Applied Physics **125**, 105701 (2019); https://doi.org/10.1063/1.5061794

AIP Publishing

© 2019 Author(s).

Journal of Applied Physics ARTICLE scitation.org/journal/jap

Dislocation structure and microstrain evolution during spinodal decomposition of reactive magnetron sputtered heteroepixatial c-($Ti_{0.37}$,$Al_{0.63}$)N/c-TiN films grown on MgO(001) and (111) substrates

Cite as: J. Appl. Phys. **125**, 105301 (2019); doi: 10.1063/1.5051609
Submitted: 10 August 2018 · Accepted: 24 February 2019 ·
Published Online: 8 March 2019

View Online Export Citation CrossMark

K. M. Calamba,[1,2,a)] J. F. Pierson,[2] S. Bruyère,[2] A. L. Febvrier,[3] P. Eklund,[3] J. Barrirero,[1,4] F. Mücklich,[4] R. Boyd,[1] M. P. Johansson Jõesaar,[1,5] and M. Odén[1]

AFFILIATIONS

[1]Nanostructured Materials, Department of Physics, Chemistry and Biology (IFM), Linköping University, Linköping SE-58183, Sweden
[2]Université de Lorraine, CNRS, IJL, F-54000 Nancy, France
[3]Thin Film Physics Division, Department of Physics, Chemistry and Biology (IFM), Linköping University, Linköping SE-58183, Sweden
[4]Functional Materials, Department of Materials Science, Saarland University, Saarbrucken DE-66123, Germany
[5]SECO Tools AB, Fagersta SE-73782, Sweden

[a)]**Electronic mail:** katherine.calamba@liu.se

ABSTRACT

Heteroepitaxial c-($Ti_{0.37}$,$Al_{0.63}$)N thin films were grown on MgO(001) and MgO(111) substrates using reactive magnetron sputtering. High resolution high-angle annular dark-field scanning transmission electron micrographs show coherency between the film and the substrate. In the as-deposited state, x-ray diffraction reciprocal space maps show a strained epitaxial film. Corresponding geometric phase analysis (GPA) deformation maps show a high stress in the film. At elevated temperature (900 °C), the films decompose to form iso-structural coherent c-AlN- and c-TiN-rich domains, elongated along the elastically soft <100> directions. GPA analysis reveals that the c-TiN domains accommodate more dislocations than the c-AlN domains. This is because of the stronger directionality of the covalent bonds in c-AlN compared with c-TiN, making it more favorable for the dislocations to accumulate in c-TiN. The defect structure and strain generation in c-(Ti,Al)N during spinodal decomposition is affected by the chemical bonding state and elastic properties of the segregated domains.

Published under license by AIP Publishing. https://doi.org/10.1063/1.5051609

I. INTRODUCTION

Improved understanding of the microstructural evolution of metastable NaCl B1 structured c-(Ti,Al)N solid solutions is essential for optimizing their properties for high temperature applications.[1–3] The spinodal decomposition of c-(Ti,Al)N into isostructurally coherent c-TiN and metastable c-AlN rich domains at elevated temperatures[4–7] is particularly attractive because it results in hardening and improved wear resistance.[8–11] It has previously been reported that metal composition, vacancy concentration, and grain size affect the decomposition behavior, and improvement of thermal and mechanical properties can be achieved by microstructure optimization.[12–17] However, these studies are performed on polycrystalline materials for which investigations of the local strain evolution and details of the defect structure during decomposition are difficult. Instead, single crystal c-(Ti,Al)N films with a low level of impurities are required to obtain such information from the decomposed but still coherent microstructure.

Theoretical studies have shown that the compositional dependent anisotropic elastic properties cause strain and associated strain energy, which affect the spinodal decomposition in c-(Ti,Al)N.[18–21]

Published under license by AIP Publishing.

The approach of these studies is based on the Cahn–Hilliard equation,[22] where the solute concentration is used to describe the thermodynamic energies involved in phase separation. Additional strain effects generated by dislocations or other lattice defects are normally ignored. Recent studies on phase-field modeling of spinodal decomposition in alloys have accounted for both the formation and the dynamics of dislocations, revealing that dislocation stress field energetically and kinetically facilitates phase separation even without initial compositional fluctuation.[23,24] Dislocation structure and strain evolution in c-(Ti,Al)N alloys could play an important role during spinodal decomposition because strains in the film are generated in the process. Thus, more information on the strain fields present in this ternary alloy during phase separation is important. The use of aberration-corrected transmission electron microscope (TEM) and scanning TEM (STEM) offers significant improvement in terms of strain mapping combining electron diffraction and geometric phase analysis (GPA).[17,25,26] GPA is an image analysis method using a Fast Fourier transform algorithm to quantify the lattice displacements and strain field in crystals relative to a reference region.[27] GPA performed on high-resolution STEM images results in the best spatial resolution among recently developed strain mapping techniques.[28] In this study, GPA was performed on high-angle annular dark-field scanning transmission electron micrographs (HAADF-STEMs) to determine the local strain tensor in (Ti,Al)N during spinodal decomposition while gaining compositional information.

Single crystal c-($Ti_{0.37}$,$Al_{0.63}$)N films with a c-TiN buffer layer were grown by reactive magnetron sputtering on MgO substrates with a cube-on-cube epitaxial relationship on MgO(001) and (111) substrates with the orientational relationships (−100)[001]c-($Ti_{0.37}$,$Al_{0.63}$)N/c-TiN||(−100)[001]MgO and (−11−1)[011]c-($Ti_{0.37}$,$Al_{0.63}$)N/c-TiN||(−11-1)[011]MgO. The films were subsequently annealed at 900 °C to investigate the strain distribution caused by coherent domains formed during spinodal decomposition of the c-(Ti,Al)N film. The crystal quality of the films was examined by high-resolution TEM/scanning TEM and XRD reciprocal space maps. GPA strain maps showing symmetric strain tensor components, i.e., ε_{xx}, ε_{yy}, and ε_{xy}, were obtained. At elevated temperatures, the film segregated to form elongated c-TiN and c-AlN rich domains, wherein strain reduction is greater in c-AlN. The defect structure of (Ti,Al)N during spinodal decomposition is discussed in terms of elastic properties and chemical bonding characteristics of the domains.

II. MATERIAL AND METHODS

Epitaxial c-($Ti_{0.37}$,$Al_{0.63}$)N were grown onto magnesium oxide (MgO) substrates by UHV DC magnetron sputter deposition. Two orientations, (MgO)(001) and (111) wafers (>99.95% purity), with a size of $10 \times 10\ mm^2$ were used as substrates. MgO has been used due to its small lattice mismatch of less than 1% to that of c-$Ti_{1-x}Al_xN$ ($0 \leq x$).[29,30] Ti (>99.9% purity) and $Ti_{0.35}Al_{0.65}$ (>99.9% purity) targets with a diameter of 50 mm were used for the deposition of TiN buffer layer and (Ti,Al)N film, respectively. Additionally, the coefficients of thermal expansion of these materials are similar (i.e., $\alpha_{MgO} \approx 14 \times 10^{-6}$/°C, $\alpha_{TiN} \approx 9.4 \times 10^{-6}$/°C, and $\alpha_{(Ti,Al)N} \approx 7.5 \times 10^{-6}$/°C),[31,32] making MgO a suitable substrate for epitaxial growth for many transition metal nitrides.[33–37] The thermal strains due to cooling from the deposition temperature are 0.3% for TiN and 0.4% for (Ti,Al)N. Prior to the deposition, the substrates were subjected to wet and dry cleaning processes comprising different sonications in Hellmanex®II, acetone, and ethanol solvents and an *in situ* annealing at 900 °C for 1 h.[38] An $Ar + N_2$ gas mixture was used to synthesize the thin films, in which the argon flow rate was set to 30 sccm and the nitrogen flow rate was set to 10 sccm, resulting in a total gas pressure of 0.3 Pa. This reactive sputtering process was operated inside the hysteresis region (transition mode). The substrates were kept at 700 °C during the deposition. c-TiN buffer layers were first grown to a thickness of 15 nm before depositing the c-($Ti_{0.37}$,$Al_{0.63}$)N films to a thickness of 150 nm. Thin TiN layers were deposited in order to prevent Al in (Ti,Al)N films from diffusing to the MgO substrate, i.e., Al and Mg are known to chemical react to form a spinel at high temperature.[39] All depositions were made at a constant current of 0.1 A.

Heat treatments of the as-deposited films were conducted by post-deposition isothermal annealing using a tube furnace in 30 sccm of argon flow. The samples were heated at a rate of 20 °C/min up to a maximum temperature of either 850 °C and 900 °C and held for 120 min and then slowly cooled to room temperature.

X-ray diffraction θ-2θ scans, azimuthal scans, rocking curves, and reciprocal space maps (RSMs) of (Ti,Al)N films were acquired using a PANalytical Empyrean diffractometer with Cu K_α radiation for the phase structure and growth orientation analysis. Symmetric and asymmetric RSMs were recorded around MgO 111 and MgO 113, respectively using a four-axis goniometer and a primary optics consisting of a parabolic graded multilayer mirror, collimator, and a channel-cut 2-bounce Ge(220) monochromator. The equations used for computation of the reciprocal lattice vectors are $Q_x = 2\pi r_E[\cos\omega - \cos(2\theta - \omega)]$ and $Q_z = 2\pi r_E[\sin\omega + \sin(2\theta\text{-}\omega)]$, where ω and θ are the instrumental coordinates and r_E is Ewald's sphere radius ($1/\lambda = 1/0.1541$ nm).[40] Poisson's ratio used to measure the lattice constants is $\nu = 0.18$, the elastic modulus (E) used to determine the film stress is 490 GPa, and the elastic stiffness constants used to compute the Zener anisotropy (A) and shear modulus (G') are $C_{11} = 445$, $C_{12} = 161$, and $C_{44} = 223$.[19]

Cross-sectional transmission electron microscopy (TEM) lamella with approximately 50 nm uniform thickness were prepared using an *in situ* lift-out technique in a focused ion beam (FIB)–scanning electron microscope (SEM) dual beam system (Helios Nanolab 600i). A FEI EasyLift EX system fitted with a W needle was used as the micromanipulator.

Microstructural characterizations of the thin films were performed using a JEOL ACCEL ARM 200F–Cold FEG equipped with energy dispersive x-ray (EDX) spectrometer (JEOL Centurio EDS 1sr) for chemical analyses. The electron microscope was operated at an acceleration voltage of 200 kV. The specimen was kept in the equipment for few hours before the acquisition of the STEM images in order to sufficiently stabilize and minimize the sample drift.

The electron microscopy data were processed using Gatan's Digital Micrograph with an added geometric phase analysis (GPA) script developed by Koch and co-workers.[41] GPA of high-angle annular dark-field imaging (HAADF) STEM images was used to map the tensile and compressive strain at the atomic scale.

Samples for atom probe tomography (APT) were prepared in a dual-beam FIB/SEM workstation (Helios NanoLab 600™, FEI

Published under license by AIP Publishing.

Company, USA). Prior to FIB irradiation, the thin films were coated with an approximately 200 nm thick Ti sacrificial layer. Then, an electron beam induced Pt layer was added to protect from gallium implantation. After lift out and thinning of the samples, a low energy milling at 2 kV was performed to minimize Ga induced damage.[42] APT was carried out in a laser mode with a LEAP™ 3000X HR (CAMECA) at a pulse frequency of 200 kHz, a specimen temperature of 60 K, pressure lower than 1×10^{-10} Torr (1.33×10^{-8} Pa), and a laser pulse energy of 0.5 nJ. The evaporation rate of the specimen was set to 5 atoms per 1000 pulses. Datasets were reconstructed and analysed with the IVAS™ 3.6.14 software (CAMECA). To obtain the bulk composition of the specimens, a peak decomposition analysis routine available in IVAS was used to correct the nitrogen content due to a peak overlap in the mass-to-charge spectrum between N^+ and N_2^{++}.

III. RESULTS

The chemical composition values of the as-deposited c-(Ti_{1-x},Al_x)N_y film on MgO(111) obtained by the weighted average of 3 APT specimens are Ti = 18.4 ± 0.6, Al = 31.9 ± 0.7, and N = 48.2 ± 1 at. %. APT specimens were taken from different positions along the film and the error reported depicts the intrinsic composition fluctuation in the as-deposited state which is not higher than 1 at. % for any of the elements. The film contains impurity elements such as O and C with a total content of 1.5 at. %. The film has $x = Al/(Al + Ti)$ and $y = N/(Al + Ti)$ values of $x = 0.63$ and $y = 0.96$, respectively, and can thus be considered stoichiometric.

Figure 1 shows transmission electron microscopy (TEM) micrographs including selected area electron diffraction (SAED) and Fast Fourier Transform (FFT) patterns of the as-deposited c-($Ti_{0.37}$,$Al_{0.63}$)N films on MgO(001) and (111). Results show that c-($Ti_{0.37}$,$Al_{0.63}$)N (001) first grows epitaxial on MgO(001) to a critical thickness ranging between 30 and 50 nm [Fig. 1(a)]. Beyond the critical thickness, growth of polycrystalline c-($Ti_{0.37}$,$Al_{0.63}$)N is initiated. The SAED of the sample in Fig. 1(b) shows a combination of well-defined spots and rings, which indicates the presence of large grains oriented with an epitaxial relationship to the substrate and smaller grains randomly oriented. Combining the above with high-resolution TEM (HRTEM) data and the corresponding FFT pattern in Figs. 1(d) and 1(e), we conclude epitaxial growth of c-($Ti_{0.37}$,$Al_{0.63}$)N/c-TiN films on MgO(001) with a cube-on-cube epitaxial relationship, i.e., (−100)[001]c-($Ti_{0.37}$,$Al_{0.63}$)N/c-TiN||(−100)[001] MgO. In analogy, TEM, SAED, HRTEM, and FFT results of the c-($Ti_{0.37}$,$Al_{0.63}$)N/c-TiN grown on MgO(111) [Figs. 1(f)–1(j)] demonstrate a growth with an epitaxial relationship (−11−1)[011] c-($Ti_{0.37}$,$Al_{0.63}$)N/c-TiN||(−11−1)[011]MgO. The epitaxial growth of c-(Ti,Al)N(111) is sustained all through the film thickness.

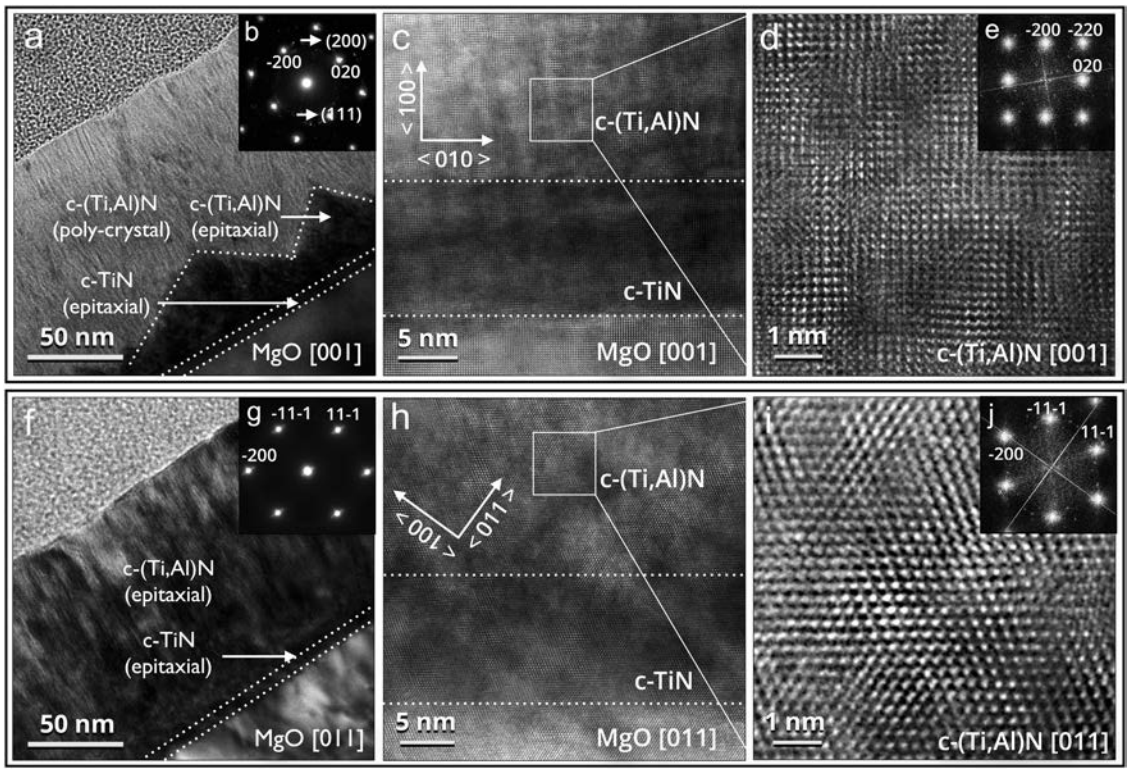

FIG. 1. (a) TEM, (b) SAED, [(c) and (d)] HRTEM, (e) FFT images of as-deposited c-($Ti_{0.37}$,$Al_{0.63}$)N/c-TiN film on MgO(001), (f) TEM, (g) SAED, [(h) and (i)] HRTEM, and (j) FFT images of (Ti,Al)N on MgO(111). The size of the sample area used for SAED is 100 nm.

Published under license by AIP Publishing.

Figure 2 shows high resolution XRD reciprocal space maps (RSMs) of the as-deposited and annealed c-($Ti_{0.37}$,$Al_{0.63}$)N/c-TiN films on MgO(111) as the function of the reciprocal lattice vector in the film growth direction (q_z) and parallel to its surface (q_x). The shape and distribution of the peaks in these maps may reveal information of crystal tilt as well as in-plane and out-of-plane strain, mismatch, and relaxation. In addition, a two-dimensional RSM covers a relatively larger area compared to TEM due to its larger probe size and it statistically represents the nitride film. However, its large probe size also leads to difficulty in resolving the reciprocal lattice point of epitaxial c-($Ti_{0.37}$,$Al_{0.63}$)N(001) film on the MgO(001) substrate because of the low epitaxial film thickness. The RSM of c-($Ti_{0.37}$,$Al_{0.63}$)N/c-TiN films on MgO(001) has only one distinct reciprocal lattice point with slight broadening to the top, which is caused by the relaxation of the epitaxial c-($Ti_{0.37}$,$Al_{0.63}$)N/TiN layers (figure not shown). Thus, the RSM analysis here is limited to the thicker epitaxial films deposited on MgO(111). Figures 2(a) and 2(d) show symmetric RSMs for the 111 plane of the c-($Ti_{0.37}$,$Al_{0.63}$)N/TiN films and the MgO substrate in as-deposited and annealed state, respectively. Larger q_z for the films indicates a smaller interplanar d-spacing for the films than the substrate in the out-of-plane direction. The 360° azimuthal scans over 002 reflection [Figs. 2(b) and 2(e)] show the characteristic feature of a cubic system oriented along the [111] direction.[43] The films

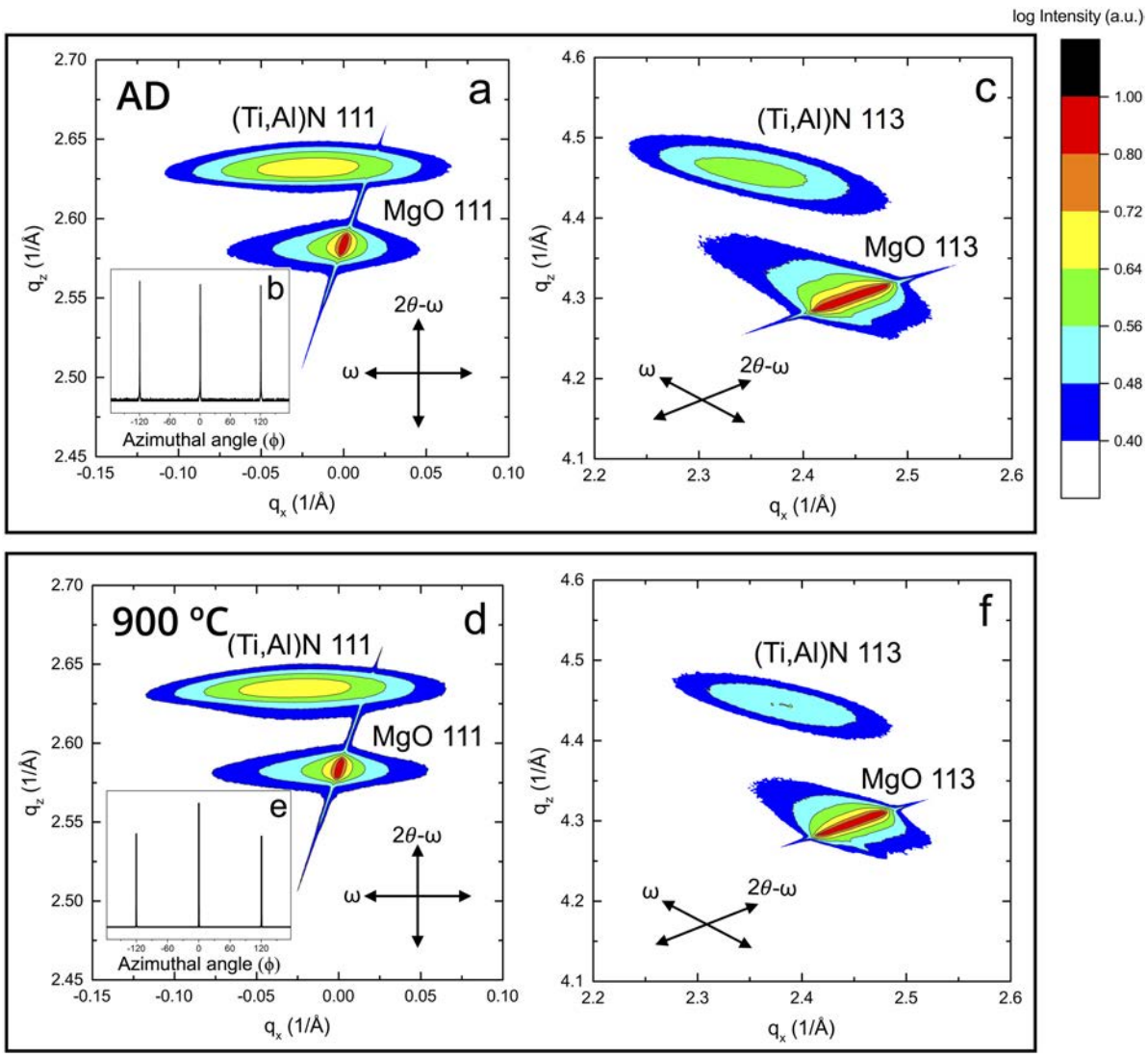

FIG. 2. (a) Symmetric RSM, (b) azimuthal XRD on (002) reflection, (c) asymmetric RSM of as-deposited, (d) symmetric RSM, (e) azimuthal XRD on (002) reflection, and (f) asymmetric RSM of annealed c-($Ti_{0.37}$,$Al_{0.63}$)N/c-TiN films on MgO(111).

Published under license by AIP Publishing.

have distinct diffraction spots from which lattice constants can be measured. The c (out-of-plane, $a_\perp$) and a (in-plane, $a_{||}$) unit-cell parameters are obtained using the equations $c = d_\perp l$ and $a = [1(h^2 + k^2)/(1/d^2_{hkl} - l^2/c^2)]^{1/2}$, where $d_\perp$ is measured from the perpendicular component of the Q_{hkl} reciprocal lattice vector, l is the length of the direction vector, and d_{hkl} is the d-spacing of the (111) plane.[29,44] The c and a lattice parameters of as-deposited c-($Ti_{0.37}$,$Al_{0.63}$)N are 4.12 Å and 4.30 Å, respectively. The c and a lattice parameters of the annealed film are 4.13 Å and 4.31 Å, respectively. The relaxed lattice constant is obtained using the equation $a_0 = c(1 - [2\nu(c - a)/a(1 + \nu)])$,[40] where ν is obtained from *ab initio* calculation.[19] The a_0 of both as-deposited and annealled (Ti,Al)N films is 4.15 Å. The a_0 of the MgO substrate and TiN buffer layer are 4.21 Å[45] and TiN = 4.24 Å,[30] resulting in a lattice misfit with respect to the film of 1.43% and 2.12%, respectively. A small variation of the d-spacing along the growth direction is observed in both films, as denoted by the broadening along the 2θ-ω direction in comparison to the ω direction (see Fig. 2). The c-(Ti,Al)N material is elastically anisotropic; however, a (111)-oriented film has an in-plane isotropy. Thus, Eqs. (1) and (2) can be used to calculate the in-plane strain (ε_a) and stress (σ_f), respectively,[44]

$$\varepsilon_a = -\frac{1-\nu}{2\nu}\left(\frac{c-a_0}{a_0}\right), \tag{1}$$

$$\sigma_f = -\frac{E}{2\nu}\left(\frac{c-a_0}{a_0}\right), \tag{2}$$

where ν is Poisson's ratio and E is the elastic modulus along the [111] direction.[19] Table I shows the strain, stress, and coherence lengths of the epitaxial films along a and c directions. The coherence lengths along the a (ξ_a) and c (ξ_c) directions are calculated using Eqs. (3) and (4), respectively,[40]

$$\xi_a = \frac{\lambda}{2\Gamma_\omega \sin\theta}, \tag{3}$$

$$\xi_c = \frac{\lambda}{\Gamma_{2\theta} \cos\theta}, \tag{4}$$

where λ is the x-ray wavelength and Γ is the full width at half maximum (FWHM) intensity. The FWHM values of the c-($Ti_{0.37}$, $Al_{0.63}$)N 111 peak of the as-deposited film are $\Gamma_{2\theta} = 0.0055$ rad and $\Gamma_\omega = 0.0027$ rad, obtained from the XRD 2θ-ω scans and ω-rocking curves, respectively. The FWHM of the c-($Ti_{0.37}$,$Al_{0.63}$)N 111 peak of the annealed film are $\Gamma_{2\theta} = 0.0057$ rad and $\Gamma_\omega = 0.0029$ rad. Asymmetric RSMs [Figs. 2(c) and 2(f)] show a horizontal shifting of the layer peak to the left of the substrate peak, which indicates that the film is partially relaxed during the deposition process.[46] The FWHM of the 113 peak in the asymmetric Q scans is directly related to the lateral uniformity of the epitaxial layer and the amount of mosaic spead present.[47] The average value of the separation of the lateral irregularities is referred to as the lateral correlation length. The range of the microscopic tilt in the layer due to its fine mosaic structure is called the mosaic spread. Table II shows the measurement of FWHM, correlation length, and mosaic spread. The annealed film has lower lateral correlation, broader FWHM, and higher mosaisity as compared to the as-deposited. This is attributed to the chemical fluctuations occurring during spinodal decomposition leading to a less perfect crystal.

The c-($Ti_{0.37}$,$Al_{0.63}$)N/c-TiN(001) and c-($Ti_{0.37}$,$Al_{0.63}$)N/c-TiN (111) films exhibit a homogeneous composition with no indication of elemental segregation in their as-deposited states. This is shown in the STEM/STEM-EDX images in Figs. 3 and 4 for c-(Ti,Al)N (001) and c-(Ti,Al)N(111), respectively. FFT insets are obtained from the STEM images [Figs. 3(a), 3(e), 4(a), and 4(e)] on either the [001] or [011] zone axis (marked). The reciprocal −200 lattice point, which is separated to two distinct spots in Fig. 3(e) is attributed to Moiré fringes observed in the STEM image of the annealed c-($Ti_{0.37}$,$Al_{0.63}$)N (001) film. The long streaks normal to the edges of the mask in the FFTs of the HRSTEM images are artifacts in the Fourier-filtering process.[48] The c-($Ti_{0.37}$,$Al_{0.63}$)N films annealed at 850 °C have a homogeneous composition similar to the as-deposited state (figures not shown). At 900 °C, the formation of coherent c-TiN and c-AlN rich domains is observed in the STEM-EDX micrographs shown in Figs. 3(f)–3(h) and 4(f)–4(h), respectively. This is consistent with the expected spinodal decomposed state at an elevated temperature.[4,5] The shape of the domains are elongated along <001> directions in both the annealed c-(Ti,Al)N(001) and c-(Ti,Al)N(111) films as shown in Figs. 3(f)–3(h) and 4(f)–4(h), similar to what have been seen after annealing of arc deposited polycrystalline c-(Ti,Al)N films.[6]

Figures 5(a) and 5(d) show high resolution HAADF-STEM micrographs over the interface region of the as-deposited and annealed c-($Ti_{0.37}$,$Al_{0.63}$)N/TiN(001) films. For such images, contrast is directly proportional to the atomic number or composition, where bright regions are attributed to Ti- and dark regions to Al-rich domains. In agreement with the HRTEM results, coherent c-($Ti_{0.37}$,$Al_{0.63}$)N/c-TiN interfaces are observed also by STEM, both in as-deposited and annealed states [Figs. 5(a) and 5(d)]. In

TABLE I. Calculated strain, stress, and coherence length of the as-deposited and annealed (Ti,Al)N(111) films.

Quantity	As-deposited	Annealed (900 °C)
In-plane strain, ε_a	0.0109	0.0119
In-plane film stress, σ_f	6.51 GPa	7.08 GPa
In-plane coherence length, $\xi_{||}$	87.2 nm	82.2 nm
Out-of-plane coherence length, $\xi_\perp$	29.8 nm	28.6 nm

TABLE II. Measured correlation length, FWHM, and mosaic spread of the as-deposited and annealed (Ti,Al)N(111) films. Reciprocal lattice units (rlu) = $Å^{-1}$.

Quantity	As-deposited	Annealed (900 °C)
FWHM	0.018 rlu	0.036 rlu
Lateral correlation length	68 nm	35 nm
Mosaic spread	2.5°	5.0°

Published under license by AIP Publishing.

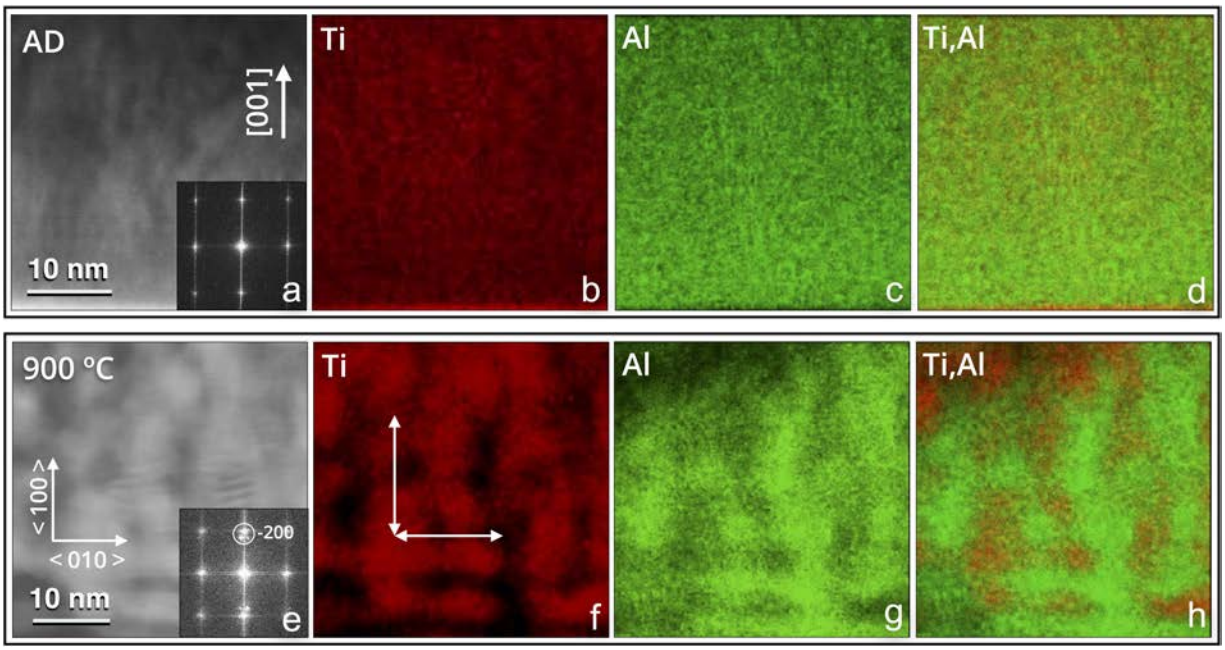

FIG. 3. (a) STEM with FFT inset, [(b)–(d)] STEM-EDX: Ti (red), Al (green) of as-deposited c-($Ti_{0.37}$,$Al_{0.63}$)N(001) film, (e) STEM with the FFT inset, and [(f)–(h)] STEM-EDX: Ti (red), Al (green) of the film annealed at 900 °C.

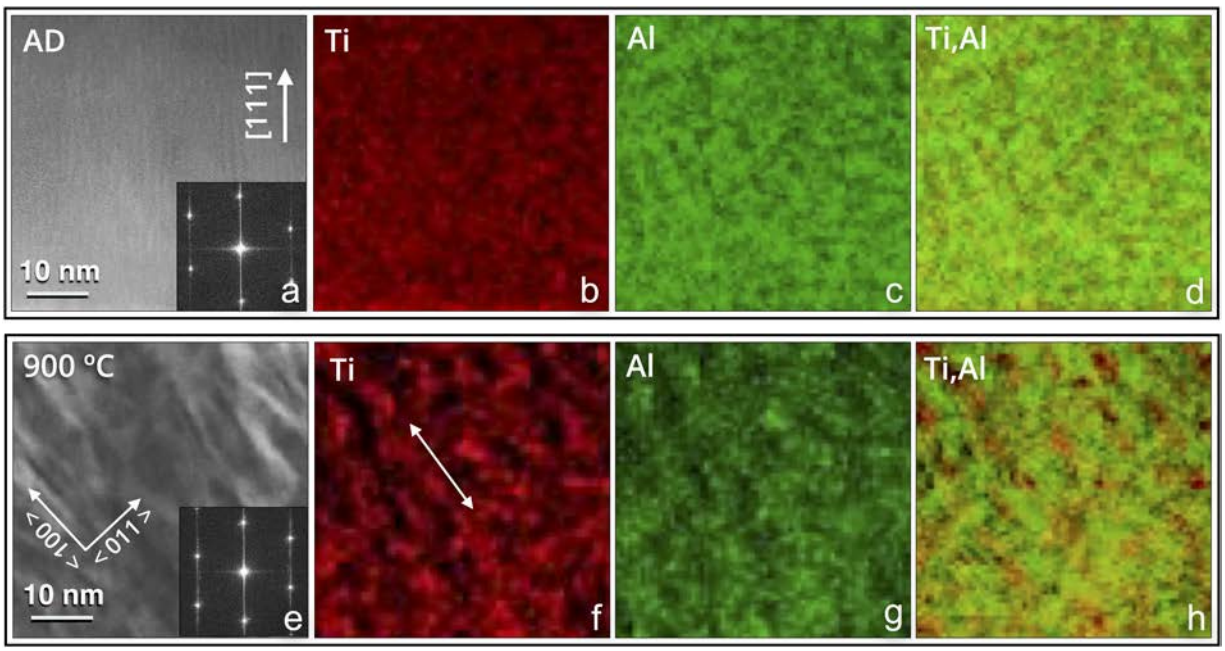

FIG. 4. (a) STEM with the FFT inset, [(b)–(d)] STEM-EDX: Ti (red), Al (green) of as-deposited c-($Ti_{0.37}$,$Al_{0.63}$)N(111) film, (e) STEM with the FFT inset, and [(f)–(h)] STEM-EDX: Ti (red), Al (green) of the film annealed at 900 °C.

Published under license by AIP Publishing.

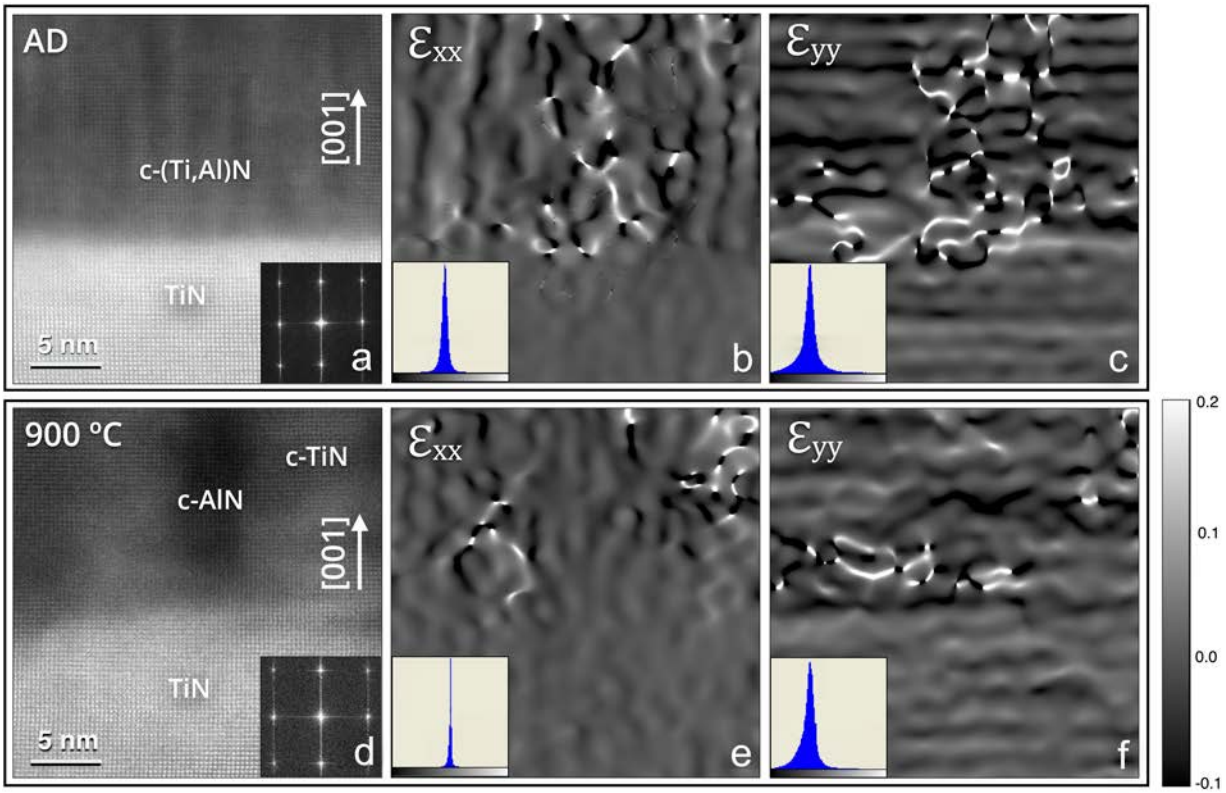

FIG. 5. (a) HAADF-STEM of as-deposited c-($Ti_{0.37}$,$Al_{0.63}$)N/c-TiN(001) with the FFT inset and the corresponding deformation maps for (b) ε_{xx} and (c) ε_{yy} directions, and (d) HAADF-STEM of annealed c-($Ti_{0.37}$,$Al_{0.63}$)N/c-TiN (001) with the FFT inset and the corresponding deformation maps for (e) ε_{xx} and (f) ε_{yy} directions. The inset histograms represent the distribution of strain values in each map.

addition, Figs. 5(b) and 5(c) show the ε_{xx} and ε_{yy} (x along the [100] direction and y along the [001] direction) components of the strain tensor, respectively. The generated histograms are from the entire area in the strain map, which includes the c-TiN buffer layer. The strain maps are deduced by GPA from the STEM image [Fig. 5(a)] and using the c-TiN buffer layer as the reference region because it contains almost no strain. A strain field is present across the entire film in the as-deposited state. After annealing, the c-($Ti_{0.37}$, $Al_{0.63}$)N film decomposes into coherent c-TiN and c-AlN rich domains [Fig. 5(d)]. The corresponding deformation maps [Figs. 5(e) and 5(f)] show that c-TiN domains contain more dislocations as compared to c-AlN, i.e., the locations with sharp contrast in the GPA strain maps correspond to the dislocations present in the sample. This was established by direct comparison of the location of dislocations and the strain concentrations. The locations of the dislocations were determined by FFT-filtering of the HR-HAADF-STEM images.[49]

Figure 6 shows HAADF-STEM micrographs and deformation maps over the interface region of the as-deposited and annealed c-($Ti_{0.37}$,$Al_{0.63}$)N/c-TiN(111) films. Overall, this orientation shows a similar trend with coherent interfaces [Figs. 5(a) and 5(d)] and strain maps [Figs. 6(b), 6(c), 6(e), and 6(f)] as the c-($Ti_{0.37}$,$Al_{0.63}$)N/c-TiN(001) films. The strains are mostly concentrated in c-TiN rich domains, indicating that strain reduction is dependent on the chemical environment. Due to the difference in the unit cell volume, the c-TiN-rich domain is mostly under compressive strain while a tensile strain is present in the c-AlN domain. The streaks in the FFTs of the STEM images are more dominant in the [001] direction because the acquisition of STEM images is through rastering of the beam across the sample in the perpendicular direction. GPA is based on the FFTs of the acquired images and it is observed that there is more contrast in the map of the strain tensor ε_{yy} than ε_{xx} because of this artifact during rastering. This is a systematic error, wherein a contrast variation appearing as thick horizontal lines is observed [Figs. 5(c), 5(f), 6(c), and 6(f)]. Nevertheless, both ε_{xx} and ε_{yy} show a similar trend that the buffer layer has the minimum strain and that the dislocations is mainly inside the c-TiN rich domains.

Higher magnification HAADF-STEM micrographs and the corresponding shear component (ε_{xy}) of the strain tensor (in the xy-plane) of the spinodal decomposed c-($Ti_{0.37}$,$Al_{0.63}$)N(001) and c-($Ti_{0.37}$,$Al_{0.63}$)N(111) films are shown in Fig. 7. The GPA strain maps in Figs. 7(b) and 7(h) demonstrate some shear strain near the interface of the segregated domains (indicated by white arrows).

Published under license by AIP Publishing.

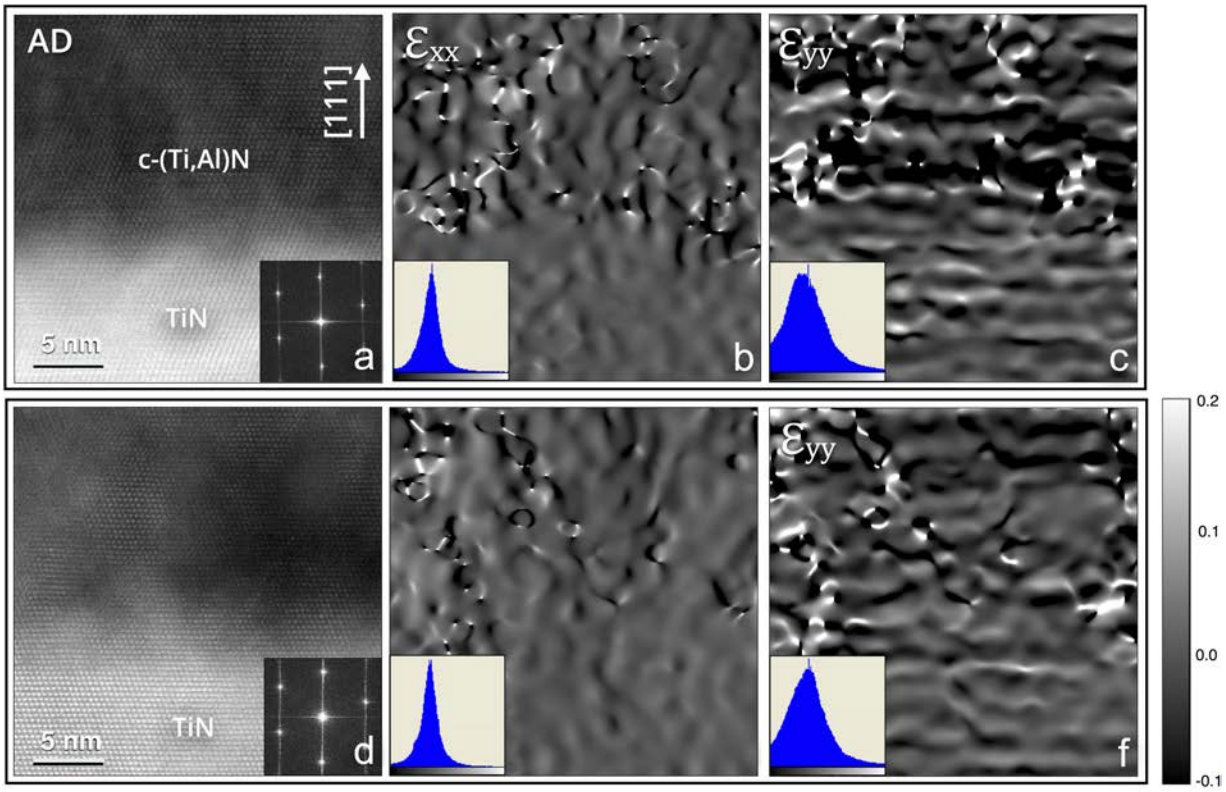

FIG. 6. (a) HAADF-STEM of as-deposited c-($Ti_{0.37}$,$Al_{0.63}$)N/c-TiN(111) with the FFT inset and the corresponding deformation maps for (b) ε_{xx} and (c) ε_{yy} directions, and (d) HAADF-STEM of annealed c-($Ti_{0.37}$,$Al_{0.63}$)N/c-TiN(111) with FFT inset the corresponding deformation maps for (e) ε_{xx} and (f) ε_{yy} directions. The inset histograms represent the distribution of strain values in each map.

Starting from the FFT of the STEM images, masks were applied on 0-20 and 020 spots of c-(Ti,Al)N(001) [Fig. 7(d)] and on −1−11 and 11−1 spots of c-(Ti,Al)N(111) [Fig. 7(g)]. Then, an inverse FFT algorithm was performed to reconstruct a filtered real space images as shown in Figs. 7(c) and 7(i). Insets 1 and 2 are different regions showing the presence of defects such as lattice distortions and dislocations in the masked planes. The comparison reveals that the local microstrain concentrations in the GPA maps are directly correlated to the presence of dislocations and the strain fields around the dislocations. The shear strain maps also show that strain field around the dislocations in the c-($Ti_{0.37}$,$Al_{0.63}$)N(111) film is larger and wider than in the c-($Ti_{0.37}$,$Al_{0.63}$)N(100) film.

IV. DISCUSSION

Epitaxial growth requires sufficient adatom surface mobility for rearrangements on the growth surface such that renucleation is avoided.[50] Using high substrate temperature during sputter deposition is a route to attain good epitaxy of the nitride film (i.e., film density close to the bulk value with high crystal coherence length) because it promotes surface diffusion and agglomeration of the impinging adatoms.[51,52] The use of MgO with a close match in lattice parameter to the film is needed to obtain epitaxial growth because the crystal structure of a substrate affects the nucleation kinetics.[53,54] In this study, c-($Ti_{0.37}$,$Al_{0.63}$)N/c-TiN(001) and c-($Ti_{0.37}$,$Al_{0.63}$)N/c-TiN(111) films were simultaneously grown at 700 °C using MgO(001) and MgO(111) substrates, respectively (i.e., all the deposition conditions are the same except the substrate orientation). Single crystal c-($Ti_{0.37}$,$Al_{0.63}$)N(001) is only achieved in the first 30-50 nm while c-($Ti_{0.37}$,$Al_{0.63}$)N(111) is sustained at large thickness. The growth orientation of transition metal nitrides is governed by growth kinetics and conditions leading to the lowest overall Gibbs free energy of the film.[53,55] Strain and surface energies contribute to the overall free energy, wherein strain energy is directly proportional to the film thickness ($H_{strain} \propto VE\varepsilon^2$, where E is the elastic modulus, ε is the strain, and V is the volume) while surface energy is independent of thickness.[56] Sangiovanni *et al.*[57] have shown in a molecular dynamic study on transition metal nitrides that incoming adatoms have higher diffusivity on fcc(100) planes than on fcc(111) of the same material at all temperatures. High-diffusivity denotes that the average residence time of surface atoms is low and the mean-free path is large, which would promote epitaxial growth. Instead, it is likely the contribution of the elastic energy to the overall Gibbs free energy of the film that causes a

Published under license by AIP Publishing.

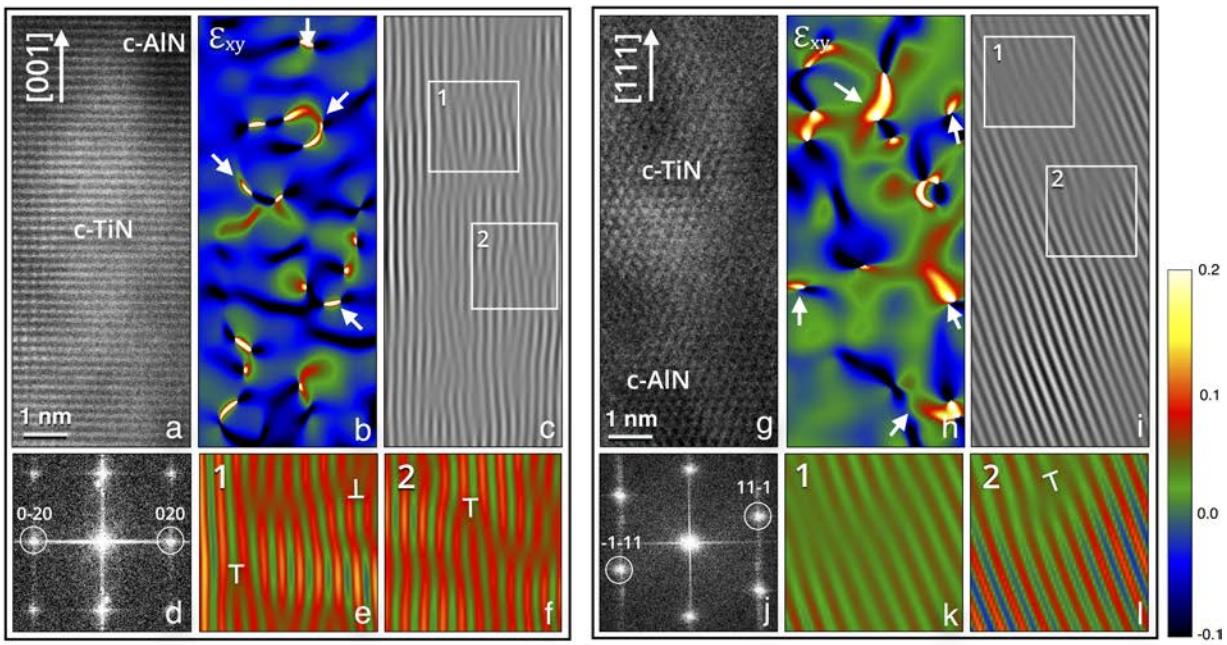

FIG. 7. High resolution HAADF-STEM of spinodally decomposed (a) c-($Ti_{0.37}$,$Al_{0.63}$)N(001) and (g) c-($Ti_{0.37}$,$Al_{0.63}$)N(111) films, their corresponding [(b) and (h)] experimental shear component ε_{xy}, and [(c) and (i)] reconstructed FFT^{-1} images of the masked planes in the [(d) and (j)] FFT patterns. [(e), (f), (k), and (l)] Insets 1 and 2 are magnifications of crystal defects in c-($Ti_{0.37}$,$Al_{0.63}$)N.

growth transition of the c-($Ti_{0.37}$,$Al_{0.63}$)N(001) film when reaching a certain thickness. The measured in-plane strain of the c-($Ti_{0.37}$,$Al_{0.63}$)N(111) by XRD is low (0.11%), which is consistent with the in-plane strain (ε_{xx}) recorded by GPA (Fig. 5) for the as-deposited c-($Ti_{0.37}$,$Al_{0.63}$)N(111) film, and distinctly lower than ε_{xx} of the c-($Ti_{0.37}$,$Al_{0.63}$)N(001) film. All involved materials (MgO, TiN, and TiAlN) have cubic symmetry and their coefficients of thermal expansion are isotropic, i.e., the induced thermal strain during cooling down from the deposition temperature does not affect the strain difference between the two samples. Hence, a higher strain energy is accumulating in the c-($Ti_{0.37}$,$Al_{0.63}$)N(001) film during growth compared to the c-($Ti_{0.37}$,$Al_{0.63}$)N(111) film that causes the break-down of the epitaxial growth mode. The result is the formation of a polycrystalline film after a certain thickness when growing on MgO(100).

The presence of a biaxial strain state causes in-plane expansion and out-of-plane compression of the c-($Ti_{0.37}$,$Al_{0.63}$)N lattice parameter in the as-deposited state (Table I). This strain occurs because of the differences in the lattice parameters and thermal expansion coefficients between the nitride films and MgO substrate. RSM reveals that the film has a minimal variation of d-spacing along the growth direction (out-of-plane). The broadening that occurs along the ω-direction (in-plane) of the symmetric and asymmetric scans signifies the occurrence of induced mosaic tilts and twists caused by dislocations.[46] The presence of dislocations in the as-deposited films is confirmed using GPA as indicated by the sharp contrast of the image in the deformation maps. These are likely threading dislocations that are formed during growth.[50,58]

Upon annealing, the c-($Ti_{0.37}$,$Al_{0.63}$)N films decompose into iso-structural and coherent c-TiN and c-AlN domains. These domains have elongated shape because the material is elastically anisotropic.[19] The Zener anisotropy, $A = 2C_{44}/(C_{11}-C_{12})$ of this cubic material is 1.57, which is greater than 1. Thus, domains elongate along the elastically soft <100> directions.[59] The observed strain changes during decomposition are caused by the lattice mismatch between c-TiN and c-AlN domains and some of the strain is relieved by the formation of misfit dislocations. For cubic materials, the elastic stiffness coefficients and shear moduli are directionally dependent.[60] *Ab initio* calculations show that c-TiN is stiffer than c-AlN along <100> implying stronger chemical bonds in c-TiN than c-AlN.[21] However, the covalent chemical bonds in c-AlN have a higher degree of directionality compared to c-TiN.[19] Our GPA analysis reveals that the c-TiN domains are more frequently populated with dislocations than c-AlN domains, i.e., misfit dislocations aggregate in c-TiN or in the chemical gradients next to c-TiN domains. This suggests that the directionality of the chemical bonding has greater effect than the bond strength on the dislocation structure. The primary slip system of TiN is [110] <1–10> for mechanically induced dislocations,[61] while it is yet to be determined for (Ti,Al)N. The generation of dislocations during spinodal decomposition is, as mentioned above, associated with misfit strain that occurs between Al and Ti-rich domains. Such misfit dislocations are not necessarily the same as the ones caused by mechanical deformation. Hence, different types of dislocations may be present. The misfit dislocations are expected to appear where they effectively

Published under license by AIP Publishing.

relieve elastic strain energy, and since the domains are coherent, separated with a chemical gradient, and elongated along <100> directions, such location would be the chemical gradient and their Burger's vectors should collectively cause lattice displacements along <100> directions. The data presented in this paper support aggregation of dislocations in the chemical gradients, while their Burger's vectors could not be conclusively determined.

The elastic shear moduli on c-($Ti_{0.37}$,$Al_{0.63}$)N(001) and c-($Ti_{0.37}$,$Al_{0.63}$)N(111) are $G'_{001} = c_{44} = 223$ GPa and $G'_{111} = \left(\frac{3}{1+2A}\right)c_{44} =$ 162 GPa, respectively.[60] The higher shear strain observed in the deformation maps on (111) planes than on (100) planes is attributed to its lower shear modulus which also causes a wider shear strain field around the dislocations when viewing the strain by (111) compared to (100) planes.

Theoretical and experimental studies on the (Ti_{1-x},Al_x)N_y system show that the kinetics of decomposition is highly dependent on chemical composition,[21,62] presence of surfaces or interfaces,[63,64] and point defects (e.g., N vacancies, metal vacancies, interstitials).[13,14,65,66] In this study, it is expected that the ($Ti_{0.37}$,$Al_{0.63}$)N film has an earlier onset of spinodal decomposition than (Ti_{1-x},Al_x)N_y films with other x compositions because this material system has an asymmetric free energy curve, which peaks at approximately x = 0.65.[3] The polycrystalline $Ti_{0.34}Al_{0.66}N$ film deposited by cathodic arc deposition shows an onset of decomposition at 817 °C,[63] while the single crystal ($Ti_{0.37}$,$Al_{0.63}$)N film has not yet decomposed when annealed at 850 °C and the segregation of the domains is only observed at 900 °C. The lower thermal stability of the polycrystalline film than the single crystal film with a similar Al-content is attributed to its large number of internal interfaces such as grain and column boundaries that affect initiation of decomposition by surface-directed spinodal decomposition (SDSD). The tendency for decomposition is enhanced by SDSD because the internal surfaces result in a chemical potential gradient that provides a preferential direction for uphill diffusion.[67,68] The film has a nitrogen to metal ratio of $y \approx 1$; thus, the effects of N and metal vacancies on its thermal stability are expected to be small.[12–14,17]

The spinodal decomposition of alloys quenched in the metastable region of the phase diagram is accelerated in the presense of dislocation stress field.[23] Thus, an interplay between dislocations and phase separation is expected. Although a direct link between the performed local strain analysis and the observed macroscopic age hardening behavior of (Ti,Al)N is still an open question, this study points out the role of the chemical nature and anisotropic elastic properties of the segregated domains in the understanding of the local strain state of the material.

V. CONCLUSIONS

Heteroepitaxial c-($Ti_{0.37}$,$Al_{0.63}$)N/c-TiN thin films were grown on MgO(001) and (111) substrates. In the as-deposited state, high resolution HAADF-STEM micrographs show coherency between the films and the substrate. By RSM, a strain field is observed across the entire film and the corresponding GPA maps reveal a high stress field, attributed to plastic deformation and condensation of self-interstitials and vacancies during growth. At elevated temperature, a clear segregation of c-AlN- and c-TiN rich domains is observed, with strain mostly accommodated near the domain interfaces as well as inside c-TiN rich domains. Further, the c-AlN rich domains contain less crystal defects, e.g., lattice distortions and edge dislocations, because the dominant component of its chemical bonding is strongly covalent. This suggests that the type of chemical bonding of the domains is a controlling factor for the dislocation structure and strain generation in c-(Ti,Al)N during spinodal decomposition.

ACKNOWLEDGMENTS

The work was supported by the European Union's Erasmus Mundus doctoral program in Materials Science and Engineering (DocMASE), the Swedish Research Council (Grant No. 621-2012-4401), the Swedish government strategic research area grant AFM—SFO MatLiU (No. 2009-00971), and VINNOVA (FunMat-II project Grant No. 2016-05156 and M-ERA.net project MC2 Grant No. 2013-02355). The Atom Probe was financed by the German Research Foundation (DFG) and the Federal State Government of Saarland, Germany (INST 256/298-1 FUGG). Per Eklund also acknowledges the Knut and Alice Wallenberg foundation through the Wallenberg Academy Fellow program. The authors thank Michelle Marie S. Villamayor for her assistance with reciprocal space map measurements, Sylvie Migot for the TEM sample preparation, and Jaafar Ghanbaja for the acquisition of TEM images.

REFERENCES

[1]W. D. Münz, J. Vac. Sci. Technol. A **4**, 2717 (1986).
[2]P. H. Mayrhofer, C. Mitterer, L. Hultman, and H. Clemens, Prog. Mater. Sci. **51**, 1032 (2006).
[3]B. Alling, M. Odén, L. Hultman, and I. Abrikosov, Appl. Phys. Lett. **95**, 181906 (2009).
[4]M. Oden, L. Rogström, A. Knutsson, M. Terner, P. Hedström, J. Almer, and J. Ilavsky, Appl. Phys. Lett. **94**, 053114 (2009).
[5]A. Hörling, L. Hultman, M. Odén, J. Sjölén, and L. Karlsson, Surf. Coat. Technol. **191**, 384 (2005).
[6]A. Knutsson, J. Ullbrand, L. Rogström, N. Norrby, L. Johnson, L. Hultman, J. Almer, M. J. Jöesaar, B. Jansson, and M. Odén, J. Appl. Phys. **113**, 213518 (2013).
[7]I. Povstugar, P.-P. Choi, D. Tytko, J.-P. Ahn, and D. Raabe, Acta Mater. **61**, 7534 (2013).
[8]P. H. Mayrhofer, C. Mitterer, and H. Clemens, Adv. Eng. Mater. **7**, 1071 (2005).
[9]P. Jindal, A. Santhanam, U. Schleinkofer, and A. Shuster, Int. J. Refract. Met. Hard Mater. **17**, 163 (1999).
[10]A. Knutsson, M. P. Johansson, L. Karlsson, and M. Odén, Surf. Coat. Technol. **205**, 4005 (2011).
[11]M. Kato, T. Mori, and L. H. Schwartz, Acta Metallur. **28**, 285 (1980).
[12]I. C. Schramm, C. Pauly, M. P. Johansson Jõesaar, S. Slawik, S. Suarez, F. Mücklich, and M. Odén, Surf. Coat. Technol. **330**, 77 (2017).
[13]K. Calamba, I. Schramm, M. Johansson Jõesaar, J. Ghanbaja, J. Pierson, F. Mücklich, and M. Odén, J. Appl. Phys. **122**, 065301 (2017).
[14]I. C. Schramm, M. P. Johansson Jõesaar, J. Jensen, F. Mücklich, and M. Odén, Acta Mater. **119**, 218 (2016).
[15]S. PalDey and S. Deevi, Mater. Sci. Eng. A **342**, 58 (2003).
[16]H. Gleiter, Acta Mater. **48**, 1 (2000).
[17]K. Grönhagen, J. Ågren, and M. Odén, Scripta Mater. **95**, 42 (2015).
[18]D. J. Seol, S. Y. Hu, Y. L. Li, J. Shen, K. H. Oh, and L. Q. Chen, Acta Mater. **51**, 5173 (2003).
[19]F. Tasnádi, I. A. Abrikosov, L. Rogström, J. Almer, M. P. Johansson, and M. Odén, Appl. Phys. Lett. **97**, 231902 (2010).
[20]L. Rogström, J. Ullbrand, J. Almer, L. Hultman, B. Jansson, and M. Odén, Thin Solid Films **520**, 5542 (2012).

Published under license by AIP Publishing.

[21]N. Shulumba, O. Hellman, L. Rogström, Z. Raza, F. Tasnádi, I. A. Abrikosov, and M. Odén, Appl. Phys. Lett. **107**, 231901 (2015).
[22]J. W. Cahn and J. E. Hilliard, J. Chem. Phys. **28**, 258 (1958).
[23]Y.-S. Li, S.-X. Li, and T.-Y. Zhang, J. Nucl. Mater. **395**, 120 (2009).
[24]S. Y. Hu and L. Q. Chen, Acta Mater. **52**, 3069 (2004).
[25]Y. Zhu, C. Ophus, J. Ciston, and H. Wang, Acta Mater. **61**, 5646 (2013).
[26]M. Hÿtch, J.-L. Putaux, and J. Thibault, Philos. Mag. **86**, 4641 (2006).
[27]M. J. Hÿtch, E. Snoeck, and R. Kilaas, Ultramicroscopy **74**, 131 (1998).
[28]D. Cooper, T. Denneulin, N. Bernier, A. Béché, and J.-L. Rouvière, Micron **80**, 145 (2016).
[29]M. Moser and P. H. Mayrhofer, Scripta Mater. **57**, 357 (2007).
[30]E. Etchessahar, J. P. Bars, and J. Debuigne, J. Less Common Met. **134**, 123 (1987).
[31]S. Jeon, C. J. Van Tyne, and H. Lee, Ceramics Int. **40**, 8677 (2014).
[32]A. S. M. Rao and K. Narender, J. Thermodyn. **2014**, 123478 (2014).
[33]H. Ljungcrantz, M. Odén, L. Hultman, J. Greene, and J. E. Sundgren, J. Appl. Phys. **80**, 6725 (1996).
[34]C.-S. Shin, D. Gall, P. Desjardins, A. Vailionis, H. Kim, I. Petrov, J. Greene, and M. Odén, Appl. Phys. Lett. **75**, 3808 (1999).
[35]D. Gall, C.-S. Shin, T. Spila, M. Odén, M. Senna, J. Greene, and I. Petrov, J. Appl. Phys. **91**, 3589 (2002).
[36]H. Söderberg, M. Odén, A. Flink, J. Birch, POÅ Persson, M. Beckers, and L. Hultman, J. Mater. Res. **22**, 3255 (2011).
[37]N. Ghafoor, L. J. Johnson, D. O. Klenov, J. Demeulemeester, P. Desjardins, I. Petrov, L. Hultman, and M. Odén, APL Mater. **1**, 022105 (2013).
[38]A. Le Febvrier, J. Jensen, and P. Eklund, J. Vac. Sci. Technol. A **35**, 021407 (2017).
[39]A. McLeod and C. Gabryel, Metall. Trans. A **23**, 1279 (1992).
[40]H.-S. Seo, T.-Y. Lee, I. Petrov, J. Greene, and D. Gall, J. Appl. Phys. **97**, 083521 (2005).
[41]H. Rösner, C. T. Koch, and G. Wilde, Acta Mater. **58**, 162 (2010).
[42]K. Thompson, D. Lawrence, D. J. Larson, J. D. Olson, T. F. Kelly, and B. Gorman, Ultramicroscopy **107**, 131 (2007).
[43]H. Willmann, M. Beckers, J. Birch, P. H. Mayrhofer, C. Mitterer, and L. Hultman, Thin Solid Films **517**, 598 (2008).
[44]M. A. Moram, Z. H. Barber, C. J. Humphreys, T. Joyce, and P. Chalker, J. Appl. Phys. **100**, 023514 (2006).
[45]A. Kern and W. Eysel, Mineralogisch-Petrograph Inst., University Heidelberg, Germany, ICDD Grant-in-Aid, 1993.
[46]M. Moram and M. Vickers, Rep. Prog. Phys. **72**, 036502 (2009).
[47]P. F. Fewster, *X-Ray Scattering from Semiconductors and Other Materials* (World Scientific, 2015).
[48]G. Möbus, G. Necker, and M. Rühle, Ultramicroscopy **49**, 46 (1993).
[49]Z. Wang, M. Saito, K. P. McKenna, and Y. Ikuhara, Nat. Commun. **5**, 3239 (2014).
[50]M. Ohring, *Materials Science of Thin Films* (Elsevier, 2001).
[51]A. Ingason, F. Magnus, S. Olafsson, and J. Gudmundsson, J. Vac. Sci. Technol., A **28**, 912 (2010).
[52]D.-H. Kim, E. Byon, G.-H. Lee, and S. Cho, Thin Solid Films **510**, 148 (2006).
[53]I. Petrov, P. Barna, L. Hultman, and J. Greene, J. Vac. Sci. Technol. A **21**, S117 (2003).
[54]J. Narayan, Acta Mater. **61**, 2703 (2013).
[55]U. Oh and J. H. Je, J. Appl. Phys. **74**, 1692 (1993).
[56]J. Pelleg, L. Z. Zevin, S. Lungo, and N. Croitoru, Thin Solid Films **197**, 117 (1991).
[57]D. G. Sangiovanni, F. Tasnádi, L. Hultman, I. Petrov, J. E. Greene, and V. Chirita, Surf. Sci. **649**, 72 (2016).
[58]F. Adibi, I. Petrov, L. Hultman, U. Wahlström, T. Shimizu, D. McIntyre, J. Greene, and J. E. Sundgren, J. Appl. Phys. **69**, 6437 (1991).
[59]J. W. Cahn, Acta Metallur. **10**, 179 (1962).
[60]K. M. Knowles and P. R. Howie, J. Elast. **120**, 87 (2015).
[61]M. Odén, H. Ljungcrantz, and L. Hultman, J. Mater. Res. **12**, 2134 (2011).
[62]I. A. Abrikosov, A. Knutsson, B. Alling, F. Tasnádi, H. Lind, L. Hultman, and M. Odén, Materials **4**, 1599 (2011).
[63]A. Knutsson, I. Schramm, K. Asp Grönhagen, F. Mücklich, and M. Odén, J. Appl. Phys. **113**, 114305 (2013).
[64]R. C. Ball and R. L. H. Essery, J. Phys. Condens. Matter **2**, 10303 (1990).
[65]B. Alling, A. Karimi, L. Hultman, and I. Abrikosov, Appl. Phys. Lett. **92**, 071903 (2008).
[66]M. to Baben, M. Hans, D. Primetzhofer, S. Evertz, H. Ruess, and J. M. Schneider, Mater. Res. Lett. **5**, 158 (2017).
[67]S. K. Das, S. Puri, J. Horbach, and K. Binder, Phys. Rev. Lett. **96**, 016107 (2006).
[68]G. Brown and A. Chakrabarti, Phys. Rev. A **46**, 4829 (1992).

Published under license by AIP Publishing.

Paper 4

Growth and high temperature decomposition of epitaxial metastable wurtzite $(Ti_{1-x},Al_x)N(0001)$ thin films

K. Calamba, J. Barrirero, M. Johansson Jõesaar, S. Bruyère, J. Pierson, A. Febvrier, Mücklich, R. Boyd, and M. Odén

Submitted for publication

Growth and high temperature decomposition of epitaxial metastable wurtzite $(Ti_{1-x},Al_x)N(0001)$ thin films

K.M. Calamba[1,2], J. Barrirero[1,3], M.P. Johansson Jõesaar[4], S. Bruyère[2], R. Boyd[1], J.F. Pierson[2], A. Le Febvrier[5], F. Mücklich[3], and M. Odén[1]

[1]*Nanostructured Materials, Department of Physics, Chemistry and Biology (IFM), Linköping University, Linköping, SE-581 83, Sweden*
[2]*Université de Lorraine, CNRS, IJL, F-54000 Nancy, France*
[3]*Functional Materials, Department of Materials Science, Saarland University, Saarbrücken, D-66123, Germany*
[4]*SECO Tools AB, Fagersta, SE-73 782, Sweden*
[5]*Thin Film Physics Division, Department of Physics, Chemistry and Biology (IFM), Linköping University, Linköping, SE-581 83, Sweden*

Abstract

The structure, growth, and phase stability of $(Ti_{1-x},Al_x)N$ films with high Al content were investigated. $(Ti_{1-x},Al_x)N$ (x = 0.63 and 0.77) thin films were grown on MgO(111) substrates at 700 °C using a UHV DC magnetron sputtering system. The $(Ti_{0.37},Al_{0.63})N$ film is a single crystal with a cubic NaCl (B1) structure while the $(Ti_{0.23},Al_{0.77})N$ film only shows epitaxial growth of the same cubic phase in the first few atomic layers. With increasing film thickness, epitaxial wurtzite (B4) forms. The thin cubic layer and the wurtzite film has an orientation relationship of c-$(Ti_{0.23},Al_{0.77})N$ $(111)[1\bar{1}0]$ ||w-$(Ti_{0.23},Al_{0.77})N$ $(0001)[11\bar{2}0]$. Continued deposition results in a gradual break-down of the epitaxial growth. It is replaced by polycrystalline growth of wurtzite columns with a high degree of 0001 texture, separated by a Ti-enriched cubic phase. In the as-deposited state, c-$(Ti_{0.27},Al_{0.63})N$ displays a homogeneous chemical distribution while the w-$(Ti_{0.23},Al_{0.77})N$ has segregated to Al- and Ti-rich domains. Annealing at 900 °C resulted in the spinodal decomposition of the metastable c-$(Ti_{0.27},Al_{0.63})N$ film and formation of coherent elongated c-AlN and c-TiN-rich domains with an average width of 4.5 ± 0.2 nm while the width of the domains in the w-$(Ti_{0.23},Al_{0.77})N$ film only marginally increases to 2.8 ± 0.1 nm. The slower coarsening rate of the wurtzite structure compared to cubic is indicative of a higher thermal stability.

Introduction

Transition metal nitrides (TMN) are commonly used as protective coatings in a wide range of industrial applications. Significant attention has been devoted to the cubic metastable B1 (NaCl) structure of titanium aluminum nitride c-($Ti_{1-x}Al_x$)N. ($Ti_{1-x}Al_x$)N exhibits oxidation resistance properties with a high hardness at elevated temperatures [1] including age hardening, typically resulting in high wear resistance during metal cutting [2, 3]. Age hardening occurs because of a spinodal decomposition of the solid solution c-(Ti,Al)N into coherent c-TiN- and c-AlN-rich domains at an elevated temperature [4, 5]. As the decomposition proceeds, the c-AlN transforms to wurtzite w-AlN [6-8]. Although the decomposition route of c-(Ti_{1-x},Al_x)N material system has been extensively studied, information regarding wurtzite (Ti_{1-x},Al_x)N is limited, despite its frequent presence and influence on both microstructure and properties of (Ti_{1-x},Al_x)N films [9]. Wurtzite-AlN is well studied because of its semiconducting, optical, and thermal properties [10, 11]. Spinodal decomposition has been shown to take place at elevated temperature in the similar w-(Zr,Al)N materials system [12]. For the same materials system Yalamnchili et al. [13] showed that transformation induced plasticity including transformations between cubic and wurtzite (Zr,Al)N resulted in improved mechanical properties. In addition, there are several reports claiming that semicoherent interfaces between w-AlN rich nanodomains in both (Ti,Al)N and (Zr,Al)N positively influence the mechanical stability at elevated temperatures [14-16]. Consequently, a need for preparing films where the intrinsic properties of the w-(Ti,Al)N can be determined as well as an understanding of how it forms in relation to other phases is needed, due to its strong influence on the overall functional properties of (Ti,Al)N films.

Most TMN material systems crystallize in cubic B1, hexagonal B_k, and wurtzite B4 structures, wherein the nonmetal atoms occupy the interstitial sites [17]. The crystal structure of these nitrides are primarily determined by their electronic properties (i.e. number of sp valence electrons per atom, e/a) [18, 19] and it can be stabilized to a different phase (e.g. cubic B1 to wurtzite B4) under high pressure [20, 21] or by depositing onto a substrate with a similar lattice parameter [22]. It is known that (Ti_{1-x},Al_x)N films deposited using cathodic arc techniques have fcc structure for $0.3 \leq x \leq 0.7$ and a high amount of Al ($x > 0.7$) is required to grow films with a wurtzite structure [23, 24]. In addition, the film thickness has recently been shown to influence the crystal structure, wherein polycrystalline c-($Ti_{0.38}$,$Al_{0.62}$)N exhibit a

transition in growth mode to yield a wurtzite structure above a critical thickness of approximately 3μm [25].

In this study, we pioneer the growth of wurtzite $(Ti_{1-x},Al_x)N$ with x = 0.77 single crystals using an epitaxial stabilization technique. Stabilization occurs because a single crystal cubic c-$(Ti_{0.23},Al_{0.77})N$ film is grown to a critical thickness (few nanometers) using a TiN(111) buffer layer deposited on MgO(111). Above this thickness a transition occurs and a wurtzite (B4) film forms. The interface is coherent with an orientation relationship of c-$(Ti_{0.23},Al_{0.77})N$ $(111)[1\bar{1}0]$ ||w-$(Ti_{0.23},Al_{0.77})N$ $(0001)[11\bar{2}0]$. As the film continues to grow, a change to a polycrystalline growth of cubic and wurtzite structures occurs. Distinct microstructural features are observed between these two structures, which are characterized using high-resolution imaging methods. The defect structures of the cubic phase before the transition are quantified in terms of strain using geometric phase analysis (GPA) on high resolution high-angle annular dark-field scanning transmission electron micrographs (HAADF-STEM). The thermal stability of $(Ti_{1-x},Al_x)N$ films is also discussed.

Experimental details

$(Ti_{1-x}Al_x)N_y$ thin films were deposited on MgO(111) substrates (>99.95 % purity, 10x10 mm^2 size) using a UHV DC magnetron sputtering system equipped with four magnetrons in a strong unbalanced configuration. The design of the deposition chamber used in this study is described in detail by le Febvrier et al. [26]. A Ti target was used to deposit TiN buffer layers while $Ti_{0.35}Al_{0.65}$ and $Ti_{0.22}Al_{0.78}$ composite targets were used to deposit $(Ti_{1-x}Al_x)N_y$ thin films with different compositions. Ti target was used to deposit pure TiN thin films as a reference material and to deposit the TiN buffer layer. The buffer layer prevents high temperature chemical reaction between Al and Mg. All targets have a diameter of 50 mm with >99.9 % purity. MgO were used as substrates for epitaxial growth because they have similar lattice parameter as the c-TiN buffer layer and c-$Ti_{1-x}Al_xN$ film with a lattice mismatch of less than 1% [27] and similar coefficient of thermal expansion (i.e. $\alpha_{MgO} \approx 14 \times 10^{-6}$/°C, $\alpha_{TiN} \approx 9.4 \times 10^{-6}$/°C, and $\alpha_{(Ti,Al)N} \approx 7.5 \times 10^{-6}$/°C [28, 29]). The MgO substrates were cleaned by sonication in 2 vol. % Hellmanex®II aqueous solution, acetone, and ethanol before inserted in the deposition chamber and evacuated to a base pressure of

< 4 x 10^{-7} Pa [30]. Prior to the deposition, the substrates were subjected to annealing at 900 °C for 1 h. The distance between the targets and the substrates is ~140 mm. The flow rates of Ar and N_2 were set to 30 sccm and 10 sccm, respectively. The Ar+N_2 gas mixture results in a total gas pressure of 0.3 Pa. The substrates were kept at 700 °C to attain an epitaxial growth of the nitride films [31]. A constant discharge current of 0.2 A was used for the depositions, which resulted in a deposition rate of 1.25 nm/min. $(Ti_{1-x}Al_x)N_y$ films were grown to approximate thicknesses of either 150 nm or 1000 nm. All depositions were made with a continuous substrate rotation of 14 rpm with the rotation axis parallel to the growth direction.

The as-deposited films were heat treated isothermally in an argon atmosphere using a BN tube furnace. The films were heated at a rate of 20 °C/min to a maximum temperature of 900 °C and held for 120 min and then slowly cooled to room temperature.

X-ray diffractometry (XRD) θ-2θ scans and pole figures of $(Ti_{1-x}Al_x)N_y$ films were obtained using a PANalytical Empyrean diffractometer with Cu K_α radiation. A parabolic graded multilayer mirror, a collimator and a channel-cut 2-bounce Ge(220) monochromator were used as the incoming x-ray beam optics and a parallel plate collimator as the receiving optics for the diffracted beam.

Cross-sectional transmission electron microscope (TEM) samples were prepared using an *in situ* lift-out technique in a focused ion beam (FIB) - scanning electron microscope (SEM) dual beam system (Helios Nanolab 600i). The micromanipulator used was a FEI EasyLift EX system fitted with a W needle. The samples have approximately 50 nm uniform thickness. Plan-view TEM samples were prepared by FIB-SEM dual beam system (Zeiss 1540 crossbeam) in order to extract the samples at different distances from the substrate-film interface.

Electron micrographs of the thin films were obtained using an aberration-corrected TEM (JEOL ARM 200F - Cold FEG TEM/STEM) operated at 200 kV. Chemical analyses were performed using an energy dispersive x-ray spectrometer (EDS JEOL Centurio EDS 1sr) attached to the TEM. Strain mapping analysis was performed using Digital Micrograph (Gatan, CA) with an added geometric phase analysis (GPA) script [32]. GPA is an imaging technique that measures the lattice displacements and strain field in crystals relative to a reference region by using a Fast

Fourier transform (FFT) algorithm on a high resolution TEM image acquired in a high symmetry crystal orientation - zone axis [33].

Atom probe tomography (APT) was performed in a LEAP 3000X HR (CAMECA), which was operated in pulsed laser mode at 0.5 nJ energy at a frequency of 200 kHz. Data acquisition was carried out at a specimen temperature of 60 K and chamber pressures lower than 1 x 10^{-10} Torr (1.33 x 10^{-8} Pa). The evaporation rate of the specimen was set to 5 atoms per 1000 laser pulses. Specimens for APT were prepared in a dual-beam FIB/SEM workstation (Helios NanoLab 600, FEI). The surface of the samples was coated with an approximately 200 nm thick Ti sacrificial layer. On top of that, an electron beam induced Pt layer was added prior to FIB irradiation to protect from gallium implantation. After lift out and thinning of the APT specimens, a low energy milling at 2 kV was performed to minimize the influence from Ga induced damage [34]. Datasets were reconstructed and analyzed in the software IVAS 3.6.14 (CAMECA). Overall compositions were obtained by a peak decomposition analysis routine included in the software to correct for peak overlap in the mass-to-charge spectrum between N^+ and N_2^{++}.

The hardness values of the films were obtained using an UMIS nanoindenter with a Berkovich diamond tip. A minimum of 20 indents in each sample to a maximum load of 10 mN was used to obtain the average hardness from the load-displacement curves [35]. A fused silica sample was used as reference to determine the contact area of the tip versus penetration depth.

Results

A. Chemical composition of $(Ti_{1-x}Al_x)N$

Table 1 shows the APT chemical composition of the $(Ti_{1-x}Al_x)N_y$ thin films on MgO(111) substrates with a c-TiN buffer from $Ti_{0.35}Al_{0.65}$ and $Ti_{0.22}Al_{0.78}$ targets, respectively. The reported values correspond to the weighted average of 3 APT specimens for the film deposited with the $Ti_{0.35}Al_{0.65}$ target and 4 specimens of the film deposited with the $Ti_{0.22}Al_{0.78}$ target. APT specimens were taken from different positions on the films and the error reported depicts the intrinsic composition fluctuation in the as-deposited state which is not higher than 1 at. % for any of the elements. Both films contain less than 1.7 at. % impurities, such as C and O. The Al content x = (Al/(Al+Ti)) and N content y = (N/(Al+Ti)) of the film deposited from a $Ti_{0.35}Al_{0.65}$ target was evaluated as x = 0.63 and y = 0.96, respectively. Similar for the

film deposited from the $Ti_{0.22}Al_{0.78}$ target, the Al and N contents were evaluated as x = 0.77 and y = 1.0, respectively.

Table 1. APT chemical compositions of c-$(Ti_{1-x}Al_x)N_y$ thin films deposited on MgO(111) substrate with a c-TiN buffer layer from $Ti_{0.35}Al_{0.65}$ and $Ti_{0.22}Al_{0.78}$ targets.

Element	$(Ti_{0.37},Al_{0.63})N$	$(Ti_{0.23},Al_{0.77})N$
Ti [at.%]	18.4 ± 0.6	11.3 ± 0.2
Al [at.%]	31.9 ± 0.7	38.2 ± 0.3
N [at.%]	48.2 ± 1.0	50.0 ± 0.5
x = Al/(Al+Ti)	**0.63**	**0.77**

B. Microstructure of as-deposited $(Ti_{1-x}Al_x)N$

$(Ti_{0.37},Al_{0.63})N$ films deposited on MgO(111) substrates with a c-TiN buffer layer reveal cubic B1 structured single crystals recently reported by us [31]. The following section focus on the growth structure of the mixed cubic and wurtzite phase $(Ti_{0.23},Al_{0.77})N$ films on MgO(111) substrates with a TiN buffer layer with respect to the as-referred study.

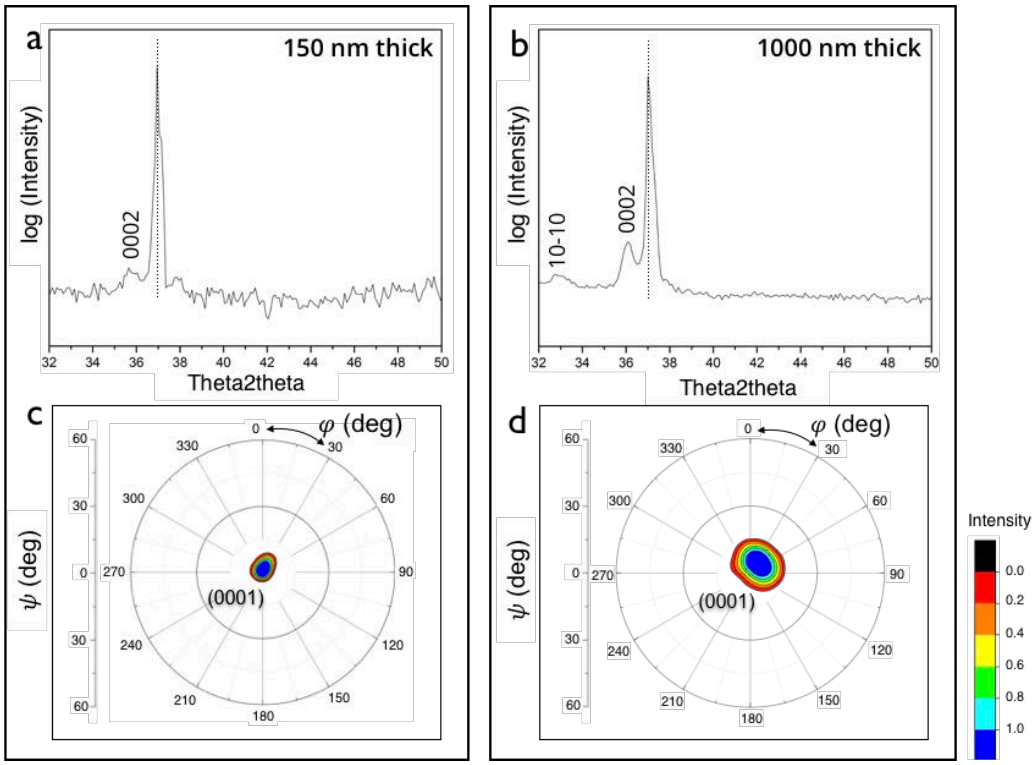

Figure 1. X-ray diffractograms of as-deposited mixed cubic and wurtzite phase $(Ti_{0.23},Al_{0.77})N$ films with thickness of (a) 150 nm and (b) 1000 nm on MgO(111) substrate with a c-TiN buffer layer. Figures (c) and (d) show the corresponding 0002 pole figures of the films. The substrate peaks in the diffractograms are marked with dotted lines.

Figure 1 shows XRD θ-2θ scans and pole figures of as-deposited mixed cubic and wurtzite phase $(Ti_{0.23},Al_{0.77})N$ films with different thicknesses on MgO (111) substrates with a c-TiN buffer layer. The diffractogram of the 150 nm thick $(Ti_{0.23},Al_{0.77})N$ film in Figure 1a shows, besides the substrate peak (marked), a contribution of a single hexagonal close packed wurtzite B4 structure 0002 peak. As the film grows thicker (Figure 1b), second weaker $10\bar{1}0$ peak occurs in the diffractogram indicating a textured polycrystalline film. The corresponding 0002 pole figures of the 150 nm and 1000 nm thick $(Ti_{0.23},Al_{0.77})N$ films are shown in Figure 1c and Figure 1d, respectively. The pole figures indicate high orientation along 0001 direction with a distinct peak at the center, which is broader for the thicker film.

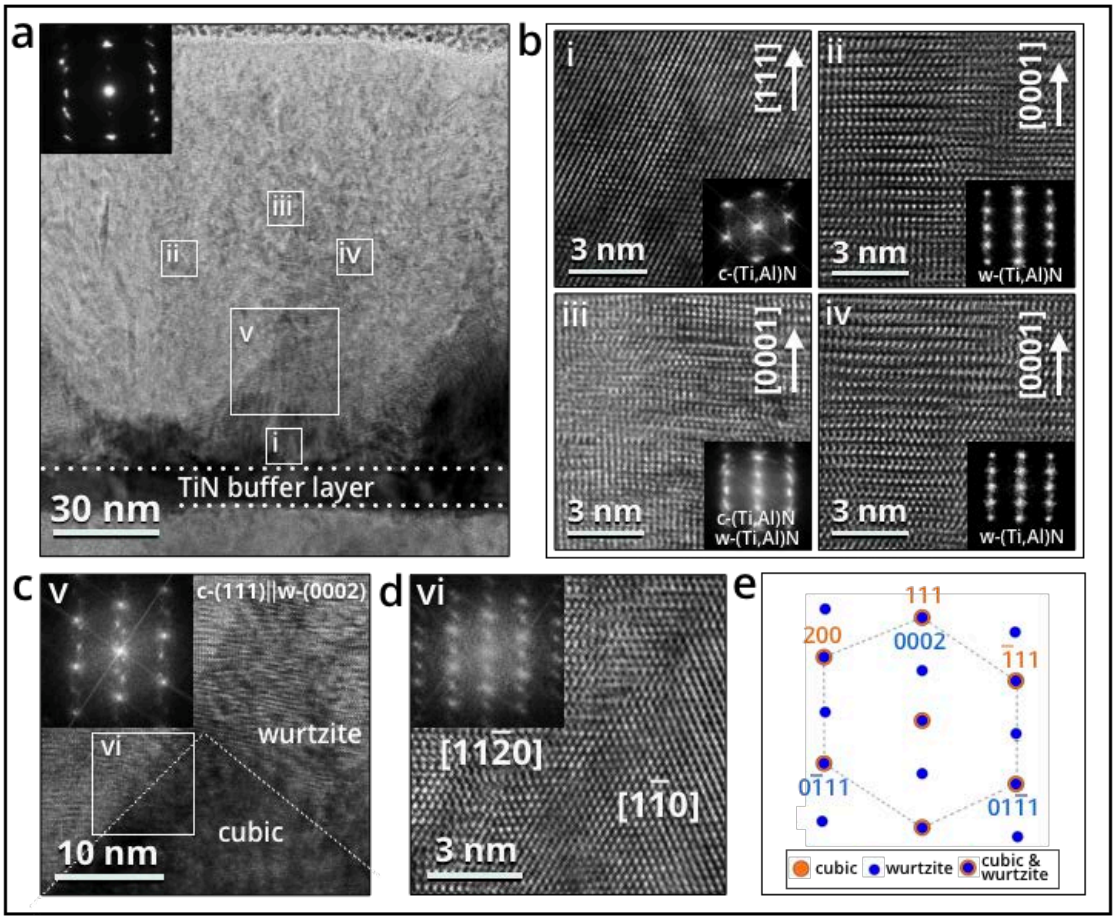

Figure 2. Cross-sectional (a) TEM with SAED inset, (b) high resolution TEM images with FFT insets of (i) bottom region near buffer layer, (ii) upper left grain, (iii) interface between grains, and (iv) upper right grain, (c) high resolution TEM images with FFT insets of (c) region v and (d) region vi with coherent cubic and wurtzite interface, and (e) an illustration of the FFT image of this coherent interface of as-deposited mixed cubic and wurtzite phase $Ti_{0.23}Al_{0.77}N$ film with 150 nm thickness on MgO(111) substrate with a c-TiN buffer layer. The SAED pattern is collected from an area with a diameter of 100 nm.

Figure 2 show cross-sectional TEM micrographs of the 150 nm thick $(Ti_{0.23},Al_{0.77})N$ film on the c-TiN buffer layer/MgO (111) substrate. The selected area electron diffraction SAED pattern of this sample (Figure 2a) also shows an overlap of the cubic and wurtzite signals with aligned c-[111] and w-[0001] along the growth direction. A thin cubic c-$(Ti_{0.23},Al_{0.77})N(111)$ layer grows epitaxially on the TiN(111) buffer layer to a thickness ranging between 10 and 30 nm. Figure 2b.i. shows a high-resolution TEM (HRTEM) image and the corresponding FFT pattern (inset) of the c-$(Ti_{0.23},Al_{0.77})N$ layer from a region next to the buffer layer. Above the cubic c-$(Ti_{0.23},Al_{0.77})N$ layer, an epitaxial wurtzite w-$(Ti_{0.23},Al_{0.77})N$ layer has formed oriented with its [0001] axis parallel to the growth direction. Figure 2c shows a HRTEM image and corresponding FFT pattern from region v, i.e., the transition region with c-$(Ti_{0.23},Al_{0.77})N(111)$ lattice planes epitaxially oriented parallel to w-$(Ti_{0.23},Al_{0.77})N(0001)$. The vertical streaks in the FFT pattern originate from stacking faults present in this region. Figure 2d shows a higher resolution TEM image and FFT inset of region vi in Figure 2c, obtained closer to the cubic c-$(Ti_{0.23},Al_{0.77})N$ layer, demonstrating coherent wurtzite and cubic $(Ti_{0.23},Al_{0.77})N$ regions. The FFT pattern in Figure 2d can be constructed by superposition of these structures as illustrated in Figure 2e. The epitaxial relationship between the two layers can, based on these overlaps, be determined as c-$(Ti_{0.23},Al_{0.77})N$ $(111)[1\bar{1}0]$ ||w-$(Ti_{0.23},Al_{0.77})N$ $(0001)[11\bar{2}0]$. The epitaxial wurtzite layer is about 100 nm thick. Beyond this thickness, two wurtzite regions are separated by a thin cubic phase (~3 nm), which is shown in Fig. 2b.iii. This cubic phase displays a larger orientation dispersion seen as arcs in the FFT pattern of the cubic phase. Figures 2b.ii and 2b.iv show HRTEM images with FFT pattern insets collected from different regions in the wurtzite layer displaying identical crystallographic orientation.

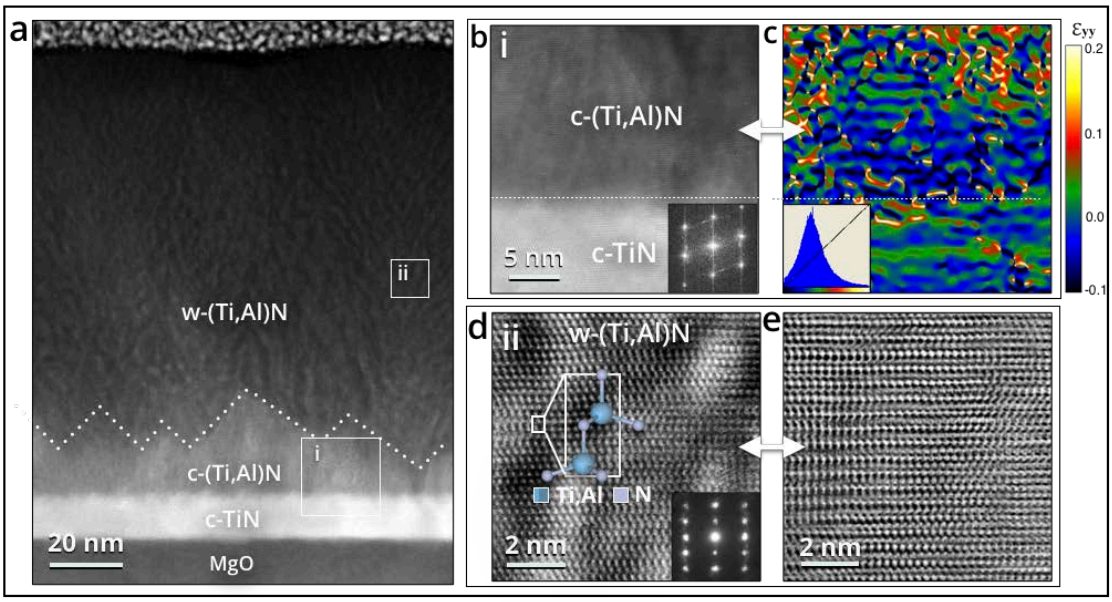

Figure 3. Cross-sectional (a) HAADF STEM, (b) higher magnification HAADF STEM with FFT inset of (i) lower region and buffer layer and (c) the corresponding deformation maps for ε_{yy} direction, and (d) higher magnification HAADF STEM with SAED inset inside the (ii) wurtzite layer and (e) the corresponding HAADF STEM of as-deposited $Ti_{0.23}Al_{0.77}N$/c-TiN film. The SAED pattern is collected from an area with a diameter of 100 nm.

Figure 3a shows the HAADF-STEM image of the mixed cubic and wurtzite phase $(Ti_{0.23},Al_{0.77})N$ with c-$(Ti_{0.23},Al_{0.77})N$ facets (marked) that defines the interface and onset of w-$(Ti_{0.23},Al_{0.77})N$. The magnified STEM image of the cubic region cubic region, the FFT pattern from the same region and the corresponding GPA strain map are shown in Figure 3b and Figure 3c, respectively. The strain concentration in the upper part of the cubic structure is higher as compared to the bottom part, i.e. there is a higher strain next to the wurtzite layer. Atomic resolution HAADF-STEM and bright field BF-STEM micrographs of as-deposited w-$(Ti_{0.23},Al_{0.77})N$ are shown in Figure 3d and Figure 3e, respectively. Based on the image contrast in Figure 3d, chemical segregation has occurred during growth and coherent domains with an average width of 1.4 ± 0.2 nm have formed in the wurtzite layer, which is not the case in the cubic layer below.

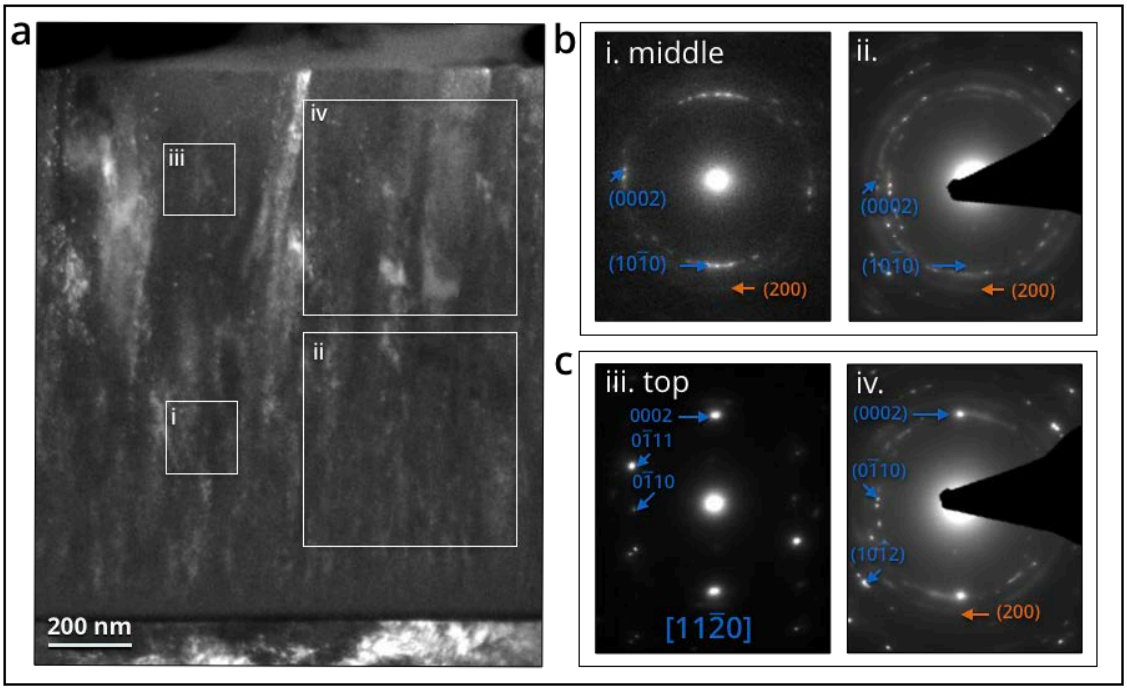

Figure 4. Cross-sectional (a) dark field TEM of as-deposited mixed cubic and wurtzite phase ($Ti_{0.23}$,$Al_{0.77}$)N film with 1000 nm thickness, (b) SAED patterns of (i) middle region and (ii) top region collected from an area with a diameter of 200 nm and SAED patterns of (iii) middle region (iv) top region collected from an area with a diameter of 700 nm.

Figure 4 shows the microstructure evolution when the growth of ($Ti_{0.23}$,$Al_{0.77}$)N is continued. Above the region described in Fig. 2 and 3, the film gradually becomes more columnar and the SAED shows ring patterns from both cubic and wurtzite structures (Figure 4b.i and Figure 4b.ii). In the top region, a columnar structure has developed with columns that are approximately 200 nm wide. In general, the film [0001] orientation parallel to the growth direction is maintained (Figure 4b.iii and Figure 4b.iv), which is in good agreement with the strong texture seen by XRD (Figure 1d). The SAED in Figure 4d.iv (recorded with a large aperture) of the top region shows distinct diffraction spots from the (0001) oriented wurtzite phase while the diffraction rings are seen from the cubic phase.

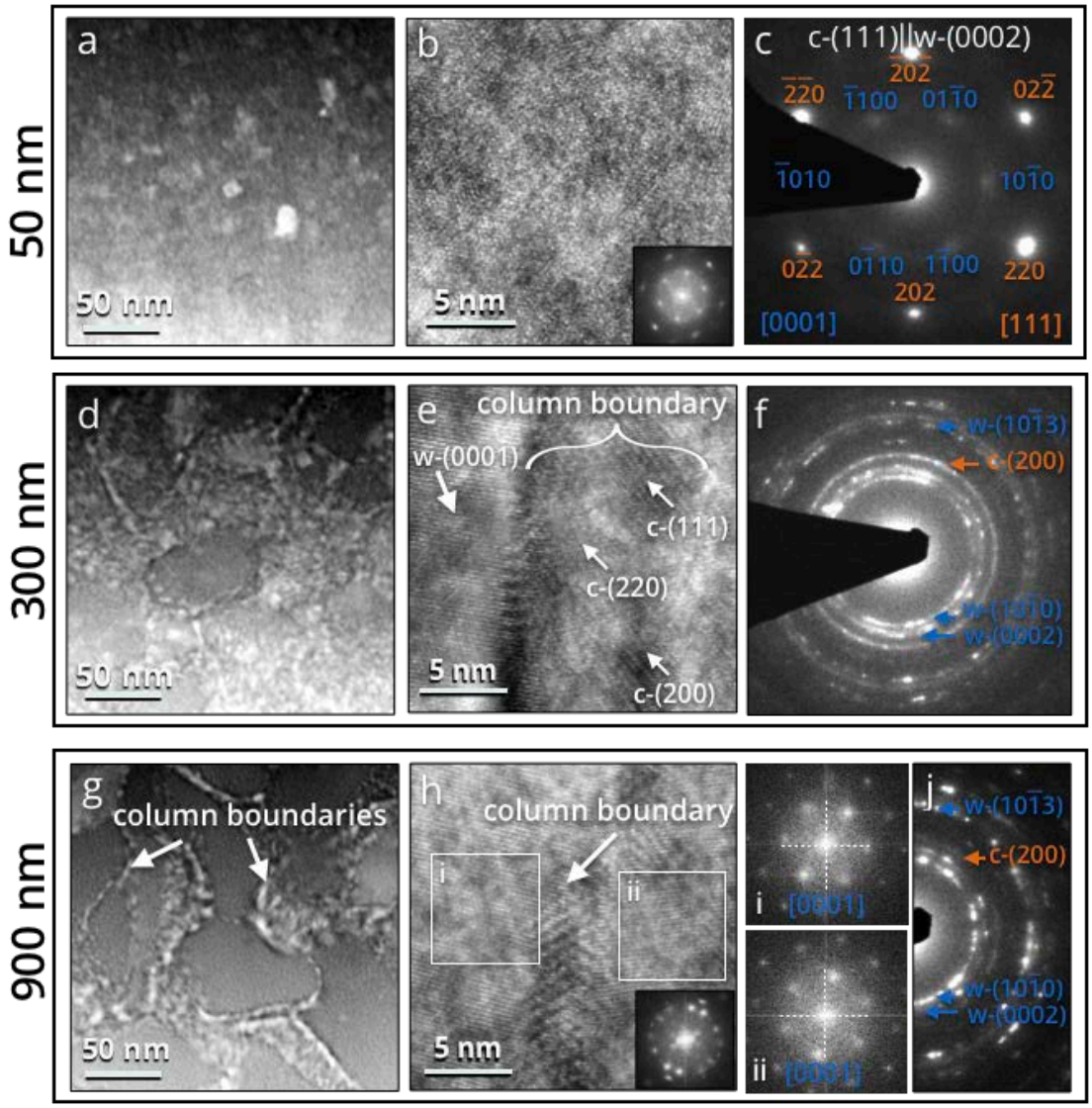

Figure 5. Plan-view (a) HAADF STEM, (b) high-resolution TEM with FFT inset, and (c) SAED images of bottom region (~50 nm from the buffer layer), (d) HAADF STEM, (e) high-resolution TEM, and (f) SAED images of middle region (~300 nm from the buffer layer), and (g) HAADF STEM, (h) high-resolution TEM with FFT inset, and (i) SAED images of top region (~900 nm from the buffer layer) of as-deposited mixed cubic and wurtzite phase $(Ti_{0.23},Al_{0.77})N$ film. The SAED patterns are collected from a circular area with a 200 nm diameter

The plan-view STEM, high resolution HR-TEM with FFT pattern insets, and SAED images of the mixed cubic and wurtzite phase ($Ti_{0.23}Al_{0.77}$)N film at three different depths (approximately 50 nm, 300 nm, and 900 nm above the substrate/film interface) are shown in Figure 5. The plan-view STEM images show that the size of the columns increases as the film grows (Figures 5d and 5g). The HRTEM with FFT inset (Figure 5b) and the SAED pattern of the bottom region (Figure 5c) confirms the coherent interface between cubic and wurtzite structures. In the middle region, HRTEM shows polycrystalline cubic grains in between the wurtzite columns (Figure 5e). The SAED pattern in Figure 5f reveals that the film becomes more polycrystalline in the sense that the [0001]-orientation displays a larger angular spread around the growth direction, which is consistent with the enlargement of the diffraction peak observed on the pole figures (cf. Figure 1). Most of these w-(Ti,Al)N columns are [0001]-oriented in the growth direction even in the top region, but slighted rotated with respect to each other in the growth plane, see FFTs of the HRTEM images in Figure 5h.

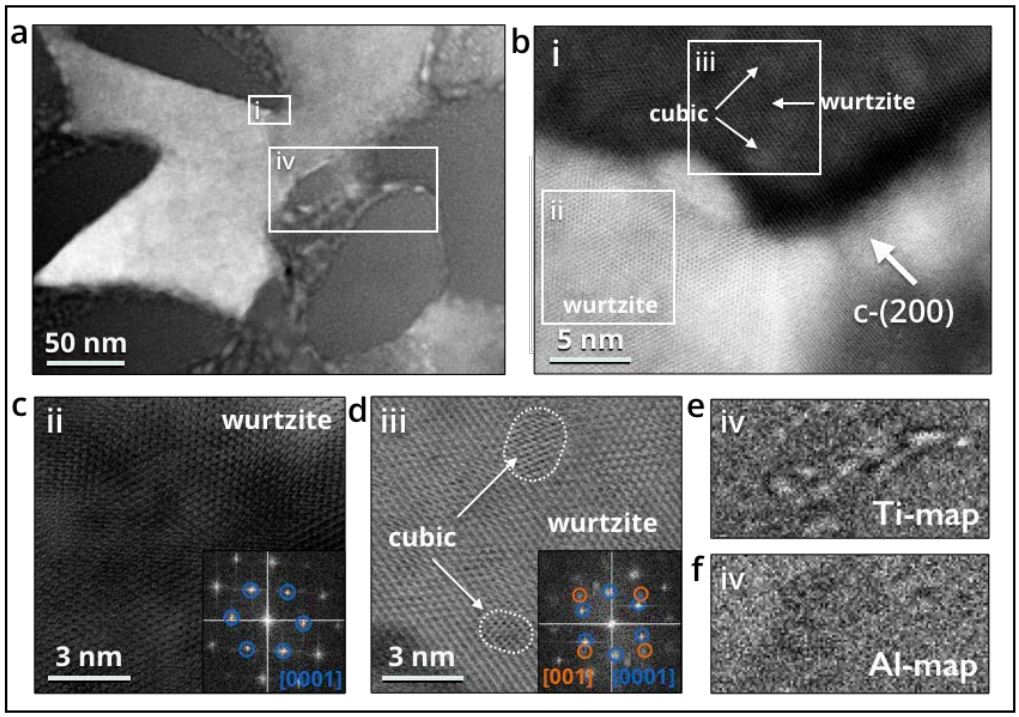

Figure 6. Plan-view (a) HAADF STEM image of top region of as-deposited mixed cubic and wurtzite phase ($Ti_{0.23}$,$Al_{0.77}$)N film with 1000 nm thickness, (b) high resolution HAADF STEM image of region i, (c) higher resolution BF STEM image of region ii with FFT inset, (d) higher resolution BF STEM image of region iii with FFT inset, and (e) Al-map and (f) Ti-map of region iv.

Figure 6a shows a plan-view STEM image of the mixed cubic and wurtzite phase $(Ti_{0.23}Al_{0.77})N$ film top region. The higher resolution HAADF STEM image of region i shows a thin cubic phase (~5 nm) separating the columns (Figure 6b). The cubic interface phase contains more Ti as indicated by the brighter contrast in the HAADF STEM images. There is also contrast variations inside the wurtzite columns due to the formation of nm sized domains (Figure 6b.ii and 6b.iii). In general, these domains are coherent with the same wurtzite crystal structure but in some cases coherent nm sized cubic domains are observed (Figure 6d), wherein the cubic domains contain more Ti as indicated by the brighter contrast in the HAADF STEM in Figure 6b.ii. The STEM-EDX maps in Fig. 6 (d-f) show that the cubic interface phase is enriched with Ti.

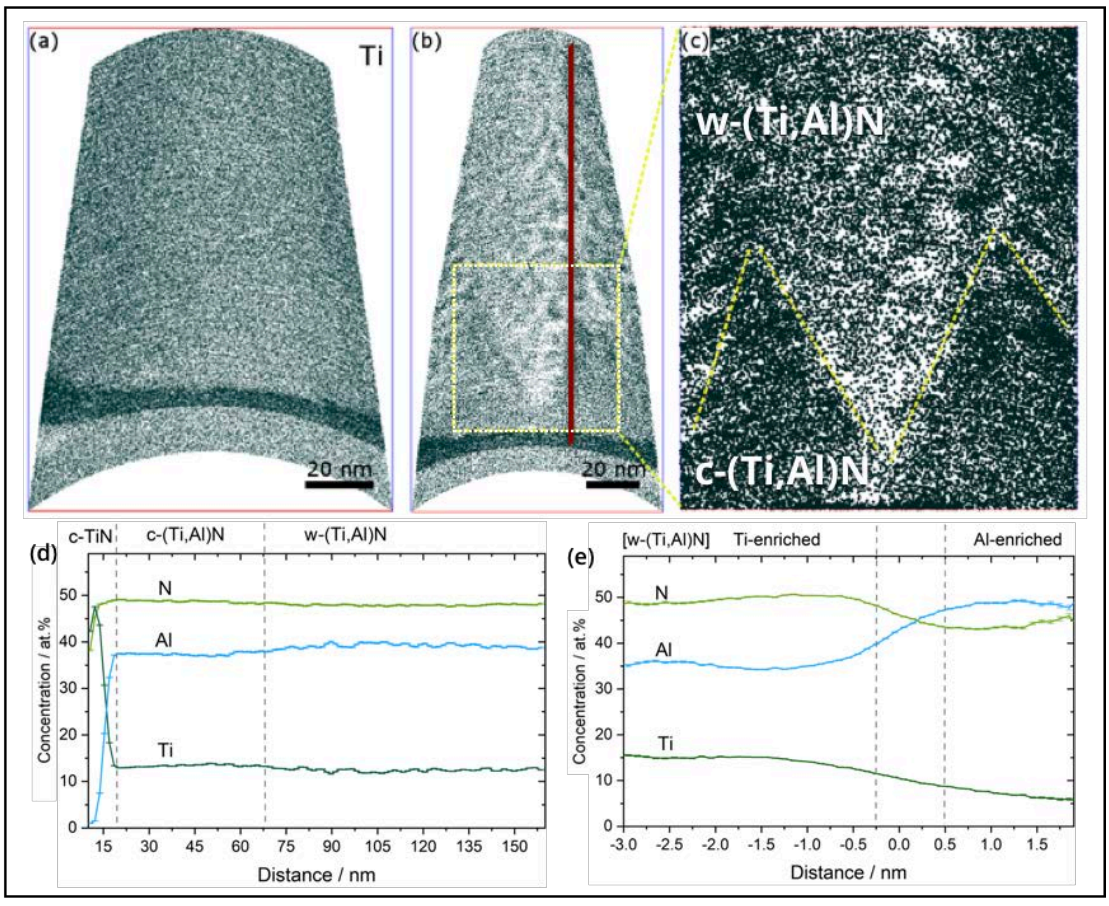

Figure 7. APT atomic maps showing a 5 nm slices through reconstructions [Ti(green)] of as-deposited (a) c-$(Ti_{0.37},Al_{0.63})N$ and (b) mixed cubic and wurtzite phase $(Ti_{0.23},Al_{0.77})N$ films with (c) a magnified image. (d) 1D concentration profile along the $(Ti_{0.23},Al_{0.77})N$ film. From left to right the c-TiN buffer layer and the concentration evolution of the film up to the surface can be observed. The profile was calculated in a 50x50x160 nm^3 region of interest. (e) Composition profile of the domains formed in $(Ti_{0.23},Al_{0.77})N$ (proximity histogram constructed on a 41 at.% Al iso-concentration surface).

Table 2. Chemical composition in the domains formed in mixed cubic and wurtzite phase ($Ti_{0.23}$,$Al_{0.77}$)N films.

	Ti-enriched domains	Al-enriched domains
Ti	15 ± 0.5	6.5 ± 0.6
Al	35 ± 0.6	49 ± 0.4
N	49 ± 0.4	44 ± 0.4
x = Al/(Al+N)	0.70	0.88

APT reconstructions of the epitaxial layers in c-($Ti_{0.37}$,$Al_{0.63}$)N and mixed cubic and wurtzite phase ($Ti_{0.23}$,$Al_{0.77}$)N films are shown in Figures 7a and 7b, respectively. The Ti and Al atoms in the mixed phase ($Ti_{0.23}Al_{0.77}$)N film have inhomogeneous spatial distribution while the c-($Ti_{0.37}$,$Al_{0.63}$)N film is chemically homogeneous. The formation of domains in the ($Ti_{0.23}Al_{0.77}$)N film is only observed in the wurtzite structure while the cubic layer in the bottom region is a homogeneous solid-solution (Figure 7c). This is seen as larger chemical fluctuations in the wurtzite layer compared to the cubic layer in the 1D concentration profile across the film (Figure 7d). The average N, Al, and Ti compositions of the ($Ti_{0.23}Al_{0.77}$)N film is similar all through its thickness. The composition profile of the domains formed in the w-(Ti,Al)N film is shown by a proximity histogram in Figure 7e. Table 2 shows the average chemical composition of the domains formed in mixed cubic and wurtzite phase ($Ti_{0.23}$,$Al_{0.77}$)N films. The domains are either Al-enriched or Ti-enriched in comparison to the overall alloy composition.

C. Thermal Stability of ($Ti_{1-x}Al_x$)N

Figure 8 shows STEM images and the corresponding FFT pattern insets of as-deposited and annealed at 900 °C of the mixed cubic and wurtzite phase ($Ti_{0.23}$,$Al_{0.77}$)N and c-($Ti_{0.37}$,$Al_{0.63}$)N epitaxial films. The wurtzite layer in the ($Ti_{0.23}$,$Al_{0.77}$)N film contains domains with an average width of 2.8 nm after annealing (Figure 8b), which is slightly larger than the domains in the as-deposited state (Figure 8a). The c-($Ti_{0.37}$,$Al_{0.63}$N/c-TiN film is homogeneous in the as-deposited state (Figure 8c) then it exhibits elongated c-AlN and c-TiN- rich domains along [001] directions with an average width of 4.1 nm caused by spinodal decomposition during annealing (Figure 8d). Annealing the films at higher temperatures than 900 °C results in diffusion of Mg from the substrate in to the films accompanied with a chemical reaction of Al and Mg to form spinel [36].

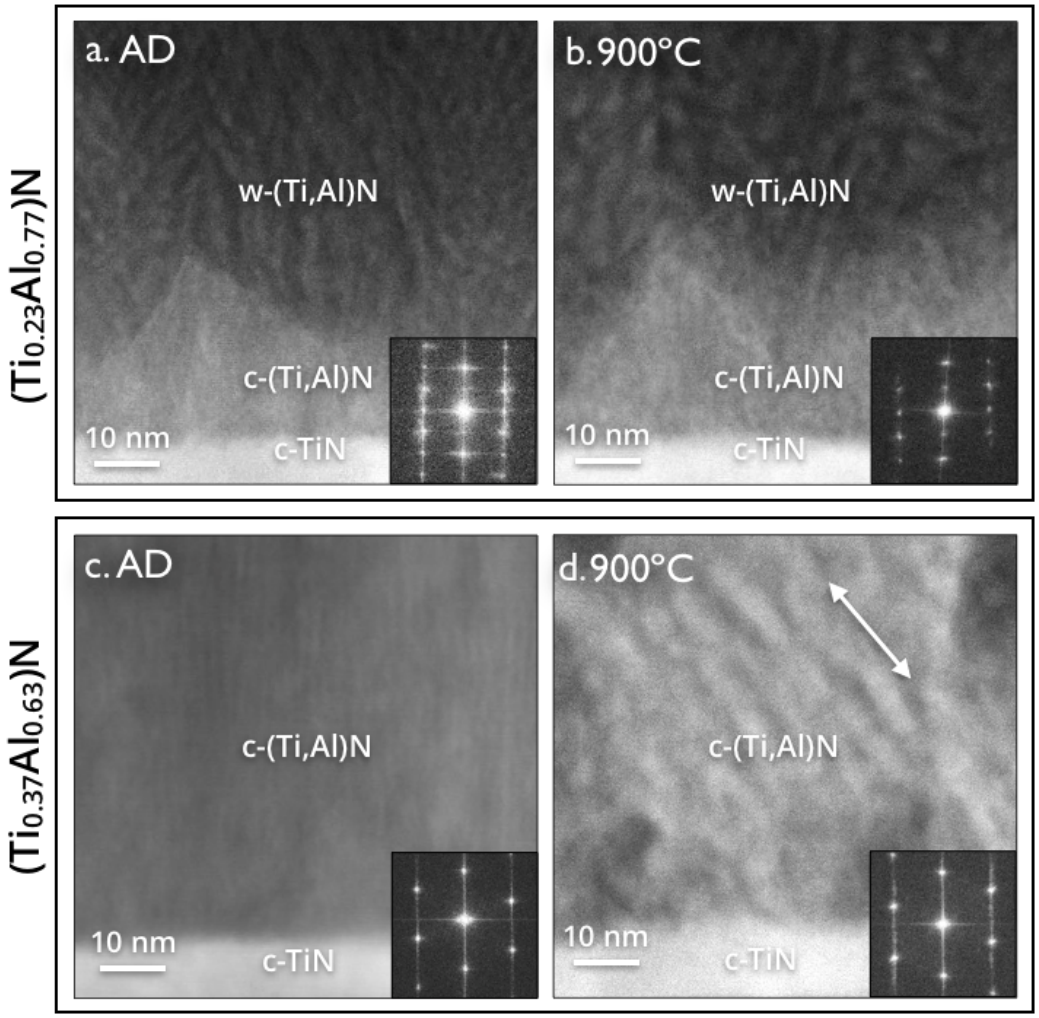

Figure 8. STEM with FFT pattern inset of (a) as-deposited and (b) annealed mixed c- and w-phase $(Ti_{0.23},Al_{0.77})N$ films with 150 nm thickness and STEM with FFT inset of (c) as-deposited and (d) annealed c-$(Ti_{0.37},Al_{0.63})N$ films with 150 nm thickness.

Figure 9 shows the plan-view STEM images of an annealed a mixed cubic and wurtzite phase $(Ti_{0.23},Al_{0.77})N$ film at three different distance from substrate (approximately 300 nm, 700 nm, and 900 nm above the substrate/film interface). Neither the dimensions nor the orientations of the columns have changed during annealing (Figures 9a-9c). It is possible that the aggregation of Ti to the interface phase in the column boundaries (Figures 9d-9f) is more pronounced. High-resolution STEM imaging within a column shows that the domains remain coherent during annealing (Figure 9g).

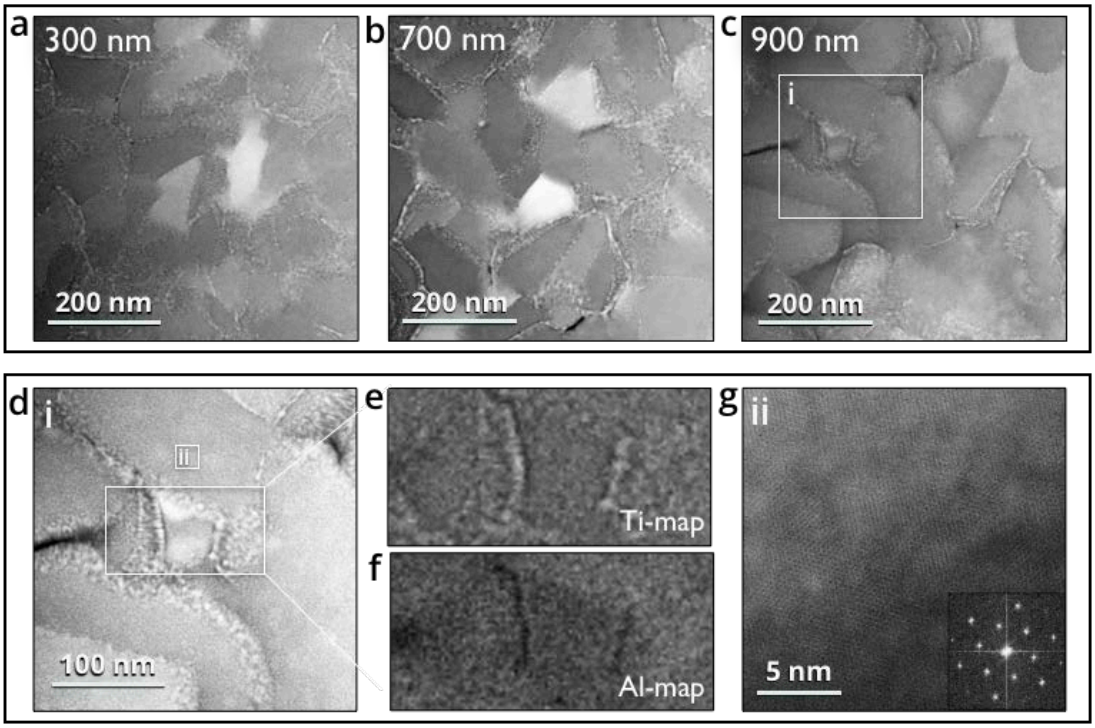

Figure 9. Plan-view HAADF STEM images of a mixed cubic and wurtzite phase $(Ti_{0.23},Al_{0.77})N$ film annealed at 900 °C at thicknesses from the film-substrate interface of approximately (a) 300, (b) 700, and (c) 900 nm and the (d) HAADF STEM image, corresponding EDX (e) Ti-map and (f) Al-map, and higher resolution HAADF STEM image with FFT inset of the top most region.

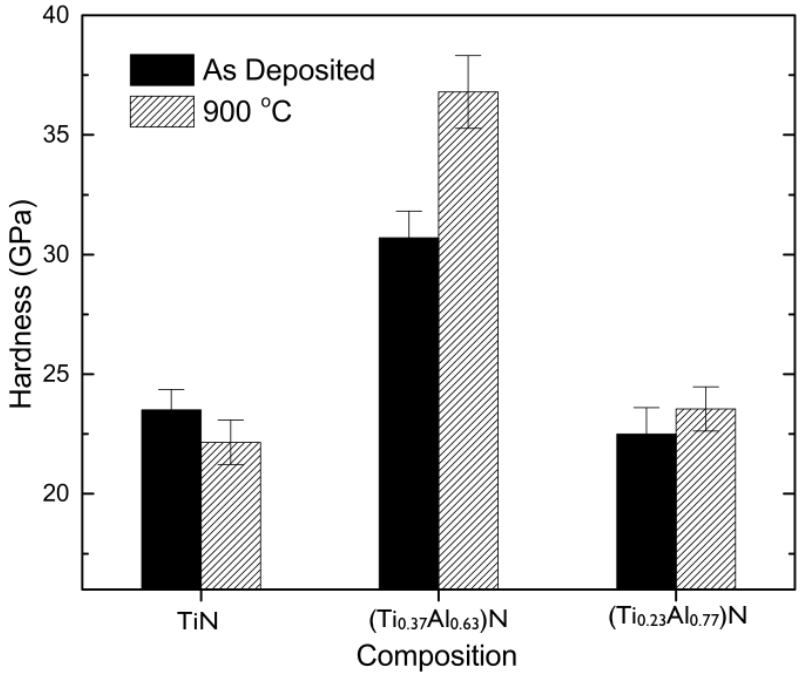

Figure 10. Hardness of as-deposited and annealed c-TiN, c-$(Ti_{0.37},Al_{0.63})N$, and mixed cubic and wurtzite phase $(Ti_{0.23},Al_{0.77})N$ films with approximately 1000 nm thickness.

The hardness values of the as-deposited and annealed pure TiN and (Ti_{1-x},Al_x)N (x = 0.63 and 0.77) thin films are shown in Figure 10. The c-($Ti_{0.37}$,$Al_{0.63}$)N film has the highest hardness among the films while c-TiN and mixed cubic and wurtzite phase ($Ti_{0.23}$,$Al_{0.77}$)N films have similar values. After annealing, the hardness of the spinodally decomposed c-($Ti_{0.37}$,$Al_{0.63}$)N film has increased while the hardness of the TiN film has decreased. There is a slight increase in hardness of the mixed phase ($Ti_{0.23}$,$Al_{0.77}$)N film after the heat treatment.

Discussion

The stabilization of thin c-($Ti_{0.23}$,$Al_{0.77}$)N(111) layer on the c-TiN(111) buffer layer is due to the epitaxial growth of the nitride film. A high growth temperature enhances the adatom surface mobility during nucleation, which promotes heteroepitaxy between the growing c-($Ti_{0.23}$,$Al_{0.77}$)N(111) layer and the c-TiN buffer layer [37]. Within the thin cubic layer, a high strain is observed as a consequence of lattice defects (dislocations and stacking faults) that tend to accumulate as the cubic film grows thicker. At a critical thickness of the c-($Ti_{0.23}$,$Al_{0.77}$)N layer, nucleation and growth of wurtzite w-($Ti_{0.23}$,$Al_{0.77}$)N occurs, coherently oriented with (0001) lattice planes parallel to c-($Ti_{0.23}$,$Al_{0.77}$)N(111).

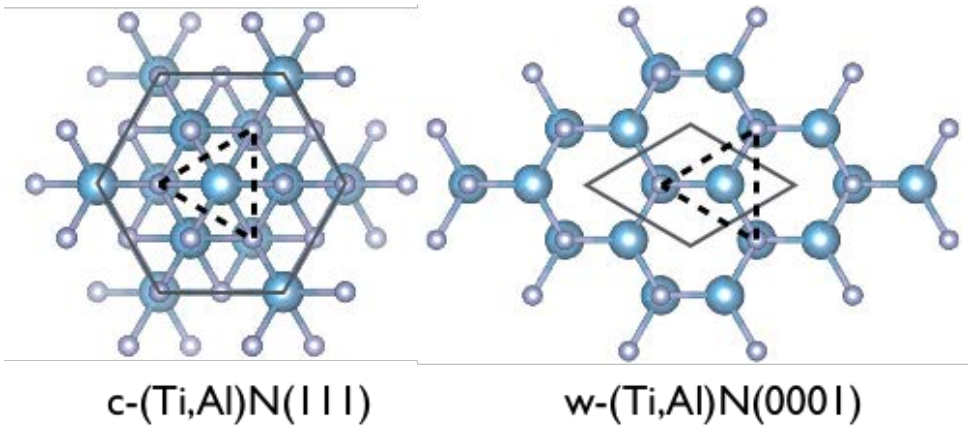

Figure 11. Fcc (left) and wurtzite (right) crystal structures projected along the directions c-[111] and w-[0001], respectively with the mutual orientation of c-(111)||w-(0002).

Figure 11 shows that the coherency relationship between the cubic and wurtzite layers is c-(111)||w-(0002, which indicates that their interfaces have the same crystallographic in-plane symmetry. The habitus planes c-(111)||w-(0002) can maintain the same symmetry since the inversion axis -3 along the c-[111] and the screw axis 6_3 along the w-[0001] has the same motif [38]. In this case, stacking faults

facilitate a direct transition from c-(Ti,Al)N to w-(Ti,Al)N. This transition has coherent interfaces with an orientation relationship of c-$(Ti_{0.23},Al_{0.77})N(111)[1\bar{1}0]$||w-$(Ti_{0.23},Al_{0.77})N(0001)[11\bar{2}0]$.

First-principles calculations show that the density of states and binding character of c-$(Ti_{1-x},Al_x)N$ alloys are dependent on the aluminum composition [39, 40]. When Al is added to the c-TiN system, the Ti 3d t_{2g} – Ti 3d t_{2g} next-nearest neighbor bonds are broken because Al lacks d-states that can participate in the bonding. This localizes the Ti 3d nonbonding states, which form a sharp unfavorable state at the Fermi level and consequently increases the tendency for phase separation in local environments where the aluminum content is high [39, 41]. A small segregation of Ti and Al on the cubic growth front could then be enough to initiate nucleation of the wurtzite phase by forming a stacking fault. The probability of locally forming an Al-concentration on the c-$(Ti_{1-x},Al_x)N$ crystal during growth is higher because Al have higher mobility as compared to Ti [5]. Once wurtzite nuclei have formed, they are expected to grow slightly faster along [0001] than the surrounding [111] oriented cubic phase because of its larger lattice parameter. This competitive growth results in v-shaped wurtzite regions that eventually merge to form a single-phase film with stacking faults and misfit dislocations present where the different parts of the crystal merge.

The formation of domains in the epitaxial w-$(Ti_{0.23},Al_{0.77})N$ layer occurs during growth. The domains have the same crystal structure but with different compositions (i.e., Al- or Ti-enriched domains). Their interfaces are coherent with a chemical gradient about 1 nm wide. Such domain formation does not occur during growth in the cubic layer below despite both layers having the same chemical composition. Phase separation during growth has also been observed in other material systems such as c-(Ti,Al)N [42] and w-(Zr,Al)N [16, 43] films. The phase separation occurring at the growth front of w-$(Ti_{0.23},Al_{0.77})N$ is driven by minimization of Gibb's free energy of this immiscible system and facilitated by surface diffusion. The fact that segregation occurs on w-$(Ti_{0.23},Al_{0.77})N(0001)$ surfaces and not on c-$(Ti_{0.23},Al_{0.77})N(111)$ surfaces suggests that the driving force for separation at this chemical composition is higher on the wurtzite surface than on the cubic surface at this chemical composition since surface diffusion is expected to be similar for both surfaces.

After a certain thickness, a coherent thin cubic interphase phase exists in between wurtzite columns, i.e. in the regions that carry a memory of merging different parts of the crystal in the form of crystallographic defects (misfit dislocations and stacking faults). These defects appear to aggregate Ti to an extent that trigger formation of a cubic phase. This cubic phase is coherent to the surrounding wurtzite and appears discontinuous in the beginning. As the film grows thicker, the thin cubic interface phase between the (0001)-oriented wurtzite-columns becomes continuous, wider and eventually displays a polycrystalline microstructure. This breakdown of the coherency between the cubic and wurtzite structures is likely triggered by a shift in growth mode from a 2D, layer-by-layer growth, to a 3D growth mode causing an undulating growth surface, i.e. the film structure resembles the transition Zone T in the structure zone model [44]. The generated throughs appear to cause sufficient segregation such that Ti-rich cubic crystals are nucleated.

During annealing, the coarsening of the domains in w-($Ti_{0.23}$,$Al_{0.77}$)N is driven by minimization of Gibbs energy and surface energy. The first causes purification of the domains while the second causes coalescence of domains to form larger ones [45]. Both these processes are driven by metal diffusion, which is enhanced at elevated temperature. However, the relative extent of coarsening in w-($Ti_{0.23}$,$Al_{0.77}$)N is less compared to size of domains formed by spinodal decomposition in c-($Ti_{0.37}$,$Al_{0.63}$)N during the same heat treatment. This indicates that the domains formed during growth through surface diffusion in w-($Ti_{0.23}$,$Al_{0.77}$)N are more stable against coarsening than c-($Ti_{0.37}$,$Al_{0.63}$)N when bulk diffusion is required.

When Al is added in the c-TiN material system to form c-(Ti_{1-x},Al_x)N, the hardness increases because of the solid-solution hardening mechanism [46] and the decrease in interatomic distance, which increases the covalent energy [47]. As Al is further increased, the w-AlN phase becomes dominant and the bonds become more directional. However, the average strength between the arrangements of atoms in the wurtzite structure is weaker [48]. This causes a lower hardness value of mixed cubic and wurtzite phase ($Ti_{0.23}$,$Al_{0.77}$)N film in its as-deposited state. At elevated temperature, the hardness of c-TiN decreases due to the annihilation of defects [49] while the hardness of c-($Ti_{0.37}$,$Al_{0.63}$)N film increases due to the coherency strains and elastic stiffness differences during decomposition, which obstruct dislocation motion and improve its resistance to plastic deformation [50, 51]. The slight increase in hardness of the ($Ti_{0.23}$,$Al_{0.77}$)N film stems from the same origins as the c-

($Ti_{0.37}$,$Al_{0.63}$)N film. However, in this case the increase is smaller since the domains are already present in the as-deposited sample and is the result of slightly more chemically purified domains. Such purification causes larger coherency strains and elastic stiffness differences.

Conclusions

Epitaxial wurtzite w-($Ti_{0.23}$,$Al_{0.77}$)N thin layers are grown on cubic c-($Ti_{0.23}$,$Al_{0.77}$)N with an epitaxial orientation relationship of c-($Ti_{0.23}$,$Al_{0.77}$)N(111)[1-10]||w-($Ti_{0.23}$,$Al_{0.77}$)N (0001)[11-20]. During growth, the w-($Ti_{0.23}$,$Al_{0.77}$)N segregates and forms coherent Al- and Ti-enriched nm-sized domains. These domains remain stable even after annealing at 900 ºC. The cubic c-($Ti_{0.23}$,$Al_{0.77}$)N layer does not phase segregate during growth but displays a spinodal decomposition when annealed.

As the films grow thicker, wurtzite columns are formed, separated by a Ti-rich cubic phase. The wurtzite columns retain a high degree of (0001) texture in the growth-direction. The w-($Ti_{0.23}$,$Al_{0.77}$)N films displays a hardness of 22 GPa that is slightly enhanced after annealing.

Acknowledgments

The work was financed by the European Union´s Erasmus Mundus doctoral program in Materials Science and Engineering (DocMASE), the Swedish Research Council (grant no 2017-03813), the Swedish government strategic research area grant AFM – SFO MatLiU (2009-00971) and VINNOVA (FunMat-II project grant no. 2016-05156). The authors thank Sylvie Migot for the TEM sample preparation and Jaafar Ghanbaja for the acquisition of TEM images.

References

[1] B.F. Coll, P. Sathrum, R. Fontana, J.P. Peyre, D. Duchateau, M. Benmalek. Optimization of arc evaporated (Ti,Al)N film composition for cutting tool applications, Surf. Coat. Technol. 52 (1992) 57-64.

[2] S. PalDey, S. Deevi. Single layer and multilayer wear resistant coatings of (Ti, Al) N: a review, Mater. Sci. Eng., A 342 (2003) 58-79.

[3] P. Jindal, A. Santhanam, U. Schleinkofer, A. Shuster. Performance of PVD TiN, TiCN, and TiAlN coated cemented carbide tools in turning, Int. J. Refract. Met. Hard Mater. 17 (1999) 163-170.

[4] R. Rachbauer, S. Massl, E. Stergar, D. Holec, D. Kiener, J. Keckes, J. Patscheider, M. Stiefel, H. Leitner, P. Mayrhofer. Decomposition pathways in age hardening of Ti-Al-N films, J. Appl. Phys. 110 (2011) 023515.

[5] L.J.S. Johnson, M. Thuvander, K. Stiller, M. Odén, L. Hultman. Spinodal decomposition of Ti0.33Al0.67N thin films studied by atom probe tomography, Thin Solid Films 520 (2012) 4362-4368.
[6] P.H. Mayrhofer, A. Hörling, L. Karlsson, J. Sjölén, T. Larsson, C. Mitterer, L. Hultman. Self-organized nanostructures in the Ti–Al–N system, Appl. Phys. Lett. 83 (2003) 2049-2051.
[7] A. Hörling, L. Hultman, M. Odén, J. Sjölén, L. Karlsson. Mechanical properties and machining performance of Ti1−xAlxN-coated cutting tools, Surf. Coat. Technol. 191 (2005) 384-392.
[8] A. Knutsson, J. Ullbrand, L. Rogström, N. Norrby, L. Johnson, L. Hultman, J. Almer, M.J. Jöesaar, B. Jansson, M. Odén. Microstructure evolution during the isostructural decomposition of TiAlN—A combined in-situ small angle x-ray scattering and phase field study, J. Appl. Phys. 113 (2013) 213518.
[9] N. Norrby, L. Rogström, M.P. Johansson-Jõesaar, N. Schell, M. Odén. In situ X-ray scattering study of the cubic to hexagonal transformation of AlN in Ti1−xAlxN, Acta Mater. 73 (2014) 205-214.
[10] Y. Taniyasu, M. Kasu, T. Makimoto. An aluminium nitride light-emitting diode with a wavelength of 210 nanometres, Nature 441 (2006) 325.
[11] N. Shulumba, Z. Raza, O. Hellman, E. Janzén, I.A. Abrikosov, M. Odén. Impact of anharmonic effects on the phase stability, thermal transport, and electronic properties of AlN, Phys. Rev. B 94 (2016) 104305.
[12] L. Rogström, N. Ghafoor, J. Schroeder, N. Schell, J. Birch, M. Ahlgren, M. Odén. Thermal stability of wurtzite Zr1− xAlxN coatings studied by in situ high-energy x-ray diffraction during annealing, J. Appl. Phys. 118 (2015) 035309.
[13] K. Yalamanchili, I.C. Schramm, E. Jiménez-Piqué, L. Rogström, F. Mücklich, M. Odén, N. Ghafoor. Tuning hardness and fracture resistance of ZrN/Zr0.63Al0.37N nanoscale multilayers by stress-induced transformation toughening, Acta Mater. 89 (2015) 22-31.
[14] D. Rafaja, M. Šíma, V. Klemm, G. Schreiber, D. Heger, L. Havela, R. Kužel. X-ray diffraction on nanocrystalline Ti1−xAlxN thin films, Journal of Alloys and Compounds 378 (2004) 107-111.
[15] L. Rogström, L.J.S. Johnson, M.P. Johansson, M. Ahlgren, L. Hultman, M. Odén. Age hardening in arc-evaporated ZrAlN thin films, Scripta Mater. 62 (2010) 739-741.
[16] N. Ghafoor, L.J. Johnson, D.O. Klenov, J. Demeulemeester, P. Desjardins, I. Petrov, L. Hultman, M. Odén. Nanolabyrinthine ZrAlN thin films by self-organization of interwoven single-crystal cubic and hexagonal phases, APL Materials 1 (2013) 022105.
[17] S.T. Oyama. Introduction to the chemistry of transition metal carbides and nitrides. The chemistry of transition metal carbides and nitrides. Springer, 1996. pp. 1-27.
[18] L. Brewer. A most striking confirmation of the Engel metallic correlation, Acta Metallurgica 15 (1967) 553-556.
[19] N. Engel. Copper, copper alloys and the electron concentration concept, Acta Metallurgica 15 (1967) 557-563.
[20] S. Uehara, T. Masamoto, A. Onodera, M. Ueno, O. Shimomura, K. Takemura. Equation of state of the rocksalt phase of III–V nitrides to 72 GPa or higher, Journal of Physics and Chemistry of Solids 58 (1997) 2093-2099.
[21] T. Sasaki, M. Akaishi, S. Yamaoka, Y. Fujiki, T. Oikawa. Simultaneous crystallization of diamond and cubic boron nitride from the graphite relative boron

carbide nitride (BC2N) under high pressure/high temperature conditions, Chemistry of Materials 5 (1993) 695-699.
[22] M. Garbrecht, L. Hultman, M. Fawey, T. Sands, B. Saha. Void-mediated coherency-strain relaxation and impediment of cubic-to-hexagonal transformation in epitaxial metastable metal/semiconductor TiN/Al0.72Sc0.28N multilayers, Physical Review Materials 1 (2017) 033402.
[23] A. Kimura, H. Hasegawa, K. Yamada, T. Suzuki. Effects of Al content on hardness, lattice parameter and microstructure of Ti1−xAlxN films, Surf. Coat. Technol. 120-121 (1999) 438-441.
[24] I. Tsutomu, S. Hiroshi. Phase formation and characterization of hard coatings in the Ti-Al-N system prepared by the cathodic arc ion plating method, Thin Solid Films 195 (1991) 99-110.
[25] Y. Pinot, M.H. Tuilier, M.J. Pac, C. Rousselot, D. Thiaudière, C. Ulhaq-Bouillet. Influence of film thickness on the structural transition cubic/hexagonal within Ti0.38Al0.62N films, Thin Solid Films 649 (2018) 160-166.
[26] A. Le Febvrier, L. Landälv, T. Liersch, D. Sandmark, P. Sandström, P. Eklund. System for magnetron sputtering in a ultra-high vacuum system for deposition of oxide, oxynitride, nitride, metallic thin films, Unpublished results.
[27] H. Ljungcrantz, M. Odén, L. Hultman, J. Greene, J.E. Sundgren. Nanoindentation studies of single‐crystal (001)‐,(011)‐, and (111)‐oriented TiN layers on MgO, J. Appl. Phys. 80 (1996) 6725-6733.
[28] S. Jeon, C.J. Van Tyne, H. Lee. Degradation of TiAlN coatings by the accelerated life test using pulsed laser ablation, Ceramics International 40 (2014) 8677-8685.
[29] A.S.M. Rao, K. Narender. Studies on Thermophysical Properties of CaO and MgO by -Ray Attenuation, Journal of Thermodynamics 2014 (2014) 8.
[30] A. Le Febvrier, J. Jensen, P. Eklund. Wet-cleaning of MgO (001): Modification of surface chemistry and effects on thin film growth investigated by x-ray photoelectron spectroscopy and time-of-flight secondary ion mass spectroscopy, J. Vac. Sci. Technol., A 35 (2017) 021407.
[31] K. Calamba, J. Pierson, S. Bruyère, A.l. Febvrier, P. Eklund, J. Barrirero, F. Mücklich, R. Boyd, M.P. Johansson Jõesaar, M. Odén. Dislocation structure and microstrain evolution during spinodal decomposition of reactive magnetron sputtered heteroepixatial c-(Ti0.36,Al0.64)N/c-TiN films grown on MgO(001) and (111) substrates, J. Appl. Phys. 125 (2019) 105301.
[32] H. Rösner, C.T. Koch, G. Wilde. Strain mapping along Al–Pb interfaces, Acta Mater. 58 (2010) 162-172.
[33] M.J. Hÿtch, E. Snoeck, R. Kilaas. Quantitative measurement of displacement and strain fields from HREM micrographs, Ultramicroscopy 74 (1998) 131-146.
[34] K. Thompson, D. Lawrence, D.J. Larson, J.D. Olson, T.F. Kelly, B. Gorman. In situ site-specific specimen preparation for atom probe tomography, Ultramicroscopy 107 (2007) 131-139.
[35] W.C. Oliver, G.M. Pharr. An improved technique for determining hardness and elastic modulus using load and displacement sensing indentation experiments, Journal of Materials Research 7 (2011) 1564-1583.
[36] A. McLeod, C. Gabryel. Kinetics of the growth of spinel, MgAl2O4, on alumina particulate in aluminum alloys containing magnesium, Metall. Trans. A 23 (1992) 1279-1283.

[37] J.E. Greene. Epitaxial crystal growth by sputter deposition: Applications to semiconductors. Part I, Critical Reviews in Solid State and Materials Sciences 11 (1983) 47-97.
[38] D. Rafaja, C. Wüstefeld, M. Dopita, M. Motylenko, C. Baehtz, C. Michotte, M. Kathrein. Crystallography of phase transitions in metastable titanium aluminium nitride nanocomposites, Surf. Coat. Technol. 257 (2014) 26-37.
[39] B. Alling, A.V. Ruban, A. Karimi, O.E. Peil, S.I. Simak, L. Hultman, I.A. Abrikosov. Mixing and decomposition thermodynamics of c-Ti1-xAlxN from first-principles calculations, Phys. Rev. B 75 (2007) 045123.
[40] B. Alling, A. Karimi, I.A. Abrikosov. Electronic origin of the isostructural decomposition in cubic M1−xAlxN (M=Ti, Cr, Sc, Hf): A first-principles study, Surf. Coat. Technol. 203 (2008) 883-886.
[41] F. Tasnádi, A.V. Lugovskoy, M. Odén, I.A. Abrikosov. Non-equilibrium vacancy formation energies in metastable alloys — A case study of Ti0.5Al0.5N, Materials & Design 114 (2017) 484-493.
[42] F. Adibi, I. Petrov, L. Hultman, U. Wahlström, T. Shimizu, D. McIntyre, J. Greene, J.E. Sundgren. Defect structure and phase transitions in epitaxial metastable cubic Ti0. 5Al0. 5N alloys grown on MgO (001) by ultra‐high‐vacuum magnetron sputter deposition, J. Appl. Phys. 69 (1991) 6437-6450.
[43] L.J.S. Johnson, N. Ghafoor, D. Engberg, M. Thuvander, K. Stiller, M. Odén, L. Hultman. Self-organized nanostructuring in Zr0.69Al0.31N thin films studied by atom probe tomography, Thin Solid Films 615 (2016) 233-238.
[44] P.B. Barna, M. Adamik. Fundamental structure forming phenomena of polycrystalline films and the structure zone models, Thin Solid Films 317 (1998) 27-33.
[45] M. Ohring. Materials science of thin films, Elsevier, 2001.
[46] R.L. Fleischer. Substitutional solution hardening, Acta Metallurgica 11 (1963) 203-209.
[47] M. Zhou, Y. Makino, M. Nose, K. Nogi. Phase transition and properties of Ti–Al–N thin films prepared by r.f.-plasma assisted magnetron sputtering, Thin Solid Films 339 (1999) 203-208.
[48] F. Tasnádi, I.A. Abrikosov, L. Rogström, J. Almer, M.P. Johansson, M. Odén. Significant elastic anisotropy in Ti1−xAlxN alloys, Appl. Phys. Lett. 97 (2010) 231902.
[49] I.A. Abrikosov, A. Knutsson, B. Alling, F. Tasnádi, H. Lind, L. Hultman, M. Odén. Phase stability and elasticity of TiAlN, Materials 4 (2011) 1599-1618.
[50] L. Rogström, J. Ullbrand, J. Almer, L. Hultman, B. Jansson, M. Odén. Strain evolution during spinodal decomposition of TiAlN thin films, Thin Solid Films 520 (2012) 5542-5549.
[51] N. Shulumba, O. Hellman, L. Rogström, Z. Raza, F. Tasnádi, I.A. Abrikosov, M. Odén. Temperature-dependent elastic properties of Ti1−xAlxN alloys, Appl. Phys. Lett. 107 (2015) 231901.

Paper 5

Effect of vacancies on the dislocation structure and phase stability of nitrogen deficient single crystal $(Ti_{1-x},Al_x)N_y$ thin films

K. Calamba, J. Salamania, M. Johansson Jõesaar, R. Boyd, J. Pierson, M. Sortica, D. Primetzhofer, and M. Odén

In manuscript

Effect of vacancies on the dislocation structure and thermal stability of nitrogen deficient single crystal $(Ti_{1-x},Al_x)N_y$ thin films

K.M. Calamba[1,2,a)], J. Salamania[1], M.P. Johansson Jõesaar[1,3], R. Boyd[1], S. Bruyère[2], J.F. Pierson[2], M.A. Sortica[4], D. Primetzhofer[4], and M. Odén[1]

[1]*Nanostructured Materials, Department of Physics, Chemistry and Biology (IFM), Linköping University, Linköping, SE-581 83, Sweden*
[2]*Université de Lorraine, CNRS, IJL, F-54000 Nancy, France*
[3]*SECO Tools AB, Fagersta, SE-737 82, Sweden*
[4]*Department of Physics and Astronomy, Uppsala University, Uppsala, SE-751 05, Sweden*

Abstract

The defect structures and phase stability of nitrogen deficient single crystal $(Ti_{1-x},Al_x)N_y$ were investigated. Epitaxial layers of c-$(Ti_{1-x}Al_x)N_y$ (y = 0.67, 0.79, and 0.92) are grown on MgO(111) and MgO(001) substrates by sputtering deposition. As the film grows thicker, unique features are observed in the y = 0.67 films, which have the highest N vacancy concentration. The c-$(Ti_{1-x}Al_x)N_{0.67}$ film on MgO(111) contains coherently oriented w-(0001) structures while the c-$(Ti_{1-x}Al_x)N_{0.67}$ film on MgO(001) contains conical features that have segregated during growth. In the as-deposited state, strain maps of the high resolution scanning transmission electron microscopy (STEM) images of epitaxial c-$(Ti_{1-x}Al_x)N_y$(111) films show that films with higher N vacancies contain more strain concentration. After annealing at 950 ºC, $(Ti_{1-x}Al_x)N_y$ films with different N contents exhibit spinodal decomposition, which resulted to an increase in strain fluctuation in the system. The coherency strain and dislocations generated during decomposition have resulted to an increase in hardness of the thin films. The coarsening rate of the epitaxial layers in c-$(Ti_{1-x}Al_x)N_y$ films increases with N content. After annealing at 1100 ºC, the domain sizes of the films grow larger and the strain concentration becomes lesser. At this temperature, the lower hardness values of y = 0.92 and 0.79 films is attributed to release of the strain during coarsening.

Introduction

Defect engineering of transition metal nitrides (TMN) has attracted special attention due to its capability to tune their electronic and thermodynamic properties [1]. Cubic $(Ti_{1-x},Al_x)N_y$ is a metastable material system that is widely used as protective coatings because of its oxidation resistance and ability to harden at elevated temperatures effect due to spinodal decomposition [2-4]. The isostructural spinodal decomposition results in formation of coherent TiN-rich and AlN-rich domains [5]. The domains have different lattice parameter [6] and elastic stiffness [7] that results in coherency strains which when combined effectively obstruct dislocation motion. How the decomposition can be affected and controlled have been investigated in terms of pressure [8, 9], alloying [10, 11], and multilayer structuring of the material [12]. The presence of point defects such as vacancies, interstitials, and anti-sites may alter the materials' functional properties. Based on the formation energy of defects in $(Ti_{1-x},Al_x)N_y$, *ab initio* calculations have shown that nitrogen substoichiometry ($y < 1$) and superstoichiometry ($y > 1$) is due to nitrogen vacancies and metal vacancies, respectively [13]. Metal vacancies result in faster decomposition of c-$(Ti_{1-x},Al_x)N_y$ because they enhance diffusivity [14, 15] while nitrogen vacancies delay the decomposition because they suppress the spinodal line to lower temperatures [16].

Recent study has shown a significant enhancement in the thermal stability of nitrogen deficient c-$(Ti_{0.54},Al_{0.46})N_{0.87}$ arc deposited coatings, wherein age hardening is extended to about 1100 °C, which is approximately 200 ºC higher than for stoichiometric coatings [17]. The age hardening ends when the decomposition proceeds by formation of wurtzite AlN. The delay in w-AlN formation also improves its crater wear resistance during metal machining because it suppresses diffusion of elements from the workpiece and the substrate into the coatings [18]. However, coatings grown by cathodic arc deposition contain varying density of macroparticles [19] and grain boundaries [20] that also influence their functional properties [21]. Such defects also prevent detailed microstructural studies. Growth of epitaxial films on single crystal substrates overcomes these obstacles and provides insight to growth mechanisms [22], detailed microstructural features [23, 24], deformation behavior [25, 26], and functional properties [27, 28]. Thus, synthesis of single crystal materials with tunable defect concentrations may provide fundamental and detailed information of the effect of nitrogen vacancies, such as microstrain evolution and thermal stability of $(Ti_{1-x},Al_x)N_y$ films.

In this study, (001)- and (111)- oriented epitaxial c-$(Ti_{1-x}Al_x)N_y$ ($y < 1$) thin films with different N concentration were grown using ultrahigh vacuum reactive magnetron sputtering deposition. Geometric phase analysis (GPA) on high resolution high-angle annular dark-field

STEM (HAADF-STEM) micrographs is used to gain local strain information. Differences in population of strain concentrations of films in their as-deposited state and during annealing at different temperatures and nitrogen content are observed and the role of nitrogen content on the defect structure, phase stability, and functional properties of epitaxial films is discussed.

Experimental

The c-$(Ti_{1-x}Al_x)N_y$ ($y < 1$) thin films were fabricated using an ultrahigh vacuum DC magnetron sputtering system with a base pressure of $< 4 \times 10^{-7}$ Pa. The deposition chamber used in this study is described in detail by le Febrier et al. [29]. The substrates used were MgO(001) and MgO(111) bulk crystals with >99.95 % purity, which were subjected to cleaning and annealing processes prior to the deposition [30, 31]. During the deposition, the substrates were held at 700 °C and are continuously rotated at 14 rpm. Pure Ti (99.9% purity) target was used for the deposition of buffer layers. A gas mixture of 30 sccm Ar and 10 sccm N_2 was used to synthesize the buffer layer to a thickness of 10 nm. $Ti_{0.35}Al_{0.65}$ alloy (99.9% purity) target was used for the deposition of the films. The distance between the substrates and the targets is ~140 mm. The argon flow was set to 30 sccm and the nitrogen flow was set to either 6, 8, or 10 sccm to synthesize films with different N contents. The DC supplied current was set to 0.2 A, resulting in a deposition rate of approximately 1.25 nm/min. The films were grown to ~150 nm thickness.

The thin films were subjected to post-deposition isothermal annealing using a tube furnace with a base pressure of $\sim 5 \times 10^{-4}$ Pa. The samples were heated at a rate of 20 °C/min up to maximum temperature of either 950 °C or 1100 °C and held for 120 min then cooled to room temperature at a rate of 20 °C/min.

X-ray diffractograms of the thin films were acquired using a PANalytical Empyrean diffractometer for crystal structure and growth orientation analysis. Symmetric and asymmetric reciprocal space maps (RSM) were recorded around MgO 111 and MgO 113, respectively. A channel-cut 2-bounce Ge(220) monochromator was used as the primary optics for the measurements. All measurements were performed using Cu Kα radiation. The equations used for the computation of the reciprocal lattice vectors, lattice constants, correlation length, and mosaic spread are described in detail by Calamba et al. [31].

Cross-sectional transmission electron microscope (TEM) samples were prepared through mechanical grinding and polishing, followed by Ar-ion etching using Gatan 691 precision ion polishing system and an *in situ* lift-out technique in a focused ion beam (FIB) - scanning electron microscope (SEM) dual beam system (Zeis Neon 40).

Morphological and microstructural information of the thin films were obtained using scanning electron microscopy (FEI Helios Nanolab 600) and aberration-corrected TEM (JEOL ARM 200F and FEI Titan^3). A geometric phase analysis (GPA) script [32] added to Gatan's Digital Micrograph was used for the strain map analysis of HAADF-STEM images.

The atomic compositions of the thin films were measured by Rutherford backscattering spectrometry (RBS) and time-of-flight elastic recoil detection analysis (TOF-ERDA). ERDA was used to obtain the elemental distributions while RBS was used to determine the stoichiometry and thickness of the films. Both techniques employ ion beams provided by the 5 MV 15SDH-2 tandem accelerator at the Tandem Laboratory at Uppsala University. ERDA experiments were performed with a 36 MeV $^{127}I^{8+}$ beam with a recoil angle of 45° and incident angle of 67.5° with respect to the surface normal. RBS experiments were performed with a 2 MeV $^4He^+$ beam with scattering angle of 170°. The incidence angle was 5° with respect to the surface normal and a wiggling algorithm was used during acquisition to perform series of random small angle tilts on the sample, in order to minimize channeling effects on the crystalline substrate.

The hardness values of the films were obtained using a nanoindentator (Hysitron Triboindenter Ti 950) with a standard Berkovich diamond tip. The area function of the tip was calibrated using a fused silica reference sample. The Oliver and Pharr method [33] was used to extract the values from the load-displacement curves and a minimum of 20 indents were made in each sample. The reported values are the average hardness and corresponding standard deviation.

Results

The chemical compositions of the $(Ti_{1-x}Al_x)N_y$ ($y < 1$) thin films that were synthesized using different N flow rates are shown in Table 1. The resulting N_2 partial fraction $f_{N2}=[N_2/(N_2+Ar)]$ for each flow rate is also listed in the table. Composition values of $x=[Al]/([Al]+[Ti])$ and $y=[N]/([Al]+[Ti])$ were obtained using ERDA/RBS. The films contain traces of the impurity elements C, H, and Ar. The sum of their concentration is less than 1.4 at. %. The films synthesized with N_2 partial fraction of 0.17, 0.21, and 0.25 have nitrogen content of $y = 0.67$, 0.79, and 0.92, respectively. There is an increase in N content of the film as the N_2 partial fraction is increased during the deposition.

Table 1. Atomic % composition using ERDA/RBS of the c-$(Ti_{1-x}Al_x)N_y$ thin films that were synthesized using different N flow rates.

Nitrogen flow	f_{N2}	Ti (at.%)	Al (at.%)	N (at.%)	$(Ti_{1-x},Al_x)N_y$
6 sccm	0.17	0.26	0.34	0.40	$(Ti_{0.43},Al_{0.57})N_{0.67}$
8 sccm	0.21	0.22	0.34	0.44	$(Ti_{0.39},Al_{0.61})N_{0.79}$
10 sccm	0.25	0.18	0.34	0.48	$(Ti_{0.35},Al_{0.65})N_{0.92}$

The morphologies of the as-deposited $(Ti_{1-x}Al_x)N_y$ thin films with average N concentration of y = 0.67, 0.79, and 0.92 are shown in Figure 1. Smoother surfaces are obtained when growing films with high N on MgO(001) substrates, while films grown on MgO(111) have a smooth appearance for all N contents. The $(Ti_{0.43},Al_{0.57})N_{0.67}$ film on MgO(001) has the roughest surface among samples.

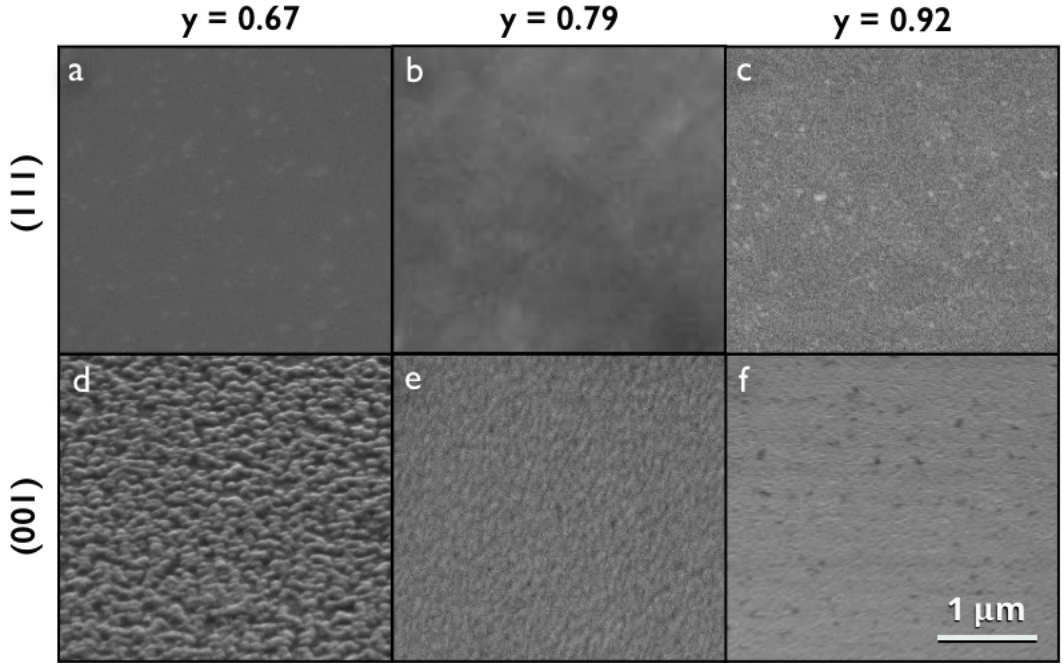

Figure 1. SEM micrographs of $(Ti_{1-x}Al_x)N_y$ (y < 1) thin films with average N concentration of (a) y = 0.67, (b) 0.79, and (c) 0.92 on MgO (111) and c-$(Ti_{1-x}Al_x)N_y$ (y < 1) thin films with average N concentration of (d) y = 0.67, (e) 0.79, and (f) 0.92 MgO (001) substrates.

Figure 2 shows the XRD θ-2θ diffractograms of as-deposited $(Ti_{1-x}Al_x)N_y$ (y < 1) films with an average N concentration of y = 0.67, 0.79, and 0.92 on MgO(111) and MgO(001) substrates. The $(Ti_{1-x}Al_x)N_y$ films with y = 0.79 and 0.92 on MgO(111) have a single peak corresponding to 111 of cubic NaCl (B1) structure, indicating single crystal films or films with a high degree of crystallographic texture. The diffractogram of y = 0.67 film on MgO(111) contains both a 111-peak from cubic (B1) and a 0001-peak from wurtzite (B4). All

the $(Ti_{1-x}Al_x)N_y$ films on MgO(001) have multiple peaks from cubic NaCl (B1) structure, which denote that the films contain multiple grains.

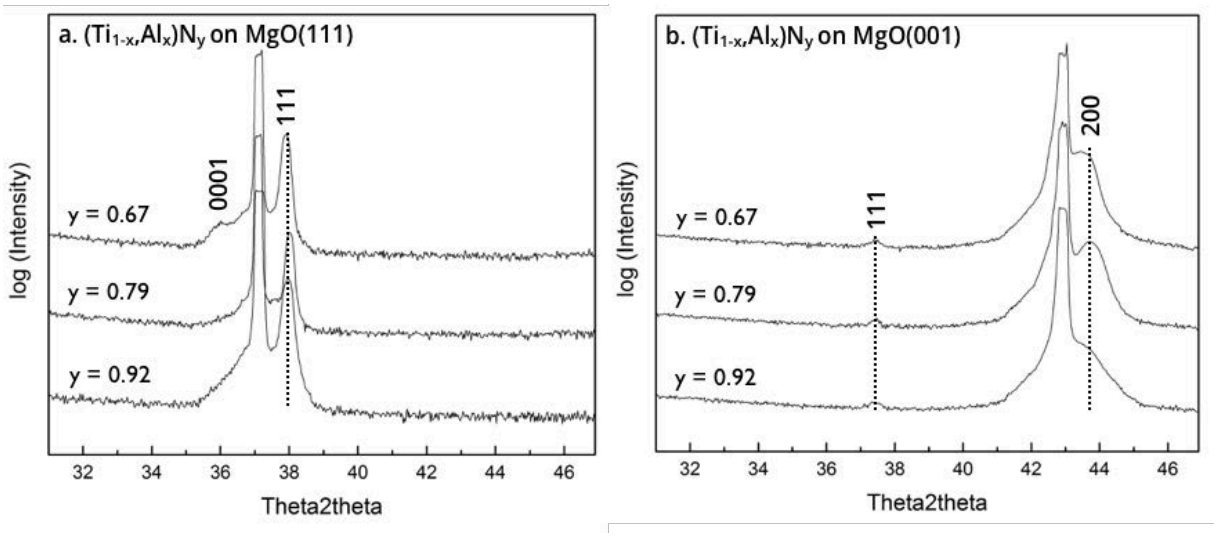

Figure 2. XRD diffractograms of c-$(Ti_{1-x}Al_x)N_y$ (y < 1) thin films on (a) MgO (111) and (b) MgO (001) substrates with different N contents.

Figure 3a shows the symmetric RSM of the as-deposited c-$(Ti_{1-x}Al_x)N_y$ thin films with average N concentration of y = 0.67, 0.79, and 0.92 on MgO(111) substrates. The films grown on MgO(001) substrates are not single crystals all through the film thickness thus RSM measurements are not applicable. The y = 0.67 sample has two distinct peaks (below and above the MgO substrate), which corresponds to the cubic and wurtzite structures that have different lattice distance. The y = 0.79 and y = 0.92 samples (Figure 3a) only have one distinct peak above the peak of the substrate, which indicates that they are primarily a solid solution of c-(Ti,Al)N with lower lattice parameter than the substrate. The unit-cell parameters of as-deposited y = 0.67, 0.79, and 0.92 films are *c* (out-of-plane, $a_\perp$) = 4.11 Å, 4.10 Å, and 4.11 Å, respectively and *a* (in-plane, $a_\parallel$) = 4.37 Å, 4.39 Å, and 4.38 Å, respectively. Asymmetric RSM maps of $(Ti_{1-x}Al_x)N_y(111)$ films show a distinct reciprocal lattice point vertically displaced with respect to the spot of the substrate, which indicates a strained epitaxial layer (Figure 4b). The slight broadening of the lattice points along the omega direction signifies the presence of mosaic spread within the films. The correlation length, mosaic spread, and FWHM of the as-deposited $(Ti,Al)N_y(111)$ films with different N contents based from the asymmetric RSM are presented in Table 2. The y = 0.79 film has the highest lateral correlation length and lowest mosaic spread and FWHM among samples, which signifies that it has the best crystal quality. The y = 0.67 sample contains peak from both the cubic and wurtzite structures, which could affect the asymmetric RSM measurements for lateral correlation length and mosaic spread.

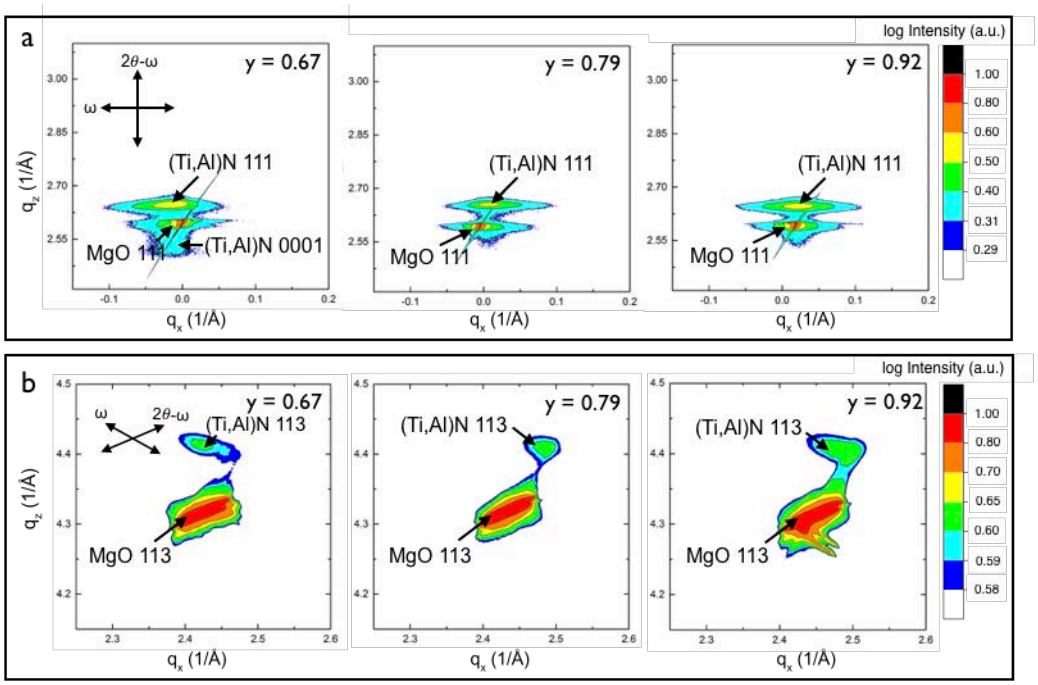

Figure 3. (a) Symmetric and (b) asymmetric RSM of as-deposited c-$(Ti_{1-x}Al_x)N_y$ thin films with average N concentration of y = 0.67, 0.79, and 0.92 on MgO(111) substrate.

Table 2. Measured correlation length, FWHM, and mosaic spread of the as-deposited (Ti,Al)Ny(111) films from the asymmetric RSM.

Nitrogen Content	Lateral Correlation Length (nm)	Mosaic Spread (˚)	FWHM (rlu)
y = 0.67*	991	0.737	0.008619
y = 0.79	1311	0.629	0.007308
y = 0.92	815	0.890	0.010453

**Contains both cubic and wurtzite peaks*

Cross sectional STEM and high resolution TEM images of as-deposited c-$(Ti_{1-x}Al_x)N_y$ thin films with average N concentration of y = 0.92, 0.79, and 0.67 on MgO(111) substrates are shown in Figure 4. All films display a single crystal film epitaxially grown on the TiN buffer layer and MgO-substrate. The SAED patterns (Figure 4a and 4b) and higher resolution TEM images (Figure 4d and 4e) of y = 0.92 and 0.79 films confirm that they are single crystals with cubic NaCl (B1) structure in 111 growth direction. In the case of y = 0.67 film some regions at the top of the film contain 0001 oriented wurtzite (B4) (Figures 4c and 4f). The SAED image of the film reveals that both structures are vertically aligned, which indicates a coherent interface. Higher resolution TEM shows that the interfaces of both structures has a relationship of c-$(Ti_{1-x},Al_x)N_{0.67}$(111)[1-10]||w-$(Ti_{1-x},Al_x)N_{0.67}$(0001)[11-20] (Figure 4f.iv).

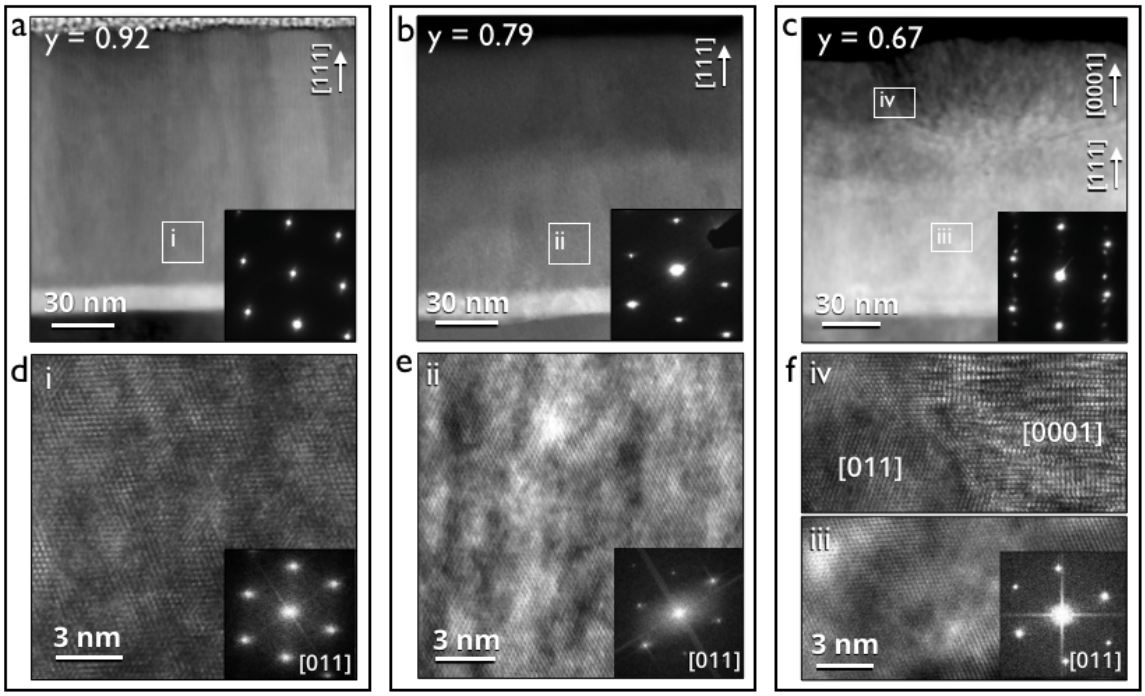

Figure 4. HAADF-STEM micrographs with SAED insets of as-deposited c-$(Ti_{1-x}Al_x)N_y$ thin films with (a) y = 0.92, (b) y = 0.79, and (c) y = 0.67 and HRTEM micrographs with FFT insets of as-deposited c-$(Ti_{1-x}Al_x)N_y$ thin films with (d) y = 0.92, (e) y = 0.79, and (f) y = 0.67 on MgO (111) substrates. The difference in image contrast in the STEM micrographs (darker for the upper region while brighter for the lower region) is due to the difference in the sample thickness.

Figure 5 shows HAADF-STEM images of epitaxial $(Ti_{1-x}Al_x)N_y$ thin films with average N concentration of y = 0.92, 0.79, and 0.67 on MgO(111) and MgO(001) substrates after annealing at 950 °C. FFT insets indicate that all films with different N concentration contain epitaxial regions, which are oriented either on 111 (Figure 5a to 5c) or 001 (Figure 5d to 5f) growth directions. $(Ti_{1-x}Al_x)N_y$(111) single crystals have Ti- and Al-rich domains that are elongated along the 001 direction (Figure 5a to 5c). The wurtzite structure of the y = 0.67 film on MgO(111) at the top region also contains elongated domains but on varying orientations (Figure 5c). Epitaxial c-$(Ti_{1-x}Al_x)N_y$(001) layers are not sustained through the film thickness (Figure 5d to 5f). The y = 0.92 sample has a single crystal layer up to 20 to 40 nm thickness (marked with zigzag lines in Figure 5d) then a transition to a polycrystalline layer occurs. This transition is also observed in stoichiometric c-$(Ti_{0.37},Al_{0.63})N$ film grown on MgO(001) [31]. The y = 0.79 sample has higher thickness of epitaxial layer up to 80 to 120 nm before the transition to polycrystalline (Figure 5e). The y = 0.67 sample contains epitaxial layer all through the film thickness however it also contains conical features in some regions of the film (Figure 5f). The epitaxial c-$(Ti_{1-x}Al_x)N_y$(001) layer with different N contents also have Ti- and Al-rich domains that are elongated along the 001 direction.

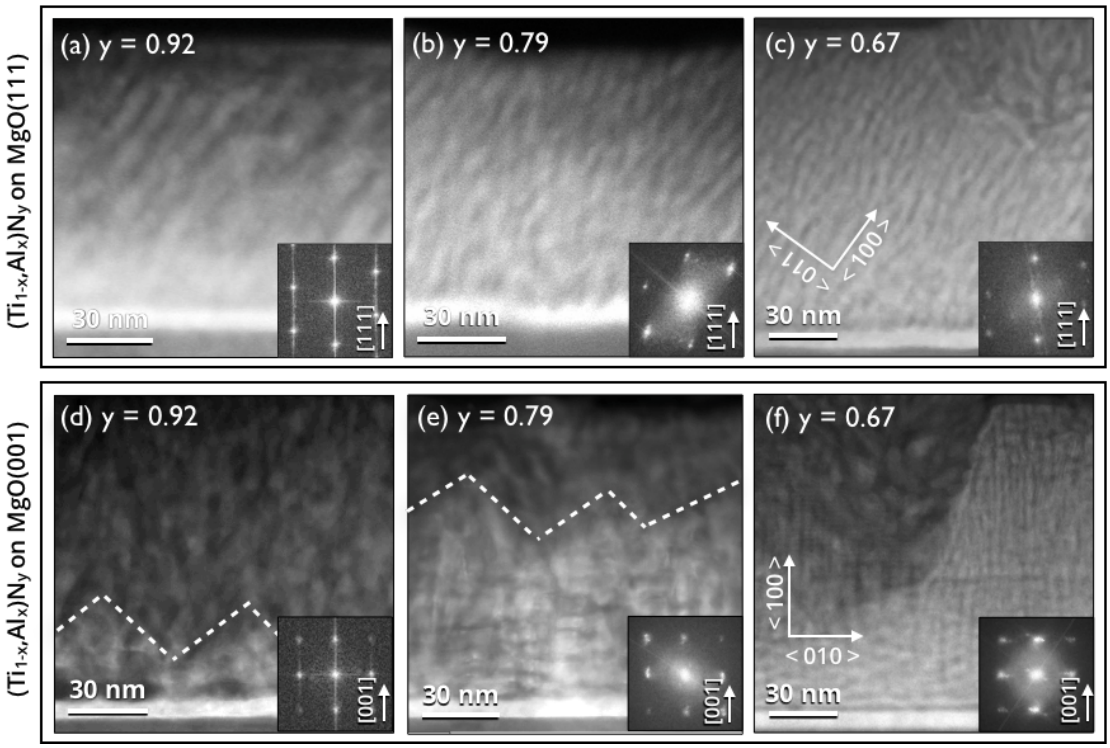

Figure 5. HAADF-STEM micrographs and FFTs of the epitaxial cubic regions of $(Ti_{1-x}Al_x)N_y$ (y < 1) thin films annealed at 950 °C with N concentration of (a) y = 0.92, (b) y = 0.79, and (c) y = 0.67 on MgO (111) substrates and (d) y = 0.92, (e) y = 0.79, and (f) y = 0.67on MgO(001) substrates.

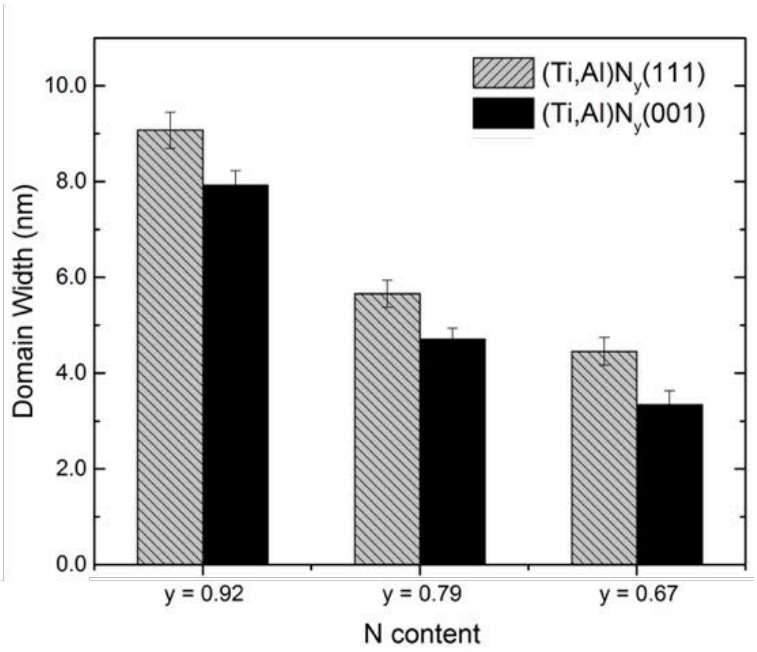

Figure 6. Domain width of (001)- and (111)- oriented c-$(Ti_{1-x}Al_x)N_y$ (y < 1) thin films annealed at 950 °C with y = 0.92, 0.79, and 0.67.

The width of domains in the epitaxial regions of the c-$(Ti_{1-x}Al_x)N_y$(111) and c-$(Ti_{1-x}Al_x)N_y$(001) films with average N concentration of y = 0.92, 0.79, and 0.67 after

annealing at 950 °C are shown in Figure 6. The domain size decreases with the N content of the film. The domains in (111)-oriented film are larger than in the (001)-oriented film due to a projection phenomenon.

GPA strain maps of epitaxial c-$(Ti_{1-x},Al_x)N_y$/c-TiN(111) thin films with y = 0.92, 0.79, and 0.67 are shown in Figures 7 to 9. The strain maps are deduced from high-resolution HAADF-STEM images with c-TiN buffer layer as the reference. All HAADF-STEM micrographs of c-$(Ti_{1-x},Al_x)N_y$ with different N contents display a coherent interface to the buffer layer and have composition fluctuations. In the as-deposited cases the compositional fluctuations are small and perpendicular to the growth direction while the heat treatments introduce stronger chemical fluctuations with domains elongated along [100]-directions.

Figure 7a shows the strain maps (in-plane ε_{xx} and out-of-plane ε_{yy}) of the as-deposited y = 0.92 film. The maps show a film with homogenous low strain and one strain concentration in the upper right corner. After annealing at 950 °C (Figure 7b), the film has decomposed with domains larger than the y = 0.67 and 0.79. The strain is greater with a substantially higher number of strain concentrations compared to the as-deposited state. Al-rich domains are generally in compression while Ti-rich ones are in tension, which is caused by the difference in unit cell volume. The location of the strain concentrations is at the interface between the Ti-rich and Al-rich domains and inside the Ti-rich domains. Previous work has shown that such strain concentrations are associated with dislocations [31]. The inset histogram of the annealed film is broader than that of the as-deposited film, which indicates that strain fluctuation is higher after decomposition. Annealing at 1100 °C, results in a decrease in the number of dislocations as the domain size increases (Figure 7c). Similar trends are consistently observed in the films with lower N contents (Figures 8 and 9). The small circles in the STEM image are Pt particles, which are artifact from the TEM sample preparation via FIB. These particles do not affect the strain map analysis because GPA only accounts the strain derived from the diffraction spots of the film. At 1100 °C, the STEM image of y = 0.92 film (Figure 7c) shows indications of formation of subcrystals slighted tilted with respect to each other. This is also indicated in the FFT inset of the STEM image, which reveals an overlap of two patterns of the same crystal structure.

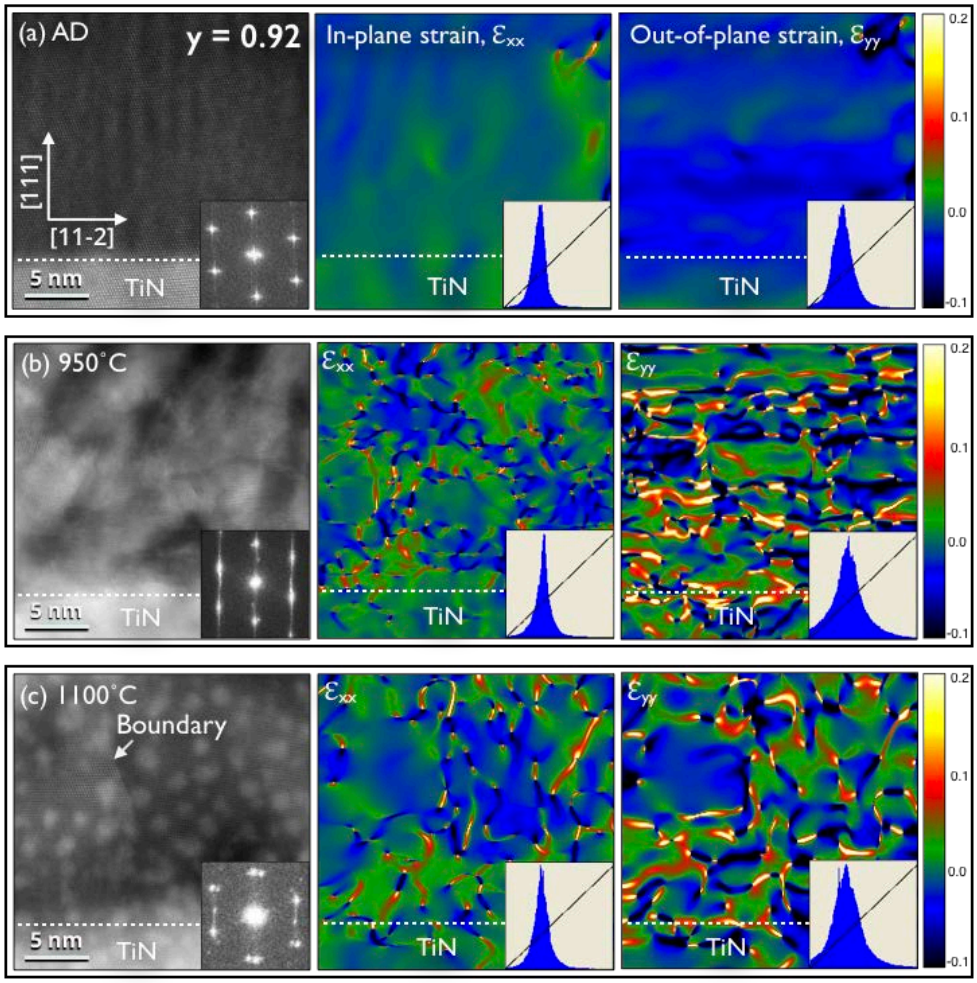

Figure 7. High-resolution HAADF-STEM with FFT inset and the corresponding deformation maps for ε_{xx} (in-plane strain) and ε_{yy} (out-of-plane strain) of (a) as-deposited, (b) annealed at 950 °C, and (c) annealed at 1100 °C c-$(Ti_{1-x},Al_x)N_y$/c-TiN(111) thin film with y = 0.92. The inset histograms represent the distribution of strain values in each map. The STEM image in (c) was recorded from a sample prepared by FIB and contains round nm-sized Pt surface contaminations that appear as dots. These Pt-dots do not affect the strain maps.

The ε_{xx} and ε_{yy} strain maps of as-deposited c-$(Ti_{1-x},Al_x)N_y$ thin film with y = 0.79 are shown in Figure 8a. The strain maps of y = 0.79 film are uniform and similar to y = 0.92. At 950 °C, the film has decomposed to form c-TiN- and c-AlN -rich domains, which cause strain fluctuation in film (Figure 8b). Similar to y = 0.92, most dislocations are observed near the interface of the domains. However, the number of strain concentrations after annealing y = 0.79 is lower compared to y = 0.92 annealed at the same temperature. At 1100 °C, the domains have grown, which has resulted in fewer strain concentration (Figure 8c).

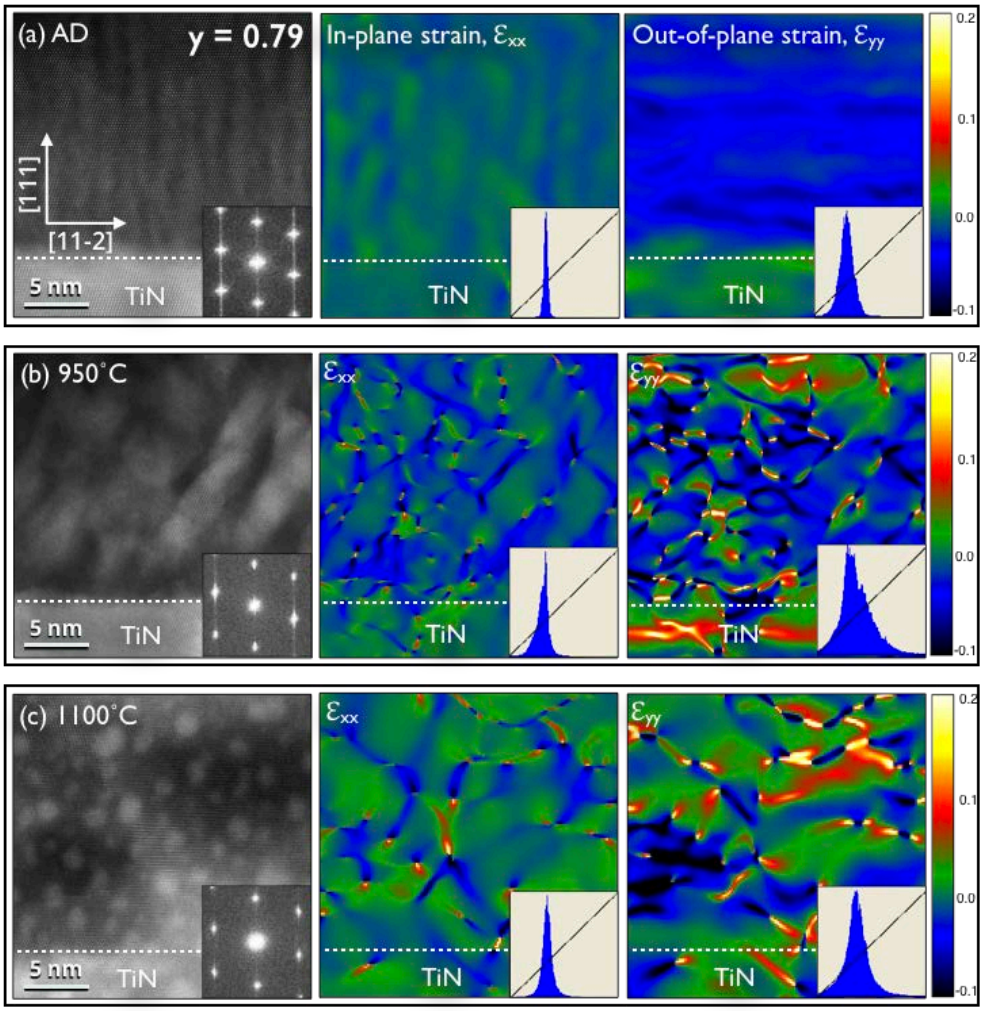

Figure 8. High-resolution HAADF-STEM with FFT inset and the corresponding deformation maps for ε_{xx} (in-plane strain) and ε_{yy} (out-of-plane strain) of (a) as-deposited, (b) annealed at 950 °C, and (c) annealed at 1100 °C c-$(Ti_{1-x},Al_x)N_y$/c-TiN(111) thin film with y = 0.79. The inset histograms represent the distribution of strain values in each map. The STEM image in (c) was recorded from a sample prepared by FIB and contains round nm-sized Pt surface contaminations that appear as dots. These Pt-dots do not affect the strain maps.

Figure 9 shows STEM and strain maps of c-$(Ti_{1-x},Al_x)N_y$(111) with y = 0.67. Figure 9a shows a film with low strain that contains some strain concentrations. Similar to samples y = 0.92 and y = 0.79, annealing at 950 °C results in an increase of the number of dislocations (Figure 9b), which then decreases slightly when the annealing temperature is increased to 1100 °C (Figure 9c).

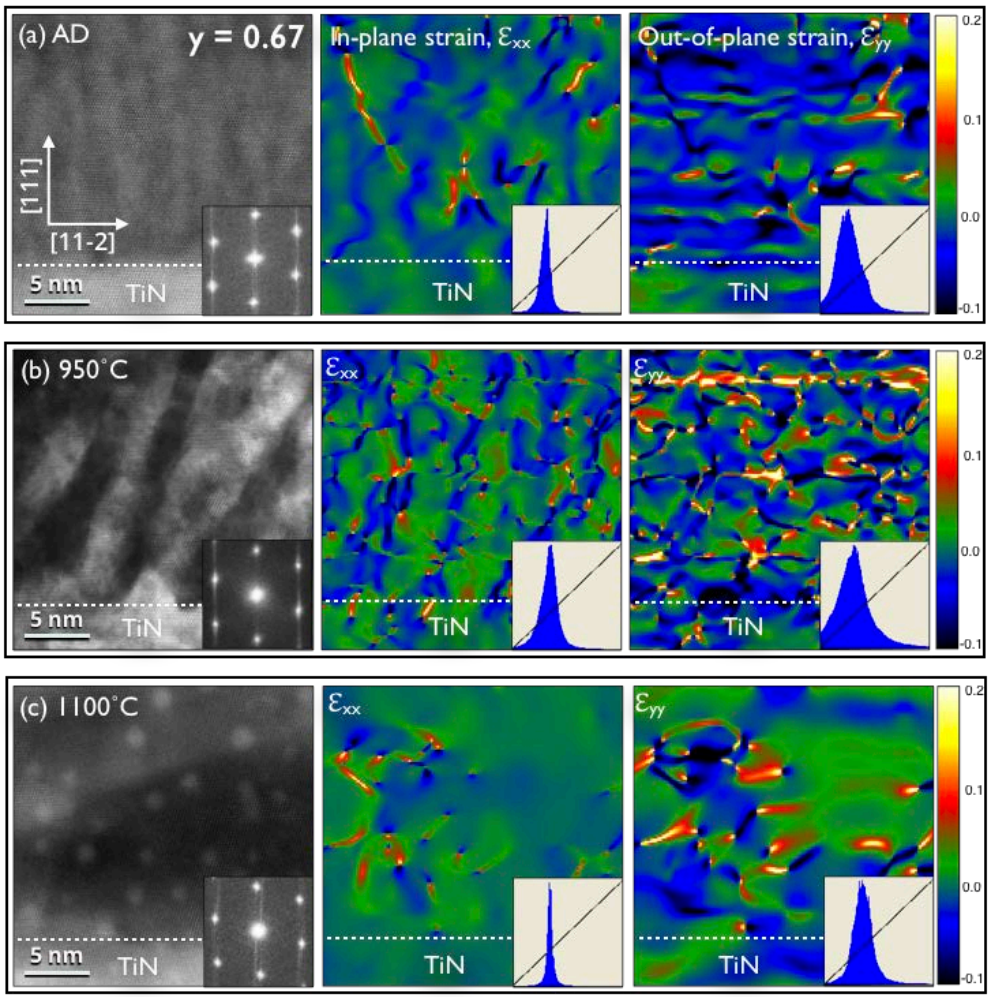

Figure 9. High-resolution HAADF-STEM with FFT inset and the corresponding deformation maps for ε_{xx} (in-plane strain) and ε_{yy} (out-of-plane strain) of (a) as-deposited, (b) annealed at 950 °C, and (c) annealed at 1100 °C c-$(Ti_{1-x},Al_x)N_y$/c-TiN(111) thin film with y = 0.67. The inset histograms represent the distribution of strain values in each map. The STEM image in (c) was recorded from a sample prepared by FIB and contains round nm-sized Pt surface contaminations that appear as dots. These Pt-dots do not affect the strain maps.

Figure 10 shows the HAADF-STEM images of as-deposited $(Ti_{0.43},Al_{0.57})N_{0.67}$ thin film on MgO(001) substrate and when annealed at 950 °C and 1100 °C. In the as-deposited state, epitaxial layer contains small compositional fluctuations perpendicular to the growth direction (Figure 10a and 10b), which is also observed in epitaxial $(Ti_{0.43},Al_{0.57})N_{0.67}$(111) films. The domains in the epitaxial layer grow in size after annealing temperature at 950 °C (Figure 10c and 10d) and continue to grow at 1100 °C (Figure 10c and 10f). The FFT insets of the high-resolution images (Figure 10d and 10f) reveal that the epitaxial $(Ti_{0.43},Al_{0.57})N_{0.67}$ layers remain cubic single crystals. In the as deposited state, the conical features contain Ti- and Al-rich domains, which are larger than the epitaxial layer (Figure 10a). The size of the domains inside the conical features is similar after annealing at 950 °C (Figure 10c) and has

slightly grown at 1100 °C (Figure 10e). At 1100 °C, the domains inside the conical features are smaller than the segregated domains in the epitaxial layer.

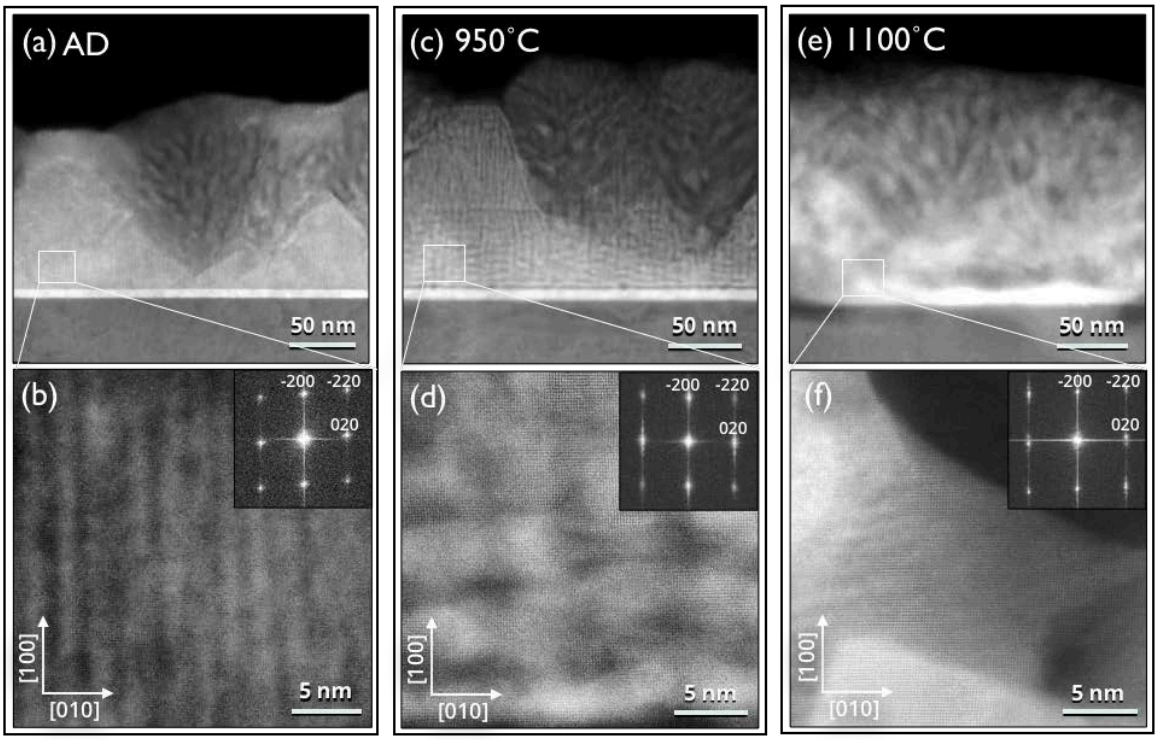

Figure 10. HAADF-STEM and higher resolution HAADF-STEM micrographs with FFT inset of (a, b) as-deposited c-$(Ti_{1-x}Al_x)N_{0.67}$(001) and c-$(Ti_{0.43}Al_{0.57})N_{0.67}$(001) annealed (c, d) at 950 °C and (e, f) 1100 °C.

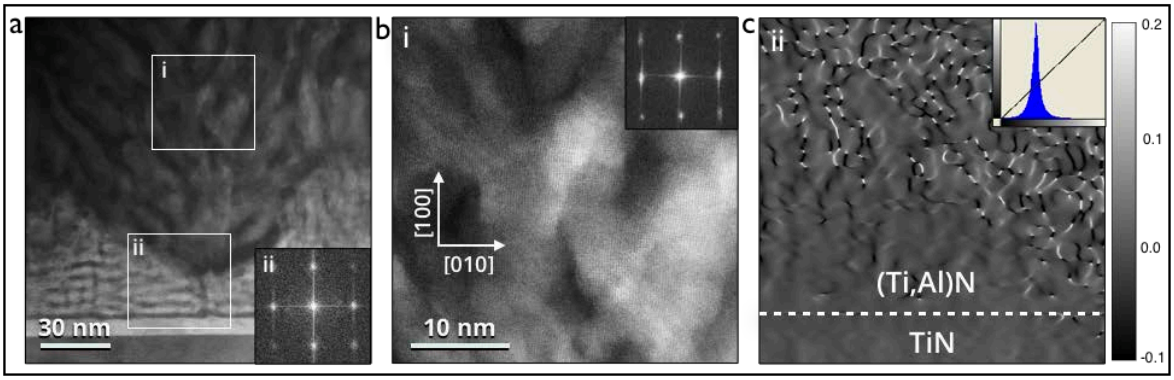

Figure 11. (a) HAADF-STEM micrograph with FFT inset, (b) higher magnification HAADF-STEM with FFT inset, and (c) strain map c-$(Ti_{0.43}Al_{0.57})N_{0.67}$(001) annealed at 950 °C.

The HAADF-STEM images and the corresponding strain map of the $(Ti_{0.43},Al_{0.57})N_{0.67}$ thin film on MgO(001) substrate annealed at 950 °C are shown in Figure 11. The Ti- and Al-rich domains inside the conical feature (Figure 11a) are also elongated but on varying directions. Figure 11a.ii shows the coherency between the conical feature and the epitaxial layer. The FFT inset of the high resolution HAADF-STEM image inside the cone reveals that

this region is cubic oriented along the 001 direction (Figure 11b). The strain map shows that there is a high strain concentration in the region near the conical feature as well as inside it (Figure 11c).

The hardness as a function of temperature of c-$(Ti_{1-x}Al_x)N_y$ thin films with average N concentration of y = 0.67, 0.79, and 0.92 on MgO(111) and MgO(001) substrates are shown in Figure 12a and Figure 12b, respectively. The hardness values of the films on both substrates show similar trends. In the as-deposited state, the hardness increases with the N content of the thin films. After annealing at 950 °C, all samples have increased their hardness because of the formation of coherent domains via spinodal decomposition. Further annealing at 1100 °C has caused a harness drop for the 0.92 and 0.79 samples while an increase in hardness is observed for the 0.67 samples. The c-$(Ti_{1-x}Al_x)N_y$ thin films on MgO(111) has slightly higher hardness than thin films on MgO(111) at all temperatures.

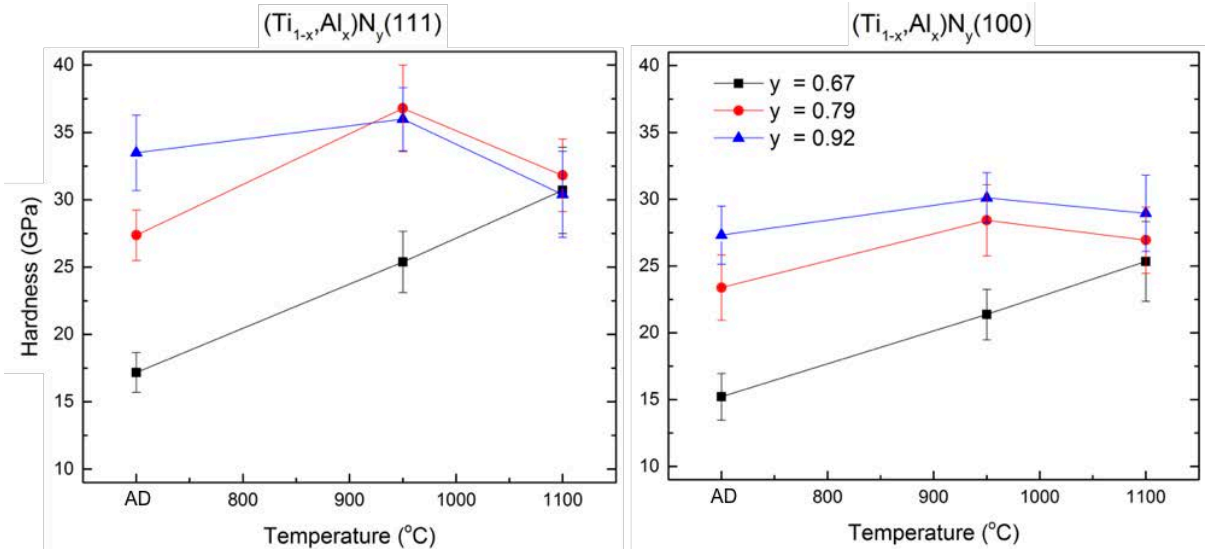

Figure 12. Hardness values of as-deposited and annealed $(Ti_{1-x}Al_x)N_y$ (y < 1) thin films on (a) MgO(001) and (b) MgO(111) substrates.

Discussion

The $(Ti_{1-x}Al_x)N_y$ (y = 0.67, 0.79, and 0.92) films on MgO(001) and MgO(111) substrates with TiN buffer layers grow epitaxially to form a single crystal next to the substrate-film interface. The epitaxial growth is promoted by high surface diffusion, which was obtained by using a high substrate temperature used during the depositions [34]. For longer deposition times, the growth mode of these films may change and this change depends on the crystal orientation and N concentration.

Epitaxial $(Ti_{1-x}Al_x)N_y$(111) thin films on MgO(111) are sustained all through the film thickness (150 nm) and the higher crystal quality of y = 0.79 film than y = 0.92 is attributed to

the higher surface mobility of metal adatoms during growth in low N conditions [35]. Epitaxial c-$(Ti_{1-x}Al_x)N_y(111)$ with y = 0.67 has transitioned to w-$(Ti_{1-x}Al_x)N_y(0001)$ phase as the film grows thicker. This transition has also been observed for $(Ti_{1-x}Al_x)N_y$ films with high Al content, wherein the nucleation of wurtzite phase is initiated by the small segregation of Ti and Al on the cubic growth front [36]. For c-(Ti,Al)N films with high N vacancies, N atoms prefers to stick to Al [37] and in such case there is a higher tendency to form a wurtzite nuclei. The cubic to wurtzite phase transition also occurs in other ternary material systems containing vacancies, wherein ordered vacancies form and such system energetically favors the hexagonal phase formation in comparison to cubic [38, 39].

The epitaxial $(Ti_{1-x}Al_x)N_y(001)$ layers are not sustained all through the film thickness, as similarly observed in a previous study of stoichiometric c-(Ti,Al)N film on MgO(001) [31]. The transition of the epitaxial growth mode to polycrystalline is attributed to the higher strain energy accumulating in the c-(Ti,Al)N(001) film than the c-(Ti,Al)N(111) film of the same chemical composition [31]. The $(Ti_{1-x}Al_x)N_y(001)$ thin films on MgO(001) with lower N contents have higher thickness of epitaxial layer. This is due to the high surface mobility of adatoms in N deficient conditions, which promotes epitaxial growth. Conical features that are oriented along 001 direction are nucleated in $(Ti_{1-x}Al_x)N_{0.67}(001)$ film, which contain segregated Al- and Ti-rich domains. The tendency of N to stick to Al in N deficient (Ti,Al)N system has likely initiated the phase segregation during growth.

In the as-deposited state, epitaxial $(Ti_{1-x}Al_x)N_y(111)$ film with the highest N vacancy concentration has the highest local strain. This is attributed to the change in lattice parameter in N deficient films [40, 41]. After annealing at 950ºC, the $(Ti_{1-x}Al_x)N_y$ films with different N concentration have undergone spinodal decomposition that causes more strain fluctuation in the system. This is due to the elastic differences and lattice mismatch of the Ti-rich and Al-rich domains, wherein some of the strain are relieved through misfit dislocations [42]. The strain maps of films after annealing at 950ºC validate these high strain regions, which are more pronounced and concentrated in the domain interfaces. The domains of the annealed films show elongations in the elastically soft [001] directions which is accord with what have previously been seen for annealed single crystal [31] and polycrystalline c-(Ti,Al)N films [43]. The elongation along the elastically soft directions is related to the minimization of the stored elastic energy. The coarsening is more pronounced for films with with higher N content (lesser N vacancy) as similarly observed in nitrogen-deficient arc deposited $(Ti_{1-x}Al_x)N_y$ films [16]. The smaller domain widths of the annealed films as N decreases is associated with the increased lattice mismatch which increases the elastic strain [40]. It was

shown that for decomposed domains, a more elongated structure signifies a more elastically constrained system [40]. Thus, it is presumed that N vacancies generally increase the coherency strain.

At 1100 ºC, the domain sizes of the $(Ti_{1-x}Al_x)N_y(111)$ films grow larger since coarsening has proceeded further. Domain coarsening is mainly driven by reduction of the interfacial energy in the system [40], while the coarsening rate is diffusion controlled and it increases with increasing temperature [43]. As the domains grow larger their interfaces become more separated and since the strain concentrations are located at the domain interfaces they also appear sparse. It is possible that the temperature is also sufficient for dislocation climb such that grain boundaries are formed at domain boundaries.

The decrease in hardness of the as-deposited c-$(Ti_{1-x}Al_x)N_y$ (y = 0.92, 0.79, and 0.67) films as the N content decreases is similar to what has been observed nitrogen deficient polycrystalline c-(Ti,Al)N [44]. Such softening due to vacancies has also been reported in other transition metal nitride systems, such as TiN [45, 46]. Their argument for vacancy softening is based on a predicted change in the nature of the atomic bonding in the presence vacancies that decreases the shear modulus and thereby the hardness [45]. However, others have reported vacancy hardening for the TiN and they attribute the observed vacancy hardening to pinning of dislocations at vacancies [35]. When annealed at 950 °C, hardness of the films with different N contents have increased because of the coherency strains and dislocation generated during decomposition. In addition to the coherency strains preventing propagation of dislocations during hardness measurements [47, 48], the dislocations generated by spinodal decomposition further acts as obstacles for dislocation motion. Some of this strain is possibly released in the films with high N contents that have formed grain boundaries when annealed at 1100 °C. Such grain boundaries may annihilate some of the dislocations formed during decomposition and combined with the strain release they increase the probability of dislocation movements resulting in a hardness decrease.

Conclusion

Epitaxial c-$(Ti_{1-x}Al_x)N_y(111)$ and c-$(Ti_{1-x}Al_x)N_y(001)$ thin films with average N concentration of y = 0.92, 0.79, and 0.67 were synthesized by sputtering deposition. $(Ti_{1-x}Al_x)N_y$ films with y = 0.92 and 0.79 films on MgO(111) substrates are single crystals all through the film thickness while the y = 0.67 film on MgO(111) contains coherently oriented w-(0001) structure as the film grows thicker. For the y = 0.92 and 0.79 films grown on MgO(001), a transition to a polycrystalline growth occurs after a certain thickness while y =

0.67 film on MgO(001) contains conical features, with segregated domains during growth. In the as-deposited state, GPA strain maps of the epitaxial c-$(Ti_{1-x}Al_x)N_y$(111) films show low strain field and the film with the highest N vacancies contain the most stain fluctuations among samples. After annealing at 950 ºC, epitaxial c-$(Ti_{1-x}Al_x)N_y$(111) and c-$(Ti_{1-x}Al_x)N_y$(001) have undergone spinodal decomposition and the domains are elongated along the [001] direction. The coarsening of TiN- rich and AlN- rich domains increases with N content. The formation of domains has caused an increase in the strain fluctuation of the c-$(Ti_{1-x}Al_x)N_y$ films. At this temperature, all films exhibit higher hardness as compared to its as-deposited state because of the higher strain field generated during decomposition. After annealing at 1100 ºC, the domain sizes of the films have further increased while strain concentration have decreased. At this temperature, most of the strains and dislocation in films with high N contents are released, which cause a decrease in their hardness values.

Acknowledgements

The work was supported by the European Union´s Erasmus Mundus doctoral program in Materials Science and Engineering (DocMASE), the Swedish Research Council (grants no 2017-03813 and 2017-06701), the Swedish government strategic research area grant AFM – SFO MatLiU (2009-00971) and VINNOVA (FunMat-II project grant no. 2016-05156).

Reference

[1] S.T. Oyama. Introduction to the chemistry of transition metal carbides and nitrides. The chemistry of transition metal carbides and nitrides. Springer, 1996. pp. 1-27.
[2] P. Jindal, A. Santhanam, U. Schleinkofer, A. Shuster. Performance of PVD TiN, TiCN, and TiAlN coated cemented carbide tools in turning, Int. J. Refract. Met. Hard Mater. 17 (1999) 163-170.
[3] S. PalDey, S. Deevi. Single layer and multilayer wear resistant coatings of (Ti, Al) N: a review, Mater. Sci. Eng., A 342 (2003) 58-79.
[4] M. Oden, L. Rogström, A. Knutsson, M. Terner, P. Hedström, J. Almer, J. Ilavsky. In situ small-angle x-ray scattering study of nanostructure evolution during decomposition of arc evaporated TiAlN coatings, Appl. Phys. Lett. 94 (2009) 053114.
[5] A. Knutsson, M. Johansson, P.Å. Persson, L. Hultman, M. Odén. Thermal decomposition products in arc evaporated TiAlN/TiN multilayers, Appl. Phys. Lett. 93 (2008) 143110.
[6] L. Rogström, J. Ullbrand, J. Almer, L. Hultman, B. Jansson, M. Odén. Strain evolution during spinodal decomposition of TiAlN thin films, Thin Solid Films 520 (2012) 5542-5549.
[7] F. Tasnádi, I.A. Abrikosov, L. Rogström, J. Almer, M.P. Johansson, M. Odén. Significant elastic anisotropy in Ti1−xAlxN alloys, Appl. Phys. Lett. 97 (2010) 231902.
[8] B. Alling, M. Odén, L. Hultman, I. Abrikosov. Pressure enhancement of the isostructural cubic decomposition in Ti 1− x Al x N, Appl. Phys. Lett. 95 (2009) 181906.

[9] N. Norrby, H. Lind, G. Parakhonskiy, M.P. Johansson, F. Tasnádi, L.S. Dubrovinsky, N. Dubrovinskaia, I.A. Abrikosov, M. Odén. High pressure and high temperature stabilization of cubic AlN in Ti0.60Al0.40N, J. Appl. Phys. 113 (2013) 053515.
[10] H. Lind, R. Forsén, B. Alling, N. Ghafoor, F. Tasnadi, M. Johansson, I. Abrikosov, M. Odén. Improving thermal stability of hard coating films via a concept of multicomponent alloying, Appl. Phys. Lett. 99 (2011) 091903.
[11] R. Forsén, M. Johansson, M. Odén, N. Ghafoor. Decomposition and phase transformation in TiCrAlN thin coatings, J. Vac. Sci. Technol., A 30 (2012) 061506.
[12] A. Knutsson, M. Johansson, L. Karlsson, M. Odén. Thermally enhanced mechanical properties of arc evaporated Ti0. 34Al0. 66N/TiN multilayer coatings, J. Appl. Phys. 108 (2010) 044312.
[13] M. to Baben, L. Raumann, D. Music, J.M. Schneider. Origin of the nitrogen over- and understoichiometry in Ti0.5Al0.5N thin films, J Phys-Condens Mat 24 (2012) 155401.
[14] M. to Baben, M. Hans, D. Primetzhofer, S. Evertz, H. Ruess, J.M. Schneider. Unprecedented thermal stability of inherently metastable titanium aluminum nitride by point defect engineering, Mater. Res. Lett. (2016) 1-12.
[15] K. Grönhagen, J. Ågren, M. Odén. Phase-field modelling of spinodal decomposition in TiAlN including the effect of metal vacancies, Scripta Mater. 95 (2015) 42-45.
[16] I.C. Schramm, M.P. Johansson Jõesaar, J. Jensen, F. Mücklich, M. Odén. Impact of nitrogen vacancies on the high temperature behavior of (Ti1−xAlx)Ny alloys, Acta Mater. 119 (2016) 218-228.
[17] K. Calamba, I. Schramm, M. Johansson Jõesaar, J. Ghanbaja, J. Pierson, F. Mücklich, M. Odén. Enhanced thermal stability and mechanical properties of nitrogen deficient titanium aluminum nitride (Ti0. 54Al0. 46Ny) thin films by tuning the applied negative bias voltage, J. Appl. Phys. 122 (2017) 065301.
[18] K.M. Calamba, M.P. Johansson Jõesaar, S. Bruyère, J.F. Pierson, R. Boyd, J.M. Andersson, M. Odén. The effect of nitrogen vacancies on initial wear in arc deposited (Ti0.52,Al0.48)Ny, (y < 1) coatings during machining, Surf. Coat. Technol. 358 (2019) 452-460.
[19] B. Syed, M.J. Jöesaar, P. Polcik, S. Kolozsvari, G. Håkansson, L. Johnson, M. Ahlgren, M. Odén. Effect of work function and cohesive energy of the constituent phases of Ti-50 at.% Al cathode during arc deposition of Ti-Al-N coatings, Surf. Coat. Technol. 357 (2019) 393-401.
[20] A. Hörling, L. Hultman, M. Odén, J. Sjölén, L. Karlsson. Thermal stability of arc evaporated high aluminum-content Ti1−xAlxN thin films, J. Vac. Sci. Technol., A 20 (2002) 1815-1823.
[21] N. Norrby, M.P. Johansson, R. M'Saoubi, M. Odén. Pressure and temperature effects on the decomposition of arc evaporated Ti0.6Al0.4N coatings in continuous turning, Surf. Coat. Technol. 209 (2012) 203-207.
[22] D. Gall, C.-S. Shin, T. Spila, M. Odén, M. Senna, J. Greene, I. Petrov. Growth of single-crystal CrN on MgO (001): Effects of low-energy ion-irradiation on surface morphological evolution and physical properties, J. Appl. Phys. 91 (2002) 3589-3597.
[23] N. Ghafoor, L.J. Johnson, D.O. Klenov, J. Demeulemeester, P. Desjardins, I. Petrov, L. Hultman, M. Odén. Nanolabyrinthine ZrAlN thin films by self-organization of interwoven single-crystal cubic and hexagonal phases, APL Materials 1 (2013) 022105.
[24] H. Söderberg, M. Odén, T. Larsson, L. Hultman, J.M. Molina-Aldareguia. Epitaxial stabilization of cubic-Si N x in Ti N⁄Si N x multilayers, Appl. Phys. Lett. 88 (2006) 191902.
[25] M. Odén, H. Ljungcrantz, L. Hultman. Characterization of the induced plastic zone in a single crystal TiN (001) film by nanoindentation and transmission electron microscopy, Journal of materials research 12 (1997) 2134-2142.

[26] J.M. Molina-aldareguia, S.J. Lloyd, M. Odén, T. Joelsson, L. Hultman, W.J. Clegg. Deformation structures under indentations in TiN/NbN single-crystal multilayers deposited by magnetron sputtering at different bombarding ion energies, Philosophical Magazine A 82 (2002) 1983-1992.
[27] C.-S. Shin, D. Gall, P. Desjardins, A. Vailionis, H. Kim, I. Petrov, J. Greene, M. Odén. Growth and physical properties of epitaxial metastable cubic TaN (001), Appl. Phys. Lett. 75 (1999) 3808-3810.
[28] C.-S. Shin, D. Gall, Y.-W. Kim, P. Desjardins, I. Petrov, J. Greene, M. Odén, L. Hultman. Epitaxial NaCl structure δ-TaN x (001): Electronic transport properties, elastic modulus, and hardness versus N/Ta ratio, J. Appl. Phys. 90 (2001) 2879-2885.
[29] A. Le Febvrier, L. Landälv, T. Liersch, D. Sandmark, P. Sandström, P. Eklund. System for magnetron sputtering in a ultra-high vacuum system for deposition of oxide, oxynitride, nitride, metallic thin films, (2019).
[30] A. Le Febvrier, J. Jensen, P. Eklund. Wet-cleaning of MgO (001): Modification of surface chemistry and effects on thin film growth investigated by x-ray photoelectron spectroscopy and time-of-flight secondary ion mass spectroscopy, J. Vac. Sci. Technol., A 35 (2017) 021407.
[31] K. Calamba, J. Pierson, S. Bruyère, A.l. Febvrier, P. Eklund, J. Barrirero, F. Mücklich, R. Boyd, M.P. Johansson Jõesaar, M. Odén. Dislocation structure and microstrain evolution during spinodal decomposition of reactive magnetron sputtered heteroepixatial c-(Ti0.36,Al0.64)N/c-TiN films grown on MgO(001) and (111) substrates.
[32] H. Rösner, C.T. Koch, G. Wilde. Strain mapping along Al–Pb interfaces, Acta Mater. 58 (2010) 162-172.
[33] W.C. Oliver, G.M. Pharr. An improved technique for determining hardness and elastic modulus using load and displacement sensing indentation experiments, Journal of Materials Research 7 (2011) 1564-1583.
[34] M. Ohring. Materials science of thin films, Elsevier, 2001.
[35] C.-S. Shin, D. Gall, N. Hellgren, J. Patscheider, I. Petrov, J. Greene. Vacancy hardening in single-crystal TiN x (001) layers, J. Appl. Phys. 93 (2003) 6025-6028.
[36] K. Calamba, J. Barrirero, M.P. Johansson Jõesaar, S. Bruyère, J. Pierson, A.l. Febvrier, P. Eklund, F. Mücklich, R. Boyd, M. Odén. Growth and high temperature decomposition of epitaxial metastable wurtzite (Ti1-x,Alx)N(0001) thin films
[37] B. Alling, A. Karimi, L. Hultman, I.A. Abrikosov. First-principles study of the effect of nitrogen vacancies on the decomposition pattern in cubic Ti1−xAlxN1−y, Appl. Phys. Lett. 92 (2008) 071903.
[38] B. Zhang, X.-P. Wang, Z.-J. Shen, X.-B. Li, C.-S. Wang, Y.-J. Chen, J.-X. Li, J.-X. Zhang, Z. Zhang, S.-B. Zhang, X.-D. Han. Vacancy Structures and Melting Behavior in Rock-Salt GeSbTe, Scientific Reports 6 (2016) 25453.
[39] Y. Zheng, Y. Cheng, R. Huang, R. Qi, F. Rao, K. Ding, W. Yin, S. Song, W. Liu, Z. Song, S. Feng. Surface Energy Driven Cubic-to-Hexagonal Grain Growth of Ge2Sb2Te5 Thin Film, Scientific Reports 7 (2017) 5915.
[40] M. Doi. Elasticity effects on the microstructure of alloys containing coherent precipitates, Prog. Mater Sci. 40 (1996) 79-180.
[41] R. Forsén, N. Ghafoor, M. Odén. Coherency strain engineered decomposition of unstable multilayer alloys for improved thermal stability, J. Appl. Phys. 114 (2013) 244303.
[42] J. Ullbrand, K. Grönhagen, F. Tasnádi, B. Jansson, M. Odén. Microstructure evolution of TiAlN-a phase field study.
[43] A. Knutsson, J. Ullbrand, L. Rogström, N. Norrby, L. Johnson, L. Hultman, J. Almer, M.J. Jöesaar, B. Jansson, M. Odén. Microstructure evolution during the isostructural

decomposition of TiAlN—A combined in-situ small angle x-ray scattering and phase field study, J. Appl. Phys. 113 (2013) 213518.
[44] I.C. Schramm, C. Pauly, M.P. Johansson Jõesaar, S. Slawik, S. Suarez, F. Mücklich, M. Odén. Effects of nitrogen vacancies on phase stability and mechanical properties of arc deposited (Ti0.52Al0.48)Ny (y<1) coatings, Surf. Coat. Technol. 330 (2017) 77-86.
[45] S.-H. Jhi, S.G. Louie, M.L. Cohen, J. Ihm. Vacancy Hardening and Softening in Transition Metal Carbides and Nitrides, Phys. Rev. Lett. 86 (2001) 3348-3351.
[46] H. Holleck. Material selection for hard coatings, J. Vac. Sci. Technol., A 4 (1986) 2661-2669.
[47] A. Hörling, L. Hultman, M. Odén, J. Sjölén, L. Karlsson. Mechanical properties and machining performance of Ti1−xAlxN-coated cutting tools, Surf. Coat. Technol. 191 (2005) 384-392.
[48] I.A. Abrikosov, A. Knutsson, B. Alling, F. Tasnádi, H. Lind, L. Hultman, M. Odén. Phase stability and elasticity of TiAlN, Materials 4 (2011) 1599-1618.